Collagen Anchoring Agonist Antibodies for Cancer Immunotherapy

By
Joseph Robert Palmeri

B.S.E. Chemical Engineering, Case Western Reserve University (2017)

Submitted to the Department of Chemical Engineering in partial fulfillment of the requirements for the degree of

DOCTOR OF PHILOSOPHY IN CHEMICAL ENGINEERING

at the

MASSACHUSETTS INSTITUTE OF TECHNOLOGY
June 2023

Authored by: _____
Joseph Robert Palmeri
Department of Chemical Engineering
March 14th, 2023

Certified by: _____
K. Dane Wittrup, Ph.D.
Carbon P. Dubbs Professor of Chemical and Biological Engineering, MIT
Thesis Advisor

Accepted by: _____
Patrick S. Doyle, Ph.D.
Robert T. Haslam Professor of Chemical Engineering, MIT
Chairman, Committee for Graduate Students

Thesis Committee Members

K. Dane Wittrup, Ph.D. *(Thesis Advisor)*
Carbon P. Dubbs Professor of Chemical Engineering and Biological Engineering
Koch Institute for Integrative Cancer Research at Massachusetts Institute of Technology

J. Christopher Love, Ph.D.
Raymond A. (1921) and Helen E. St. Laurent Professor of Chemical Engineering
Koch Institute for Integrative Cancer Research at Massachusetts Institute of Technology

Darrell J. Irvine, Ph.D.
Professor of Material Science & Engineering and Biological Engineering
Koch Institute for Integrative Cancer Research at Massachusetts Institute of Technology

Michael Dougan, M.D., Ph.D.
Assistant Professor of Medicine, Division of Gastroenterology
Massachusetts General Hospital and Harvard School of Medicine

Collagen Anchoring Agonist Antibodies for Cancer Immunotherapy
by
Joseph R. Palmeri

Submitted to the Department of Chemical Engineering on March 14th, 2023
In partial fulfillment of the requirements for the degree of
Doctor of Philosophy in Chemical Engineering

Abstract

While traditional cancer interventions such as surgery, radiation, and chemotherapy are aimed at killing or removing the tumor cells themselves, immunotherapies instead seek to establish long-lasting, robust antitumor immune responses. One approach that has shown promising results in preclinical mouse models is the use of agonist antibodies targeting costimulatory, or activating, receptors on effector immune cells, particularly $CD8^+$ T cells. Translation of these therapeutics into the clinic has been hampered by severe, sometimes fatal, on-target, off-tumor toxicities. Thus, the field at large has shifted focus to developing agonist antibodies with tumor restricted activity. To that end, we developed collagen anchored agonist antibodies, an approach we have previously validated with collagen anchored cytokines. When injected directly into the tumor, these collagen anchoring therapies are preferentially retained in the tumor microenvironment (TME), enhancing efficacy while limiting systemic toxicities.

We first attempted to engineer a generalizable antibody-anchoring platform by constructing fusions of IgG binding domains (IgGBs) to collagen binding domains. However, due to the weak affinity of existing IgGBs and rapid *in vivo* exchange with endogenous IgG, this platform underperformed at retaining agonist antibodies in the TME.

We then pivoted to constructing direct agonist antibody fusions to collagen binding domains, demonstrating that this is a strategy generalizable to a range of antibody therapeutics. *In vivo*, we tested agonist antibodies targeting 4-1BB and CD28 fused to the collagen binding domain LAIR (α4-1BB-LAIR and αCD28-LAIR, respectively), in a range of monotherapy and combination therapies. We observed that while combination treatment of α4-1BB-LAIR with an antitumor antibody (TA99) displayed only modest efficacy in the B16F10 murine melanoma model, simultaneous depletion of $CD4^+$ T cells during treatment boosted cure rates to over 90% of mice. We elucidated two mechanisms of action for this synergy: αCD4 eliminated tumor draining lymph node Tregs, enhancing priming and activation of $CD8^+$ T cells, and TA99 + α4-1BB-LAIR supported the cytotoxic program of these newly primed $CD8^+$ T cells within the TME. Replacement of αCD4 with αCTLA-4, a clinically approved antibody that enhances T cell priming, produced equivalent cure rates while additionally generating robust immunological memory. Together, my thesis work demonstrates that collagen anchoring is an effective strategy to improve the therapeutic index of agonist antibody therapies and furthermore uncovers a fundamental two-step approach to designing effective cancer immunotherapy combinations.

Thesis Supervisor: K. Dane Wittrup, Ph.D.
Title: Carbon P. Dubbs Professor of Chemical Engineering and Biological Engineering

Acknowledgements

A PhD often feels like a solo endeavor. Even within a cohesive research group such as ours, everyone has their own independent project that come with unique challenges. Riding the highs and lows of research can feel isolating at times. However, the truth is a *successful* PhD is truly a community effort. Good science takes collaborations and contributions from colleagues. And more importantly, pushing through unavoidable bouts of science gone wrong requires support from colleagues and friends near and far. I could write another 200 pages about the people, places, and experiences that have gotten me through these past 5+ years of grad school, but to spare you all (and make sure I have time to finish the scientific parts of this work) I'll try to be brief.

First and foremost, I owe a huge debt of gratitude to my PhD advisor, Dane. Thanks for taking a chance on some kid who had never held a micropipette and didn't know the difference between a $CD4^+$ and $CD8^+$ T cell. Dane has been nothing but supportive during my graduate studies since day one. Staying engaged enough to provide guidance while still allowing me to steer my own projects and grow as independent researchers is a fine line to walk, and Dane navigated it exceedingly well. I am grateful that he allowed me to follow the research questions that interested me - even as I pushed the bounds of our group's collective immunology skillset. This freedom has allowed me to discover my own research interests and passions and become a better scientist. I wouldn't be where I am today without Dane's unwavering support, and I hope I can be just as effective as a mentor in my own independent research career.

I credit my initial love for research to Dr. Mohan Sankaran, my undergraduate research advisor at CWRU (he has since moved his lab to UIUC). I spent all 4 years of undergrad working in Mohan's lab and even though I was a clueless 18-year-old he let me take on my own project and always made me feel like I was a part of the team. I thought I was working in his lab just to gain some hands-on experience to put on my resume and quickly found my love for research in his group. Without his encouragement and guidance, I do not know if I would have pursued a PhD. Also, thank you to Andres Bujanda and Derek Demaree, my research mentors at ARL, who helped to reaffirm my love for research (and gave me a taste of what non-academic research is like). Derek and Andy were not only great mentors but became close friends during my time in Baltimore.

A special thanks to my committee members Chris Love, Darrell Irvine, and Michael Dougan who have been a constant source of support and scientific insight throughout my PhD. You all helped to push the science further and I am thankful you all agreed to serve on my committee. It has been a pleasure learning from all of you over the years. I am particularly thankful to Michael who took extra time to provide career advice outside of our regularly scheduled committee meetings.

The Wittrup lab has been a phenomenal environment to train in and I've learned so much from all my colleagues. Alison, Adrienne, Naveen, Noor, Emi, Alli, Yash, Sarah, Bri, Keith, Anthony, Jordan, Luciano, Megan, Lauren, Owen, Liz, David, Bill, Henry, and Cora - thanks for fostering such a supportive, collaborative, and fun environment. You all were not only great colleagues but even better friends. I will miss our meandering office chats, group runs, and after work happy hours. I greatly

appreciate you all putting up with my vast, and often obscure, music taste in lab. I don't know a lot of labs that go from running 12 hour flow cytometry experiments one week to physically running 200 mile relay races the next, but I do know I am grateful to have been a part of this group.

A few people in particular - Alli, Yash, Sarah, and I joined the lab together and it has been a pleasure to get to know you all and go through this journey alongside you three. To Lauren, Luciano, and Jordan: I've truly enjoyed all our lunch breaks, science haikus, memes, and productive collaborations. You all have been some of my closest friends in grad school. Thanks for making the lab such a fun place. I will miss you all dearly and I look forward to our continued friendships after grad school!

A special thanks to Bri, who has been not only a critical collaborator but also one of my closest friends in grad school. Thanks for putting up with me bothering you in the office all day. Our friendship has evolved a lot along the way, and you are truly one of my closest friends here. I know I can always count on you for advice in and out of lab and I cannot picture my time in the Wittrup lab, or in Boston, without you. It has been a privilege to work alongside you and see you grow as a scientist and I look forward to seeing all that you accomplish in the future. I will truly miss seeing you all day long, but I know that we have many adventures ahead of us. And an extra thank you for adopting Tucker (temporarily) and Cookie (permanently). Having a lab pup has been one of the unexpected perks of the Wittrup lab and I will really miss them.

I had the pleasure of mentoring two phenomenal undergraduate students during my PhD - Izumi and Shira. I learned so much about how to be a good mentor and educator working with you both. I'm excited to see what you all accomplish in your careers. Thanks in particular to Izumi for entrusting me (and her co-mentor Noor) to guide her through her senior thesis research and who has remained a close friend after graduating. Looking forward to visiting you on the west coast!

A huge thanks to the rotating cast of Elm Street roommates - Atti, Josh, Tomer, Raph, Jake, Chatty, Spencer, Trey, and Ashwin. Our culinary adventures, DIY projects, and admiration for obscure competition reality TV shows kept me sane throughout grad school. It's been wonderful living with you all over the years. Many days in grad school I found myself drained and having such a supportive environment to come home to was invaluable. I'm glad to call you all close friends. I will really miss living in that apartment and I will certainly cherish the countless memories we have from our time there.

I wouldn't have survived this PhD without my workout buddy, fellow yacht chef, and grad school best friend Atti. As the only three attendees of the MIT BE visit weekend, there was no doubt Atti, Josh, and I were going to be friends, but I couldn't have anticipated how special our friendship would be. Atti and I arrived in Boston on the same day and spent the next 5 years living together, longer than I've lived with anyone besides my immediate family. The two of us have experienced the highs and lows of these past 6 years side by side and I can't imagine my journey here any other way. Thanks for always being there for me. So many of my favorite memories from graduate school are with you and I'm looking forward to many more fun times together.

Another special note of appreciation to Jake, who moved into Elm during the depths of the

pandemic and quickly became one of my best friends. Thanks for sharing your love of music with me and introducing me to my favorite band of all time, Slaughter beach, Dog. (And thanks to SBD, whose music got me through some of the harder parts of pandemic grad school). Also thank you for getting a second job at Lamplighter and securing me a constant source of free beer after long days at lab.

A special nod to my quarantine pod Atti, Elena, Josh, Iz and Raph. I couldn't have picked a better group to be stuck inside with for three months straight and thanks for keeping me endlessly entertained during those uncertain times. Also, thanks to Juliet who proved that you can make real friends on twitter. Our weekly movie nights and baking adventures during the height of the pandemic were always a nice break from the craziness of the grad school COVID era.

I'm blessed to have so many friends in the Boston area and beyond. In addition to those I've already mentioned, thanks to the entire 2017 MIT ChemE PhD cohort (along with the 2017 MIT BE PhD cohort who allowed me to be an honorary member), Amber, Amanda, Emma, Chris, Gallagher, Alycia, Vanitha, Steph (Friend and Gaglione!), Haley, Ashley, Sasan, Howard, and Katie for being supportive friends throughout this long journey. And thanks to Robyn, Matt, Fiona, Steve, Will, Sara, and Erik for stopping through Boston throughout the years and pulling me out of the MIT bubble. Cheers to my friends across the pond from ImmunOctoberfest 2022! Hope to see you all at the next one. And thank you to those friends and family in the Buffalo area as well as in Houston and Scottsdale. I didn't get to visit as much as I would have liked these past few years (partially because of graduate school, partially because of the pandemic), but you all have been so loving and supportive when I did. Looking forward to having more time to spend together after graduation!

And lastly and most importantly thank you to my parents. I wouldn't be where I am today without your never-ending love and support. Always eager to tell anyone who will listen about their son who studies at MIT - you all have been my biggest cheerleaders and given me the support to follow my dreams. Thank you for always being understanding of my long work hours or when I needed to pop into lab while you were in town to passage my cells or check on my mice. I could not have asked for more supportive or loving parents and words cannot convey what you both mean to me. From our COVID Christmas at Elm Street to our two-week post defense Italy trip we've managed to squeeze a lot of memories into these crazy few years of grad school. Looking forward to many more family adventures in the future and I love you guys.

Table of Contents

List of Figures

List of Tables

Chapter 1: Introduction

Cancer immunotherapy: a paradigm shift in cancer treatment

Despite tens of billions of dollars invested in oncology R&D annually, cancer is still responsible for 1 out of every 6 deaths worldwide, with an estimated 10 million people succumbing to this disease annually (1). Over the past several thousand years, dating back to ancient Egypt, there have been sporadic case reports of spontaneous tumor regression, with nearly all cases occurring with concurrent infection (2, 3). Based on these case reports, in the late 1800s Dr. William Coley began injecting patients locally with various bacterial formulations and observed substantial tumor shrinkage, publishing his first results in 1891 (4). Although Coley treated thousands of patients over his career and published dozens of papers on the efficacy of this approach (termed "Coley's Toxin"), inconsistencies in his work due to poor study design and the use of various formulations and administration strategies led to extensive criticism and the practice was largely abandoned (5). Coley's toxin is now considered the first cancer immunotherapy treatment, with Coley himself often recognized as the "Father of cancer immunotherapy" (so much so that the Cancer Research Institute now gives out an annual prestigious "William B. Coley Award" to recognize outstanding work in the tumor immunology field).

Throughout the 20th century, several fundamental immunological discoveries, including the identification of T cells, dendritic cells, and NK cells, gave us a better understanding of how the immune system recognizes and kills tumor cells (3). For over 40 years now intravesical delivery of Bacillus Calmette-Guérin (BCG), a live attenuated virus, has been the standard of care for bladder

cancer and in 1990 became the one of the first U.S. Food and Drug Administration (FDA) approved cancer immunotherapies (6). Around the same time, recombinant interferon alpha (IFNα) and interleukin 2 (IL-2) also received approval for treatment in several different cancer indications (7, 8). Although these biologics induced robust antitumor immune responses, they were also hampered by severe immune related adverse events (irAEs), with treatment related adverse deaths for high dose IL-2 therapy initially in the 2-4% range. Thus, it was not until the approval of αCTLA-4, the first checkpoint blockade therapy, for metastatic melanoma in 2011 that cancer immunotherapy cemented its role as a new pillar of cancer treatment (9). This approval along with ongoing promising trials of αPD-1 therapy and CAR-T cell therapies at the time led to *Science* magazine naming cancer immunotherapy the 2013 breakthrough of the year (10). In the ensuing 10 years, cancer immunotherapy has seen a boom, with a range of checkpoint blockade approvals and CAR-T cell therapies for a number of indications (11, 12). A 2019 survey cataloged almost 4,000 active immuno-oncology drugs in development (13). This includes a wide array of modalities, including cytokines, cell therapies, antibodies, oncolytic viruses, and cancer vaccines, among others. In this thesis, we focus on agonist antibody therapies, a class of antibody drugs that bind to and drive signaling through activating receptors expressed on effector immune cells in an effort to improve their anticancer capacity.

Agonist antibodies drive signaling through activating receptors

Agonist antibodies are a class of therapeutics that bind to and elicit signaling through their target receptor (differing from antagonists, such as those used in checkpoint blockade therapy, which instead seek to block signaling through their target receptor). In the context of cancer immunotherapy, agonist antibodies typically target activating or costimulatory receptors expressed on effector cells and include targets such as CD28, 4-1BB, CD40, OX40, GITR, CD27, and ICOS (14–16). Signaling through these

receptors leads to a wide range of downstream effects, some overlapping and some distinct. In general, these costimulatory receptors lead to increased proliferation and survival, improved effector function, and better antitumor immune responses.

It is widely appreciated that signaling through costimulatory receptors requires receptor clustering, and this is typically accomplished endogenously through trans presentation of dimeric (CD28 superfamily receptors) or trimeric (most tumor necrosis factor receptor superfamily (TNFRSF) receptors) ligands by antigen presenting cells (APCs). In the case of agonist antibody induced signaling, antibody affinity and epitope can play a role but often signaling is driven by Fc gamma receptor (FcγR) mediated antibody cross linking, which then drives receptor clustering (17). Mice and humans express a wide range of FcγRs, most of which are "activating" receptors that contain an immunoreceptor tyrosine-based activation motif (ITAM), which transmits positive signals to FcγR expressing (primarily myeloid) cells, leading to cell activation and antibody dependent cellular cytotoxicity (ADCC) and/or antibody dependent cellular phagocytosis (ADCP). In addition, both species express an inhibitory receptor (FcγRIIB) that instead contains an immunoreceptor tyrosine-based inhibitory motif (ITIM), which delivers an inhibitory signal and crucially does *not* elicit ADCC/ADCP (18–20). Preclinical studies have demonstrated that agonist antibodies which bind preferentially to FcγRIIB (which is also referred to having a low activating:inhibitory, or A:I, ratio) led to optimal signaling. This has been most extensively studied in the context of αCD40 agonists but has also been highlighted in the context of other agonists such as α4-1BB agonist antibodies (21–24). In these studies, use of antibody isotypes that have high A:I ratios (mIgG2a) have minimal immunostimulatory capacity (and instead can lead to target cell depletion), where antibody isotypes that have low A:I ratios (mIgG1) were potent agonists. *In vitro*, however, activating FcγR are also able to drive agonism and thus the critical role for

FcγRIIB engagement may be the lack of ADCC/ADCP, increased *in vivo* bioavailability of this receptor, or a combination of the two (16). This mechanism of action has several consequences. For one, FcγR expression on myeloid cells in the liver may contribute to the observed hepatic toxicity of both αCD40 agonists and α4-1BB agonists (25, 26). Additionally, because of the required ternary interactions between both target receptor and FcγR, these agonist antibodies often exhibit bell shaped response curves, with a "sweet spot" dose of maximum agonism (16). Furthermore, because of tumor-to-tumor heterogeneity in levels of infiltration of 1) effector cells expressing the agonist target receptor and 2) myeloid cells expressing FcγRs, this optimal dosing point can vary from patient to patient, further complicating the dosing of these agonist antibodies.

Although there is a wide range of interesting costimulatory targets being explored both preclinically and clinically, in this thesis we focus on CD28 and 4-1BB. Below we provide basic immunology background and brief summaries of preclinical development to date surrounding these two targets.

CD28

CD28 is a constitutively expressed immunoglobulin (Ig) family surface cell receptor present on the cell surface as a disulfide linked homodimer expressed on nearly all naive T cells in humans as well as nearly all $CD4^+$ T cells and about half of $CD8^+$ T cells in the periphery. In contrast, CD28 is expressed on all T cells in mice (27, 28). CD28 has two endogenous ligands, CD80 (B7.1) and CD86 (B7.2) that are both expressed at high levels on APCs, albeit with slightly altered temporal dynamics. CD28 binds to both ligands with similar affinities (4 μM and 20 μM for CD80 and CD86, respectively) (29). Notably, CD28 competes with CTLA-4 for binding to these two ligands (with CTLA-4 having a higher affinity for both), and therefore CTLA-4 represents a counter regulatory mechanism for CD28 signaling (30). CD28 is canonically thought of as "signal two" in the two-signal T cell priming

hypothesis, with "signal one" being TCR engagement with its cognate peptide displayed on MHC (31). T cells that only receive signals through the TCR without CD28 signaling become anergic or undergo apoptosis, an important aspect of peripheral tolerance and a means to prevent activation of self-reactive T cells that were not deleted in the thymus (32). Thus, CD28 signaling is critical for proper T cell priming and differentiation.

Signaling through CD28 acts on a diverse range of downstream targets (33). CD28 signaling activates phosphoinositide-3 kinase (PI3K) which increases cell metabolism and promotes cell survival by increasing expression of Bcl family pro-survival factors. Downstream signaling via growth factor receptor-bound protein 2 (Grb2), on the other hand, leads to increased IL-2 expression and activation of transcription factors such as NFAT, NFκB, and AP-1. Overall, CD28 signaling leads to enhanced proliferation and survival, altered cell metabolism, actin cytoskeleton rearrangement, co-stimulatory receptor expression, and cytokine production.

Early preclinical work in the cancer immunology field demonstrated that tumor cells lines engineered to express B7, the endogenous ligand for CD28, were spontaneously rejected after implantation in a $CD8^+$ T cell dependent manner. Additionally, there were early reports of evidence of tumor growth delay in tumor bearing mice with treated with αCD28 (34, 35). However, development of αCD28 agonists was largely halted after a phase I clinical trial of an αCD28 superagonist (TGN1412) had disastrous results, with 6 health volunteers hospitalized in the ICU after experiencing severe cytokine release syndrome (CRS) mere hours after infusion of the drug (36). It was later found that effector memory $CD4^+$ T cells were the likely culprit of this life-threatening case of CRS, and all development of this biologic was stopped (37). More recently, there has been renewed interest in targeting CD28

for cancer immunotherapy, specifically using trispecifics/bispecifics targeting PD-L1 or tumor antigens and CD28 (and CD3 in the case of trispecifics) to restrict activity of these agonists to the tumor microenvironment (38–42). Three of these bispecifics targeting MUC16, PSMA, and EGFR have entered clinical testing and early results for the EGFRxCD28 bispecific showing it is well tolerated with no dose limiting toxicities observed thus far (43–45). An engineered CD80-Fc fusion that is able to simultaneously block PD-L1 and CTLA-4 while agonizing CD28 (ALPN-202, davoceticept) has also displayed improved efficacy over αPD-L1 alone in humanized mouse models and in early phase I trials has been well tolerated (46, 47). Thus, there has been a renewed appetite, and favorable early safety signals, for tumor localized αCD28 agonists.

4-1BB (CD137)

4-1BB, also known as CD137 or tumor necrosis factor receptor super family 9 (TNFRSF9) is a cell surface receptor not expressed on naive T cells but is upregulated on both $CD4^+$ and $CD8^+$ T cells upon activation (48). It is also expressed on a host of other cells, including activated NK cells, dendritic cells, monocytes, neutrophils, B cells, and endothelial cells (49–51). 4-1BB exists both as a monomer and dimer on the cell surface (52, 53). 4-1BB's ligand, 4-1BBL, is expressed as a trimer on the surface of APCs and successful signaling requires the trimeric ligand binding with a trimer of 4-1BB and then subsequent higher order clustering of these trimeric receptors (54, 55). The signaling cascade following trimer clustering is complicated, but is primarily mediated through two signaling adapters, TNF receptor associated factors 1 and 2 (TRAF1 and TRAF2), which bind to the cytoplasmic tail of 4-1BB. When multiple TRAF2 proteins are brought in close proximity to one another a polyubiquitin chain is formed which recruits additional adaptor proteins leading to further signal transmission and eventual activation of NFκB. The exact function of TRAF1 in 4-1BB signaling is, on the other hand, not as well understood (56).

4-1BB signaling can lead to Th1 polarization, prevention of antigen induced cell death (AICD), increased proliferation, improved effector function, and increased cytokine production (56–60). 4-1BB also plays a pivotal role in the formation and maintenance of memory $CD8^+$ T cells via modulation of autocrine IL-2 signaling (60). Furthermore, on NK cells 4-1BB signaling can lead to upregulation of the high affinity IL-2Rα (CD25) as well as increased proliferation, IFNγ production, and in some cases enhanced cytotoxicity (61–64).

It was first demonstrated over 25 years ago by Melero and colleagues that agonist antibodies targeting 4-1BB could enhance $CD8^+$ T cell mediated antitumor immunity and eradicate tumors in certain contexts (65). Since then, many preclinical studies have reported efficacy of α4-1BB agonist antibodies alone and in combination with a wide range of immunomodulators, including but not limited to other agonist antibodies, cytokine therapies, vaccines, and checkpoint blockade therapies (66). Clinical stage α4-1BB agonists first entered human trials in 2005, with Urelumab and Utomilumab being the first two agonist antibodies targeting 4-1BB tested in patients. Urelumab was initially promising in early phase I trials, but severe liver toxicities in phase II trials, including two cases of fatal liver toxicity, has necessitated drastically decreasing the dose of this antibody. At safe doses, this antibody has seen limited efficacy (67). Utomilumab, on the other hand, has an excellent safety profile but little clinical activity, and thus development has been discontinued (68, 69). The different isotypes of these antibodies (Urelumab being human IgG4 and Utomilumab human IgG2) and their different epitopes (Urelumab does not compete with 4-1BBL, while Utomilumab) likely explains the different agonistic capabilities of these two biologics (68). Since these two antibodies first entered the clinic, a slew of second generation α4-1BB agonists have followed suit, with at least 41 new α4-1BB agonists entering

clinical testing between January 2017 and December 2022 (66, 70). Some of these agonists are standard IgG formats with engineered Fc regions to modulate FcγRIIB binding (and thus differential reliance of FcγR mediated clustering) and/or targeting different epitopes than Urelumab/Utomilumab, with hopes that these changes will be enough to identify a "sweet spot" between these two agonists with optimal clinical activity and tolerability. However, the vast majority of new α4-1BB agonists entering the clinic employ various strategies to limit activity to the tumor microenvironment (TME) (and/or the tumor draining lymphoid tissue), either through the use of bispecifics that bind to 4-1BB and either a tumor associated antigen such as HER2 or another immunological target such as PD-L1, or by engineering antibodies that only function in tumor specific biochemical niches, such as antibodies that only bind in ATP rich environments or antibodies whose binding domains are masked and only rendered functional after cleavage by tumor specific proteases (71–75). Many of these next generation α4-1BB agonists have just begun phase I trials and data on their safety and clinical efficacy is not yet available. However, taking a holistic view of the state of α4-1BB agonist development, it is clear that the field has largely converged onto efforts to engineer α4-1BB agonists with TME restricted activity.

Intratumoral immunotherapy

Intratumoral immunotherapy is as old as immunotherapy itself, with the aforementioned Coley's toxin injected directly into visible sarcoma and carcinoma lesions. BCG, discussed previously in the context of bladder cancer, has also been tested as an intratumoral therapy in other indications outside of bladder cancer, such as malignant melanoma and head and neck sarcoma (76, 77). In 2015, the first intratumoral oncolytic viral therapy, Talimogene laplherparepvec (T-VEC) was approved by the FDA for treatment of unresectable melanoma based on high response rates reported in phase III trials (78,

79). However, difficulties with accessing tumors beyond cutaneous/subcutaneous lesions limited widespread adoption of intratumoral strategies.

Improvements in interventional radiology, endoscopy, and laparoscopy have made once inaccessible lesions accessible, expanding the number of patients that can benefit from intratumoral therapies (80–82). The number of ongoing clinical trials examining intratumoral immunotherapy has grown exponentially in recent years (83).

One of the guiding principles of intratumoral immunotherapy is the hypothesis that robust, local immunostimulation can generate a systemic antitumor immune response (84). Coined an "abscopal response", this would allow injection of one or a few accessible lesions to promote tumor regression at distant, uninjectable lesions. Clinical reports indeed support this hypothesis. In a clinical trial of intratumoral BCG in metastatic melanoma, tumor regression was observed in 90% of injected lesions and almost 20% of uninjected lesions (76). Indeed, T-VEC has also been reported to elicit responses in both visceral and non-visceral uninjected lesions, with some legions regressing completely (78, 85).

However, intratumoral injection of free biologics does not necessarily limit systemic exposure. Therapeutic payloads injected into the tumor can easily enter systemic circulation via lymphatic drainage and/or through leaky tumor vasculature. In our own group, we observed that systemically administered MSA-IL-12 (intraperitoneally, i.p.) and intratumorally administered MSA-IL-12 elicited nearly identical toxicity in mice, as assessed by treatment related weight loss (86). Even larger molecules, such as αCD40 agonist antibodies, completely leak out of tumors within 48 hours of injection (87). Similar results have been observed in human clinical intratumoral immunotherapy trials,

with rhIL-12 detectable in the serum within 30 minutes of local injection into head and neck squamous cell carcinoma and side effects associated with local administration of recombinant tumor necrosis factor alpha similar to those experienced with systemic administration (88, 89). Although technical advances have made intratumoral injections feasible in a wide array of clinical presentations, the rapid systemic dissemination after local administration highlights the need for better engineered strategies to retain locally administered payloads. In this thesis, we use a collagen anchoring strategy to tether locally intratumorally administered agonist antibody payloads to collagen located in the tumor extracellular matrix (ECM).

Targeting the extracellular matrix

Collagen is a promising candidate for tumor localization for several reasons. Collagen is ubiquitously expressed (comprising one third of all protein in the body, by mass) and is the most abundant protein within the ECM (90). Furthermore, collagen is often overexpressed in tumors compared to healthy tissue and, because of its ubiquitous expression, this approach is relatively tumor type agonistic (91). Collagen has a relatively long half-life, limiting the amount of collagen-turnover mediated drug degradation. Indeed, modeling work from our own group confirmed that collagen turnover leads to negligible drug degradation (92). Imaging studies have also revealed that immune cells are often in close proximity to collagen rich regions of the tumor and even travel along collagen fibrils (93, 94). Thus, collagen localization of immunotherapy payloads will position these drugs in close proximity to infiltrating immune cells. Lastly, although we do not explore the role of targeting different collagen isoforms (or other ECM components for that matter) in this thesis, their non-uniform spatial distributions in the tumor suggest that it may be possible to fine tune delivery of different immunotherapeutic payloads to different regions of the TME (95). How targeting different ECM

components and collagen isoforms impacts tumor localization and therapeutic outcomes is an active area of research in our group.

Our group and others have demonstrated that collagen anchoring of a wide array of immunomodulatory payloads can improve their therapeutic index (86, 92, 96–103). In this work, we focus on the use of two different collagen binding domains, lumican and LAIR. A brief background on each is provided below.

Lumican

Lumican is a ~40kDa protein that naturally binds to several collagen isoforms, notably collagen I and collagen IV (which are the most abundant form of collagen and a member of the basement membrane, respectively) (86). Lumican is a member of the small leucine-rich repeat proteoglycan family (SLRP) and is thought to play a role in regulating collagen fibrillogenesis, with lumican knockout mice showing increased skin laxity/fragility and corneal opacification (104, 105). Although no crystal structure for lumican has been published, like most SLPR members it is thought to have a horseshoe like structure with the concave portion of the protein binding to collagen (106). Measured in our lab, lumican has a dissociation constant (K_D) for collagen I and IV in the hundreds of nanomolar range, indicating a moderately high affinity (86, 103). Interestingly, lumican may also play a role in innate immune responses, with evidence that lumican can present lipopolysaccharide (LPS) to CD14, a TLR co-receptor (107). *In vitro*, lumican-deficient macrophages have impaired responses to LPS.

Leukocyte associated Immunoglobulin-like Receptor (LAIR)

Leukocyte associated Immunoglobulin -like Receptor 1, or LAIR1 (often abbreviated as simply "LAIR" herein), is an inhibitory receptor containing a cytoplasmic ITIM that is expressed on immune

cells. Evidence suggests that LAIR is not critical for preventing immune cell overactivation or autoimmunity, with LAIR knockout mice being relatively healthy with only minor altered immune phenotypes (slightly higher percentages of activated T cells in the spleen and lowered serum IgG1 levels, among other minor changes) (108). This suggests that any inhibitory function LAIR plays is primarily redundant *in vivo* with other inhibitory receptors. This is in stark contrast to inhibitory receptors such as CTLA-4 and PD-1, which play a crucial role in preventing severe, sometimes fatal, autoimmunity (109–111). One interesting consequence of selecting LAIR as a collagen binding domain is that it will likely compete with endogenous LAIR for binding sites and may block inhibitory LAIR signaling within the tumor. Indeed, tumor cells engineered to constitutively express hLAIR2 or treatment with hLAIR2-Fc fusion proteins sensitizes tumors to αPD-1 therapy (112, 113). It is impossible to de-couple these effects of blocking endogenous LAIR signaling with collagen anchoring in our work, and we cannot rule out if this has some impact on therapeutic outcomes.

Outline of thesis

Chapter two outlines our initial efforts to develop a generalizable platform for retention of antibody payloads in the TME. To do this, we utilized a collagen anchoring strategy, in which various IgG binding (IgGB) domains were fused to the collagen binding protein lumican (termed "IgGB-lumican" fusions). Although these fusions were functional *in vitro* and we observed evidence of intratumoral retention of IgGB-lumican fusions in the TME, IgG was poorly retained in the TME due to rapid exchange with endogenous IgG.

In chapter three, we instead direct our efforts towards constructing direct antibody fusions to collagen binding domains. We show that this strategy is applicable to both a wide range of antibodies and

collagen binding proteins. We then proceed to study collagen anchoring versions of αCD28 and αCD28 by fusing them to the ectodomain of Leukocyte Associated Immunoglobulin -like Receptor 1 (LAIR1) and testing them *in vivo* in a number of immunotherapy combinations. Unlike our previously published cytokine work (86, 92), where we saw striking increases in efficacy and decreases in treatment related toxicity, we did not observe major improvements of collagen anchoring antibody formats for most combinations tested. In fact, for some αCD28 combinations we observed diminished efficacy for the collagen anchoring formants when compared to free cytokine. However, we did observe a small improvement in efficacy for one combination, TA99 + α4-1BB-LAIR, when compared to non-collagen anchoring TA99 + α4-1BB.

In chapter 4, we further explore this combination and, in the course of performing cellular depletion studies to dissect out which immune populations are important for efficacy, we found that simultaneous depletion of $CD4^+$ T cells boosted cure rates to over 90% of mice. Using flow cytometry and bulk RNA-sequencing, we probed the immunological mechanism of this combination. We elucidated two mechanisms of action for this synergy: αCD4 eliminated tumor draining lymph node Tregs, enhancing priming and activation of $CD8^+$ T cells, and TA99 + α4-1BB-LAIR supported the cytotoxic program of these newly primed $CD8^+$ T cells within the tumor microenvironment. Although we observed robust primary tumor efficacy, these mice failed to form long-term immunological memory and ultimately succumbed to tumor rechallenge. Because of this poor memory response and the translational infeasibility of long term $CD4^+$ T cell depletion, we sought out alternative clinically relevant "priming agents" to replace αCD4. We observed replacement of αCD4 with αCTLA-4, a clinically approved antibody that enhances T cell priming, resulted in equivalent cure rates while additionally aiding mice in generating robust immunological memory against secondary tumor

rechallenge. Holistically, this thesis outlines efforts to develop collagen anchored agonist antibodies for cancer immunotherapy. Furthermore, our work in chapter three and more so chapter four uncovers a fundamental two-step approach to combination immunotherapy: 1) prime $CD8^+$ T cells by regulatory T cell depletion/inhibition; and then 2) support these infiltrating $CD8^+$ T cells with tumor-localized immune agonism (in this work with a α4-1BB agonist antibody).

Chapter 2: Collagen anchored IgG binders (IgGBs)

2.1: Introduction

In this chapter we outline efforts to engineer a generalizable strategy to anchor agonist antibodies to the tumor microenvironment. To do this, we constructed fusion proteins consisting of 1) a panel of IgG binding domains (IgGBs) and 2) lumican, a collagen binding domain previously validated in our lab to improve tumor localization of cytokine fusions (86). We termed these fusion proteins IgGB-lumican fusions and envisioned this platform would allow us to rapidly screen a wide range of available preclinical agonist antibodies for tumor localization, including commercial antibodies for which sequences to express in-house were not readily available. In theory, agonist antibodies of interest would be co-incubated with our IgGB-lumican fusion and administered intratumorally - the IgGB-lumican fusion acting as a bispecific tether linking the therapeutic antibodies to the collagen rich extracellular matrix (ECM). This platform would be generalizable beyond agonist antibodies to any Fc containing protein, including antitumor antibodies, antagonistic antibodies, and cytokine-Fc fusions. A range of different IgGB have been reported in the literature, primarily for use in affinity purification of IgG or as detection agents for biosensors, western blots, flow cytometry, and other bioassays (114). Ultimately, this strategy failed because weak affinity for IgG of available IgGBs limited tumor retention and varying affinity to different IgG isotypes of available IgGBs would complicate head-to-head comparisons. Below, we provide background on the various sources of IgGBs used in this study.

Protein A/G

Perhaps the best characterized IgG binding proteins are Protein A and Protein G, derived from *Staphylococcus aureus* and the group C and G *Streptococcus* bacteria, respectively. These proteins are

displayed on the bacterial surface and prevent antibody opsonization (and thus bacterial clearance) by binding to the Fc region of IgGs (115, 116). These proteins are routinely used to purify recombinantly expressed antibodies and Fc fusions, including for production of clinical stage biologics (117). More specifically, protein A is composed of 5 different IgG binding domains (A, B, C, D, and E) with approximately 80% sequence homology and a C-terminal hydrophobic transmembrane tail to anchor the protein to the bacterial surface. A modified version of the B domain, referred to as domain Z, has been extensively characterized and studied in the literature (118–120). This 58 amino acid protein consists of three alpha helices and contains several mutations to improve chemical stability (121). It has been reported in the literature that protein A or the engineered Z domain bind to IgG with a dissociation constant (K_D) of 10-100 nM, depending on the specific construct and IgG species/isotype (122–124). Additionally, data has suggested that dimers of two Z domains have a two-fold improvement in affinity over monomeric Z domains (118). Thus, we included a dimeric Z domain (termed "ZZ") in our IgGB panel.

Protein G consists of two (B1 and B2) or three (C1, C2 and C3) highly homologous Fc binding domains with several N-terminal albumin binding domains, depending on which bacterial strain it is derived from (125–129). The amino acid sequences of B1 and B2 are identical to C1 and C3. Whereas Protein A primarily interacts with the Fc region via hydrophobic interactions, Protein G interacts with the Fc region via polar and electrostatic contacts (126). Similar to Protein A, Protein G and its various subdomains bind to IgG with a K_D in the 10-100 nM range (130, 131). However, Protein G exhibits weak Fab interactions, which can lead to aggregation when in solution with IgG. Fortunately, a single N37Y point mutation has been identified which abrogates Fab binding (132). A dimer of protein G

(B1 and B2) binding domains (containing N37Y point mutations) separated by a 15 amino acid linker derived from the native *streptococcal* protein, was included in our IgGB panel.

Fibronectin scaffold

Fibronectin is a large protein that forms a significant part of the extracellular matrix. One of fibronectin's subdomains, the fibronectin Type III domain (FN3), is a member of the immunoglobulin superfamily and found in many proteins involved in molecular recognition, including cell-adhesion molecules, cytokine receptors, hormone receptors, and carbohydrate binding domains (133, 134). The 10th FN3 domain (^{10}FN3, out of 15 repeats total) of human fibronectin has been reported in the literature as a suitable "antibody mimic" scaffold for designing novel protein binders (133, 135). ^{10}FN3 consists of 94 residues and forms a "beta sandwich" structure, similar to the antibody V_H domain. This "beta sandwich" contains 7 individual beta sheets connected by several unstructured loop domains. The three solvent accessible loops on the N-terminal face of the protein are the basis of the molecular recognition abilities of FN3 and are analogous to the complementarity-determining regions (CDRs) of antibody variable regions (136). By introducing mutations specifically into the loops of these domains, one can engineer large libraries of novel proteins and screen for binders, often termed "monobodies", to specific target proteins. mRNA, phage display, and yeast display ^{10}FN3 libraries have been developed and used to engineer novel binders with affinities in the micromolar to picomolar range (137–139). A PEG-ylated ^{10}FN3 derived VEGFR2 inhibitor has been tested clinically for the treatment of recurrent glioblastoma (140–142). Although trials were terminated early due to lack of efficacy, this nevertheless demonstrates the translational potential of ^{10}FN3 derived binders.

Work from our own lab developing ^{10}FN3 yeast libraries demonstrated that limited diversity libraries with just 7 mutations in each of two of the three solvent accessible loops (BC and FG loops, 14

mutations total) could still generate binders with sub-nanomolar affinity to lysozyme, a model antigen (143). Additionally, the highest affinity binders from this library all contained an interloop disulfide bond between the two mutated loops (between residues 28 and 77). Notably, this interloop disulfide bond is similar to those found in both camel and shark antibody binding domains (144, 145). Data suggested that this disulfide was critical to the high binding affinities of the isolated ^{10}FN3 mutants, likely through increases in thermodynamic stability. Parallel work conducted by our group demonstrated that ^{10}FN3 loops are also amenable to changes in loop length and that loop length diversity, in addition to loop composition, is a critical component of successful ^{10}FN3 binder engineering (146). Subsequently our group generated a ^{10}FN3 library with antibody-like CDR diversity while conserving some WT loop amino acid identities to improve stability. This library, termed G4, was demonstrably better at selecting high affinity binders when compared to naive, unbiased libraries (147). A high affinity binder to mIgG was isolated from this fibronectin library and subsequently used in the study outlined in this chapter.

Sso7d scaffold

Hyperthermophylic archaea and bacteria have evolved to thrive in extreme temperatures and pH, and thus proteins from these organisms often display increased stability and make suitable candidates for protein binding scaffolds. In particular, the Sso7d DNA-binding protein from *Sulfolobus solfataricus* has been used by our lab and others to engineer novel binders (148–150). The high stability and rigid structure of the Sso7d protein makes it more tolerable to mutations, a trait that has been demonstrated to improve the evolvability of proteins (151). Its small size (7 kDa) and high stability also make it highly amenable to fusion protein construction and expression. Additionally, unlike antibody and antibody-like binders (such as ^{10}FN3 domains), which bind epitopes with flexible loops, the Sso7d binding paratope is a rigid beta sheet, which reduces the entropic penalty of binding (150). In the first

published demonstration of using the Sso7d platform to engineer novel binders, a high affinity binder to mIgG was identified and this Sso7d binder was included in our panel of IgGB (149).

Peptide IgG binders

To diversify our approach, we also included several smaller peptide IgGB. We selected two synthetic peptides from the literature. One was a small, 4 amino acid computationally designed peptide, RRGW (152). This peptide was designed specifically to bind a mouse IgG2a Fc region, and was demonstrated to bind IgG by SPR. In another approach, cyclic peptide phage display libraries were screened for IgG binders, and several binders that bound to consensus regions also involved in Protein A and Protein G binding were identified (153). Follow up work identified a second disulfide bridge that further stabilized the cyclic structure of the highest affinity peptide (123). This new peptide, Fc-III-4C, was reported to have 30-fold higher affinity for human IgG (while still maintaining binding to a broad range of IgG from different species). This peptide was also included in our IgGB panel.

Conjugating binding handles onto IgGs

An alternative approach to using binders that bind to the Fc itself is to chemically conjugate ligand "handles" onto the IgG of interest and use fusions of known binders to these ligand handles to collagen binding domains to localize the IgG. Our lab has previously engineered an αFITC single chain variable region (scFv) antibody fragment, 4m5.3, that binds FITC with femtomolar affinity (154). Because FITC is a relatively cheap reagent available with a range of conjugation formulations (such as the amine reactive NHS ester conjugation strategy used in this study) we employed this as a complementary strategy. In this approach, FITC labeled IgG would bind to 4m5.3-MSA-lumican, which would then bind tumor collagen.

2.2: Results

IgGB-lumican fusions bind collagen and IgG's with varying affinity

We developed a panel of IgGBs fused to the collagen binding domain lumican as a generalizable IgG retention strategy. All constructs contained a mouse serum albumin (MSA) spacer between the IgGB and lumican and short flexible $(G_3S)_{1-2}$ linkers separated each domain (Table 2-1). Specifically, we designed two constructs based on Protein A/G - the first a dimer of the protein Z domain from Protein A (termed ZZ-MSA-Lumican) and the second a truncated version of Protein G containing a point mutation to eliminate Fab binding (termed Lumican-MSA-SpG_2). We also identified IgGBs engineered from a fibronectin library and an Sso7d library, both developed by previous members of our lab, and constructed MSA-lumican fusions to both of these binders (147, 149). These constructs were termed lumican-MSA-Fn3 and Sso7d-MSA-lumican, respectively. Lastly, we identified two peptide IgG binders from the literature - one a short, positively charged peptide RRGW and the second a cyclic peptide (Fc-III-4C) identified from a phage library (123, 152). These constructs were termed lumican-MSA-RRGW, lumican-MSA-WGRR, and lumican-MSA-Fc-III-4C respectively. Decisions to construct N-terminus or C-terminus fusions for each IgG binder were made based on prior literature examples, except RRGW, which was constructed in both orientations, although collectively we refer to them as IgGB-lumican fusions regardless of orientation. All constructs contained a His tag for purification purposes.

All 6 of these binders were recombinantly expressed in mammalian cells and confirmed to be the appropriate size by SDS-PAGE gel. Sso7d-MSA-Lumican appeared to contain a large fraction of aggregates by SDS-PAGE gel, and this was further confirmed by size exclusion (SEC)

chromatography (Fig. 2-1). Sso7d is naturally a positively charged protein as its endogenous ligand is DNA. Our lab has developed charge neutralized libraries which have decreased off-target binding and increased developability, but the IgG binding Sso7d we utilized in this study was isolated from a prior library (150). Thus, it is unsurprising that this charged Sso7d is aggregation prone. Because of its poor developability characteristics, we discontinued evaluation of this candidate.

We next assessed the ability of the IgGB-lumican fusions to bind an isotype control mouse IgG2a (mIgG2a) via ELISA (Fig. 2-2). Both ZZ-MSA-lumican and lumican-MSA-SpG_2 bound relatively high affinities (K_D = 0.662 nM and K_D = 94.4 nM, respectively). Lumican-MSA-Fn3 also bound mIgG2a with a measurable, albeit weak, affinity (K_D = 1170 nM). Lumican-MSA-Fc-III-4C, lumican-MSA-RRGW, and lumican-MSA-WGRR all displayed minimal binding to mIgG2a. In fact, any binding signal was equivalent to or below the non-specific binding signal of each of these constructs (determined using blocked but uncoated wells). Therefore, lumican-MSA-Fc-III-4C, lumican-MSA-RRGW, and lumican-MSA-WGRR were discontinued from further development.

As an alternative strategy, we recombinantly expressed an αFITC scFv fused to lumican, again with a mouse serum albumin (MSA) spacer between the scFv and lumican and short flexible $(G_3S)_{1-2}$ linkers separating each domain. We utilized clone 4m5.3, a high affinity αFITC scFv developed in our lab with a femto-molar affinity for FITC (K_D = 400 fM). This construct was termed 4m5.3-MSA-lumican. By chemically conjugating FITC onto IgGs of interest (with a polyethylene glycol (PEG) linker to ensure the FITC motif is accessible to 4m5.3) this strategy allows the localization of any FITC labeled IgG regardless of isotype.

We next confirmed that lumican-MSA-Fn3, lumican-MSA-SpG_2, ZZ-MSA-lumican, and 4m5.3-MSA-lumican were able to bind collagen I and collagen IV via ELISA (Fig. 2-3). Indeed, we saw that all four constructs bound collagen with similar affinities to control lumican protein. All constructs displayed a higher affinity for collagen IV when compared to collagen I, consistent with prior reports in the literature and work from our own lab with cytokine-lumican fusions.

IgGB-lumican fusions are ineffective at retaining IgG's in the TME

To assess the ability of our reduced panel of IgGB-lumican fusions to retain IgGs in the TME we utilized longitudinal *in vivo* fluorescence imaging. ZZ-MSA-lumican, lumican-MSA-SpG_2, lumincan-MSA-Fn3, and 4m5.3-MSA-lumican were labeled with AF568 and isotype control mIgG2a was labeled with AF647. Additionally, for pairing with the 4m5.3-MSA-lumican construct, we labeled isotype control mIgG2a with both AF647 and PEG-FITC. For this initial pilot study, BALB/c mice were inoculated with 4T1 tumors and intratumorally administered IgGB-lumican:IgG complexes on day 5. Prior to intratumoral injection we co-incubated mIgG2a (or mIgG2a-PEG-FITC) with IgGB-lumican fusions (or 4m5.3-MSA-Lumican) at a molar ratio of 0.9. The higher the ratio, the higher the free mIgG2a upon injection. However, dropping the ratio too low risks sacrificing the fluorescent signal. Based on equilibrium binding (assuming 1 nmol IgGB-lumican and 20 μL incubation volume) 0.9 was chosen as the ideal ratio (Fig. 2-4). 4T1 tumors were chosen for their high collagen content (155). For this pilot experiment, two mice were injected per construct with IgG:IgGB-lumican complexes and a single mouse was injected with IgGB-lumican alone. Mice were monitored longitudinally for retention of labeled IgG in the TME. Technical issues precluded monitoring analysis of IgGB-lumican fusions signal *in vivo*.

Unfortunately, all IgGs leaked out at a similar rate to control mIgG2a, indicating that none of the IgG retention strategies were successful (Fig. 2-5A). In addition to IVIS imaging, we collected serum from all animals 24 hours following intratumoral administration. We then measured fluorescence in the serum of both labeled mIgG2a and labeled IgGB-lumican fusions. We observed a high concentration of mIgG2a in the serum at this time point, consistent with our IVIS data. However, we observed a ~10-fold lower concentration of IgGB-lumican in the serum for all constructs (Fig. 2-5B). Despite a lack of longitudinal IVIS data for the IgGB-lumican fusions, we interpreted the serum data to indicate that although the IgGB-lumican constructs were likely retained in the tumor microenvironment, mIgG2a quickly fell off of these constructs and leaked out of the tumor. Interestingly, we also observed a significant difference in retention of N-terminal versus C-terminal IgGB-lumican fusions retention based on serum data, with 4m5.3-MSA-Lumican and ZZ-MSA-Lumican exhibiting a lower serum concentration than Lumican-MSA-Fn3 and Lumican-MSA-SpG_2. Measured affinity of these constructs via ELISA did not predict this outcome of N-terminal versus C-terminal retention differences.

Given the measured *in vitro* affinities for IgGB-lumican constructs to mIgG2a, this is not an unsurprising outcome. However, because of the high affinity for 4m5.3-MSA-lumican to mIgG2a-FITC, we did not expect this construct to exhibit such poor IgG retention *in vivo*. Post hoc analysis revealed that labeled mIgG2a-FITC had a poor degree of labeling (DOL) of only 0.9 moles of dye per mole of IgG. It is well documented that the lysine amine chemical conjugation strategy employed in this study typically results in a dye to antibody ratio that follows a Poisson distribution (156). Thus, using just the average DOL we can calculate what fraction of the mIgG2a pool contained 0, 1, 2, etc. dye labels. Given a measured DOL of 0.9, we calculated that over 40% of all mIgG2a were unlabeled.

Seeing that almost half of the injected mIgG2a-FITC was actually unlabeled and thus unable to bind to 4m5.3-MSA-lumican, this likely explains why this strategy underperformed in intratumoral IgG retention.

2.3: Discussion

In this chapter, we designed a panel of IgG binding domain proteins fused to the collagen binding domain lumican in an effort to generate a plug-and-play system to rapidly test tumor localized agonist antibodies. We hypothesized that this system would allow us to screen a wide range of tumor localized agonist antibodies in preclinical mouse tumor models. Direct fusion of collagen binding domains to agonist antibodies requires sourcing sequences, in-house expression, purification, and *in vitro* validation for each individual antibody candidate. We reasoned that our strategy would allow us to pick a single IgGB-lumican fusion that would pair with any and all available preclinical agonist antibodies, significantly cutting down on protein production and *in vitro* validation time. We quickly realized that this approach had two major drawbacks. First, the affinity of available IgGBs was insufficient to retain therapeutic IgGs in the TME over freely injected IgG, likely because high concentrations of endogenous IgG *in vivo* rapidly competed off our pre-loaded therapeutic antibodies. Secondly, IgGBs display varying affinity depending on antibody isotype and species. As preclinical agonist antibodies are often of rat and hamster origin (and to a lesser extent murine origin) and come in a range of isotypes, this meant that it would be nearly impossible to ensure uniform retention from antibody to antibody, making head-to-head comparisons of different locally retained agonists difficult. Although we could have undertaken a protein engineering campaign to generate IgGBs with higher affinity and/or more uniform binding profiles to different IgG species/isotypes, this likely would have been a time consuming endeavor without guaranteed success. Our second approach of chemically

conjugating FITC "handles" onto antibodies of interest and anchoring them to the TME with a αFITC-MSA-lumican fusion (specifically 4m5.3-MSA-lumican) solved the challenges associated with the IgGB-lumican fusions, but introduced new complicating factors. Batch-to-batch DOL variations again meant that different lots of prepared FITC labeled antibodies would have different tumor retention times, impeding on both head-to-head agonist comparisons and the reproducibility of this work. Indeed, the field of antibody drug conjugates has largely moved away from random amine labeling and instead relies on engineering free cysteines into the Fc region, allowing for controlled DOL (157). This approach would be useful in our use case as well, but again requires in-house antibody expression and purification. Instead, we chose to develop and express direct fusions of agonist antibodies to collagen binding domains, which we detail in the following chapters.

2.4: Figures

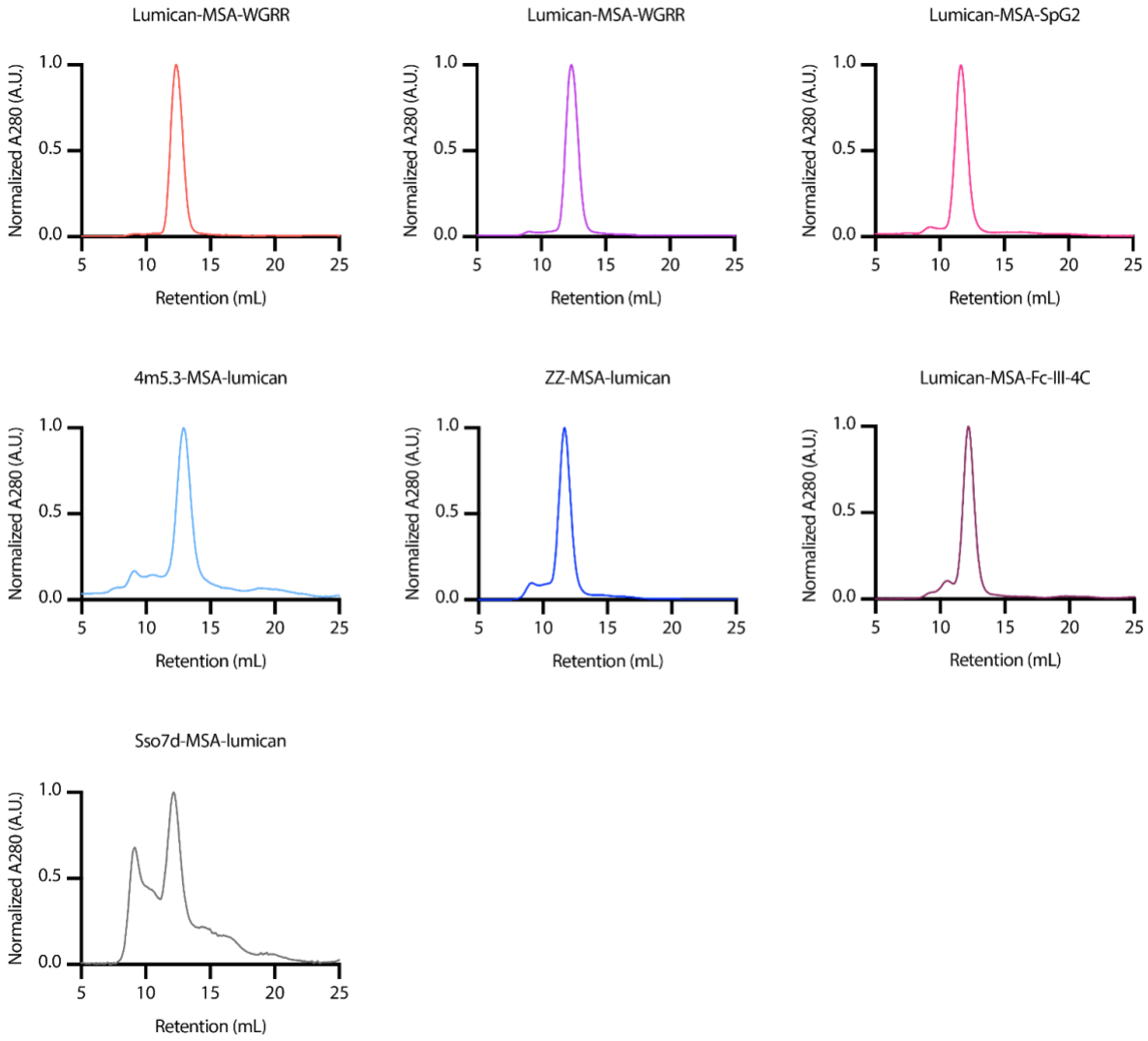

Figure 2-1: Sso7d-MSA-lumican is highly aggregated

SEC chromatogram of indicated proteins on a Superdex 200 increase 10/300GL column.

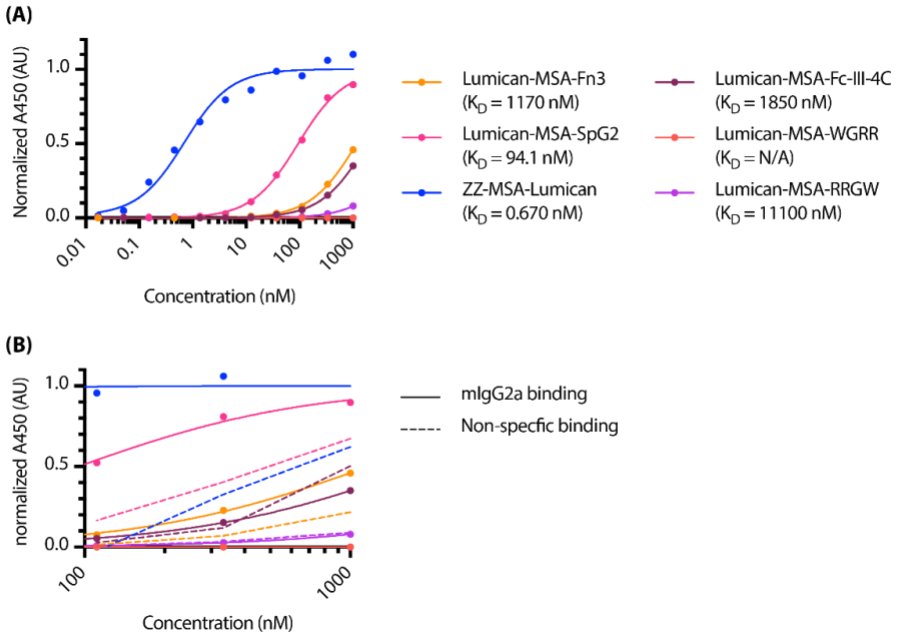

Figure 2-2: A subset of IgGB-lumican fusions display binding to mouse IgG2a

(A) Equilibrium binding curve of indicated proteins to plate bound mouse IgG2a isotype control antibody (n = 1). **(B)** Non-specific binding to uncoated ELISA plate of indicated proteins (dotted lines) at highest concentrations with data from **(A)** replotted (solid lines) (n = 1).

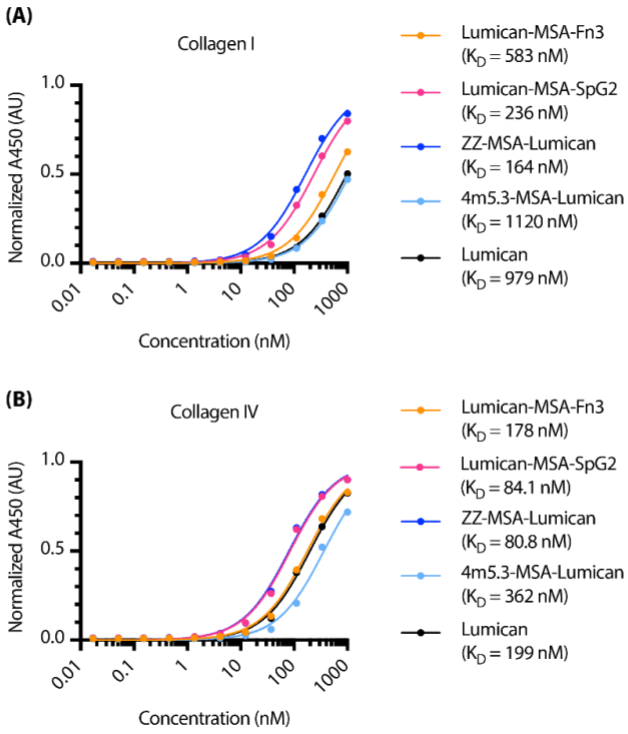

Figure 2-3: All IgGB-lumican fusions exhibit binding to plate bound collagen

Equilibrium binding curve of indicated proteins to plate bound **(A)** collagen I and **(B)** collagen IV (n = 1).

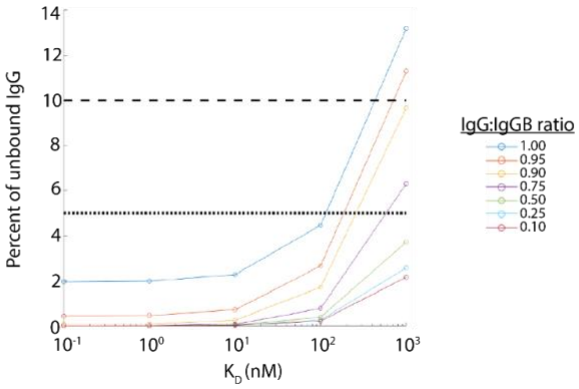

Figure 2-4: IgG:IgGB-Lumican complex formation

Calculated free IgG at equilibrium binding conditions based on affinity of IgG binder (IgGB) and ratio of IgG to IgGB.

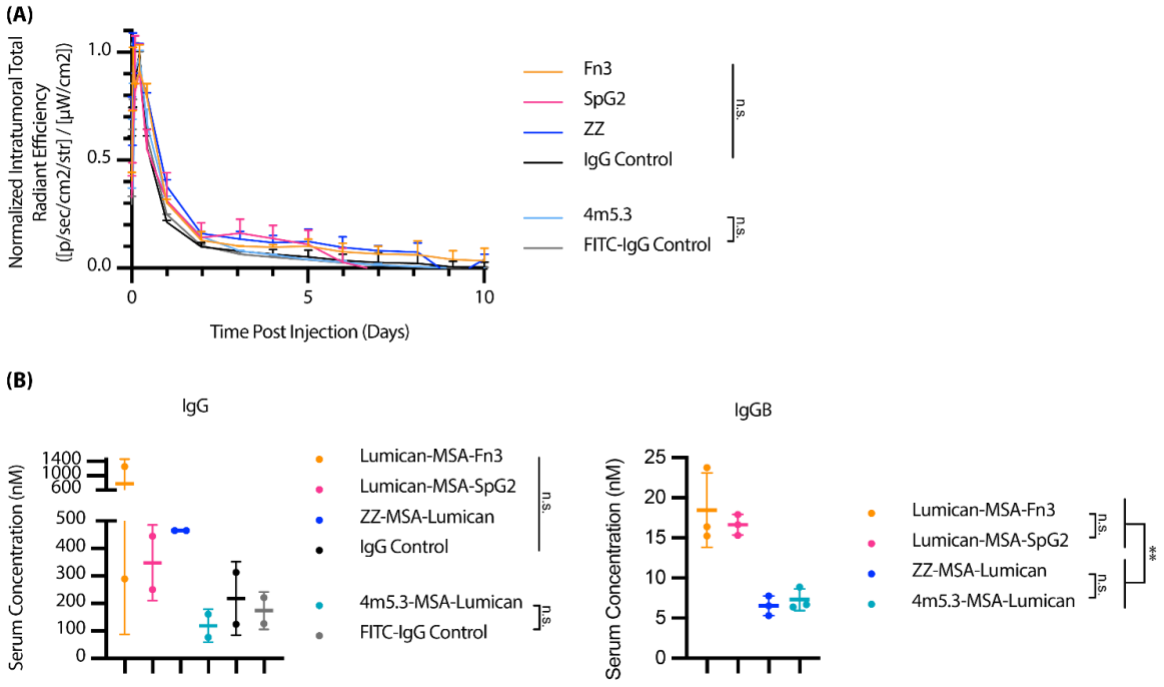

Figure 2-5: IgGB-lumican fusions do a poor job of retaining IgG in TME

(A) Quantification of normalized radiant efficiency in mice receiving free IgG or IgG pre-complexed with indicated IgGB-lumican fusion (mean ± S.D, n = 2). **(B)** quantification of free IgG (left, mean ± S.D, n = 2) and IgGB-lumican fusions (right, mean ± S.D, n = 3) in serum 24 hours after injection. Retention data were compared using two-way ANOVA with Tukey's multiple hypothesis testing correction and serum data was compared using one way ANOVA with Tukey's multiple hypothesis testing correction. *$P < 0.05$, **$P < 0.01$, ***$P < 0.001$, ****$P < 0.0001$.

2.5: Tables

Table 2-1: Amino acid sequence table

Key: signal peptide, binder, MSA, linker, lumican, His tag

ZZ-MSA-lumican	MRVPAQLLGLLLLWLPGARCAMRVPAQL LGLLLLWLPGARCAVDNKFNKEQQNAF YEILHLPNLNEEQRNAFIQSLKDDPSQSA NLLAEAKKLNDAQAPKVDNKFNKEQQ NAFYEILHLPNLNEEQRNAFIQSLKDDPS QSANLLAEAKKLNDAQAPKGGGSEAHK SEIAHRYNDLGEQHFKGLVLIAFSQYLQ KCSYDEHAKLVQEVTDFAKTCVADESA ANCDKSLHTLFGDKLCAIPNLRENYGEL ADCCTKQEPERNECFLQHKDDNPSLPPF ERPEAEAMCTSFKENPTTFMGHYLHEVA RRHPYFYAPELLYYAEQYNEILTQCCAEA DKESCLTPKLDGVKEKALVSSVRQRMKC SSMQKFGERAFKAWAVARLSQTFPNADF AEITKLATDLTKVNKECCHGDLLECAD DRAELAKYMCENQATISSKLQTCCDKPL LKKAHCLSEVEHDTMPADLPAIAADFVE DQEVCKNYAEAKDVFLGTFLYEYSRRHP DYSVSLLLRLAKKYEATLEKCCAEANPPA CYGTVLAEFQPLVEEPKNLVKTNCDLYE KLGEYGFQNAILVRYTQKAPQVSTPTLV EAARNLGRVGTKCCTLPEDQRLPCVEDY LSAILNRVCLLHEKTPVSEHVTKCCSGSL VERRPCFSALTVDETYVPKEFKAETFTFH SDICTLPEKEKQIKKQTALAELVKHKPK ATAEQLKTVMDDFAQFLDTCCKAADKD TCFSTEGPNLVTRCKDALAGGGSGGGSQ YYDYDIPLFMYGQISPNCAPECNCPHSYP TAMYCDDLKLKSVPMVPPGIKYLYLRNN QIDHIDEKAFENVTDLQWLILDHNLLEN SKIKGKVFSKLKQLKKLHINYNNLTESV GPLPKSLQDLQLTNNKISKLGSFDGLVN LTFIYLQHNQLKEDAVSASLKGLKSLEYL DLSFNQMSKLPAGLPTSLLTLYLDNNKIS NIPDEYFKRFTGLQYLRLSHNELADSGVP GNSFNISSLLELDLSYNKLKSIPTVNENLE NYYLEVNELEKFDVKSFCKILGPLSYSKI

	KHLRLDGNPLTQSSLPPDMYECLRVANEI TVNGGGSHHHHHH
Sso7d-MSA-lumican	MRVPAQLLGLLLLWLPGARCAATVKFKY KGEEKQVDISKIYLVLRLGKFIYFYYDLG GGKLGLGHVSEKDAPKELLQMLEKQKK GGGSEAHKSEIAHRYNDLGEQHFKGLV LIAFSQYLQKCSYDEHAKLVQEVTDFAK TCVADESAANCDKSLHTLFGDKLCAIPN LRENYGELADCCTKQEPERNECFLQHK DDNPSLPPFERPEAEAMCTSFKENPTTFM GHYLHEVARRHPYFYAPELLYYAEQYNE ILTQCCAEADKESCLTPKLDGVKEKALV SSVRQRMKCSSMQKFGERAFKAWAVARL SQTFPNADFAEITKLATDLTKVNKECCH GDLLECADDRAELAKYMCENQATISSKL QTCCDKPLLKKAHCLSEVEHDTMPADLP AIAADFVEDQEVCKNYAEAKDVFLGTFL YEYSRRHPDYSVSLLLRLAKKYEATLEKC CAEANPPACYGTVLAEFQPLVEEPKNLV KTNCDLYEKLGEYGFQNAILVRYTQKAP QVSTPTLVEAARNLGRVGTKCCTLPEDQ RLPCVEDYLSAILNRVCLLHEKTPVSEHV TKCCSGSLVERRPCFSALTVDETYVPKEF KAETFTFHSDICTLPEKEKQIKKQTALAE LVKHKPKATAEQLKTVMDDFAQFLDTC CKAADKDTCFSTEGPNLVTRCKDALAG GGSGGGSQYYDYDIPLFMYGQISPNCAP ECNCPHSYPTAMYCDDLKLKSVPMVPPG IKYLYLRNNQIDHIDEKAFENVTDLQWL ILDHNLLENSKIKGKVFSKLKQLKKLHI NYNNLTESVGPLPKSLQDLQLTNNKISK LGSFDGLVNLTFIYLQHNQLKEDAVSASL KGLKSLEYLDLSFNQMSKLPAGLPTSLLT LYLDNNKISNIPDEYFKRFTGLQYLRLSH NELADSGVPGNSFNISSLLELDLSYNKLK SIPTVNENLENYYLEVNELEKFDVKSFC KILGPLSYSKIKHLRLDGNPLTQSSLPPDM YECLRVANEITVNGGGSHHHHHH
4m5.3-MSA-lumican	MRVPAQLLGLLLLWLPGARCAADVVMT QTPLSLPVSLGDQASISCRSSQSLVHSNGN TYLRWYLQKPGQSPKVLIYKVSNRVSGV PDRFSGSGSGTDFTLKINRVEAEDLGVYF CSQSTHVPWTFGGGTKLEIKSSADDAKK

	DAAKKDDAKKDDAKKDGGVKLDETG GGLVQPGGAMKLSCVTSGFTFGHYWMN WVRQSPEKGLEWVAQFRNKPYNYETYY SDSVKGRFTISRDDSKSSVYLQMNNLRVE DTGIYYCTGASYGMEYLGQGTSVTVSGG GSEAHKSEIAHRYNDLGEQHFKGLVLIA FSQYLQKCSYDEHAKLVQEVTDFAKTCV ADESAANCDKSLHTLFGDKLCAIPNLRE NYGELADCCTKQEPERNECFLQHKDDN PSLPPFERPEAEAMCTSFKENPTTFMGHY LHEVARRHPYFYAPELLYYAEQYNEILTQ CCAEADKESCLTPKLDGVKEKALVSSVR QRMKCSSMQKFGERAFKAWAVARLSQT FPNADFAEITKLATDLTKVNKECCHGDL LECADDRAELAKYMCENQATISSKLQTC CDKPLLKKAHCLSEVEHDTMPADLPAIA ADFVEDQEVCKNYAEAKDVFLGTFLYE YSRRHPDYSVSLLLRLAKKYEATLEKCCA EANPPACYGTVLAEFQPLVEEPKNLVKT NCDLYEKLGEYGFQNAILVRYTQKAPQ VSTPTLVEAARNLGRVGTKCCTLPEDQR LPCVEDYLSAILNRVCLLHEKTPVSEHVT KCCSGSLVERRPCFSALTVDETYVPKEFK AETFTFHSDICTLPEKEKQIKKQTALAEL VKHKPKATAEQLKTVMDDFAQFLDTCC KAADKDTCFSTEGPNLVTRCKDALAGG GSGGGSQYYDYDIPLFMYGQISPNCAPE CNCPHSYPTAMYCDDLKLKSVPMVPPGI KYLYLRNNQIDHIDEKAFENVTDLQWLI LDHNLLENSKIKGKVFSKLKQLKKLHIN YNNLTESVGPLPKSLQDLQLTNNKISKL GSFDGLVNLTFIYLQHNQLKEDAVSASL KGLKSLEYLDLSFNQMSKLPAGLPTSLLT LYLDNNKISNIPDEYFKRFTGLQYLRLSH NELADSGVPGNSFNISSLLELDLSYNKLK SIPTVNENLENYYLEVNELEKFDVKSFC KILGPLSYSKIKHLRLDGNPLTQSSLPPDM YECLRVANEITVNGGGSHHHHHH
Lumican-MSA-SpG$_2$	MRVPAQLLGLLLLWLPGARCAQYYDYDI PLFMYGQISPNCAPECNCPHSYPTAMYC DDLKLKSVPMVPPGIKYLYLRNNQIDHI DEKAFENVTDLQWLILDHNLLENSKIKG KVFSKLKQLKKLHINYNNLTESVGPLPK SLQDLQLTNNKISKLGSFDGLVNLTFIYL

	QHNQLKEDAVSASLKGLKSLEYLDLSFN QMSKLPAGLPTSLLTLYLDNNKISNIPDE YFKRFTGLQYLRLSHNELADSGVPGNSF NISSLLELDLSYNKLKSIPTVNENLENYYL EVNELEKFDVKSFCKILGPLSYSKIKHLR LDGNPLTQSSLPPDMYECLRVANEITVN GGGSGGGSEAHKSEIAHRYNDLGEQHF KGLVLIAFSQYLQKCSYDEHAKLVQEVT DFAKTCVADESAANCDKSLHTLFGDKLC AIPNLRENYGELADCCTKQEPERNECFL QHKDDNPSLPPFERPEAEAMCTSFKENP TTFMGHYLHEVARRHPYFYAPELLYYAE QYNEILTQCCAEADKESCLTPKLDGVKE KALVSSVRQRMKCSSMQKFGERAFKAW AVARLSQTFPNADFAEITKLATDLTKVN KECCHGDLLECADDRAELAKYMCENQA TISSKLQTCCDKPLLKKAHCLSEVEHDT MPADLPAIAADFVEDQEVCKNYAEAKD VFLGTFLYEYSRRHPDYSVSLLLRLAKKY EATLEKCCAEANPPACYGTVLAEFQPLV EEPKNLVKTNCDLYEKLGEYGFQNAILV RYTQKAPQVSTPTLVEAARNLGRVGTKC CTLPEDQRLPCVEDYLSAILNRVCLLHEK TPVSEHVTKCCSGSLVERRPCFSALTVDE TYVPKEFKAETFTFHSDICTLPEKEKQIK KQTALAELVKHKPKATAEQLKTVMDDF AQFLDTCCKAADKDTCFSTEGPNLVTRC KDALAGGGSTYKLVINGKTLKGETTTEA VDAATAEKVFKQYANDYGVDGEWTYD DATKTFTVTEKPEVIDASELTPAVTTYKL VINGKTLKGETTTKAVDAETAEKAFKQ YANDYGVDGVWTYDDATKTFTVTEHH HHHH
Lumican-MSA-Fc-III-4C	MRVPAQLLGLLLLWLPGARCAQYYDYDI PLFMYGQISPNCAPECNCPHSYPTAMYC DDLKLKSVPMVPPGIKYLYLRNNQIDHI DEKAFENVTDLQWLILDHNLLENSKIKG KVFSKLKQLKKLHINYNNLTESVGPLPK SLQDLQLTNNKISKLGSFDGLVNLTFIYL QHNQLKEDAVSASLKGLKSLEYLDLSFN QMSKLPAGLPTSLLTLYLDNNKISNIPDE YFKRFTGLQYLRLSHNELADSGVPGNSF NISSLLELDLSYNKLKSIPTVNENLENYYL EVNELEKFDVKSFCKILGPLSYSKIKHLR

	LDGNPLTQSSLPPDMYECLRVANEITVN GGGSGGGSEAHKSEIAHRYNDLGEQHF KGLVLIAFSQYLQKCSYDEHAKLVQEVT DFAKTCVADESAANCDKSLHTLFGDKLC AIPNLRENYGELADCCTKQEPERNECFL QHKDDNPSLPPFERPEAEAMCTSFKENP TTFMGHYLHEVARRHPYFYAPELLYYAE QYNEILTQCCAEADKESCLTPKLDGVKE KALVSSVRQRMKCSSMQKFGERAFKAW AVARLSQTFPNADFAEITKLATDLTKVN KECCHGDLLECADDRAELAKYMCENQA TISSKLQTCCDKPLLKKAHCLSEVEHDT MPADLPAIAADFVEDQEVCKNYAEAKD VFLGTFLYEYSRRHPDYSVSLLLRLAKKY EATLEKCCAEANPPACYGTVLAEFQPLV EEPKNLVKTNCDLYEKLGEYGFQNAILV RYTQKAPQVSTPTLVEAARNLGRVGTKC CTLPEDQRLPCVEDYLSAILNRVCLLHEK TPVSEHVTKCCSGSLVERRPCFSALTVDE TYVPKEFKAETFTFHSDICTLPEKEKQIK KQTALAELVKHKPKATAEQLKTVMDDF AQFLDTCCKAADKDTCFSTEGPNLVTRC KDALAGGGSCDCAWHLGELVWCTCHH HHHH
Lumican-MSA-Fn3	MRVPAQLLGLLLLWLPGARCAQYYDYDI PLFMYGQISPNCAPECNCPHSYPTAMYC DDLKLKSVPMVPPGIKYLYLRNNQIDHI DEKAFENVTDLQWLILDHNLLENSKIKG KVFSKLKQLKKLHINYNNLTESVGPLPK SLQDLQLTNNKISKLGSFDGLVNLTFIYL QHNQLKEDAVSASLKGLKSLEYLDLSFN QMSKLPAGLPTSLLTLYLDNNKISNIPDE YFKRFTGLQYLRLSHNELADSGVPGNSF NISSLLELDLSYNKLKSIPTVNENLENYYL EVNELEKFDVKSFCKILGPLSYSKIKHLR LDGNPLTQSSLPPDMYECLRVANEITVN GGGSGGGSEAHKSEIAHRYNDLGEQHF KGLVLIAFSQYLQKCSYDEHAKLVQEVT DFAKTCVADESAANCDKSLHTLFGDKLC AIPNLRENYGELADCCTKQEPERNECFL QHKDDNPSLPPFERPEAEAMCTSFKENP TTFMGHYLHEVARRHPYFYAPELLYYAE QYNEILTQCCAEADKESCLTPKLDGVKE KALVSSVRQRMKCSSMQKFGERAFKAW

	AVARLSQTFPNADFAEITKLATDLTKVN KECCHGDLLECADDRAELAKYMCENQA TISSKLQTCCDKPLLKKAHCLSEVEHDT MPADLPAIAADFVEDQEVCKNYAEAKD VFLGTFLYEYSRRHPDYSVSLLLRLAKKY EATLEKCCAEANPPACYGTVLAEFQPLV EEPKNLVKTNCDLYEKLGEYGFQNAILV RYTQKAPQVSTPTLVEAARNLGRVGTKC CTLPEDQRLPCVEDYLSAILNRVCLLHEK TPVSEHVTKCCSGSLVERRPCFSALTVDE TYVPKEFKAETFTFHSDICTLPEKEKQIK KQTALAELVKHKPKATAEQLKTVMDDF AQFLDTCCKAADKDTCFSTEGPNLVTRC KDALAGGGGSVSDVPRDLEVVAATPTSLLI SWCCSDNCSNSYRITYGETGGNSPVQEFT VPRSCFMATISGLKPGVDYTITAYAVTDS NGPHPISINYRTHHHHHH
Lumican-MSA-RRGW	MRVPAQLLGLLLLWLPGARCAQYYDYDI PLFMYGQISPNCAPECNCPHSYPTAMYC DDLKLKSVPMVPPGIKYLYLRNNQIDHI DEKAFENVTDLQWLILDHNLLENSKIKG KVFSKLKQLKKLHINYNNLTESVGPLPK SLQDLQLTNNKISKLGSFDGLVNLTFIYL QHNQLKEDAVSASLKGLKSLEYLDLSFN QMSKLPAGLPTSLLTLYLDNNKISNIPDE YFKRFTGLQYLRLSHNELADSGVPGNSF NISSLLELDLSYNKLKSIPTVNENLENYYL EVNELEKFDVKSFCKILGPLSYSKIKHLR LDGNPLTQSSLPPDMYECLRVANEITVN GGGSGGGSEAHKSEIAHRYNDLGEQHF KGLVLIAFSQYLQKCSYDEHAKLVQEVT DFAKTCVADESAANCDKSLHTLFGDKLC AIPNLRENYGELADCCTKQEPERNECFL QHKDDNPSLPPFERPEAEAMCTSFKENP TTFMGHYLHEVARRHPYFYAPELLYYAE QYNEILTQCCAEADKESCLTPKLDGVKE KALVSSVRQRMKCSSMQKFGERAFKAW AVARLSQTFPNADFAEITKLATDLTKVN KECCHGDLLECADDRAELAKYMCENQA TISSKLQTCCDKPLLKKAHCLSEVEHDT MPADLPAIAADFVEDQEVCKNYAEAKD VFLGTFLYEYSRRHPDYSVSLLLRLAKKY EATLEKCCAEANPPACYGTVLAEFQPLV EEPKNLVKTNCDLYEKLGEYGFQNAILV

	RYTQKAPQVSTPTLVEAARNLGRVGTKC CTLPEDQRLPCVEDYLSAILNRVCLLHEK TPVSEHVTKCCSGSLVERRPCFSALTVDE TYVPKEFKAETFTFHSDICTLPEKEKQIK KQTALAELVKHKPKATAEQLKTVMDDF AQFLDTCCKAADKDTCFSTEGPNLVTRC KDALAGGGSRRGWHHHHHH
Lumican-MSA-WGRR	MRVPAQLLGLLLLWLPGARCAQYYDYDI PLFMYGQISPNCAPECNCPHSYPTAMYC DDLKLKSVPMVPPGIKYLYLRNNQIDHI DEKAFENVTDLQWLILDHNLLENSKIKG KVFSKLKQLKKLHINYNNLTESVGPLPK SLQDLQLTNNKISKLGSFDGLVNLTFIYL QHNQLKEDAVSASLKGLKSLEYLDLSFN QMSKLPAGLPTSLLTLYLDNNKISNIPDE YFKRFTGLQYLRLSHNELADSGVPGNSF NISSLLELDLSYNKLKSIPTVNENLENYYL EVNELEKFDVKSFCKILGPLSYSKIKHLR LDGNPLTQSSLPPDMYECLRVANEITVN GGGSGGGSEAHKSEIAHRYNDLGEQHF KGLVLIAFSQYLQKCSYDEHAKLVQEVT DFAKTCVADESAANCDKSLHTLFGDKLC AIPNLRENYGELADCCTKQEPERNECFL QHKDDNPSLPPFERPEAEAMCTSFKENP TTFMGHYLHEVARRHPYFYAPELLYYAE QYNEILTQCCAEADKESCLTPKLDGVKE KALVSSVRQRMKCSSMQKFGERAFKAW AVARLSQTFPNADFAEITKLATDLTKVN KECCHGDLLECADDRAELAKYMCENQA TISSKLQTCCDKPLLKKAHCLSEVEHDT MPADLPAIAADFVEDQEVCKNYAEAKD VFLGTFLYEYSRRHPDYSVSLLLRLAKKY EATLEKCCAEANPPACYGTVLAEFQPLV EEPKNLVKTNCDLYEKLGEYGFQNAILV RYTQKAPQVSTPTLVEAARNLGRVGTKC CTLPEDQRLPCVEDYLSAILNRVCLLHEK TPVSEHVTKCCSGSLVERRPCFSALTVDE TYVPKEFKAETFTFHSDICTLPEKEKQIK KQTALAELVKHKPKATAEQLKTVMDDF AQFLDTCCKAADKDTCFSTEGPNLVTRC KDALAGGGSWGRRHHHHHH

2.6: Materials and Methods

Cloning and Protein Production

The various IgG binders were synthesized as gBlock gene fragments (Integrated DNA technologies) and cloned into the gWiz expression vector (Genlantis) using In-fusion cloning (Takara Bio). Cassettes encoding for Lumican-MSA-IL-2 and IL-12-MSA-Lumican from previously published work were used as templates for constructing IgGB-Lumican fusions (86). All constructs contained a C-terminus 6x His tag for purification purposes. See Table 2.1 for amino acid sequences. Plasmids were transformed into Stellar competent cells for amplification and isolated with Nucleobond Xtra endotoxin-free kits (Macherey-Nagel).

IgGB-lumican fusions were produced using the FreeStyle HEK293-F expression system (Gibco). Briefly, Freestyle 293-F cells were transiently transfected by mixing 1 mg/mL of plasmid DNA and 2 mg/mL of polyethylenimine (Polysciences) in OptiPRO Serum Free Medium (Gibco) and, after incubating, adding dropwise to the cells. 7 days after transfection, supernatant was harvested and His-tagged proteins were purified using TALON metal affinity purification resin (Takara Bio, Inc.)

Following purification, proteins were buffer exchanged into PBS (Corning) using Amicon Spin Filters (Sigma Aldrich), 0.22 μm sterile filtered (Pall), and confirmed for minimal endotoxin (<0.1 EU/dose) using a chromogenic LAL assay (Lonza). Molecular weight was confirmed with SDS-PAGE. Proteins run alongside a Novex Sharp Pre-Stained Protein Standard (Invitrogen) on a NuPAGE 4 to 12% Bis-Tris gel (Invitrogen) with 2-(*N*-morpholino) ethanesulfonic acid (MES) running buffer (VWR) and stained for visualization with SimplyBlue Safe Stain (Life Technologies). Proteins were confirmed to

be free of aggregates by size exclusion chromatography using a Superdex 200 Increase 10/300 GL column on an Äkta Explorer FPLC system (Cytiva). All proteins were flash frozen in liquid nitrogen and stored at -80°C.

Collagen ELISA

96 well plates precoated with rat collagen I (Gibco) or rat collagen IV (Coring) were blocked with PBSTA (PBS (Corning) + 0.1% w/v BSA (Sigma Aldrich) + 0.05% v/v Tween-20 (Millipore Sigma)) for 1 hour at RT. After washing with 3 times PBST (PBS (Corning) + 0.05% v/v Tween-20 (Millipore Sigma)) and 3 times with PBS (Corning), IgGB-lumican fusions were incubated in PBSTA for 3 hours at RT while shaking. Wells were washed 3 times with PBST and 3 times with PBS and then incubated with rabbit polyclonal α6xHis-Horseradish peroxidase (HRP) (1:4000, Abcam) in PBSTA for 1 hour at RT while shaking. Wells were again washed 3 times with PBST and 3 times with PBS and then 1-Step Ultra TMB-ELISA Substrate Solution (Thermo Fisher) was added for 5-15 min, followed by 1 M sulfuric acid to quench the reaction. Absorbance at 450 nm (using absorbance at 570 nm as a reference) was measured on an Infinite M200 microplate reader (Tecan). Binding curves were generated with GraphPad Prism software V9. K_D values were calculated using a nonlinear regression fit for one site total binding with no non-specificity and curves were normalized to the B_{max} values.

IgG binding ELISA

Clear Flat-bottom Immuno Nonsterile Nunc 96-well MaxiSorp Plates (Invitrogen) were coated with mouse IgG2a isotype control antibody (C1.18.4, BioXcell) at a concentration of 2.5 μg/mL in 350 μL of PBS (Corning). After washing with 3 times PBST (PBS (Corning) + 0.05% v/v Tween-20 (Millipore Sigma)) and 3 times with PBS (Corning), Plates were blocked PBSTA (PBS (Corning) + 0.1% w/v BSA (Sigma Aldrich) + 0.05% v/v Tween-20 (Millipore Sigma)) for 1 hour at RT. Plates

were again washed 3 times with PBST (PBS (Corning) + 0.05% v/v Tween-20 (Millipore Sigma)) and 3 times with PBS (Corning), IgGB-lumican fusions were incubated in PBSTA for 3 hours at RT while shaking. Wells were washed 3 times with PBST and 3 times with PBS and then incubated with rabbit polyclonal α6xHis-Horseradish peroxidase (HRP) (1:4000, Abcam) in PBSTA for 1 hour at RT while shaking. Wells were again washed 3 times with PBST and 3 times with PBS and then 1-Step Ultra TMB-ELISA Substrate Solution (Thermo Fisher) was added for 5-15 min, followed by 1 M sulfuric acid to quench the reaction. Absorbance at 450 nm (using absorbance at 570 nm as a reference) was measured on an Infinite M200 microplate reader (Tecan). Binding curves were generated with GraphPad Prism software V9. K_D values were calculated using a nonlinear regression fit for one site total binding with no non-specificity and curves were normalized to the B_{max} values.

Cells

4T1 mammary carcinoma cells were purchased from ATCC. Cells were cultured in Dulbecco's Modified Eagle Medium (DMEM, ATCC) supplemented with 10% Fetal Bovine Serum (FBS, Gibco). Cells were maintained at 37°C and 5% CO_2.

Mice

BALB/c (BALB/cAnNTac) mice were purchased from Taconic. All animal work was conducted under the approval of the Massachusetts Institute of Technology Committee on Animal Care in accordance with federal, state, and local guidelines.

IVIS and serum measurements

IgGB-lumican fusions were labeled with Alexa Fluor 568 NHS Ester (Life Technologies) and murine IgG2a isotype control antibodies (C1.18.4, BioXcell) were labeled with Alexa Fluor 647 NHS Ester (Life Technologies). A Zeba desalting column (Thermo Scientific) was used to remove excess dye. 1

nmol of IgGB-lumican were pre-incubated at a molar ratio of IgG:IgGB-lumican of 0.9. Total molar amount of dye injected per sample was normalized between groups before injection. Balb/c mice were inoculated with 5 x 10^5 4T1 cells and labeled proteins were injected i.t. on day 5. Fluorescence at the site of the tumor was measured longitudinally using the IVIS Spectrum Imaging System (Perkin Elmer). One week prior to study initiation, mice were switched to an alfalfa-free casein chow (Test Diet) to reduce background fluorescence. Total radiant efficiency was calculated after subtracting background fluorescence and normalizing to the maximum value for each protein using Living Image software (Caliper Life Sciences). For serum measurements of labeled proteins, 50 μL of blood was collected in MiniCollect serum sep tubes (Greiner) via cheek bleed. Fluorescence was read out on an Infinite M200 microplate reader (Tecan) and concentrations were calculated using a standard curve. Total mouse blood volume was assumed to be 2 mL for concentration calculations.

Statistical Methods

Statistics were computed in GraphPad Prism v9 as indicated in figure captions. IVIS retention data and serum fluorescence data were compared using two-way and one-way ANOVA, respectively, with Tukey's multiple comparison correction. Sample size and *P*-value cutoffs are indicated in figure captions.

Acknowledgements

We thank the Koch Institute's Robert A. Swanson (1969) Biotechnology Center (National Cancer Institute Grant P30-CA14051) for technical support, specifically the Preclinical Imaging and Testing Facility.

Chapter 3: Testing collagen anchoring agonist antibodies in preclinical cancer models

3.1: Introduction

In this chapter we recombinantly express direct collagen binding domain fusions to agonist antibodies and, after *in vitro* validation and proof-of-concept *in vivo* retention studies with control antibodies, we test these payloads *in vivo* in murine cancer models. Specifically, we studied collagen anchoring agonist antibodies against 4-1BB, a TNFSFR co-stimulatory receptor, and CD28, the canonical T cell co-stimulatory receptor. We begin using lumican as our collagen binding domain, the same domain employed in chapter two. However, the bulk of the work covered in this chapter instead uses the ectodomain of murine LAIR1 ("LAIR") as a collagen binding domain. As a brief reminder, LAIR is an inhibitory receptor containing a cytoplasmic ITIM and expressed on a wide range of immune cells (158, 159). The ectodomain is a small 13 kDa protein that has been previously validated as a suitable collagen binding domain for retention of the cytokine IL-2 in the tumor microenvironment (TME) (92, 103). Some chapter specific background is provided below:

The role of CD28 signaling in the PD-1 pathway

PD-1 ligation can inhibit T cell activation, and it was initially thought that it did so by recruiting phosphatases to the immunological synapse and dampening T cell receptor (TCR) signaling. Recent literature evidence instead demonstrates that PD-1 preferentially inhibits signaling downstream of CD28 over other immunological synapse members (160). This suggests that the functional consequence of blocking the PD-1 pathway may be restoration of CD28 costimulatory signaling.

Indeed, Kamphorst et al., demonstrated in the same issue of *Science* that CD28 signaling is necessary for successful responses to αPD-L1 therapy in both a chronic viral infection model and subcutaneous tumor model (via both genetic deletion of CD28 and αB7 blocking antibodies) (161). Additionally, in a small cohort of non-small cell lung cancer (NSCLC) patients treated with either αPD-1 or αPD-L1, proliferating $CD8^+$ T cells in the blood were also largely $CD28^+$, providing circumstantial evidence that CD28 signaling may also be important for antitumor responses to αPD-1/αPD-L1 in humans (161). Further evidence in ovarian cancer suggests that intraepithelial myeloid antigen presenting cells (mAPC) niches provide CD28 costimulation to tumor infiltrating lymphocytes (TILs), maintaining their polyfunctionality and preventing exhaustion. Moreso, these CD28 costimulated TILs, and their proximity to mAPCs, was associated with response to αPD-1 in solid tumors (162). All of the above evidence makes a strong case that CD28 signaling is crucial for responses to αPD-1 therapy, and that perhaps αPD-1 therapeutic efficacy can be improved by providing additional exogenous CD28 signaling.

Bystander T cell in tumors

It has been well documented that many tumors are highly infiltrated with a large fraction of "bystander T cells" that do not recognize tumor cell antigens (these are instead often viral antigen reactive T cells). This infiltration of non-tumor specific T cells is driven by several chemokines, including CCL5, CXCL9, and CXCL10, in an antigen independent manner and these cells typically represent a sampling of the overall T cell repertoire in a given patient (163). Additionally, because these cells do not experience chronic antigen stimulation in the tumor, they do not become exhausted and are phenotypically distinct from tumor retrieve T cells (164). A recent study exploring TCR affinity additionally identified a subset of tumor-reactive T cells that are unable to kill tumor cells on their

own but remain functional *ex vivo*, a state termed "functional inertness" (165). Furthermore, it has been suggested that tumor reactive T cells can kill nearby antigen negative T cells in a Fas dependent mechanism (166). Thus, these two cell populations (bystander T cells and functionally inert tumor reactive cells) represent a relatively large, highly functional T cell pool that, if properly channeled, could exert a potent antitumor effect. Indeed, bispecific T cell engagers that simultaneously engage tumor specific antigens and the TCR complex can do just that - artificially clustering the TCR and re-directing cytotoxic T cells towards tumor cells independent of TCR specificity. In part of this chapter, we briefly explore exploiting these cells in an antigen independent manner using collagen anchoring αCD3-LAIR agonist antibodies, in combination with αCD28-LAIR agonist antibodies, to broadly activate T cells in the TME.

Alum anchoring

In addition to collagen anchoring, in this chapter we briefly explore the use of an alum anchoring approach previously validated in the contexts of tumor localized cytokine and interferons by our lab in collaboration with the Irvine lab at MIT (167–170). Aluminum hydroxide (Alum) is an FDA approved vaccine adjuvant that has been used safely in humans for over 100 years. When injected in tissues, micrometer sized alum particles form a physical depot in the tumor that can persist for weeks (171). It has been demonstrated that phosphorylated proteins can bind tightly to these alum depots, allowing for long term retention of biologic payloads at the site of injection (172). Yash Agarwal, a former graduate student in our lab and Darrell Irvine's lab, engineered short peptide tags containing phosphorylation motifs recognized by the mammalian Fam20C kinase (termed alum-binding peptides, or ABPs, with "ABP10" being the peptide used in the majority of our published alum anchoring work) (168, 170). Co-expression of tagged cytokines and Fam20C kinase allowed for efficient recombinant expression of phosphorylated cytokines and simple mixing with alum led to rapid adsorption of these

cytokines onto alum. When injected intratumorally, these cytokines are retained for over a week and, in the context of alum retained IL-12, improved response rates and decreased systemic toxicities are observed. This system was also validated to improve the therapeutic index of interferon therapy (167, 169). In this chapter, we briefly explore the development of alum anchored αCD28 agonists.

3.2: Results

α4-1BB, αCD3, αCD40, and αOX40 are amenable to lumican and LAIR fusion

To construct tumor localized agonist antibody therapies, we designed direct fusions of validated agonist antibodies to two collagen binding domains, lumican and LAIR. We recombinantly expressed α4-1BB (clone LOB12.3), αCD3 (clone 145-2C11), αCD40 (clone 3/23) and αOX40 (clone OX-86) with lumican fused to the C-terminus of the heavy chain separated by a short linker. Additionally, we recombinantly expressed α4-1BB (clone LOB12.3) with the ectodomain of murine LAIR1 fused to the C-terminus of the heavy chain, also separated by a short linker (Table 3-1). After confirming expected size by SDS-PAGE, we validated their ability to bind collagen I coated plates by ELISA (Fig. 3-1). As expected, based on reported literature values and prior cytokine fusion work in our lab, α4-1BB-LAIR fusions had higher measured affinity for collagen I than α4-1BB-lumican fusions. Due to the improved affinity of LAIR fusions and the smaller, more modular size of LAIR compared to lumican, we proceeded with using LAIR as the collagen binding domain in all subsequent work.

IgG-LAIR is preferentially retained in the tumor microenvironment

To assess retention of LAIR antibody fusions and validate that this collagen anchoring strategy improves the residence time of these payloads in the tumor, we utilized *in vivo* fluorescence imaging (IVIS). To eliminate any potential confounding target-mediated drug disposition (TMDD), we

constructed a αFITC-LAIR antibody fusion (and a αFITC control antibody), as these antibodies have no natural target in a mouse. Additionally, these antibodies were constructed with murine IgG2c heavy chain constant regions with LALA-PG silencing mutations to ablate any Fc gamma receptor (FcγR) binding (173). Fluorescently labeled protein was injected intratumorally and tracked longitudinally using IVIS. αFITC-LAIR displayed enhanced retention in the tumor over free αFITC antibody (Fig 3-2).

α4-1BB-LAIR + LAIR-MSA-IL-2 has minimal efficacy in B16F10 model

Prior work by our lab (in collaboration with the Irvine lab) has highlighted the potential synergy between IL-2 and α4-1BB therapy. Specifically, formulation of liposome bound IL-2 and α4-1BB and direct injection of these liposomes into the tumor microenvironment led to enhanced retention of these payloads in the tumor, increased efficacy, and reduced toxicity in a B16F10 melanoma model (174). Additionally, it has been reported that 4-1BB signaling increases CD25 expression on $CD8^+$ T cells, thus making these cells more sensitive to IL-2 signaling and IL-2 mediated $CD8^+$ T cell expansion (60). Thus, we felt collagen anchored α4-1BB-LAIR and LAIR-MSA-IL-2 was a promising therapeutic combination to test. After validating that α4-1BB-LAIR and α4-1BB bound surface expressed 4-1BB with similar affinity, we began testing these constructs *in vivo* (Fig. 3-3). B16F10 tumor bearing mice were treated with either PBS, α4-1BB + LAIR-MSA-IL-2, or α4-1BB-LAIR + LAIR-MSA-IL-2. For this initial survival experiment, we did not interrogate the effect of collagen anchored vs. non-collagen anchored IL-2 and instead used collagen anchored IL-2 exclusively. Both groups had statistically significant growth delay when compared to PBS, and although only the collagen anchored α4-1BB-LAIR + LAIR-MSA-IL-2 experimental cohort had any mice that completely rejected their tumors (2/9 vs. 0/8 tumor free mice when compared to α4-1BB + LAIR-MSA-IL-2), these two groups were

not statistically different (Fig. 3-4A). Because the overall efficacy of this combination was poor and there did not to be any clear major difference between the collagen anchored and non-collagen anchored formats of the α4-1BB agonist in this setting, we did not further investigate this combination therapy. No toxicity, as assessed by weight loss, was observed with either treatment group (Fig. 3-4B).

Localized α4-1BB-LAIR is ineffective as a monotherapy in inflamed tumor models

We next sought to interrogate the efficacy of collagen anchored α4-1BB as a monotherapy in more inflamed tumor models. We hypothesized that these tumors would be better poised to respond to tumor localized α4-1BB therapy, as there would be a larger intratumoral $CD8^+$ T cell pool at time of treatment. We therefore tested α4-1BB and α4-1BB-LAIR in the MC38 colon carcinoma model, which is more inflamed than the B16F10 model with a larger T cell infiltrate (175). We observed a modest growth delay from this therapy, but there was no difference between the collagen anchored and non-collagen anchored versions of the α4-1BB agonist (Fig. 3-5A). In fact, although not statistically significant, only the non-collagen anchored α4-1BB agonist group had any long-term survivors that were able to completely reject their tumor. We did not observe any therapy-associated weight loss with either treatment (Fig. 3-5B).

As a final attempt to test α4-1BB monotherapy in a more inflamed model, we turned to the CT26 colon carcinoma model. This tumor model has an increased $CD8^+$ T cell infiltrate compared to both B16F10 and MC38 (175). Additionally, prior literature has shown that ~80% of CT26 tumor bearing mice are able to reject their tumors when treated with just two 1 mg/kg (2 μg total) doses 9 and 11 days after tumor implantation. Growth delay was also reported with 0.1 mg/kg (0.2 μg total) dosing (176). We reasoned that given the enhanced retention of collagen anchored α4-1BB, a single dose

should be sufficient to see responses. We therefore performed a pilot experiment treating mice CT26 tumor bearing mice with a single dose of 20 μg, 2 μg, or 0.2 μg of α4-1BB or molar equivalent doses of α4-1BB-LAIR. Although we observed some cures at the high dose, we again did not see major differences in efficacy between collagen anchored and non-collagen anchored α4-1BB therapy (Fig. 3-5C). Once again, we did not observe any therapy-associated weight loss with either treatment (Fig. 3-5D). Because we were unable to observe monotherapy efficacy differences between collagen anchored and non-collagen anchored formats of α4-1BB, we ceased efforts to study this monotherapy and instead focused our efforts on α4-1BB-LAIR combination therapies.

TA99 + α4-1BB-LAIR demonstrates modest efficacy in B16F10 melanoma model

The human α4-1BB agonist Urelumab is being clinically tested in combination with antitumor antibodies Rituximab, Cetuximab, and Elotuzumab which target CD20, EGFR, and SLAMF7, respectively (NCT01775631, NCT02110082, NCT02252263). Preliminary data has not been encouraging, with early reports from the Rituximab combo suggesting that Rituximab + Urelumab is no more efficacious than Rituximab monotherapy (177). Preclinical data supports the exploration of this combination, as it has been shown that antitumor antibody engagement with FcγRs on NK cells increases expression of 4-1BB, and subsequent treatment with an α4-1BB agonist enhances their cytotoxicity capacity. Additionally, published data from the Urelumab + Cetuximab trial suggests that this combination enhances the activation state of dendritic cells through a NK cell mediated mechanism[1]. We sought to evaluate if our collagen anchoring α4-1BB agonists would improve the

[1] At the time these studies were carried out, three preclinical studies also suggested that α4-1BB synergized robustly with Rituximab, Cetuximab, and Trastuzumab in xenograft and/or humanized

efficacy of this combination. Mice were inoculated with B16F10 melanoma flank tumors and treated systemically (intraperitoneally, or i.p.) with TA99, an antitumor antibody that binds to Trp1 expressed on the surface of B16F10 cells, followed by intratumorally (i.t.) administered α4-1BB-LAIR one day later for a total of 4 weekly cycles (this combination of TA99 + α4-1BB-LAIR is referred to collectively as the treatment, or "Tx", henceforth) (Fig. 3-6A). Although this combination leads to a statistically significant growth delay compared to PBS treated mice, nearly all mice eventually succumb to their tumor burden, with only ~5% of mice achieving a complete response (CR, defined as no palpable tumor at day 100) (Fig. 3-6B). Once again, we did not observe any therapy-associated weight loss with this combination (Fig. 3-6C).

Single dose TA99 + α4-1BB-LAIR does not synergize with αPD-1 in B16F10 melanoma model

The poorly immunogenic B16F10 cell line does not typically respond to αPD-1 therapy. Recent work examining heterogeneous responses to dual immune checkpoint blockade (ICB) therapy (αPD-L1 and

---

mouse models. These influenced our selected dosing schedule (weekly cycles and more importantly α4-1BB given 24 hours after antitumor antibody treatment, as this delay has been shown to be critical to efficacy). However, around the time we began our studies, these papers were retracted with specific concerns regarding the *in vivo* efficacy data. Citations to the retraction notices, but not the original articles themselves, are included here for full transparency of our study design motivation: Kohrt et al., *Blood* (2019), Kohrt et al., *J. Clin. Investig.* (2019), Kohrt et al., *J. Clin. Investig.* (2019).

αCTLA-4) found that infiltration of activated NK cells and STAT1 activation gene signatures are correlated with response to ICB (178). More importantly, this work demonstrated that treating with a short course of "sensitizing" therapies (peritumoral interferon-gamma (IFNγ), peritumoral poly:IC, and intraperitoneal αIL-10) prior to initiation of dual ICB therapy improved response rates. It has been reported that NK cells upregulate 4-1BB in patients treated with antitumor antibodies or when co-cultured *ex vivo* with antitumor antibody coated tumor cells via an FcγR mediated mechanism (179, 180). Additionally, there is (albeit mixed) evidence that 4-1BB signaling on NK cells increases their cytotoxicity and activation state (61–63). Therefore, we hypothesized that a single dose of TA99 + α4-1BB-LAIR would reprogram tumor resident NK cells, leading to an activated NK cell state in the tumor and improve responsiveness to ICB therapy. To test this, we treated B16F10 tumor bearing mice with a single cycle of TA99 + α4-1BB-LAIR followed by αPD-1 every three days. To our disappointment, we did not observe any improvement to αPD-1 therapy responsiveness in these mice (Fig. 3-7A). again, we did not observe any therapy-associated weight loss with this combination (Fig. 3-7B). Note that the transient weight loss dip seen at day 12 occurred in both the treatment groups and untreated mice (and to equivalent levels) and is believed to be a technical artifact.

No evidence of toxicity is seen with α4-1BB constructs in our model system

Although agonist antibody therapies have an exceedingly narrow therapeutic index in the clinic, hampering their translational potential, often little to no toxicities are observed in preclinical mouse studies. This has impaired our ability as a field to *a priori* predict associated irAEs with agonist immunotherapies, which was most exemplified by the Tegenero αCD28 superagonist trial (36). Indeed, we did not observe any toxicity in any of the above previously described α4-1BB therapies (Fig. 3-4, 3-5, 3-6, 3-7). In particular, we were interested in further probing treatment related toxicity

observed from the TA99 + α4-1BB combination. It has been previously documented that the specific antibody clone we have employed in these studies (LOB12.3) displays minimal toxicity in mouse models. However, a second antibody clone (3H3) that can display modest levels of toxicity in mouse models (181, 182). Interestingly, this may be explained by the 3H3 clone's ability to cluster 4-1BB independent of FcγRs, while LOB12.3 relies on FcγR mediated 4-1BB clustering. Nonetheless, it has been documented that human toxicities often manifest as liver toxicity, and in mouse models this liver toxicity is driven by 4-1BB activation on liver resident myeloid and macrophage populations and subsequent T cell infiltration and activation (26). Work from the Murphy lab has highlighted how aging can predispose mice to cytokine storm and lethal autoimmunity following treatment with certain immunotherapies. Mechanistically, aging induced increases in adiposity increases the basal inflammatory state of peripheral macrophage populations which mediates this increase in toxicity (183, 184). Although they did not examine the effects of α4-1BB agonists in this model system, we reasoned that because 1) the toxicity they observed was macrophage mediated and 2) α4-1BB agonist toxicity has also been shown to be myeloid/macrophage mediated then perhaps this would be a good model system to explore α4-1BB toxicity and demonstrate how tumor localization can improve the therapeutic index of these modalities.

To that end, we purchased aged C57Bl/6 mice (aged 51 weeks at time of tumor inoculation) and treated them with either PBS, TA99 + α4-1BB (i.p.), TA99 + α4-1BB (i.t.), or TA99 + α4-1BB-LAIR (i.t.). In addition to monitoring weight loss as a readout of treatment related toxicity, we also monitored body temperature (via infrared rectal readings) and collected serum 24, 48, and 72 hours post α4-1BB treatment for the first two rounds of treatment. As mice reached the euthanasia criteria, we also harvested and formalin fixed spleens, livers, and lungs. As expected, only the intratumoral collagen

anchored combination therapy had a minor but statistically significant therapeutic benefit (Fig. 3-8A). We did not observe any weight loss or consistent changes in body temperature with any of the treatment groups, including the mice treated with systemic α4-1BB agonist (Fig. 3-8B-C). The only body temperature decreases observed were correlated with mice that had reached the euthanasia criteria and had a large tumor burden and general poor body condition. The time period in which serum was being collected is highlighted in gray in each plot.

To further assess the safety profile of these various α4-1BB agonists in this aged mouse model, we profiled serum samples 24, 48, and 72 hours post first treatment with a 13-analyte cytokine panel looking mainly at innate cell produced inflammatory cytokines (specifically IL-1α, IL-1β, IL-6, IL-10, IL-12p70, IL-17A, IL-23, IL-27, MCP-1, IFNβ, IFNγ, TNFα, and GM-CSF). We did not observe any elevation of these cytokines in any of the treatment groups when compared to PBS (Fig. 3-9). Thus, even in aged mice predisposed to inflammatory responses to immunotherapy we did not observe any signs of systemic immune activation or irAEs with local or systemically dosed α4-1BB agonist antibody therapy. Because we did not observe any toxicity at the gross (weight loss/body temperature) or serum protein level, we ceased efforts to examine treatment related toxicity with α4-1BB therapy. We reason that the observed toxicity of systemically delivered α4-1BB antibody therapy in clinical trials is sufficient motivation to develop tumor localized collagen anchored α4-1BB agonist therapy, regardless of the toxicity profiles observed in preclinical murine cancer models.

αCD28 amenable to expression as Fab, binds cell-surface expressed CD28

Because αCD28 antibody sequences were not readily available in the literature or from collaborators, we obtained a hybridoma line from the Allison lab that produces the commonly used clone 37.51

αCD28 agonist antibody. This antibody is commonly used in *in vitro* T cell activation protocols. We sequenced the hybridoma line and produced the full Syrian Hamster αCD28 antibody and confirmed that it binds to murine CD28 with a similar affinity to commercially produced αCD28 antibody (Fig. 3-10). As we have done with previously described agonist antibodies, we then grafted the variable regions of the light chain and heavy chain onto a murine kappa light chain constant region and murine IgG1 heavy chain constant region, respectively.

To validate that this antibody properly folds in this chimeric format, we titrated it on HEK cells transiently transfected to express murine CD28 on their cell surface. Unfortunately, we did not observe any binding activity for this chimeric antibody (Fig. 3-11A-B). Although we were able to calculate a dissociation constant (K_D) for the chimeric antibody, the significantly attenuated B_{max} binding signal for the chimera compared to the WT Syrian hamster antibody suggested that this antibody likely has compromised function compared to the WT construct and it is likely the calculated dissociation constant and normalized binding curve is simply an artifact. This is likely due to a mismatch between Syrian hamster variable region and mouse constant region contact residues and subsequent misfolding. We instead tried expressing these as fully Syrian hamster Fabs (antibody fragments consisting of the full light chain and a truncated portion of the heavy chain (V_H and C_H1 domains only)). In this format, the Fabs were able to bind to HEK cells expressing murine CD28 with relatively high measured affinity (Fig. 3-11C).

Because these constructs are monovalent and lack an Fc region necessary for FcγR mediated clustering, we did not expect these Fabs on their own to exhibit activity *in vivo*. We additionally constructed Fab constructs with fusion of LAIR or ABP10 to allow for collagen anchored or alum

anchored retention of the Fabs in the TME. We hypothesized that collagen binding and/or alum anchoring would be able to drive sufficient receptor clustering to mediate downstream signaling. We confirmed that these variants also bound cell-surface expressed CD28, the LAIR fusions bound collagen I coated plates, and using a malachite green assay we confirmed that ABP10K fusions were properly phosphorylated (Fig. 3-11C-E).

αCD28 Fab construct does not display agonistic activity *in vitro* or *in vivo*

We next sought to text these constructs *in vivo* in combination with αPD-1. MC38 tumor bearing mice were treated with αPD-1 monotherapy or αPD-1 + αCD28, αPD-1 + αCD28-LAIR, or αPD-1 + αCD28-ABP10K + alum, with the αCD28 Fab constructs given at two different doses. Unfortunately, we observed a relatively high baseline αPD-1 response rate in this study, making it difficult to distinguish improved efficacy of combination therapies. Only the αPD-1 + αCD28-ABP10K + alum (at the low dose, but not high dose) demonstrated improved efficacy over αPD-1 alone (Fig. 3-12A). We did not observe any treatment related toxicity, as measured by weight loss, for any of the treatments (Fig. 3-12B).

Due to the disappointingly low activity observed *in vivo*, we developed a functional assay to test the ability of these Fabs to elicit CD28 signaling *in vitro*. Activating $CD8^+$ T cells with αCD3 and αCD28 antibodies results in a range of phenotypic changes, including upregulation of activation markers such as PD-1, CD69, CD25, and 4-1BB and release of cytokines such as IL-2 (185, 186). We chose to use IL-2 secretion, measured by ELISA, as a readout for T cell activation. Using commercial αCD3 and αCD28 (the same clones as our in-house recombinantly expressed αCD3 and αCD28 antibodies) we performed a pilot assay scanning a range of antibody coating concentration and assaying IL-2 secretion

at two time points, 24 hours and 72 hours, using purified naive $CD8^+$ T cells (Fig. 3-13AB). We observed that IL-2 secretion is detectable quickly, with large increases in supernatant IL-2 observed at the 24 hour time point, and most future assays were run for only 24 hours to increase the throughput of this development process.

We next tested the ability of our αCD28 Fabs to elicit IL-2 secretion. Plates were coated with commercial αCD3 antibody and a range of αCD28, αCD28-LAIR, or αCD28-ABP10K Fab concentrations. At the concentrations tested, no detectable IL-2 secretion was seen after 24 hours or 72 hours in culture (Fig. 3-13C-D). We repeated this assay a second time scanning a larger concentration range and similarly observed no IL-2 secretion (this time looking only after 24 hours in culture) (Fig. 3-13E). Thus, these assays seem to suggest that even at high concentrations, these Fabs are unable to elicit T cell activation *in vitro* and this may explain the poor activity *in vivo*.

αCD28 hamster-mouse hinge chimera antibody is active *in vitro* and amenable to LAIR fusion

To rectify the lack of activity we observed with αCD28 Fabs both *in vitro* and *in vivo* and the apparent lack of binding for murinized chimeric αCD28 antibodies, we explored other chimeric formats of this antibody. Importantly, we wished to preserve the murine Fc region of this antibody, as Fc:FcγR interactions are important for agonist antibody activity *in vivo* and little is known about Syrian hamster Fc interactions with murine FcγR, complicating our ability to properly interpret experimental outcomes. As we had hypothesized that earlier attempts to graft Syrian hamster αCD28 variable regions onto fully mouse constant regions failed due to issues with variable region and C_L/C_H1 contact residues, we decided to construct a chimeric antibody with a fully Syrian hamster αCD28 light chain

and an αCD28 heavy chain with a Syrian hamster variable region and C_H1 domain and murine IgG1 hinge, C_H2, and C_H3 domains.

We found that this αCD28 antibody, which we termed αCD28 hinge chimera, was able to activate $CD8^+$ T cells *in vitro* with a similar EC_{50} as commercial fully Syrian hamster αCD28. We then constructed αCD28-LAIR and αCD28-ABP10K hinge chimera antibodies and also confirmed their ability to activate $CD8^+$ T cells *in vitro* (Fig. 3-14A). Due to expression issues, both LAIR and ABP10K were fused to the C-terminus of the light chain in these constructs instead of the heavy chain. We also tested the ability of αCD28-LAIR and αCD28-ABP10K hinge chimera antibodies (paired with αCD3-LAIR and αCD3-ABP10K antibodies, respectively) to activate $CD8^+$ T cells on either collagen coated plates or co-incubated with alum, respectively. We observed that αCD28-LAIR + αCD3-LAIR were able to stimulate $CD8^+$ T cells in a dose dependent manner on collagen I coated plates. Interestingly, we did not observe any activity from commercial control αCD3 + αCD28 antibodies, or αCD28-LAIR + control αCD3. We hypothesize this lack of activity is the result of control αCD3/αCD28 unable to adsorb onto the collagen coated plates. It is possible that other plate coating strategies, such as dry coating the plates overnight (where the coating liquid is allowed to evaporate overnight) could have remedied this issue. However, further assay development in this context was not pursued. However, the fact that αCD28-LAIR + αCD3-LAIR was able to stimulate T cells while bound to collagen is encouraging, as it suggests that collagen binding allows for sufficiently high levels of TCR/CD28 clustering to elicit productive signaling in T cells. We did not observe any IL-2 secretion with $CD8^+$ T cells incubated with αCD3-APB10K + αCD28-APB10K coated onto alum (Fig 3-14C). We confirmed that alum being present in culture with T cells in control αCD3/αCD28 coated wells

did not interfere with activation, thus this lack of activity is likely due to the loading density of these antibodies onto alum. Because of the time/effort required to optimize the ratios of both antibodies to alum to elicit successful signaling, we decided to focus our efforts instead on studying αCD28 and αCD28-LAIR *in vivo*, with plans to revisit alum anchored versions of these antibodies if initial results were promising.

αCD28 hamster-mouse chimeric antibody has minimal *in vivo* efficacy

Having developed a functional αCD28 suitable for *in vivo* agonism, we sought to test two different αCD28 agonist-based immunotherapy combinations. As discussed previously, recent evidence has suggested a role for CD28 signaling in successful αPD-1/αPD-L1 checkpoint blockade therapy, and thus we hypothesized that αCD28 agonist antibody therapy would synergize with αPD-1 checkpoint blockade. We treated MC38 tumor bearing mice with αPD-1, αPD-1 + αCD28, or αPD-1 + αCD28-LAIR, with αCD28/αCD28-LAIR given at both a low and high dose intratumorally (10 μg and 1 μg of αCD28 and molar equivalents of αCD28-LAIR, respectively).

We observed minimal efficacy of αPD-1 as a monotherapy in this study. αPD-1 + αCD28-LAIR at the high dose had a slight but statistically significant growth delay over αPD-1 alone, while the low dose αCD28-LAIR offered no additional benefit (Fig. 3-15A). To our surprise, both low and high dose non-collagen anchored αCD28 enhanced αPD-1 therapy to a greater degree than the collagen anchored versions of αCD28. Indeed, this combination led to complete tumor regression in a subset of mice, with 30% and 40% of mice completely rejecting their primary tumor and remaining tumor free until day 110 when treated with αPD-1 + αCD28 (low dose) or αPD-1 + αCD28 (high dose), respectively. No treatment-associated weight loss was seen with any of these treatments (Fig. 3-15B).

Additionally, we were interested in testing combination αCD3 + αCD28. As discussed previously, because of the often large infiltrate of "bystander" T cells in the TME this combination therapy providing the canonical "signal 1" and "signal 2" of T cell activation would broadly and robustly activate all infiltrating T cells in the tumor, leading to enhanced cytotoxicity of these cells and cytokine milieu repolarization. Simply put, we viewed this strategy as akin to activating T cells *ex vivo* in a cell culture dish. To that end, we treated MC38 tumor bearing mice with either αCD3 + αCD28 or αCD3-LAIR + αCD28-LAIR, again at both a high (10 μg αCD28, 2 μg αCD23, or molar equivalents for LAIR fusions) and low (1 μg αCD28, 0.2 μg αCD23, or molar equivalents for LAIR fusions) dose, again all intratumorally. Based on our *in vitro* data we reasoned that a 5:1 mass ratio of αCD28:αCD3 would allow for maximum T cell stimulation. To our disappointment, we did not observe growth delay for any of the treatment groups (Fig. 3-16A). Consistent with this lack of activity and with prior data no treatment-associated weight loss was seen with any of these treatments (Fig. 3-16B).

We hypothesized that tumors with a larger baseline infiltrate would be better poised to respond to this αCD3 + αCD28 combination therapy. To test this hypothesis, we tested two additional models. First, we switched to using the MC38-SIY model. This tumor line has an engineered antigen (SIYRYYGL), increasing the immunogenicity of the line and (we hypothesized) leading to higher levels of baseline T cell infiltration. In addition, we co-treated some tumors with adoptive cell transfer (ACT) of 1 million activated $CD8^+$ T cells isolated from spleens of 2C transgenic mice. These 2C $CD8^+$ T cells all express the same TCR which recognizes the SIY antigen. Thus, this represents a best case scenario where the tumor contains a large amount of freshly infiltrated and properly activated tumor reactive $CD8^+$ T cells. To reduce the number of experimental groups, we only focused on the high dose of

αCD3 + αCD28 (10 μg αCD28, 2 μg αCD23, or molar equivalents for LAIR fusions) for this survival study. Much to our disappointment, we did not observe any survival benefit for mice for any of the treatment groups (Fig. 3-16C). In fact, for the mice treated with non-collagen anchored αCD3 + αCD28 (with or without ACT) progressed *faster* than vehicle control treated tumors, and this effect was statistically significant. Again, no treatment-associated weight loss was seen with any of these treatments (Fig. 3-16D).

3.3: Discussion

In this chapter, we developed direct fusions of agonist antibodies to collagen binding domains for intratumoral retention of these therapeutic payloads. We validated that this was a generalizable strategy, successfully expressing fusions of α4-1BB, αCD28, αCD3, αOX40, and αCD40 to two different collagen binding domains, lumican and LAIR. For the latter collagen binding domain, we also confirmed that LAIR fusion to control (αFITC) IgG had enhanced *in vivo* retention in the TME. We subsequently tested a subset of these agonist antibody *in vivo* in murine tumor models. In particular, we focused on α4-1BB-LAIR and αCD28-LAIR.

Although agonist antibodies, and specifically those targeting 4-1BB and CD28, are associated with toxicities in the clinic, mice tolerate these therapies fairly well. Indeed, in none of our studies did we observe any weight loss associated toxicities when these payloads were administered, regardless of collagen anchoring status. It has been reported that older mice, due to their increased adiposity, have a higher propensity for immune related adverse events (irAEs) after immunotherapy treatment (183, 184). However, in the context of α4-1BB agonist therapy combined with antitumor antibody TA99,

we still did not observe any signs of irAEs (measured by weight loss, drops in body temperature, or increases in serum cytokine levels). In the context of αCD28 agonists, there is minimal clinical data, but early trials suggest that even low dose αCD28 agonist therapy can elicit severe, and potentially lethal, cytokine storm and this cytokine storm is primarily caused by activating effector memory $CD4^+$ T cells (36, 37). However, because mice used in our studies are raised in specific pathogen free environments, they have relatively few effector memory $CD4^+$ T cells and additionally lack the natural bacterial and fungal microbiome that free-living mammals have. A recent study found that by transferring C57Bl/6 mice embryos into wild mice, they could generate a "wildling" colony of C57Bl/6 mice with a more diverse microbiome that is more faithful to free-living mammals (187). These mice, when treated with αCD28 superagonists previously used in the clinic, had inflammatory responses that mirrored those experienced in the phase I clinical trial. Thus, this wilding mouse model may be a good platform to test collagen anchored agonist antibodies and to demonstrate the utility, from a toxicity standpoint, of this collagen anchoring strategy. Nonetheless, the enhanced intratumoral retention as demonstrated by longitudinal fluorescence tracking suggests that there is significantly less systemic dissemination of these collagen anchored payloads. Because less systemic dissemination should result in less on-target, off-tumor toxicity, it is reasonable to assume that our collagen anchoring would result in safer agonist antibody therapeutics.

In addition to improved toxicity, we were also interested in how collagen anchoring improved the efficacy of these agonist antibodies. As we have seen previously for tumor localized cytokines (using collagen anchoring and alum anchoring strategies), increased retention in the tumor improves therapeutic outcomes in preclinical studies (86, 92, 167, 168). Unfortunately, we observed minimal to

no improvements in efficacy for collagen anchored agonists versus non-collagen anchored agonists in most combinations tested.

Our studies examining collagen anchored αCD28 agonists had perplexing results. Encouragingly, we did observe that αCD28 agonists improved the efficacy of αPD-1 therapy, consistent with reports that CD28 costimulation is important for responses to αPD-1 (161, 162). However, to our disappointment we found that collagen anchored αCD28-LAIR did not synergize with αPD-1. Although we did not explore this phenomenon further experimentally, there are two hypotheses for this observation. First, collagen is not uniformly spatially distributed in the tumor, and it is possible that collagen localization of αCD28 is not the optimal distribution of this payload, with $CD8^+$ T cells poised to respond to CD28 signaling located in collagen sparse regions of the tumor. Additionally, literature indicates that the stem-like $CD8^+$ T cell populations that proliferate and respond to αPD-1 therapy are located in the tumor draining lymph node (TdLN) (188), suggesting that perhaps TdLN localization of αCD28 agonists is preferential over tumor localization. Although we did not characterize compartment distribution in our model, it is possible that free αCD28 antibody drains better to the TdLN when compared to αCD28-LAIR, thus explaining the better response rate. Because lymph nodes are also collagen rich environments, our collagen anchoring strategy is still a viable option, and future studies utilizing intranodal or perinodal injections of αCD28-LAIR in combination with αPD-1 are warranted (189).

Our studies examining collagen anchored αCD28-LAIR and αCD3-LAIR agonists also had difficult to interpret results. Although this combination was largely ineffective at altering tumor growth kinetics, with or without adoptive cell transfer (ACT) of tumor reactive T cells in the MC38-SIY

model, we observed that treatment with αCD28 and αCD3 actually *enhanced* tumor growth, with mice surviving for shorter time spans than untreated mice or mice treated with ACT alone. To reiterate, this phenomenon was restricted only to the non-collagen anchored agonists, with αCD28-LAIR and αCD3-LAIR having no impact on growth of MC38-SIY. This observation again highlights that, in the context of intratumorally administered αCD28 agonists, collagen anchoring may spatially localize these agonists to away from cells poised to respond to CD28 signaling. Why this combination of αCD28 and αCD3 (with or without ACT) led to increased tumor growth and worse survival is unclear, but we have two testable hypotheses. One hypothesis is that these agonists preferentially expand tumor Tregs, leading to an increased immunosuppressive environment and accelerated tumor growth. Some literature evidence supports this, as early work exploring αCD28 agonists in vivo found that low dose αCD28 was able to preferentially expand Tregs (190, 191). Another possibility is that the accelerated tumor growth and decreased survival we observed was an aggressive form of pseudoprogression, with αCD28 and αCD3 increasing proliferation of the adoptively transferred cells and/or endogenous T cell population and thus creating the appearance of a larger tumor. Indeed, pseudoprogression has been observed in humans receiving immunotherapy, but whether this is what we observed here (and whether or not pseudoprogression that is severe enough to cause tumors to increase beyond the euthanasia criteria is possible) is unclear (192). Nonetheless, the perplexing results observed in these αCD28-LAIR combinations, and the seeming ability of collagen anchoring to limit the *in vivo* activity of αCD28-LAIR, warrants further investigation.

Of the several monotherapy and combination therapies tested with collagen anchored α4-1BB-LAIR, only one combination showed promise. α4-1BB-LAIR combined with TA99, an antitumor antibody

targeting a surface antigen expressed on B16F10 cells, led to a modest but significant growth delay. Notably, this was the only combination tested where we saw that collagen anchored α4-1BB-LAIR outperformed non-collagen anchored α4-1BB agonist. To better understand the immunological mechanism behind this therapeutic combination and improve upon it, we performed immune cell depletion studies. During the course of these studies, we discovered that αCD4 depletion synergized robustly with TA99 + α4-1BB-LAIR, and the results of these studies and subsequent follow up work are discussed in chapter four and also covered in our recent preprint (193).

Overall, this chapter details our efforts to develop direct fusions of collagen binding domains to agonist antibody therapies. This strategy appeared to be generalizable to a wide range of agonist antibodies and collagen binding domains. However, when we tested α4-1BB-LAIR and αCD28-LAIR *in vivo* as monotherapies and combination therapies, we saw somewhat disappointing benefits of collagen anchoring. This is in stark contrast to collagen anchoring cytokines, which saw uniform increases in efficacy and decreases in toxicity in virtually all combinations tested (86). Still, we did observe efficacy improvements when combining α4-1BB-LAIR with an antitumor antibody, demonstrating that this combination does have some promise. Further studies exploring both compartment localization (tumor vs. TdLN) and more nuanced dose escalation studies (because of the aforementioned bell-shaped dose response curve of some agonists) are warranted (16).

3.4: Figures

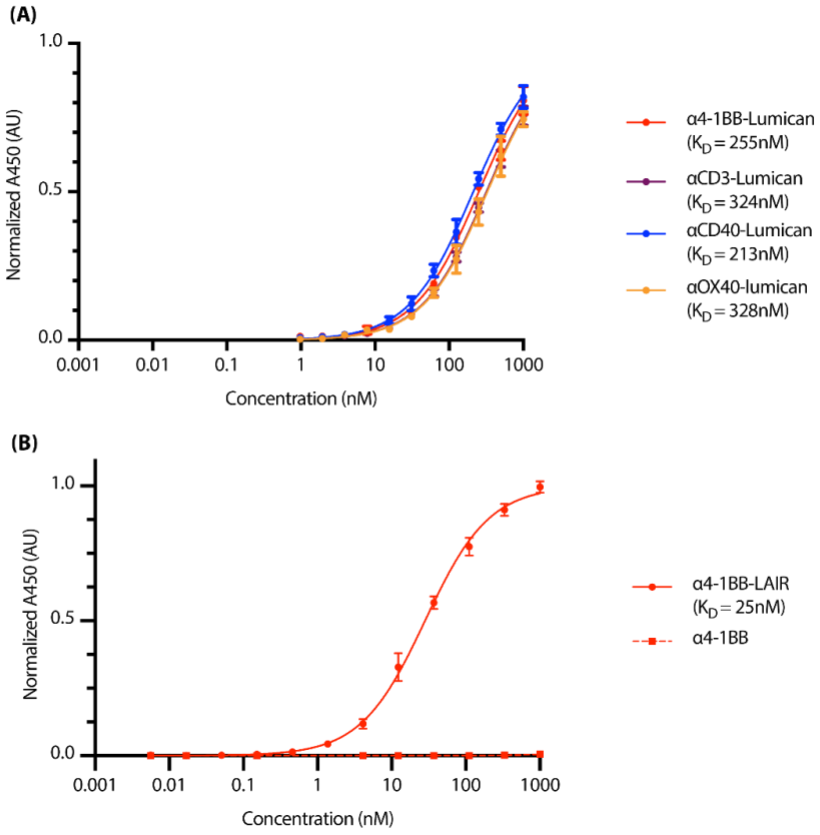

Figure 3-1: Lumican and LAIR antibody fusions bind collagen I coated plates by ELISA **(A)** Equilibrium binding curve of α4-1BB-lumican, αCD3-lumican, αCD40-lumican, and αOX86-lumican on collagen I coated plates (mean ± S.D., n = 4). **(B)** Equilibrium binding curve of α4-1BB-LAIR and α4-1BB on collagen I coated plates (mean ± S.D., n = 4).

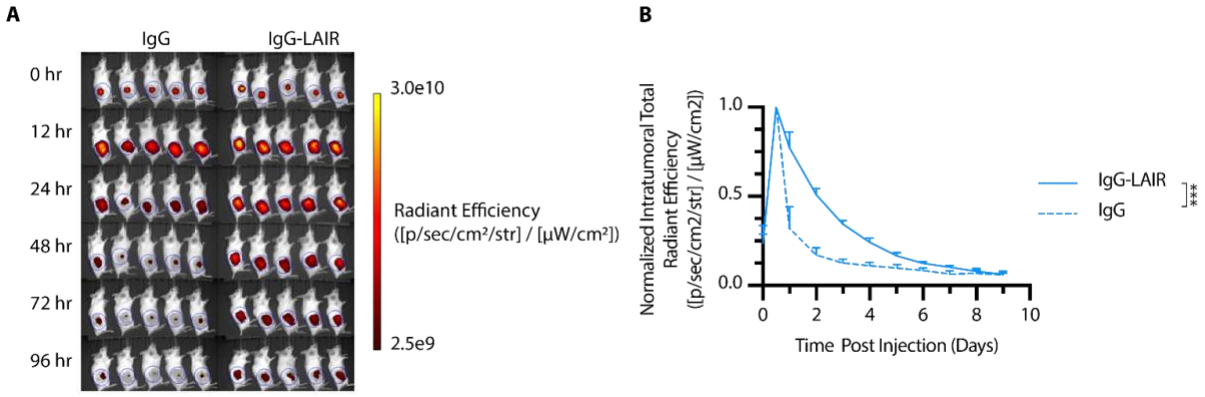

Figure 3-2: IgG-LAIR is retained in the tumor microenvironment

Mice were inoculated with 1 x 10^6 B16F10-Trp2 KO cells on day 0 and injected with control IgG or equimolar amount of IgG-LAIR and fluorescence was measured longitudinally via IVIS. **(A)** example fluorescence images from select timepoints and **(B)** Quantification of normalized radiant efficiency (mean ± S.D.) in mice receiving IgG or IgG-LAIR (n = 5). Retention data were compared using two-way ANOVA with Tukey's multiple hypothesis testing correction. *$P < 0.05$, **$P < 0.01$, *** $P < 0.001$, **** $P < 0.0001$.

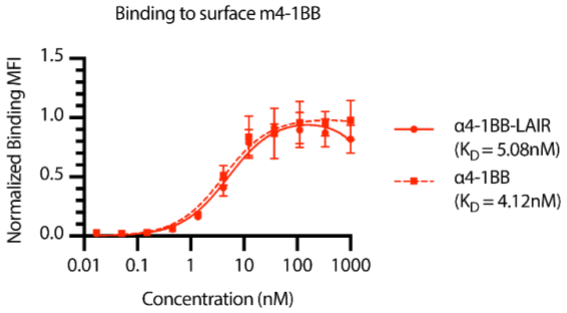

Figure 3-3: α4-1BB binding to 4-1BB is unaffected by LAIR fusion

Equilibrium binding curve of α4-1BB-LAIR and α4-1BB to HEK cells expressing murine 4-1BB (mean ± S.D., n = 4).

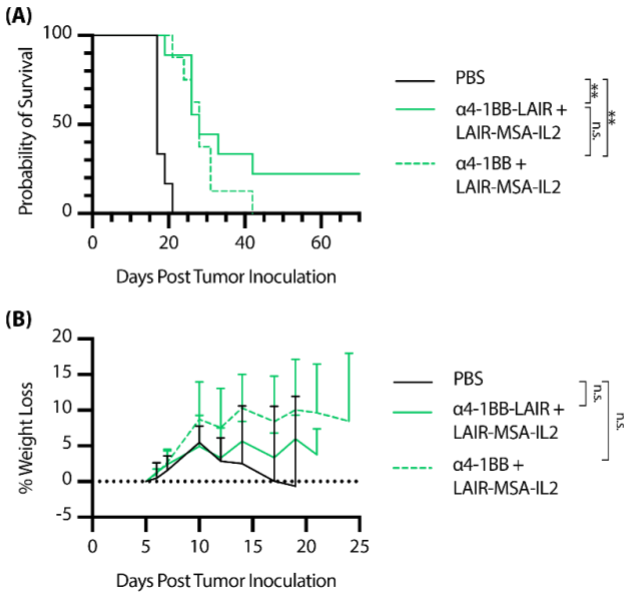

Figure 3-4: Collagen anchoring does not improve efficacy of α4-1BB combined with LAIR-MSA-IL-2

Mice were Inoculated with 1 x 10^6 B16F10 tumor cells on day 0 and treated with PBS (n = 6), α4-1BB + LAIR-MSA-IL-2 (n = 8, i.t.) or α4-1BB-LAIR + LAIR-MSA-IL-2 (n = 9, i.t.) on days 6, 10, and 14. **(A)** Overall survival of mice and **(B)** weight loss of mice from the same study. Survival was compared using the log-rank Mantel-Cox test and weight loss data were compared using two-way ANOVA with Tukey's multiple hypothesis testing correction. *$P < 0.05$, **$P < 0.01$, ***$P < 0.001$, ****$P < 0.0001$.

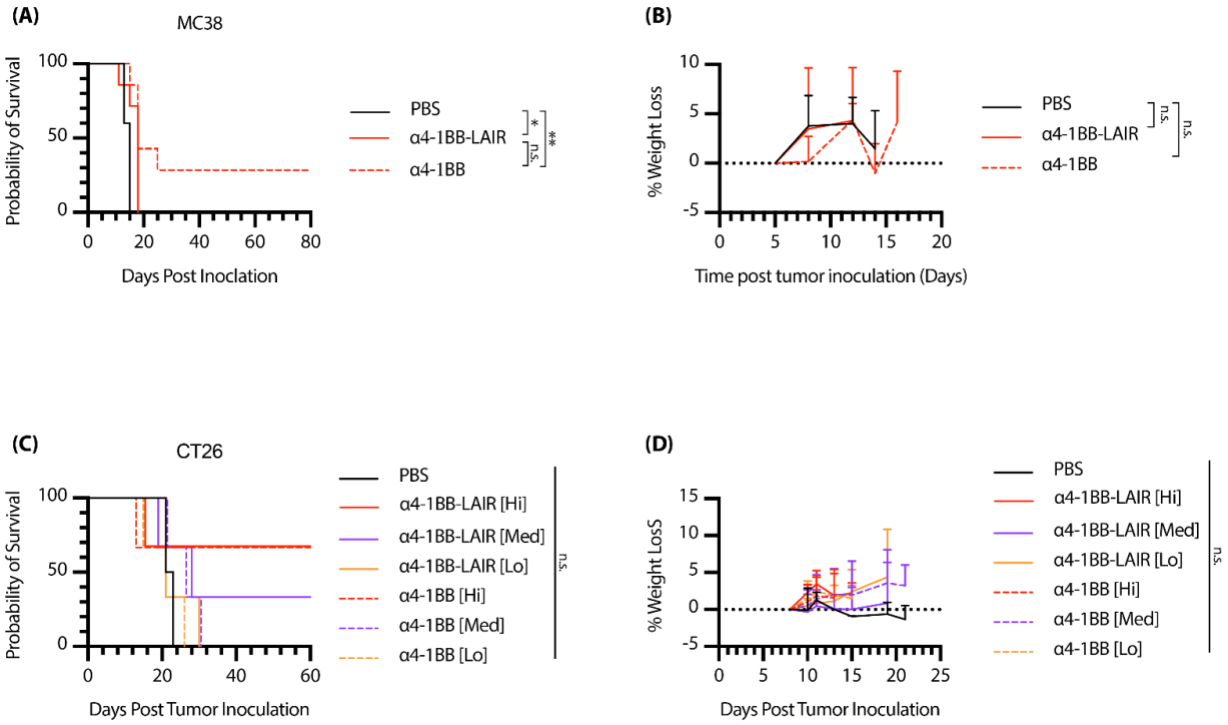

Figure 3-5: Collagen anchoring does not improve efficacy of α4-1BB monotherapy

(A-B) Mice were Inoculated with 1 x 10^6 MC38 tumor cells on day 0 and treated with PBS (n = 5), α4-1BB (i.t., n = 7) or α4-1BB-LAIR (i.t., n = 7) on days 6, 12, and 18. **(A)** Overall survival of mice and **(B)** weight loss of mice from the same study. **(C-D)** Mice were inoculated 1 x 10^6 CT26 on day 0 and treated with PBS, α4-1BB ("Hi", i.t., 20 μg), α4-1BB ("Med", i.t., 2 μg), α4-1BB ("Lo", i.t., 0.2 μg), or α4-1BB-LAIR ("Hi", i.t., 24.1 μg), α4-1BB-LAIR ("Med", i.t., 2.41 μg), α4-1BB ("Lo", i.t., 0.241 μg) (n = 2-3). **(C)** Overall survival of mice and **(D)** weight loss of mice from the same study. Survival was compared using the log-rank Mantel-Cox test and weight loss data were compared using two-way ANOVA with Tukey's multiple hypothesis testing correction. *$P < 0.05$, **$P < 0.01$, ***$P < 0.001$, ****$P < 0.0001$.

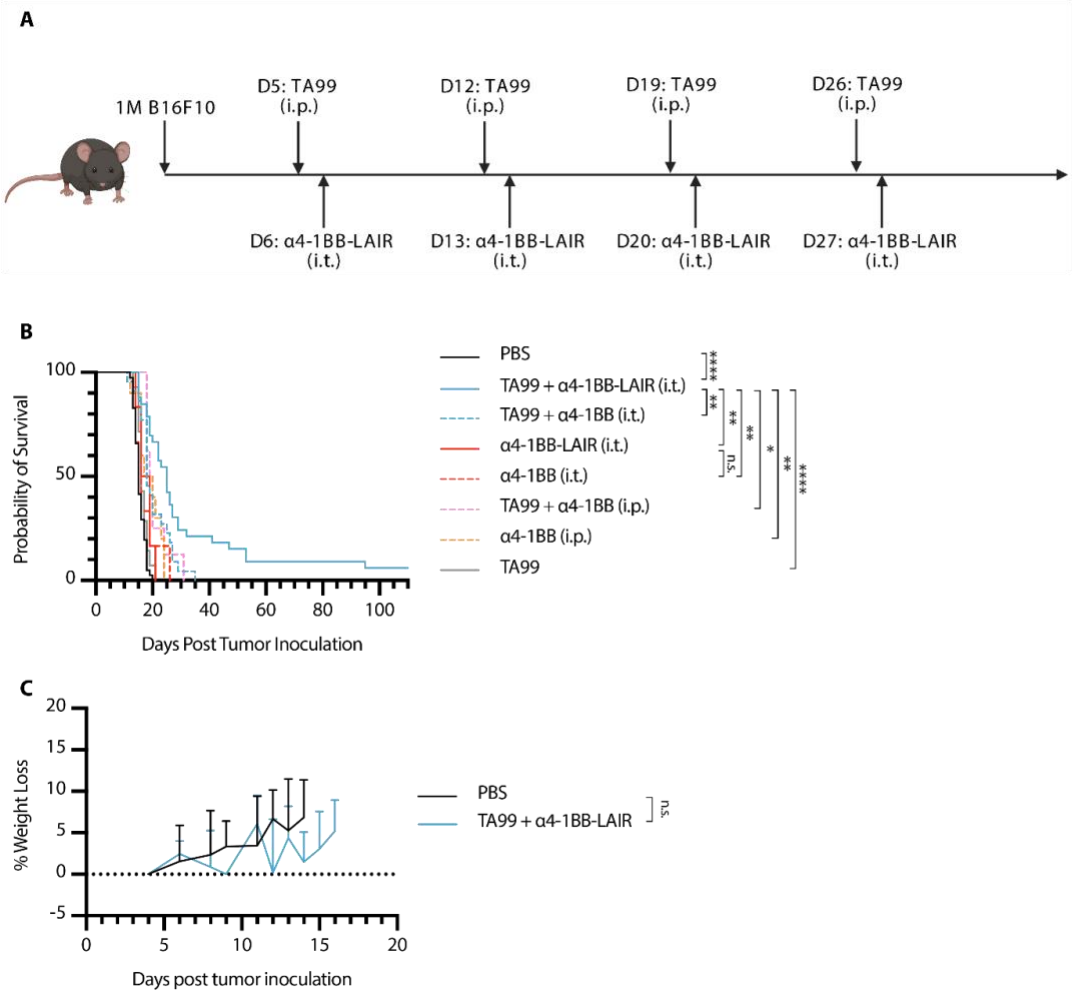

Figure 3-6: TA99 + α4-1BB-LAIR leads to minor growth delay in B16F10

Mice were inoculated with 1 x 10^6 B16F10 cells on day 0. **(A)** Treatment schedule of TA99 + α4-1BB-LAIR. Mice were treated with 200 μg of TA99 (i.p.) on days 5, 12, 19, and 26, treated with 36.1 μg α4-1BB-LAIR (i.t.) on days 6, 13, 20, and 27 or 30 μg α4-1BB (i.t.). **(B)** Overall survival of mice treated with PBS (n = 41), TA99 + α4-1BB-LAIR ("Tx", i.t., n = 33), TA99 + α4-1BB (i.t., n = 22), TA99 (n = 14), α4-1BB (i.t., n = 6), α4-1BB-LAIR (i.t., n = 6), α4-1BB (i.p., n = 10), or TA99 + α4-1BB (i.p., n = 8) (eight independent studies). **(C)** Weight loss of mice treated with PBS (n = 10) or TA99 + α4-1BB-LAIR (n = 10) from a subset of mice in **(B)** (two independent studies). Survival was compared

using the log-rank Mantel-Cox test and weight loss data were compared using two-way ANOVA with Tukey's multiple hypothesis testing correction. *$P < 0.05$, **$P < 0.01$, ***$P < 0.001$, ****$P < 0.0001$.

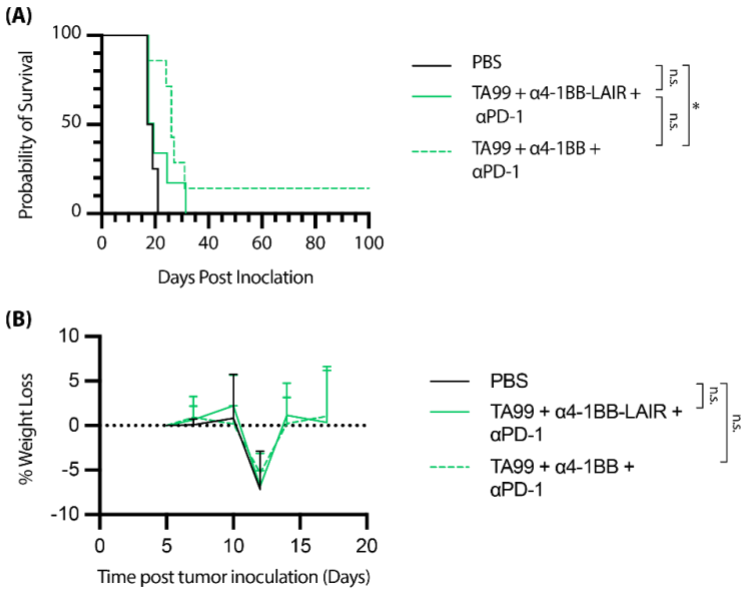

Figure 3-7: TA99 + α4-1BB does not improve αPD-1 responsiveness in B16F10 tumors

Mice were Inoculated with 1 x 10^6 B16F10 tumor cells on day 0 and treated with PBS (n = 4), TA99 + α4-1BB (i.t.) + αPD-1 (n = 7) or TA99 + α4-1BB-LAIR (i.t.) + αPD-1 (n = 6). TA99 was given on day 5, α4-1BB/α4-1BB-LAIR on day 9, and αPD-1 every 4 days starting on day 9. **(A)** Overall survival of mice and **(B)** weight loss of mice from the same study. Survival was compared using the log-rank Mantel-Cox test and weight loss data were compared using two-way ANOVA with Tukey's multiple hypothesis testing correction. *$P < 0.05$, **$P < 0.01$, ***$P < 0.001$, ****$P < 0.0001$.

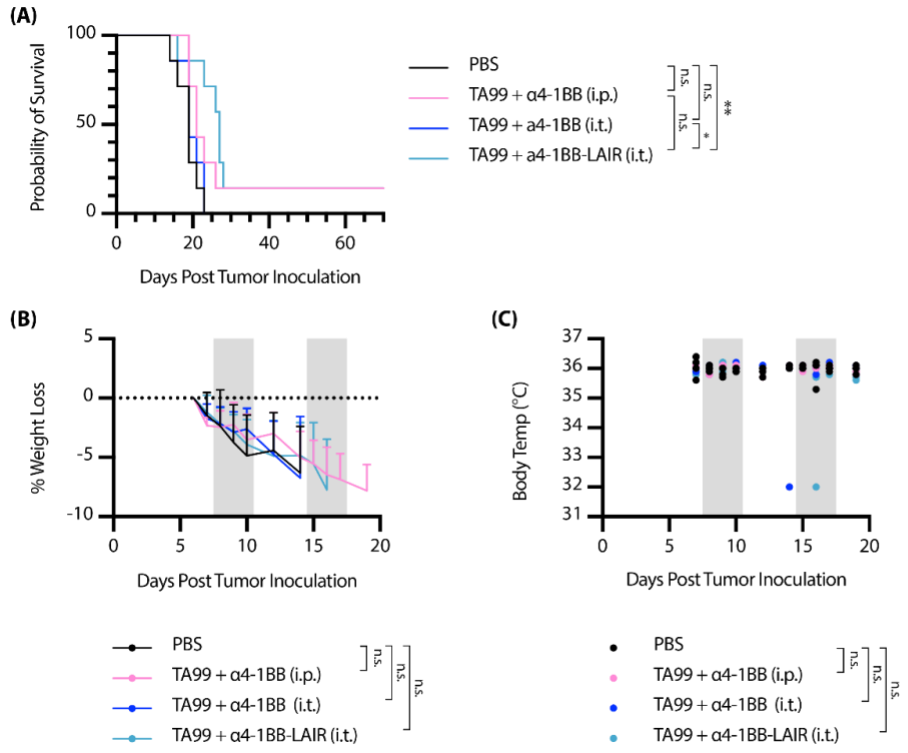

Figure 3-8: TA99 + α4-1BB has minimal efficacy and toxicity in aged mice

51-week-old C57Bl/6 mice were inoculated with 1 x 10^6 B16F10 tumors on day 0 and treated according to dose schedule in Fig. 3-6A. Systemic α4-1BB was given intraperitoneally (i.p.) at a dose of 150 μg. **(A)** Overall survival of mice treated with PBS, TA99 + α4-1BB (i.p.), TA99 + α4-1BB (i.t.), or TA99 + α4-1BB-LAIR (i.t.) (n = 7). **(B)** Weight loss and **(C)** body temperature of mice in **(A)**. Blood samples were taken daily during time periods highlighted in gray. Survival was compared using the log-rank Mantel-Cox test and weight loss and body temperature data were compared using two-way ANOVA with Tukey's multiple hypothesis testing correction. *$P < 0.05$, **$P < 0.01$, ***$P < 0.001$, ****$P < 0.0001$.

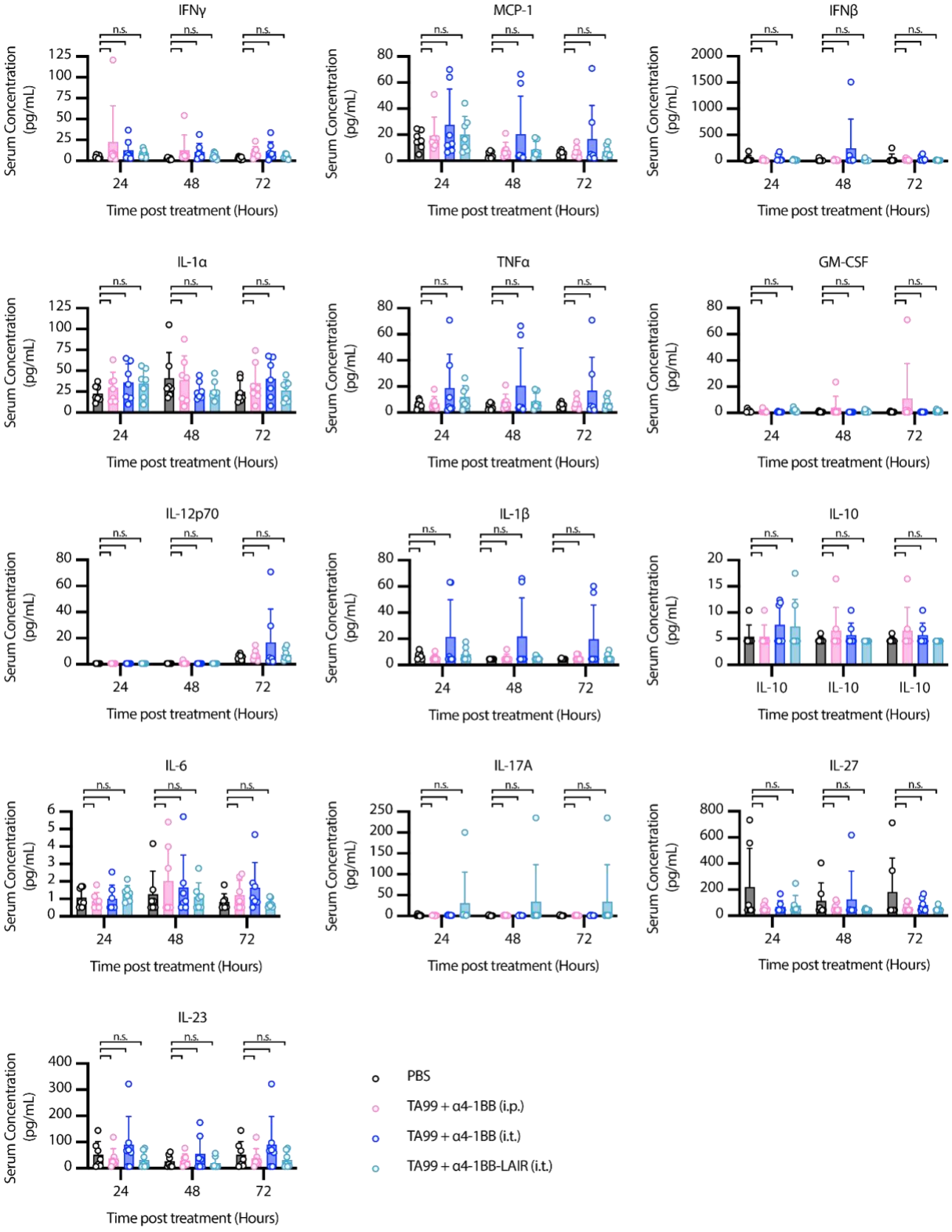
IFNγ
MCP-1
IFNβ
IL-1α
TNFα
GM-CSF
IL-12p70
IL-1β
IL-10
IL-6
IL-17A
IL-27
IL-23
Serum Concentration (pg/mL)
Time post treatment (Hours)
n.s.
24
48
72
IL-10
PBS
TA99 + α4-1BB (i.p.)
TA99 + α4-1BB (i.t.)
TA99 + α4-1BB-LAIR (i.t.)

Figure 3-9: TA99 + α4-1BB does not alter serum cytokine profile in aged mice

Serum cytokine/chemokine levels from mice in Fig. 3-8. Serum was collected 24, 48, and 72 hours after the first α4-1BB treatment. Data were compared using two-way ANOVA with Tukey's multiple hypothesis testing correction. *$P < 0.05$, **$P < 0.01$, ***$P < 0.001$, ****$P < 0.0001$.

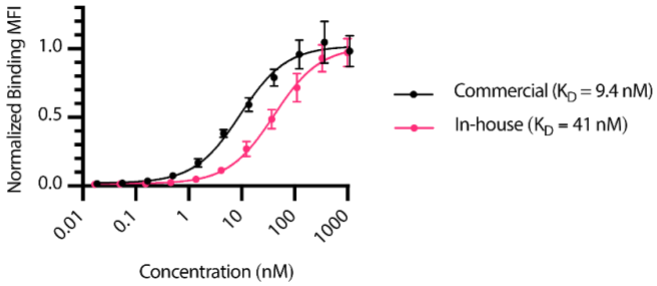

Figure 3-10: Recombinant αCD28 binds surface CD28 with similar affinity to commercial αCD28

Equilibrium binding curve of commercially purchased and in-house recombinantly produced and αCD28 antibody (clone 37.51) to HEK cells expressing murine CD28 (mean ± S.D., n = 4).

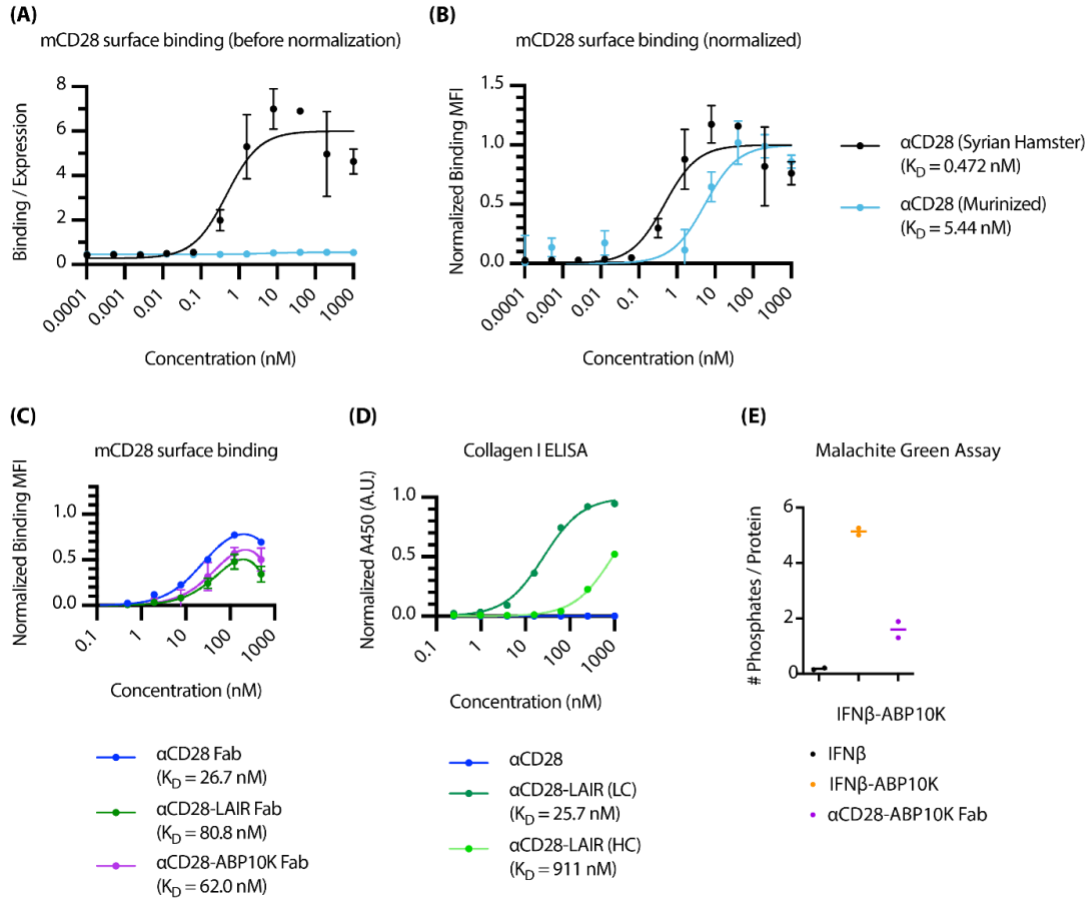

Figure 3-11: αCD28 Fabs bind surface CD28 in vitro

Equilibrium binding curve of αCD28 antibody as either fully Syrian hamster antibody or murinized chimera to HEK cells expressing murine CD28 **(A)** before and **(B)** after normalizing binding curves to B_{max} (mean ± S.D., n = 2). **(C)** Equilibrium binding curve of αCD28 Fab, αCD28-LAIR Fab, or αCD28-ABP10K Fab to HEK cells expressing murine CD28 (mean ± S.D., n = 4). **(D)** Equilibrium binding curve of αCD28 Fab, αCD28-LAIR Fab light chain (LC) fusion, or αCD28-LAIR Fab heavy chain (HC) fusion to collagen I coated plates (mean ± S.D., n = 4). **(E)** Phosphorylation quantification using malachite green assay of αCD28-ABP10K Fab, IFNβ (negative control), or IFNβ-ABP10K (positive control) (mean, n = 2).

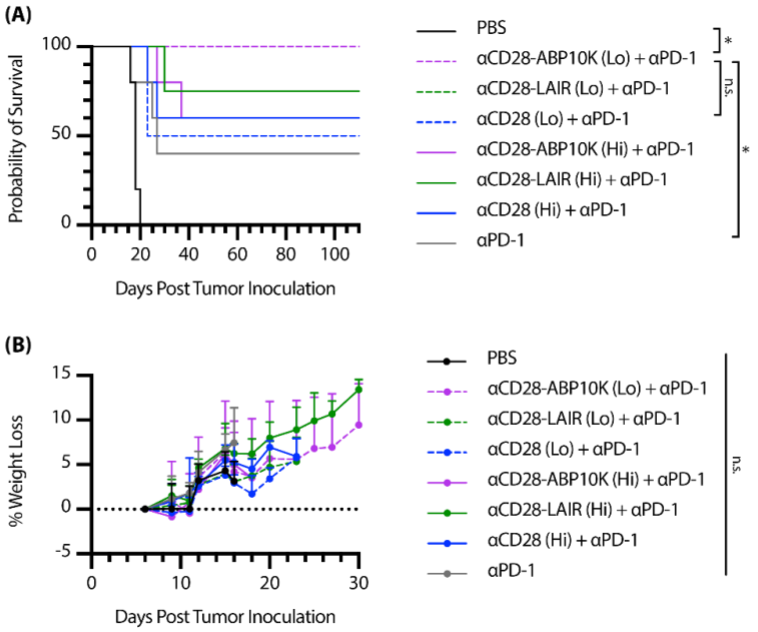

Figure 3-12: αCD28 Fabs have no activity in vivo

Mice were inoculated with 1 x 10^6 MC38 cells on day 0. **(A)** Overall survival of mice treated with PBS, αCD28 + αPD-1 ("Hi" dose, 23.9 μg and 200 μg), αCD28 + αPD-1 ("Lo" dose 4.77 μg and 200 μg), αCD28-LAIR + αPD-1 ("Hi" dose, 31.3 μg and 200 μg), αCD28-LAIR + αPD-1 ("Lo" dose 6.25 μg and 200 μg), αCD28-ABP10K + alum + αPD-1 ("Hi" dose, 26.0 μg, 130 μg, and 200 μg), αCD28-ABP10K + alum + αPD-1 ("Lo" dose 5.20 μg, 26 μg and 200 μg), or αPD-1 (200 μg) (n = 7, or n = 5 for PBS and αPD-1) and **(B)** weight loss of mice from same study. All αCD28 constructs were monomeric Fabs, administered intratumorally, and "Hi" and "Lo" doses correspond to 0.5 nmol and 0.1 nmol doses, respectively. Survival was compared using the log-rank Mantel-Cox test and weight loss data were compared using two-way ANOVA with Tukey's multiple hypothesis testing correction. *$P < 0.05$, **$P < 0.01$, ***$P < 0.001$, ****$P < 0.0001$.

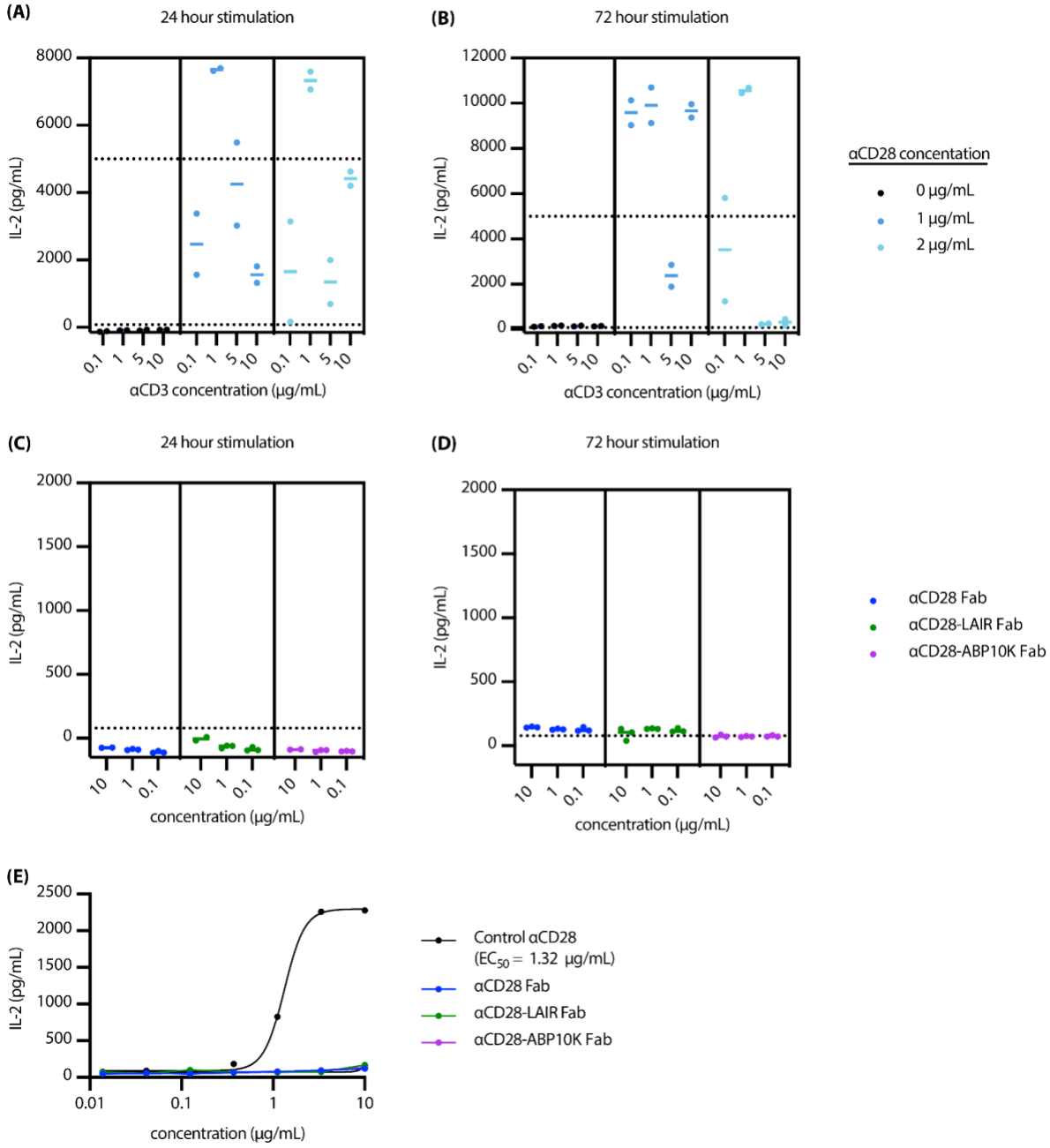

Figure 3-13: αCD28 Fabs are not active in vitro

Naive $CD8^+$ T cells were incubated for **(A)** 24 hours or **(B)** 72 hours on non-TC treated plate coated with αCD3 and αCD28 at indicated concentrations and soluble IL-2 in supernatant was measured via ELISA (n = 2). Dotted lines represent the lowest and highest standard of the standard curve. Values

falling outside of this range were extrapolated from the standard curve. Naive $CD8^+$ T cells were incubated for **(C)** 24 hours or **(D)** 72 hours on non-TC treated plate coated with αCD3 at 1 μg/mL and αCD28 Fab constructs at indicated concentrations and soluble IL-2 in supernatant was measured via ELISA (n = 2-3). Dotted line represents the lowest standard of the standard curve. Values falling outside of this range were extrapolated from the standard curve. **(E)** Naive $CD8^+$ T cells were incubated for 24 hours on non-TC treated plates coated with coated with 1 μg/mL αCD3 and indicated concentrations of αCD28 Fabs and soluble IL-2 in supernatant was measured via ELISA (n = 1).

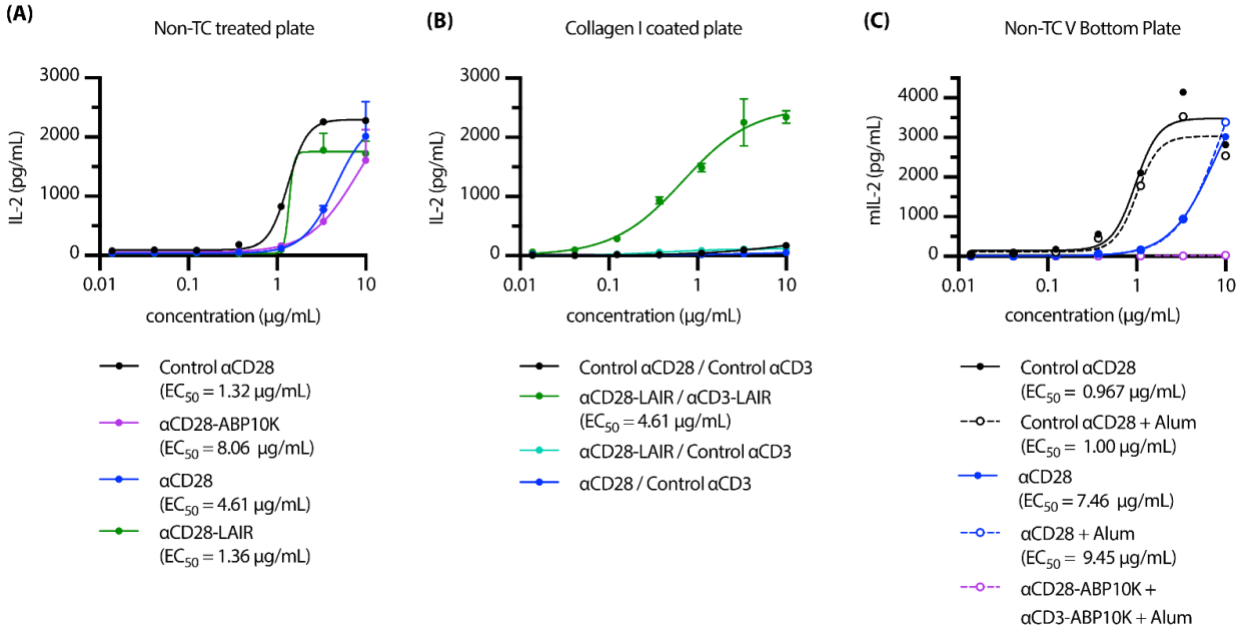

Figure 3-14: Hinge chimera αCD28 antibody is active in vitro

Naive $CD8^+$ T cells were incubated for 24 hours with indicated proteins and soluble IL-2 in supernatant was measured via ELISA. **(A)** Non-TC treated plate was coated with 1 µg/mL αCD3 and indicated concentrations of αCD28 (n = 1-2). **(B)** Collagen I coated plate was incubated with 1 µg/mL αCD3 (except for condition in dark green, where 1 µg/mL αCD3-LAIR was used) and indicated αCD28 concentration (n = 1-2). **(C)** Non-TC treated V bottom plates were coated with 1 µg/mL αCD3 and indicated αCD28 concentration, except for purple condition where αCD28-ABP10K and αCD3-ABP10K were instead preloaded onto alum and then added to wells (at indicated concentrations and 1 µg/mL, respectively). (n = 1-2).

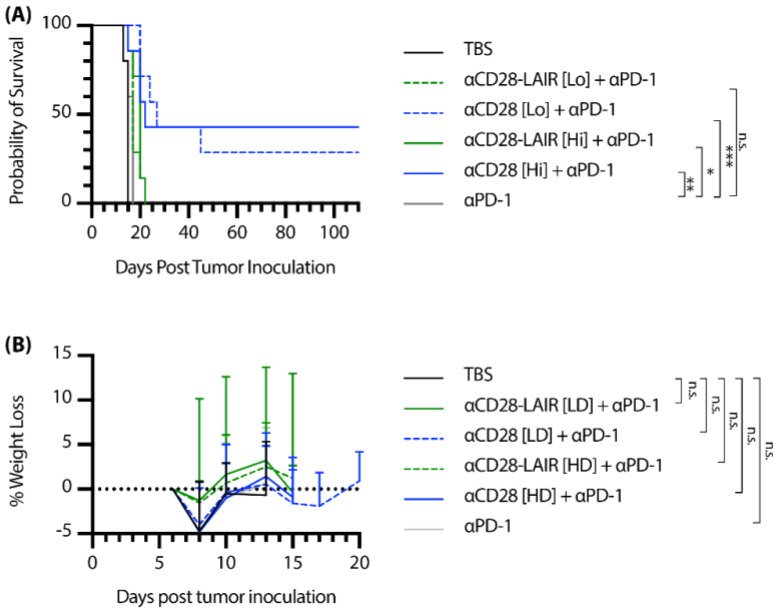

Figure 3-15: αCD28-LAIR does not synergize with αPD-1

Mice were inoculated with 1 x 10^6 MC38 cells on day 0. **(A)** Overall survival of mice treated with PBS, αCD28 + αPD-1 ("Hi" dose, 10 μg and 200 μg), αCD28 + αPD-1 ("Lo" dose 1 μg and 200 μg), αCD28-LAIR + αPD-1 ("Hi" dose, 12.1 μg and 200 μg), αCD28-LAIR + αPD-1 ("Lo" dose 1.21 μg and 200 μg), or αPD-1 (200 μg) (n = 7, or n = 5 for PBS and αPD-1) and **(B)** weight loss of mice from same study. All αCD28 constructs were administered intratumorally. Survival was compared using the log-rank Mantel-Cox test and weight loss data were compared using two-way ANOVA with Tukey's multiple hypothesis testing correction. *$P < 0.05$, **$P < 0.01$, ***$P < 0.001$, ****$P < 0.0001$.

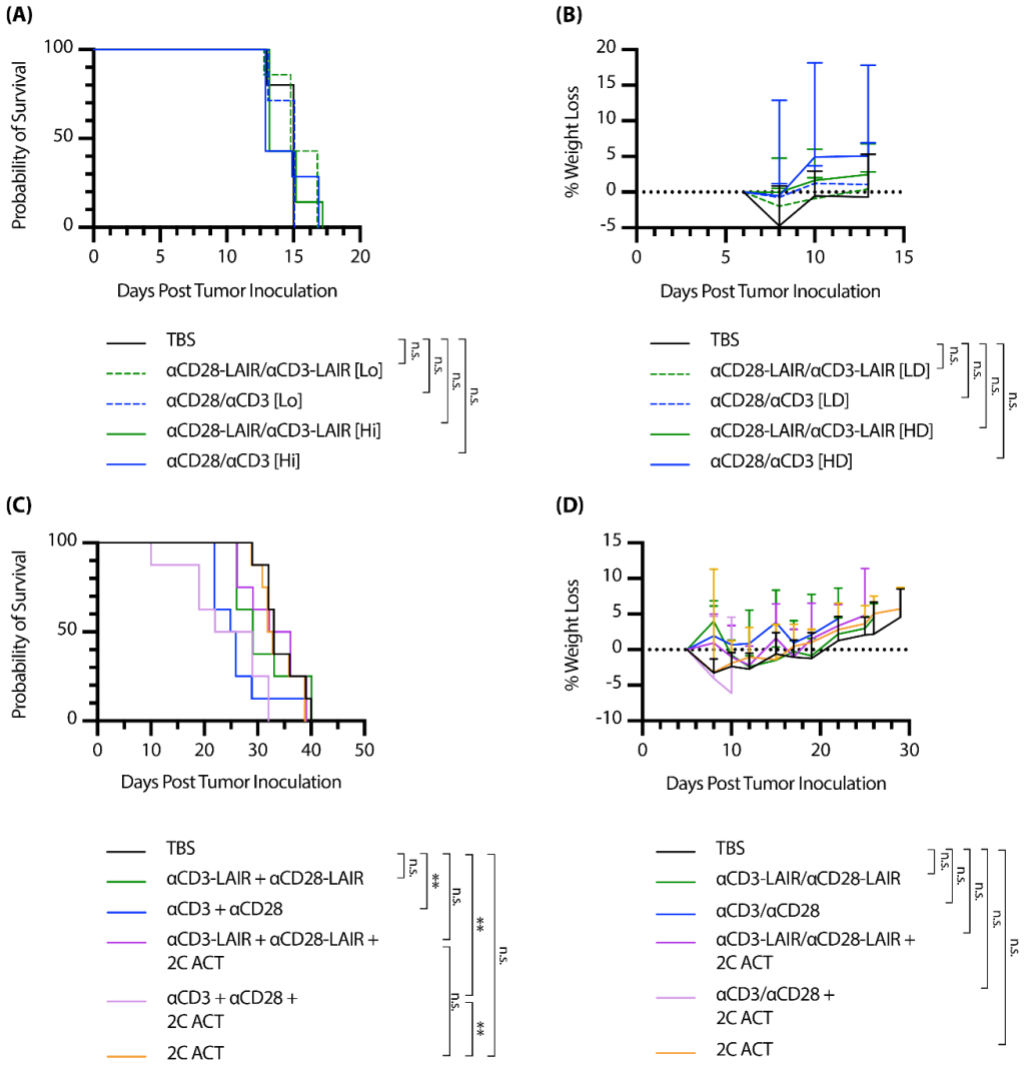

Figure 3-16: αCD28-LAIR + αCD3-LAIR have effect on tumor growth

(A-B) Mice were inoculated with 1 x 10^6 MC38 cells on day 0. **(A)** Overall survival of mice treated with PBS, αCD28 + αCD3 ("Hi" dose, i.t., 10 μg and 2 μg), αCD28 + αCD3 ("Lo" dose, i.t., 1 μg and 0.2 μg), αCD28-LAIR + αCD3-LAIR ("Hi" dose, i.t., 12.1 μg and 2.4 μg), or αCD28-LAIR + αCD3-LAIR ("Lo" dose, i.t., 1.21 μg and 0.24 μg) (n = 7, or n = 5 for PBS) and **(B)** weight loss of mice from same study. **(C-D)** Mice were inoculated with 1 x 10^6 MC38-SIY cells on day 0. **(C)** Overall survival of mice treated with PBS, 1 x 10^6 adoptively transferred T cells (ACT), ACT + αCD28 + αCD3 ("Hi"

dose, i.t.), ACT, + αCD28-LAIR + αCD3-LAIR ("Hi" dose, i.t.), αCD28 + αCD3 ("Hi" dose, i.t.), or αCD28-LAIR + αCD3-LAIR ("Hi" dose, i.t.) (n = 8) and **(D)** weight loss of mice from same study. Survival was compared using the log-rank Mantel-Cox test and weight loss data were compared using two-way ANOVA with Tukey's multiple hypothesis testing correction. $*P < 0.05$, $**P < 0.01$, $***P < 0.001$, $****P < 0.0001$.

3.5: Tables

Table 3-1: Amino acid sequence table

Key: signal peptide, variable region, constant region, linker, lumican, LAIR, ABP10, His tag

α4-1BB Light Chain (Murine kappa constant region)	MSVLTQVLALLLLWLTGARCADIQMTQSPASLSASLEEIVT ITCQASQDIGNWLAWYHQKPGKSPQLLIYGSTSLADGVP SRFSGSSSGSQYSLKISRLQVEDIGIYYCLQAYGAPWTFGG GTKLELKRADAAPTVSIFPPSSEQLTSGGASVVCFLNNFYP KDINVKWKIDGSERQNGVLNSWTDQDSKDSTYSMSSTL TLTKDEYERHNSYTCEATHKTSTSPIVKSFNRNEC
α4-1BB-lumican Heavy Chain (Murine IgG1 constant region)	MKWSWVFLFLMAMVTGVNSDVQLVESGGGLVQPGRSL KLSCAASGFIFSYFDMAWVRQAPTKGLEWVASISPDGSIP YYRDSVKGRFTVSRENAKSSLYLQMDSLRSEDTATYYCAR RSYGGYSEIDYWGQGVMVTVSSATTKGPSVYPLAPGSAA QTNSMVTLGCLVKGYFPEPVTVTWNSGSLSSGVHTFPAV LQSDLYTLSSSVTVPSSTWPSQTVTCNVAHPASSTKVDKKI VPRDCGCKPCICTVPEVSSVFIFPPKPKDVLTITLTPKVTC VVVDISKDDPEVQFSWFVDDVEVHTAQTKPREEQINSTF RSVSELPIMHQDWLNGKEFKCRVNSAAFPAPIEKTISKTK GRPKAPQVYTIPPPKEQMAKDKVSLTCMITNFFPEDITVE WQWNGQPAENYKNTQPIMDTDGSYFVYSKLNVQKSNW EAGNTFTCSVLHEGLHNHHTEKSLSHSPGKGGGGSGGG GSGGGGSQYYDYDIPLFMYGQISPNCAPECNCPHSYPTA MYCDDLKLKSVPMVPPGIKYLYLRNNQIDHIDEKAFENV TDLQWLILDHNLLENSKIKGKVFSKLKQLKKLHINYNNL TESVGPLPKSLQDLQLTNNKISKLGSFDGLVNLTFIYLQH NQLKEDAVSASLKGLKSLEYLDLSFNQMSKLPAGLPTSLL TLYLDNNKISNIPDEYFKRFTGLQYLRLSHNELADSGVPG NSFNISSLLELDLSYNKLKSIPTVNENLENYYLEVNELEKF DVKSFCKILGPLSYSKIKHLRLDGNPLTQSSLPPDMYECLR VANEITVN
α4-1BB-LAIR Heavy Chain (Murine IgG1 constant region)	MKWSWVFLFLMAMVTGVNSDVQLVESGGGLVQPGRSL KLSCAASGFIFSYFDMAWVRQAPTKGLEWVASISPDGSIP YYRDSVKGRFTVSRENAKSSLYLQMDSLRSEDTATYYCAR RSYGGYSEIDYWGQGVMVTVSSATTKGPSVYPLAPGSAA QTNSMVTLGCLVKGYFPEPVTVTWNSGSLSSGVHTFPAV LQSDLYTLSSSVTVPSSTWPSQTVTCNVAHPASSTKVDKKI VPRDCGCKPCICTVPEVSSVFIFPPKPKDVLTITLTPKVTC VVVDISKDDPEVQFSWFVDDVEVHTAQTKPREEQINSTF RSVSELPIMHQDWLNGKEFKCRVNSAAFPAPIEKTISKTK

	GRPKAPQVYTIPPPKEQMAKDKVSLTCMITNFFPEDITVE WQWNGQPAENYKNTQPIMDTDGSYFVYSKLNVQKSNW EAGNTFTCSVLHEGLHNHHTEKSLSHSPGKGGGGSGGG GSGGGGSQEGSLPDITIFPNSSLMISQGTFVTVVCSYSDKH DLYNMVRLEKDGSTFMEKSTEPYKTEDEFEIGPVNETTT GHYSCIYSKGITWSERSKTLELKVIKENVIQTPAPGPTSDT SWLKTYSIY
αCD3 Light Chain (Murine kappa constant region)	MSVLTQVLALLLLWLTGARCADIQMTQSPSSLPASLGDRV TINCQASQDISNYLNWYQQKPGKAPKLLIYYTNKLADG VPSRFSGSGSGRDSSFTISSLESEDIGSYYCQQYYNYPWTF GPGTKLEIKRRADAAPTVSIFPPSSEQLTSGGASVVCFLNN FYPKDINVKWKIDGSERQNGVLNSWTDQDSKDSTYSMS STLTLTKDEYERHNSYTCEATHKTSTSPIVKSFNRNEC
αCD3 Heavy Chain (Murine IgG1 constant region)	MKWSWVFLFLMAMVTGVNSEVQLVESGGGLVQPGKSL KLSCEASGFTFSGYGMHWVRQAPGRGLESVAYITSSSINI KYADAVKGRFTVSRDNAKNLLFLQMNILKSEDTAMYYC ARFDWDKNYWGQGTMVTVSSATTKGPSVYPLAPGSAAQ TNSMVTLGCLVKGYFPEPVTVTWNSGSLSSGVHTFPAVL QSDLYTLSSSVTVPSSTWPSQTVTCNVAHPASSTKVDKKIV PRDCGCKPCICTVPEVSSVFIFPPKPKDVLTITLTPKVTCV VVDISKDDPEVQFSWFVDDVEVHTAQTKPREEQINSTFR SVSELPIMHQDWLNGKEFKCRVNSAAFPAPIEKTISKTKG RPKAPQVYTIPPPKEQMAKDKVSLTCMITNFFPEDITVEW QWNGQPAENYKNTQPIMDTDGSYFVYSKLNVQKSNWE AGNTFTCSVLHEGLHNHHTEKSLSHSPGK
αCD3-lumican Heavy Chain (Murine IgG1 constant region)	MKWSWVFLFLMAMVTGVNSEVQLVESGGGLVQPGKSL KLSCEASGFTFSGYGMHWVRQAPGRGLESVAYITSSSINI KYADAVKGRFTVSRDNAKNLLFLQMNILKSEDTAMYYC ARFDWDKNYWGQGTMVTVSSATTKGPSVYPLAPGSAAQ TNSMVTLGCLVKGYFPEPVTVTWNSGSLSSGVHTFPAVL QSDLYTLSSSVTVPSSTWPSQTVTCNVAHPASSTKVDKKIV PRDCGCKPCICTVPEVSSVFIFPPKPKDVLTITLTPKVTCV VVDISKDDPEVQFSWFVDDVEVHTAQTKPREEQINSTFR SVSELPIMHQDWLNGKEFKCRVNSAAFPAPIEKTISKTKG RPKAPQVYTIPPPKEQMAKDKVSLTCMITNFFPEDITVEW QWNGQPAENYKNTQPIMDTDGSYFVYSKLNVQKSNWE AGNTFTCSVLHEGLHNHHTEKSLSHSPGKGGGGSGGGG SGGGGSQYYDYDIPLFMYGQISPNCAPECNCPHSYPTAM YCDDLKLKSVPMVPPGIKYLYLRNNQIDHIDEKAFENVT DLQWLILDHNLLENSKIKGKVFSKLKQLKKLHINYNNLT ESVGPLPKSLQDLQLTNNKISKLGSFDGLVNLTFIYLQHN QLKEDAVSASLKGLKSLEYLDLSFNQMSKLPAGLPTSLLT

	LYLDNNKISNIPDEYFKRFTGLQYLRLSHNELADSGVPG NSFNISSLLELDLSYNKLKSIPTVNENLENYYLEVNELEKF DVKSFCKILGPLSYSKIKHLRLDGNPLTQSSLPPDMYECLR VANEITVN
αCD3-LAIR Light Chain (Murine kappa constant region)	MSVLTQVLALLLLWLTGARCADIQMTQSPSSLPASLGDRV TINCQASQDISNYLNWYQQKPGKAPKLLIYYTNKLADG VPSRFSGSGSGRDSSFTISSLESEDIGSYYCQQYYNYPWTF GPGTKLEIKRRADAAPTVSIFPPSSEQLTSGGASVVCFLNN FYPKDINVKWKIDGSERQNGVLNSWTDQDSKDSTYSMS STLTLTKDEYERHNSYTCEATHKTSTSPIVKSFNRNECGG GGSGGGGSGGGGSQEGSLPDITIFPNSSLMISQGTFVTVV CSYSDKHDLYNMVRLEKDGSTFMEKSTEPYKTEDEFEIG PVNETITGHYSCIYSKGITWSERSKTLELKVIKENVIQTPA PGPTSDTSWLKTYSIY
αCD3-ABP10 Light Chain (Murine kappa constant region)	MSVLTQVLALLLLWLTGARCADIQMTQSPSSLPASLGDRV TINCQASQDISNYLNWYQQKPGKAPKLLIYYTNKLADG VPSRFSGSGSGRDSSFTISSLESEDIGSYYCQQYYNYPWTF GPGTKLEIKRRADAAPTVSIFPPSSEQLTSGGASVVCFLNN FYPKDINVKWKIDGSERQNGVLNSWTDQDSKDSTYSMS STLTLTKDEYERHNSYTCEATHKTSTSPIVKSFNRNECGG GGSGGGGSGGGGSFQSEEQQGGGSGGSEEGGMESEES NGGGSGGSEEGG
αCD40 Light Chain (Murine kappa constant region)	METDTLLLWVLLLWVPGSTGDTVLTQSPALAVSPGERVTI SCRASESVSTRMHWYQQRPGQPPKLLIYVASRLESGVPAR FSGGGSGTDFTLTIDPVEANDTATYFCQQSWNDPWTFG GGTKLELKRADAAPTVSIFPPSSEQLTSGGASVVCFLNNF YPKDINVKWKIDGSERQNGVLNSWTDQDSKDSTYSMSS TLTLTKDEYERHNSYTCEATHKTSTSPIVKSFNRNEC
αCD40-lumican Heavy Chain (Murine IgG1 constant region)	MDIWLSLVFLVLFIKGVQCEVQLVESGGGLVQPGRSLKLS CAASGFTLSDYYMAWVRQAPKKGLEWVASINYEGSSTYY GESVKGRFTISRDNAKSTLYLQMNSLRSEDTATYYCVRH DNYFDYWGQGVLVTVSSATTKGPSVYPLAPGSAAQTNS MVTLGCLVKGYFPEPVTVTWNSGSLSSGVHTFPAVLQSD LYTLSSSVTVPSSTWPSQTVTCNVAHPASSTKVDKKIVPRD CGCKPCICTVPEVSSVFIFPPKPKDVLTITLTPKVTCVVVDI SKDDPEVQFSWFVDDVEVHTAQTKPREEQINSTFRSVSE LPIMHQDWLNGKEFKCRVNSAAFPAPIEKTISKTKGRPK APQVYTIPPPKEQMAKDKVSLTCMITNFFPEDITVEWQW NGQPAENYKNTQPIMDTDGSYFVYSKLNVQKSNWEAG NTFTCSVLHEGLHNHHTEKSLSHSPGKGGGGSGGGGSG GGGSQYYDYDIPLFMYGQISPNCAPECNCPHSYPTAMYC

	DDLKLKSVPMVPPGIKYLYLRNNQIDHIDEKAFENVTDL QWLILDHNLLENSKIKGKVFSKLKQLKKLHINYNNLTES VGPLPKSLQDLQLTNNKISKLGSFDGLVNLTFIYLQHNQ LKEDAVSASLKGLKSLEYLDLSFNQMSKLPAGLPTSLLTL YLDNNKISNIPDEYFKRFTGLQYLRLSHNELADSGVPGN SFNISSLLELDLSYNKLKSIPTVNENLENYYLEVNELEKFD VKSFCKILGPLSYSKIKHLRLDGNPLTQSSLPPDMYECLRV ANEITVN
αCD40-LAIR Heavy Chain (Murine IgG1 constant region)	MDIWLSLVFLVLFIKGVQCEVQLVESGGGLVQPGRSLKLS CAASGFTLSDYYMAWVRQAPKKGLEWVASINYEGSSTYY GESVKGRFTISRDNAKSTLYLQMNSLRSEDTATYYCVRH DNYFDYWGQGVLVTVSSATTKGPSVYPLAPGSAAQTNS MVTLGCLVKGYFPEPVTVTWNSGSLSSGVHTFPAVLQSD LYTLSSSVTVPSSTWPSQTVTCNVAHPASSTKVDKKIVPRD CGCKPCICTVPEVSSVFIFPPKPKDVLTITLTPKVTCVVVDI SKDDPEVQFSWFVDDVEVHTAQTKPREEQINSTFRSVSE LPIMHQDWLNGKEFKCRVNSAAFPAPIEKTISKTKGRPK APQVYTIPPPKEQMAKDKVSLTCMITNFFPEDITVEWQW NGQPAENYKNTQPIMDTDGSYFVYSKLNVQKSNWEAG NTFTCSVLHEGLHNHHTEKSLSHSPGKGGGGSGGGGSG GGGSQEGSLPDITIFPNSSLMISQGTFVTVVCSYSDKHDLY NMVRLEKDGSTFMEKSTEPYKTEDEFEIGPVNETITGHY SCIYSKGITWSERSKTLELKVIKENVIQTPAPGPTSDTSWL KTYSIY
αOX40 Light Chain (Murine kappa constant region)	MSVLTQVLALLLLWLTGARCADIVMTQGALPNPVPSGES ASITCRSSQSLVYKDGQTYLNWFLQRPGQSPQLLTYWMS TRASGVSDRFSGSGSGTYFTLKISRVRAEDAGVYYCQQVR EYPFTFGSGTKLEIKRADAAPTVSIFPPSSEQLTSGGASVV CFLNNFYPKDINVKWKIDGSERQNGVLNSWTDQDSKDS TYSMSSTLTLTKDEYERHNSYTCEATHKTSTSPIVKSFNR NEC
αOX40-lumican Heavy Chain (Murine IgG1 constant region)	MKWSWVFLFLMAMVTGVNSQVQLKESGPGLVQPSQTLS LTCTVSGFSLTGYNLHWVRQPPGKGLEWMGRMRYDGD TYYNSVLKSRLSISRDTSKNQVFLKMNSLQTDDTAIYYCT RDGRGDSFDYWGQGVMVTVSSATTKGPSVYPLAPGSAA QTNSMVTLGCLVKGYFPEPVTVTWNSGSLSSGVHTFPAV LQSDLYTLSSSVTVPSSTWPSQTVTCNVAHPASSTKVDKKI VPRDCGCKPCICTVPEVSSVFIFPPKPKDVLTITLTPKVTC VVVDISKDDPEVQFSWFVDDVEVHTAQTKPREEQINSTF RSVSELPIMHQDWLNGKEFKCRVNSAAFPAPIEKTISKTK GRPKAPQVYTIPPPKEQMAKDKVSLTCMITNFFPEDITVE WQWNGQPAENYKNTQPIMDTDGSYFVYSKLNVQKSNW

	EAGNTFTCSVLHEGLHNHHTEKSLSHSPGKGGGGSGGG GSGGGGSQYYDYDIPLFMYGQISPNCAPECNCPHSYPTA MYCDDLKLKSVPMVPPGIKYLYLRNNQIDHIDEKAFENV TDLQWLILDHNLLENSKIKGKVFSKLKQLKKLHINYNNL TESVGPLPKSLQDLQLTNNKISKLGSFDGLVNLTFIYLQH NQLKEDAVSASLKGLKSLEYLDLSFNQMSKLPAGLPTSLL TLYLDNNKISNIPDEYFKRFTGLQYLRLSHNELADSGVPG NSFNISSLLELDLSYNKLKSIPTVNENLENYYLEVNELEKF DVKSFCKILGPLSYSKIKHLRLDGNPLTQSSLPPDMYECLR VANEITVN
αOX40-LAIR Heavy Chain (Murine IgG1 constant region)	MKWSWVFLFLMAMVTGVNSQVQLKESGPGLVQPSQTLS LTCTVSGFSLTGYNLHWVRQPPGKGLEWMGRMRYDGD TYYNSVLKSRLSISRDTSKNQVFLKMNSLQTDDTAIYYCT RDGRGDSFDYWGQGVMVTVSSATTKGPSVYPLAPGSAA QTNSMVTLGCLVKGYFPEPVTVTWNSGSLSSGVHTFPAV LQSDLYTLSSSVTVPSSTWPSQTVTCNVAHPASSTKVDKKI VPRDCGCKPCICTVPEVSSVFIFPPKPKDVLTITLTPKVTC VVVDISKDDPEVQFSWFVDDVEVHTAQTKPREEQINSTF RSVSELPIMHQDWLNGKEFKCRVNSAAFPAPIEKTISKTK GRPKAPQVYTIPPPKEQMAKDKVSLTCMITNFFPEDITVE WQWNGQPAENYKNTQPIMDTDGSYFVYSKLNVQKSNW EAGNTFTCSVLHEGLHNHHTEKSLSHSPGKGGGGSGGG GSGGGGSQEGSLPDITIFPNSSLMISQGTFVTVVCSYSDKH DLYNMVRLEKDGSTFMEKSTEPYKTEDEFEIGPVNETTT GHYSCIYSKGITWSERSKTLELKVIKENVIQTPAPGPTSDT SWLKTYSIY
αFITC Light Chain (Murine kappa constant region)	MSVLTQVLALLLLWLTGARCADVVMTQTPLSLPVSLGDQ ASISCRSSQSLVHSNGNTYLRWYLQKPGQSPKVLIYKVSN RFSGVPDRFSGSGSGTDFTLKISRVEAEDLGVYFCSQSTH VPWTFGGGTKLEIKRADAAPTVSIFPPSSEQLTSGGASVV CFLNNFYPKDINVKWKIDGSERQNGVLNSWTDQDSKDS TYSMSSTLTLTKDEYERHNSYTCEATHKTSTSPIVKSFNR NEC
αFITC Heavy Chain (Murine IgG2c constant region, **LALA-PG silencing mutations bolded and underlined**)	MKWSWVFLFLMAMVTGVNSDVKLDETGGGLVQPGRPM KLSCVASGFTFSDYWMNWVRQSPEKGLEWVAQIRNKPY NYETYYSDSVKGRFTISRDDSKSSVYLQMNNLRVEDMGI YYCTGSYYGMDYWGQGTSVTVSAKTTAPSVYPLAPVCG DTTGSSVTLGCLVKGYFPEPVTLTWNSGSLSSGVHTFPAV LQSDLYTLSSSVTVTSSTWPSQSITCNVAHPASSTKVDKKI EPRGPTIKPCPPCKCPAPN**AA**GGPSVFIFPPKIKDVLMISLS PIVTCVVVDVSEDDPDVQISWFVNNVEVHTAQTQTHRE DYNSTLRVVSALPIQHQDWMSGKEFKCKVNNKDL**G**API

	ERTISKPKGSVRAPQVYVLPPPEEEMTKKQVTLTCMVTD FMPEDIYVEWTNNGKTELNYKNTEPVLDSDGSYFMYSK LRVEKKNWVERNSYSCSVVHEGLHNHHTTKSFSRTPGK
αFITC-lumican Heavy Chain (Murine IgG2c constant region, **LALA-PG silencing mutations bolded and underlined**)	MKWSWVFLFLMAMVTGVNSDVKLDETGGGLVQPGRPM KLSCVASGFTFSDYWMNWVRQSPEKGLEWVAQIRNKPY NYETYYSDSVKGRFTISRDDSKSSVYLQMNNLRVEDMGI YYCTGSYYGMDYWGQGTSVTVSAKTTAPSVYPLAPVCG DTTGSSVTLGCLVKGYFPEPVTLTWNSGSLSSGVHTFPAV LQSDLYTLSSSVTVTSSTWPSQSITCNVAHPASSTKVDKKI EPRGPTIKPCPPCKCPAPN**AA**GGPSVFIFPPKIKDVLMISLS PIVTCVVVDVSEDDPDVQISWFVNNVEVHTAQTQTHRE DYNSTLRVVSALPIQHQDWMSGKEFKCKVNNKDL**G**API ERTISKPKGSVRAPQVYVLPPPEEEMTKKQVTLTCMVTD FMPEDIYVEWTNNGKTELNYKNTEPVLDSDGSYFMYSK LRVEKKNWVERNSYSCSVVHEGLHNHHTTKSFSRTPGK GGGGSGGGGSGGGGSQYYDYDIPLFMYGQISPNCAPEC NCPHSYPTAMYCDDLKLKSVPMVPPGIKYLYLRNNQIDH IDEKAFENVTDLQWLILDHNLLENSKIKGKVFSKLKQLK KLHINYNNLTESVGPLPKSLQDLQLTNNKISKLGSFDGL VNLTFIYLQHNQLKEDAVSASLKGLKSLEYLDLSFNQMS KLPAGLPTSLLTLYLDNNKISNIPDEYFKRFTGLQYLRLSH NELADSGVPGNSFNISSLLELDLSYNKLKSIPTVNENLEN YYLEVNELEKFDVKSFCKILGPLSYSKIKHLRLDGNPLTQ SSLPPDMYECLRVANEITVN
αFITC-LAIR Heavy Chain (Murine IgG2c constant region, **LALA-PG silencing mutations bolded and underlined**)	MKWSWVFLFLMAMVTGVNSDVKLDETGGGLVQPGRPM KLSCVASGFTFSDYWMNWVRQSPEKGLEWVAQIRNKPY NYETYYSDSVKGRFTISRDDSKSSVYLQMNNLRVEDMGI YYCTGSYYGMDYWGQGTSVTVSAKTTAPSVYPLAPVCG DTTGSSVTLGCLVKGYFPEPVTLTWNSGSLSSGVHTFPAV LQSDLYTLSSSVTVTSSTWPSQSITCNVAHPASSTKVDKKI EPRGPTIKPCPPCKCPAPN**AA**GGPSVFIFPPKIKDVLMISLS PIVTCVVVDVSEDDPDVQISWFVNNVEVHTAQTQTHRE DYNSTLRVVSALPIQHQDWMSGKEFKCKVNNKDL**G**API ERTISKPKGSVRAPQVYVLPPPEEEMTKKQVTLTCMVTD FMPEDIYVEWTNNGKTELNYKNTEPVLDSDGSYFMYSK LRVEKKNWVERNSYSCSVVHEGLHNHHTTKSFSRTPGK GGGGSGGGGSGGGGSQEGSLPDITIFPNSSLMISQGTFVT VVCSYSDKHDLYNMVRLEKDGSTFMEKSTEPYKTEDEF EIGPVNETITGHYSCIYSKGTWSERSKTLELKVIKENVIQ TPAPGPTSDTSWLKTYSIY

αCD28 Light Chain (Syrian hamster Lambda constant region)	MTWAPLFLIILHHLTGSYAEFVLTQPKSVSESLGRSVIISCK RSSGNIANYFVHWYQRHFGNSPKTVIYEDNKRPSGIPDRF TGSIDTSSNSASLTITDLQIEDEADYFCHSYDNSYLVFGGG TQLTVAGGPKSTPKVTVFPPSPEELQTNKATLVCLANDF YPGAATVTWKANGETITNGVMTTKPIKEGQKYIASSYLR LTADQWRSHNRVTCQVSHEGDTVEKSLSPAECL
αCD28 Heavy Chain (Syrian hamster constant region)	MRLLGLLYLVIALPGVLSQIQLEESGPGLLKPSQSLSLTCSV SGCSITSGYVWSWIRQSPGKKLEWMGYLSSGGSTNYNPTL KSRISITRDTSKNQFSLQLNSVITEDTATYYCARHGMSGT YLDFWGQGTMVTVSSATTTAPSVYPLAPGGTPDSTTVTL GCLVKGYFPEPVTVSWNSGALTSGVHTFPSVLHSGLYSLS SSVTVPSSTWPSQTVTCNVAHPASSTKVDKKIEPRSCTSLP TLCPKCPAPDLLGGPSVFIFPPNPKDVLTISLTPKVTCVVV DVSEDEPDVQFNWFVNNVEVKTAETQPRQQQFNSTYR VVSSLPIQHQDWLSSKEFKCKVNNKALPSPIEKTISKPRG QARIPQVYTLPPPTEQMTQKVVSLTCMITGFFPADVHVE WEKNGQPEQNYKNTSPVLDTDGSYFMYSKLNVPKSSWE QGNIYVCSVLHEALRNHHTTKAISRSLGN
αCD28 Light Chain (Murine kappa constant region)	MTWAPLFLIILHHLTGSYAEFVLTQPKSVSESLGRSVIISCK RSSGNIANYFVHWYQRHFGNSPKTVIYEDNKRPSGIPDRF TGSIDTSSNSASLTITDLQIEDEADYFCHSYDNSYLVFGGG TQLTVARADAAPTVSIFPPSSEQLTSGGASVVCFLNNFYPK DINVKWKIDGSERQNGVLNSWTDQDSKDSTYSMSSTLTL TKDEYERHNSYTCEATHKTSTSPIVKSFNRNEC
αCD28 Heavy Chain (Murine IgG1 constant region)	MRLLGLLYLVIALPGVLSQIQLEESGPGLLKPSQSLSLTCSV SGCSITSGYVWSWIRQSPGKKLEWMGYLSSGGSTNYNPTL KSRISITRDTSKNQFSLQLNSVITEDTATYYCARHGMSGT YLDFWGQGTMVTVSSATTKGPSVYPLAPGSAAQTNSMVT LGCLVKGYFPEPVTVTWNSGSLSSGVHTFPAVLQSDLYTL SSSVTVPSSTWPSQTVTCNVAHPASSTKVDKKIVPRDCGC KPCICTVPEVSSVFIFPPKPKDVLTITLTPKVTCVVVDISKD DPEVQFSWFVDDVEVHTAQTKPREEQINSTFRSVSELPIM HQDWLNGKEFKCRVNSAAFPAPIEKTISKTKGRPKAPQV YTIPPPKEQMAKDKVSLTCMITNFFPEDITVEWQWNGQP AENYKNTQPIMDTDGSYFVYSKLNVQKSNWEAGNTFTC SVLHEGLHNHHTEKSLSHSPGK
αCD28 Heavy Chain (Syrian hamster C_H1, murine IgG1 Hinge-C_H2-C_H3 bolded and underlined)	MRLLGLLYLVIALPGVLSQIQLEESGPGLLKPSQSLSLTCSV SGCSITSGYVWSWIRQSPGKKLEWMGYLSSGGSTNYNPTL KSRISITRDTSKNQFSLQLNSVITEDTATYYCARHGMSGT YLDFWGQGTMVTVSSATTTAPSVYPLAPGGTPDSTTVTL GCLVKGYFPEPVTVSWNSGALTSGVHTFPSVLHSGLYSLS

	SSVTVPSSTWPSQTVTCNVAHPASSTKVDKKI**VPRDCGCK PCICTVPEVSSVFIFPPKPKDVLTITLTPKVTCVVVDISK DDPEVQFSWFVDDVEVHTAQTKPREEQINSTFRSVSE LPIMHQDWLNGKEFKCRVNSAAFPAPIEKTISKTKGRP KAPQVYTIPPPKEQMAKDKVSLTCMITNFFPEDITVEW QWNGQPAENYKNTQPIMDTDGSYFVYSKLNVQKSNW EAGNTFTCSVLHEGLHNHHTEKSLSHSPGK**
αCD28-LAIR Light Chain (Syrian hamster Lambda constant region)	MTWAPLFLIILHHLTGSYAEFVLTQPKSVSESLGRSVIISCK RSSGNIANYFVHWYQRHFGNSPKTVIYEDNKRPSGIPDRF TGSIDTSSNSASLTITDLQIEDEADYFCHSYDNSYLVFGGG TQLTVAGGPKSTPKVTVFPPSPEELQTNKATLVCLANDF YPGAATVTWKANGETITNGVMTTKPIKEGQKYIASSYLR LTADQWRSHNRVTCQVSHEGDTVEKSLSPAECLGGGGS GGGGSGGGGSQEGSLPDITIFPNSSLMISQGTFVTVVCSY SDKHDLYNMVRLEKDGSTFMEKSTEPYKTEDEFEIGPV NETITGHYSCIYSKGITWSERSKTLELKVIKENVIQTPAPG PTSDTSWLKTYSIY
αCD28-ABP10 Light Chain (Syrian hamster Lambda constant region)	MTWAPLFLIILHHLTGSYAEFVLTQPKSVSESLGRSVIISCK RSSGNIANYFVHWYQRHFGNSPKTVIYEDNKRPSGIPDRF TGSIDTSSNSASLTITDLQIEDEADYFCHSYDNSYLVFGGG TQLTVAGGPKSTPKVTVFPPSPEELQTNKATLVCLANDF YPGAATVTWKANGETITNGVMTTKPIKEGQKYIASSYLR LTADQWRSHNRVTCQVSHEGDTVEKSLSPAECLGGGGS GGGGSGGGGSFQSEEQQGGGSGGSEEGGMESEESNGG GSGGSEEGG
αCD28 Fab Heavy Chain (Syrian hamster C_H1)	MRLLGLLYLVIALPGVLSQIQLEESGPGLLKPSQSLSLTCSV SGCSITSGYVWSWIRQSPGKKLEWMGYLSSGGSTNYNPTL KSRISITRDTSKNQFSLQLNSVITEDTATYYCARHGMSGT YLDFWGQGTMVTVSSATTTAPSVYPLAPGGTPDSTTVTL GCLVKGYFPEPVTVSWNSGALTSGVHTFPSVLHSGLYSLS SSVTVPSSTWPSQTVTCNVAHPASSTKVDKKIEPRSC
αCD28 Fab Light Chain (Syrian hamster Lambda constant region)	MTWAPLFLIILHHLTGSYAEFVLTQPKSVSESLGRSVIISCK RSSGNIANYFVHWYQRHFGNSPKTVIYEDNKRPSGIPDRF TGSIDTSSNSASLTITDLQIEDEADYFCHSYDNSYLVFGGG TQLTVAGGPKSTPKVTVFPPSPEELQTNKATLVCLANDF YPGAATVTWKANGETITNGVMTTKPIKEGQKYIASSYLR LTADQWRSHNRVTCQVSHEGDTVEKSLSPAECLHHHHH H

αCD28-LAIR Fab Light Chain (Syrian hamster Lambda constant region)	MTWAPLFLIILHHLTGSYAEFVLTQPKSVSESLGRSVIISCK RSSGNIANYFVHWYQRHFGNSPKTVIYEDNKRPSGIPDRF TGSIDTSSNSASLTITDLQIEDEADYFCHSYDNSYLVFGGG TQLTVAGGPKSTPKVTVFPPSPEELQTNKATLVCLANDF YPGAATVTWKANGETITNGVMTTKPIKEGQKYIASSYLR LTADQWRSHNRVTCQVSHEGDTVEKSLSPAECLGGGGS GGGGSGGGGSQEGSLPDITIFPNSSLMISQGTFVTVVCSY SDKHDLYNMVRLEKDGSTFMEKSTEPYKTEDEFEIGPV NETITGHYSCIYSKGITWSERSKTLELKVIKENVIQTPAPG PTSDTSWLKTYSIYHHHHHHH
αCD28-ABP10 Fab Light Chain (Syrian hamster Lambda constant region)	MTWAPLFLIILHHLTGSYAEFVLTQPKSVSESLGRSVIISCK RSSGNIANYFVHWYQRHFGNSPKTVIYEDNKRPSGIPDRF TGSIDTSSNSASLTITDLQIEDEADYFCHSYDNSYLVFGGG TQLTVAGGPKSTPKVTVFPPSPEELQTNKATLVCLANDF YPGAATVTWKANGETITNGVMTTKPIKEGQKYIASSYLR LTADQWRSHNRVTCQVSHEGDTVEKSLSPAECLGGGGS GGGGSGGGGSFQSEEQQGGGSGGSEEGGMESEESNGG GSGGSEEGGHHHHHHH
Fam20C-KDEL (Key: signal peptide, propeptide, kinase, linker, KDEL tag	MKMMLVRRFRVLILMVFLVACALHIALDLLPRLERRGARP SGEPGCSCAQPAAEVAAPGWAQVRGRPGEPPAASSAAG DAGWPNKHTLRILQDFSSDPSSNLSSHSLEKLPPAAEPAE RALRGRDPGALRPHDPAHRPLLRDPGPRRSESPPGPGGD ASLLARLFEHPLYRVAVPPLTEEDVLFNVNSDTRLSPKAA ENPDWPHAGAEGAEFLSPGEAAVDSYPNWLKFHIGINR YELYSRHNPAIEALLHDLSSQRITSVAMKSGGTQLKLIMT FQNYGQALFKPMKQTREQETPPDFFYFSDYERHNAEIAA FHLDRILDFRRVPPVAGRMVNMTKEIRDVTRDKKLWRTF FISPANNICFYGECSYYCSTEHALCGKPDQIEGSLAAFLPD LSLAKRKTWRNPWRRSYHKRKKAEWEVDPDYCEEVKQ TPPYDSSHRILDVMDMTIFDFLMGNMDRHHYETFEKFG NETFIIHLDNGRGFGKYSHDELSILVPLQQCCRIRKSTYLR LQLLAKEEYKLSLLMAESLRGDQVAPVLYQPHLEALDRR LRVVLKAVRDCVERNGLHSVVDDDLDTEHRAASARGGG SKDEL

3.6: Materials and Methods

Mice

C57Bl/6 (C57Bl/6NTac) mice and BALB/c (BALB/cAnNTac) mice were purchased from Taconic. B6 albino (B6(Cg)-Tyr^{c-2J}/J) mice and aged C57Bl/6 mice (C57Bl/6J) were purchased from The Jackson Laboratory. All animal work was conducted under the approval of the Massachusetts Institute of Technology Committee on Animal Care in accordance with federal, state, and local guidelines.

Cells

B16F10 and CT26 cells were purchased from ATCC. MC38 a gift from J. Schlom (National Cancer Institute, Bethesda, MD). Apigmented B16F10 cells used for imaging were generated by genetic deletion of Tyrosinase-related-protein-2 (TRP2), referred to as B16F10-Trp2 KO cells (194). Tumor cells were cultured in Dulbecco's Modified Eagle Medium (DMEM, ATCC) supplemented with 10% Fetal Bovine Serum (FBS, Gibco), except CT26 cells which were cultured in Roswell Park Memorial Institute Medium (RPMI, ATCC) supplemented with 10% Fetal Bovine Serum (FBS, Gibco). FreeStyle 293-F cells and Expi293 cells were purchased from Invitrogen and cultured in FreeStyle expression medium (Gibco) and Expi293 expression medium (Gibco), respectively. Tumor cells were maintained at 37°C and 5% CO_2 and FreeStyle 293-F cells and Expi293 cells were maintained at 37°C and 8% CO_2. All cells tested negative for mycoplasma contamination.

Tumor Inoculation and Treatment

Mice were aged six to twelve weeks before tumor inoculations. 1 x 10^6 B16F10, B16F10-Trp2KO, or cells or were suspended in 50 μL sterile PBS (Corning) and injected subcutaneously on the right flank.

Mice were randomized before beginning treatment to ensure equal tumor size in all groups. For Fig. 3-4, mice were treated with LAIR-MSA-IL-2 (i.t., 4.8 μg), and either α4-1BB (i.t., 30 μg) or α4-1BB-LAIR (i.t., 36.1 μg) on days 6, 10, and 14 post tumor inoculation. For Fig. 3-5A-B, mice were treated with either α4-1BB (i.t., 30 μg) or α4-1BB-LAIR (i.t., 36.1 μg) on days 6, 12, and 18. For Fig. 3-5C-D, mice were treated with a single dose of either α4-1BB (i.t., 20 μg, 2 μg, or 0.2 μg) or α4-1BB-LAIR (i.t., 24.1 μg, 2.41 μg, or 0.241 μg) on day 8. For Fig. 3-6, 3-8, and 3-9, mice were treated with TA99 (i.p., 200 μg) on days 5, 12, 19, and 26 and treated with α4-1BB-LAIR (i.t., 30 μg), α4-1BB (i.t., 30 μg), or α4-1BB (i.p., 150 μg) on days 6, 13, 20, and 27. For Fig. 3-7 mice were treated with TA99 (i.p., 200 μg) on day 5 and either α4-1BB-LAIR (i.t., 30 μg) or α4-1BB (i.t., 30 μg) on day 6 followed by αPD-1 (i.p., 200 μg) starting on day 9 and continuing every 3 days.

For Fig. 3-12 mice were treated with either αPD-1 (i.p., 200 μg), αCD28 Fab (i.t., "Hi" dose, 23.9 μg) + αPD-1 (i.p., 200 μg), αCD28 Fab (i.t., "Lo" dose, 4.77 μg) + αPD-1 (i.p., 200 μg), αCD28-LAIR Fab (i.t., "Hi" dose, 31.3 μg) + αPD-1 (i.p., 200 μg), αCD28-LAIR Fab (i.t., "Lo" dose 6.25 μg) + αPD-1 (i.p., 200 μg), αCD28-ABP10K Fab (i.t., "Hi" dose, 26.0 μg) + alum (i.t., 130 μg) + αPD-1 (i.p., 200 μg), αCD28-ABP10K Fab (i.t., "Lo" dose, 5.20 μg) + alum (i.t., 26 μg) + αPD-1 (i.p., 200 μg). αCD28 constructs were given on days 6, 12, and 18 and αPD-1 was initiated on day 6 and given every 3 days until euthanasia or complete tumor regression. For Fig. 3-15. Mice were treated with either αPD-1 (i.p., 200 μg), αCD28 (i.t., "Hi" dose, 10 μg) + αPD-1 (i.p., 200 μg), αCD28 (i.t., "Lo" dose, 1 μg) + αPD-1 (i.p., 200 μg), αCD28-LAIR (i.t., "Hi" dose, 12.1 μg) + αPD-1 (i.p., 200 μg), or αCD28-LAIR (i.t., "Lo" dose 1.21 μg) + αPD-1 (i.p., 200 μg). αCD28 constructs were given on days 6, 12, and 18 and αPD-1 was initiated on day 6 and given every 3 days until euthanasia or complete

tumor regression. For Fig. 3-16A-B Mice were treated with either αCD28 (i.t., "Hi" dose, 10 μg) + αCD3 (i.t.., "Hi" dose, 2 μg), αCD28 (i.t., "Lo" dose, 1 μg) + αCD3 (i.t.., "Lo" dose, 0.2 μg), αCD28-LAIR (i.t., "Hi" dose, 12.1 μg) + αCD3-LAIR (i.t.., "Hi" dose, 2.41 μg), or αCD28-LAIR (i.t., "Lo" dose, 1.21 μg) + αCD3-LAIR (i.t.., "Lo" dose, 0.241 μg) on days 6, 12, and 18. For Fig. 3-16C-D, mice were treated with either adoptive cell transfer of 1 x 10^6 2C T cells ("ACT", i.t.), ACT (i.t.) + αCD28 (i.t., 10 μg) + αCD3 (i.t., 2 μg), ACT (i.t.) + αCD28-LAIR (i.t., 12.1 μg) + αCD3-LAIR (i.t., 2.41 μg), αCD28 (i.t., 10 μg) + αCD3 (i.t., 2 μg), or αCD28-LAIR (i.t., 12.1 μg) + αCD3-LAIR (i.t., 2.41 μg).

During all tumor studies, mice were monitored continuously for tumor growth and weight change. Tumor growth was assessed by direct measurement with calipers and mice were euthanized when their tumor area (length × width) reached 100 mm^2 or mice lost more than 20% of their body weight. Mice that were cured of their primary tumor but later euthanized due to overgrooming related dermatitis were still classified as complete responders and included in analysis. For aged mice toxicity studies, mice were also monitored for body temperature via infrared rectal measurements. All measurements were taken prior to anaesthetization of mice.

Cloning and Protein Production

The heavy chain and light chain variable regions of α4-1BB (clone LOB12.3) αCD3 (clone 145-2C11), αCD40 (clone 3/23), and αOX86 (clone OX86) were synthesized as gBlock gene fragments (Integrated DNA technologies) and cloned into the gWiz expression vector (Genlantis) using In-fusion cloning (Takara Bio). The αCD28 sequence was recovered from the 37.51 hybridoma cell line using the GenScript Hybridoma sequencing service, from which codon optimized sequences were synthesized as gBlock gene fragments (Integrated DNA technologies) and cloned into the gWiz

expression vector (Genlantis) using In-fusion cloning (Takara Bio). Antibodies were expressed as chimeras with a murine kappa light chain constant region and a murine IgG1 heavy chain constant region. Antibodies were encoded in a single expression cassette with a T2A peptide inserted between the light chain and heavy chain. αFITC (clone 4420) were constructed in the same fashion, but a murine IgG2c isotype with LALA-PG silencing mutations was used for the heavy chain constant region (173). For lumican and LAIR fusions, the murine lumican or LAIR1 gene was synthesized as a gBlock gene fragment (Integrated DNA technologies) and cloned as a fusion to the C-terminus of the heavy chain constant region separated by a flexible (G4S)3 linker, except for αCD3 and αCD28 which were cloned as a fusion to the C-terminus of the light chain constant region, again separated by a flexible $(G4S)_3$ linker. For ABP10 fusions, the previously described ABP10 peptide was fused to the C-terminus of the light chain constant region separated by a flexible $(G4S)_3$ linker. αCD28 Fabs were constructed with Syrian hamster constant regions and the light chain was His tagged for purification. For LAIR and ABP10 Fab fusions, LAIR or ABP10 was fused to the Fab light chain separated by a flexible (G4S)3 linker. Human cDNA for Fam20C (Horizon, previously DharmaCon) was also cloned into gWiz with a terminal KDEL tag (without a His tag) as previously described (168). See Table 3.1 for amino acid sequences. Plasmids were transformed into Stellar competent cells for amplification and isolated with Nucleobond Xtra endotoxin-free kits (Macherey-Nagel).

Antibodies, antibody fusions, and Fabs were produced initially using the FreeStyle HEK293-F expression system (Gibco) and subsequently the Expi293 expression system (Gibco) following manufacturer's instructions. Briefly, Freestyle 293-F cells were transiently transfected by mixing 1 mg/mL of plasmid DNA and 2 mg/mL of polyethylenimine (Polysciences) in OptiPRO Serum Free Medium (Gibco) and, after incubating, adding dropwise to the cells. For the Expi293F expression

system, 1 mg/L of DNA and 3.2 mg/L of ExpiFectamine 293 were individually diluted into OptiMEM media (Gibco) and then combined dropwise. This mixture was then added dropwise to Expi293F suspension cells and 18-24 hours later ExpiFectamine 293 Transfection enhancers 1 and 2 (Gibco) were added to the culture. 7 days after transfection supernatants were harvested and antibodies were purified using Protein G Sepharose 4 Fast Flow resin (Cytiva) or rProtein A Sepharose Fast Flow resin (Cytiva) and His-tagged Fabs were purified with TALON metal affinity resin (Takara Bio, Inc.). For ABP10 fusions, proteins were co-transfected with a gWiz plasmid encoding for Fam20C at a molar ratio of 99:1 IgG-ABP10:Fam20C.

Following purification, proteins were buffer exchanged into PBS (Corning) using Amicon Spin Filters (Sigma Aldrich), 0.22 μm sterile filtered (Pall), and confirmed for minimal endotoxin (<0.1 EU/dose) using a chromogenic LAL assay (Lonza). Molecular weight was confirmed with SDS-PAGE. Proteins run alongside a Novex Sharp Pre-Stained Protein Standard (Invitrogen) on a NuPAGE 4 to 12% Bis-Tris gel (Invitrogen) with 2-(*N*-morpholino) ethanesulfonic acid (MES) running buffer (VWR) and stained for visualization with SimplyBlue Safe Stain (Life Technologies). Proteins were confirmed to be free of aggregates by size exclusion chromatography using a Superdex 200 Increase 10/300 GL column on an Äkta Explorer FPLC system (Cytiva). For ABP10 fusions, phosphorylation was confirmed by malachite green assay (Pierce Phosphoprotein Phosphate Estimation Assay Kit, Thermo Fisher Scientific) All proteins were flash frozen in liquid nitrogen and stored at -80°C.

Collagen I ELISA

96 well plates precoated with rat collagen I (Gibco) were blocked overnight with PBSTA (PBS (Corning) + 2% w/v BSA (Sigma Aldrich) + 0.05% v/v Tween-20 (Millipore Sigma)) at 4°C. After washing with 3 times PBST (PBS (Corning) + 0.05% v/v Tween-20 (Millipore Sigma)) and 3 times

with PBS (Corning), Indicated IgG, IgG-lumican, or IgG-LAIR fusions were incubated in PBSTA overnight at 4°C while shaking. Wells were washed 3 times with PBST and 3 times with PBS and then incubated with goat αmIgG1-Horseradish peroxidase (HRP) (1:2000, Abcam) in PBSTA for 1 hour at RT while shaking. Wells were again washed 3 times with PBST and 3 times with PBS and then 1-Step Ultra TMB-ELISA Substrate Solution (Thermo Fisher) was added for 5-15 min, followed by 1 M sulfuric acid to quench the reaction. Absorbance at 450 nm (using absorbance at 570 nm as a reference) was measured on an Infinite M200 microplate reader (Tecan). Binding curves were generated with GraphPad Prism software V9. K_D values were calculated using a nonlinear regression fit for one site total binding with no non-specificity and curves were normalized to the B_{max} values.

IVIS

Proteins were labeled with Alexa Fluor 647 NHS Ester (Life Technologies) and a Zeba desalting column (Thermo Scientific) was used to remove excess dye. Total molar amount of dye injected per sample was normalized between groups before injection. 20 μg of αFITC mIgG2c LALA-PG and a molar equivalent of αFITC-LAIR mIgG2c LALA-PG were used for *in vivo* retention studies. B6 albino mice were inoculated with 10^6 B16F10-Trp2 KO cells and labeled proteins were injected i.t. on day 7. Fluorescence at the site of the tumor was measured longitudinally using the IVIS Spectrum Imaging System (Perkin Elmer). One week prior to study initiation, mice were switched to an alfalfa-free casein chow (Test Diet) to reduce background fluorescence. Total radiant efficiency was calculated after subtracting background fluorescence and normalizing to the maximum value for each protein using Living Image software (Caliper Life Sciences).

Surface 4-1BB Binding Assay

The gene for murine 4-1BB (OriGene) was cloned into the pIRES2 expression vector, which encodes for GFP downstream of the inserted 4-1BB gene using an IRES site, using In-Fusion cloning (Takara Bio). Freestyle 293-F cells were transiently transfected by mixing 1 mg/mL of plasmid DNA and 2 mg/mL of polyethylenimine (Polysciences) in OptiPRO Serum Free Medium (Gibco) and, after incubating, adding dropwise to the cells. 3-5 days after transfection, cells were harvested and pelleted in V-bottom 96 well plates. Cells were titrated with a4-1BB or a4-1BB-LAIR and incubated for 3 hours shaking at 4°C. Cells were washed with PBSA (PBS (Corning) + 0.1% BSA (Sigma Aldrich)) and incubated with αmIgG1-APC (diluted 1:250, clone M1-14D12, Biolegend) for 30 minutes shaking at 4°C. Data was collected on a BD LSR II cytometer (BD Biosciences). Binding curves were generated with GraphPad Prism software V9. K_D values were calculated using a nonlinear regression fit for one site total binding with no non-specificity and curves were normalized to the B_{max} values.

In vitro T cell activation assays

One day prior to assay start, sterile flat bottom polystyrene plates were coated with various αCD3 and αCD28 constructs diluted in PBS overnight at 4°C (specific constructs and concentrations indicated in text and figure legends). Plates were washed 3 times with PBS to remove unbound protein prior to assay start. Purified naive CD8+ T cells were used for in vitro T cell activation assays. Spleens were excised from mice and mechanically dissociated through a 70 micron filter and then enriched for naive $CD8^+$ T cells using a magnetic bead negative enrichment kit (Stem Cell Technologies). Purified cells were then counted and plated for downstream assays. Purified $CD8^+$ T cells were cultured in Roswell Park Memorial Institute Medium (RPMI, ATCC) supplemented with 10% FBS (Gibco), 2mM L-glutamine (Gibco), 1X non-essential amino acids (MEM-NEAA, Gibco), 1X Penicillin/Streptomycin (Gibco), 1X Sodium Pyruvate (Gibco), and 0.055mM betamercaptoethanol (Gibco) at 37°C and 5%

CO_2. For whole splenocyte assays, 250K cells were plated per well in 200μL media, while for purified $CD8^+$ T cell assays 50K cells were plated per well in 200μL media. After 24-72 hours, depending on the assay, plates were spun down to pellet cells and 100μL of supernatant was transferred to a 96 well PCR tube rack and flash frozen and stored at -20C until analysis. IL-2 in the supernatant was measured using a mouse DuoSet IL-2 ELISA kit (R&D Systems) according to manufacturer's instructions.

Adoptive Cell Therapy (ACT)

One day prior to T cell isolation, a 6 well non-TC treated polystyrene plate (Corning) was coated overnight at 4C with 0.5 μg/mL αCD3 (clone 145-2C11, BioXCell) and 5μg/mL αCD28 (clone 37.51, BioXCell) diluted in PBS. Plates were washed with PBS before use to remove unbound antibodies. Spleens were excised from 2C transgenic mice and mechanically dissociated through a 70 micron filter and then enriched for $CD8^+$ T cells using a magnetic bead negative enrichment kit (Stem Cell Technologies). Purified $CD8^+$ T cells were cultured on αCD3/αCD28 coated plates in complete T cell media (Roswell Park Memorial Institute Medium (RPMI, ATCC) supplemented with 10% FBS (Gibco), 2mM L-glutamine (Gibco), 1X Non-essential amino acids (MEM-NEAA, Gibco), 1X Penicillin/Streptomycin (Gibco), 1X Sodium Pyruvate (Gibco), 0.055mM betamercaptoethanol (Gibco), and 10ng/mL mIL-2 (XXX)) at 37°C and 5% CO_2 for 48 hours. Cells were cultured at a density of 1M/mL of media, with 1mL per well. Cells were then transferred to a fresh TC treated 6 well plate (not coated with αCD3/αCD28 antibodies) and reseeded at a density of 1M/mL in complete T cell media for 24 hours at 37°C and 5% CO_2. Cells were passaged once more and again transferred to a fresh TC treated 6 well plate (not coated with αCD3/αCD28 antibodies) and reseeded at a density of 1M/mL in complete T cell media for 24 hours at 37°C and 5% CO_2. Activated and expanded $CD8^+$

T cells were then collected, resuspended in PBS, and administered to mice according to treatment protocol.

Tumor Cytokine/Chemokine Analysis

Tumors were excised, weighed, and mechanically dissociated and incubated in tissue protein extraction reagent (T-PER, Thermo Fisher Scientific) with 1% Halt protease and phosphatase inhibitors (Thermo Fisher Scientific) for 30 minutes at 4°C while rotating. The lysates were then centrifuged, and supernatants filtered through a Costar 0.22 micron SpinX filter (Corning) to remove any remaining debris. Lysates were flash frozen and stored at -20°C until time of analysis. Lysates were analyzed with the 13-plex mouse inflammation LEGENDplex panel (Biolegend). Data was collected on a BD LSR II cytometer (BD Biosciences).

Statistical Methods

Statistics were computed in GraphPad Prism v9 as indicated in figure captions. Survival studies were compared using the log-rank (Mantel-Cox) test. Serum cytokine/chemokine data and weight loss data were compared using two-way ANOVA with Tukey's multiple comparison correction. Sample size and *P*-value cutoffs are indicated in figure captions.

Acknowledgements

We thank the Koch Institute's Robert A. Swanson (1969) Biotechnology Center (National Cancer Institute Grant P30-CA14051) for technical support, specifically the Flow Cytometry Core Facility and the Preclinical Imaging and Testing Facility. We thank Dr. Jim Allison (MD Anderson) for the αCD28 (Clone 37.51) hybridoma line from which we recovered the antibody sequence. We also thank Dr. Stephen Beers (University of Southampton) for the sequence for αCD40 (Clone 3/23).

Chapter 4: Tregs constrain CD8$^+$ T cell priming required for curative intratumorally anchored anti-4-1BB immunotherapy

This chapter has been adapted from a preprint that is currently under review (193).

4.1: Introduction

The use of monoclonal antibodies to perturb immune cell signaling networks and improve anti-cancer immune responses has gained increased attention in recent years (195). Checkpoint blockade therapy with antagonistic antibodies is safe and efficacious, but agonistic antibodies against targets such as 4-1BB, OX40, GITR, and ICOS have proven to exhibit impractically narrow therapeutic windows due to on-target, off-tumor toxicity (16, 196–198).

4-1BB (also known as CD137 or TNFRSF9) is expressed primarily on activated CD8$^+$ and CD4$^+$ T cells, including CD4$^+$ regulatory T cells (Tregs), and natural killer (NK) cells, and is a promising target for agonist antibodies (49–51, 199, 200). Signaling through 4-1BB in CD8$^+$ T cells leads to proliferation, enhanced survival, cytokine production, improved memory formation, and altered metabolism (58, 59, 201–203). Treating mice with agonist α4-1BB antibodies as a monotherapy or in combination therapies is highly efficacious in several preclinical mouse cancer models (65, 66). However, toxicity has hampered clinical translation of such antibodies, with lethal liver toxicities reported in early phase 2 trials of Urelumab, the first α4-1BB agonistic antibody to enter the clinic (67). At reduced doses which do not elicit dose limiting toxicities (DLTs), little to no clinical efficacy has been reported (67). Utomilumab, the second α4-1BB agonist to enter the clinic, is well tolerated

but is a much weaker agonist and has little clinical activity (68, 69). Given the difficulty of uncoupling toxicity from clinical activity with systemically administered agonists, recent development around this target has focused on engineering antibodies with tumor specific activity (204). This includes several bispecific antibodies, with one arm targeting 4-1BB and the other targeting either tumor specific antigens or PD-L1, α4-1BB antibodies that bind only in tumor specific niches, such as high ATP concentrations, or pro-drug α4-1BB antibodies where the binding domain of the antibody is shielded by a peptide "mask" that is cleaved by tumor specific proteases (71–75).

Alternatively, our group and others have demonstrated the utility of using collagen binding strategies to anchor immunotherapy payloads to the tumor microenvironment (86, 92, 96–102). Collagen is a desirable target for localization due to its abundance in the tumor microenvironment (TME) (155). By directly fusing collagen binding domains to cytokines and chemokines or chemical conjugation of collagen binding peptides to αCTLA-4 and αCD40 antibodies, intratumoral administration of these therapeutic payloads results in prolonged tumor retention, enhanced efficacy, and reduced systemic toxicity.

In this work, we developed a locally retained collagen anchored α4-1BB agonist, termed α4-1BB-LAIR, by fusing an α4-1BB agonist to the ectodomain of an endogenous collagen binding protein, Leukocyte Associated Immunoglobulin Like Receptor 1 (LAIR1). Tested in combination with an antitumor antibody, TA99, in a fully syngeneic and poorly immunogenic B16F10 murine melanoma model, this combination exhibited little efficacy. Intriguingly, depletion of $CD4^+$ T cells led to long term durable cures in >90% of TA99- + α4-1BB-LAIR-treated animals. However, nearly all of these mice were unable to control a secondary tumor rechallenge. We hypothesized that depletion of Tregs,

which comprise a subset of $CD4^+$ T cells, was driving this synergy. Tregs are immunosuppressive $CD4^+$ T cells that express the transcription factor forkhead box protein P3 (Foxp3) and are critical to maintaining homeostasis and preventing autoimmunity (205, 206). Indeed, *Foxp3*$^{-/-}$ mice die at a young age from severe lymphoproliferative disease, systemic depletion of Tregs in adult mice leads to rapid lethal autoimmunity, and *Foxp3* mutations in humans cause severe immune dysregulation (207–210). Although Tregs play a critical role in curbing autoreactive T cells, they also constrict productive antitumor immune responses through a variety of mechanisms and at various stages of the tumor-immunity cycle (211, 212).

Using flow cytometry and bulk-RNA sequencing, we probed the immunological mechanism of this synergy and found that $CD4^+$ T cell depletion led to an enhanced activation state in the tumor draining lymph node (TdLN), leading to an influx of newly primed $CD8^+$ T cells into the tumor. Local remodeling of the tumor microenvironment by TA99 and α4-1BB-LAIR enhanced the cytotoxicity of these newly primed T cells, leading to tumor cell death and eventual complete tumor regression. Using a Foxp3-DTR mouse model, which allows for selective depletion of Tregs only, we confirmed that Treg depletion alone was sufficient for this synergy. Finally, we demonstrated that $CD4^+$ T cell depletion can be replaced with a more clinically relevant agent known to enhance $CD8^+$ T cell priming, αCTLA-4, without compromising efficacy. This combination of TA99 + α4-1BB-LAIR + αCTLA-4 also resulted in formation of robust immunological memory, enabling rejection of a secondary tumor rechallenge. This work suggests that locally retained 4-1BB agonist and antitumor antibody therapy can be highly efficacious when combined with modalities that enhance T cell priming, which can be restrained by TdLN Tregs.

4.2: Results

TA99 + α4-1BB-LAIR synergizes robustly with CD4 compartment depletion

As discussed in chapter 3, in order to develop a tumor-localized 4-1BB agonist, we leveraged a collagen anchoring strategy previously validated by our lab and others. We recombinantly expressed an α4-1BB antibody (clone LOB12.3, Table 4-1) as a C-terminal fusion with the ectodomain of murine LAIR1, an endogenous immune cell inhibitory receptor that naturally binds collagen (158, 159, 213). We have previously validated (in chapter 3) that this antibody fusion is able to bind both collagen I via ELISA and surface expressed 4-1BB (Fig. 3-1B, Fig. 3-3).

As demonstrated in chapter 3, the combination of TA99 + α4-1BB-LAIR (herein referred to as "Tx", dosing schedule shown in Fig. 4-1A) led to modest tumor growth delay when compared to PBS mice with a complete response rate of only ~5% (CR, defined as no palpable tumor at day 100) (Fig. 3-6). In an effort to improve this combination therapy, we explored which cell types were critical for response. Surprisingly, we observed that when we also treated these mice with an αCD4 antibody that depletes the entire $CD4^+$ T cell compartment, the complete response rate of TA99 + α4-1BB-LAIR improved dramatically, with >90% of mice achieving a complete response (Fig. 4-1B). However, when long-term survivors were rechallenged on the contralateral flank >100 days after initial tumor inoculation, nearly all mice succumbed to these secondary tumors (Fig. 4-1C). This was indicative of the inability of these mice to develop robust immune memory to B16F10 tumor cells, likely resulting from the depletion of $CD4^+$ effector T cells.

Growth delay with systemically administered αCD4 and α4-1BB has been reported previously, but we find that our specific components were necessary to achieve maximum efficacy, including TA99 (P = .0032) and, notably, retention via collagen anchoring (P = .0289) (Fig. 4-1D) (214). Consistent with other preclinical reports with this α4-1BB antibody clone, no signs of toxicity were observed for the full therapeutic combination with or without collagen anchoring (Fig. 4-1E) (182). We also tested this combination in the MC38 murine colon carcinoma model, using 2.5F-Fc as the antitumor antibody, an antibody-like molecule that targets integrins overexpressed on a wide range of tumor cells (215). We again observed that Tx + αCD4 treated mice survive longer than mice treated with Tx or αCD4 individually, although the long-term survival benefit was not as drastic as mice bearing B16F10 tumors (Fig. 4-2A, 2/10 complete responders). We did not observe any weight loss associated toxicity in this combination (Fig. 4-2B). Although αCD4 drastically improved the efficacy of Tx, the lack of immune memory formation and low translational potential of long term αCD4 treatment motivated us to understand the mechanism of this synergy and ultimately develop alternative clinically relevant synergistic combinations.

αCD4 improves priming in the TdLN

We investigated the chemokine/cytokine profile of the TME following treatments with PBS, Tx, Tx + αCD4, or αCD4 both 3 and 6 days after α4-1BB-LAIR administration. We dissociated tumors and analyzed the cytokine and chemokine milieu using a multiplexed flow cytometry-based ELISA assay. Although we observed general increases in inflammatory cytokines and chemokines in all treatment groups, only GM-CSF was specifically upregulated in the Tx + αCD4 group when compared to Tx or αCD4 alone (Fig. 4-3A). However, neutralization of this cytokine did not abrogate therapeutic efficacy

of Tx + αCD4, indicating that this spike in GM-CSF was dispensable for therapeutic efficacy (Fig. 4-3B).

We then used flow cytometry to analyze the tumors and tumor draining lymph nodes (TdLNs) of mice treated with Tx, Tx + αCD4, or αCD4 again 3 and 6 days after the first α4-1BB-LAIR treatment. As expected, we observed complete depletion of total $CD4^+$ T cells and Tregs (defined as $Foxp3^+$ $CD25^+$ $CD4^+$ T cells) in the tumor (Fig. 4-4A) and TdLN (Fig. 4-4B) in both the Tx + αCD4 and the αCD4 groups.

Using CD44 and CD62L gating, we divided $CD8^+$ T cells in the TdLN into naive ($CD44^-$ $CD62L^+$), effector/effector memory ($CD44^+$ $CD62L^-$), and central memory ($CD44^+$ $CD62L^+$) phenotypes. At both time points, we observed a shift of the $CD8^+$ T cell population towards an effector/effector memory phenotype in the Tx + αCD4 and αCD4 groups (Fig. 4-5A-B). Additionally, we observed increases in both PD-1^+ $CD8^+$ T cells (Fig. 4-5C-D) and $CD25^+$ $CD8^+$ T cells (Fig. 4-5E-F), at both time points in the Tx + αCD4 and αCD4 groups, both of which are markers of recently activated $CD8^+$ T cells in lymphoid tissue. The magnitude of these changes was equivalent between the Tx + αCD4 and αCD4 groups, indicating that the αCD4 antibody component was driving these changes to the TdLN.

Six days following treatment with either Tx + αCD4 or αCD4, we observed increased $CD8^+$ T cells infiltrating the tumor (Fig. 4-5G), which is in agreement with the enhanced activation state observed in the TdLN (Fig. 4-5C-F). This result is consistent with previous preclinical and clinical studies that have shown treatment with αCD4 can enhance T cell priming, leading to increased numbers of tumor

reactive $CD8^+$ T cells (216–218). However, only in the Tx + αCD4 group, when compared to PBS or Tx alone, do we observe an increase in degranulating $CD107a^+$ $CD8^+$ cytotoxic T cells (Fig. 4-6). No major differences in 4-1BB expression on CD8+ T cells were detected in the tumor and only minor increases were seen on $CD8^+$ T cells in the TdLN in Tx + αCD4 and αCD4 treated mice (Fig. 4-7A-C). These data suggest that αCD4 therapy, independent of Tx, induces *de novo* priming in the TdLN, leading to more $CD8^+$ T cell infiltration in the tumor. However, we hypothesized that Tx supports these newly primed cells and maintains their cytotoxic phenotype within the tumor, leading to eventual tumor regression.

TdLN has increased proliferation and T cell gene signatures by Bulk-RNA sequencing

To further interrogate immunological changes to the TdLN and tumor in an unbiased holistic manner, we performed bulk RNA-sequencing on $CD45^+$ cells from TdLN samples from mice treated with PBS, Tx, Tx + αCD4, or αCD4 3 and 6 days following α4-1BB-LAIR administration. We generated a UMAP plot of the TdLN samples and found that, at the bulk transcript level, large differences between samples were apparent only at the later time point (Fig. 4-8A). Additionally, sample clustering at this later time point was driven entirely by αCD4, with the αCD4 and Tx + αCD4 samples clustering separately from the PBS and Tx samples. In fact, we observed almost no differentially expressed genes (DEGs) in the TdLN when comparing Tx + αCD4 versus αCD4 or Tx versus PBS treated samples (Fig. 4-8B), indicating that Tx alone had no appreciable change on the transcriptional program in the TdLN.

To assess what changes αCD4 drove in the TdLN, we examined DEGs between Tx + αCD4 and Tx treated samples (Fig. 4-8B). We found 247 upregulated genes and 82 downregulated genes (FDR ≦

5%, Fig. 4-8C). We used enrichR to determine which pathways these upregulated DEGs were enriched in (219–221). Upregulated genes belonged to pathways involving cell cycling, DNA replication, and Myc related genes, indicative of a highly proliferative state in the TdLN. They were also enriched for both cycling and $CD8^+$ T cell states (Fig. 4-8D). Overall, the TdLN transcriptional data demonstrated that 1) changes to the TdLN resulted from αCD4 treatment, independent of Tx, and 2) these changes led to enhanced proliferation and T cell activation in the TdLN.

Tx + αCD4 leads to cytotoxic $CD8^+$ T cell program in the tumor

We similarly used bulk-RNA sequencing to examine immune cell gene expression programs within the tumor. We performed hierarchical clustering of the tumor samples while also independently clustering all significant DEGs (with a log 2-fold change ≥2 or ≤-2 and *p*-adj ≤ 0.05) using *k*-means clustering. This clustering identified 10 distinct gene clusters of co-expressed genes. Samples clustered imperfectly by treatment type, with two of the three Tx + αCD4 day 6 samples showing distinct transcriptional programs (Fig. 4-9). These two samples had the smallest tumor size at time of necropsy, indicating they were already robustly responding to therapy at this time point. We next performed pathway enrichment analysis on the individual gene clusters. Of particular interest were cluster 1 and 2 (and to a lesser extent cluster 4), which were upregulated specifically in the Tx + αCD4 groups, and cluster 3, which contains genes upregulated in both the Tx + αCD4 and Tx groups and represent a Tx-specific transcriptional program (Fig. 4-10A). These clusters are enriched for a range of GO terms associated with productive cellular immune responses (regulation of T cell activation, alpha-beta T cell activation, lymphocyte mediated immunity, etc.). However, only clusters 1 and 2 were enriched for genes associated with interferon gamma production, suggesting that Tx alone is not sufficient to drive IFNγ production (Fig. 4-10B). Notably, because Tx + αCD4 and αCD4 drive similar levels of

increased CD8+ T cell counts (Fig. 4-5G), but cytotoxic genes are only enriched in Tx + αCD4, we can conclude that this cytotoxic signature is not an artifact of increased CD8+ T cell counts. Cluster 7, which is highly expressed in PBS samples, contained genes enriched for, among others, pigmentation gene programs, likely representing increased $CD45^-$ tumor cells in this sample (Fig. 4-10B).

To further assess changes to the tumor microenvironment, we looked at DEGs between Tx + αCD4 tumor samples 3 and 6 days following α4-1BB-LAIR. 63 genes were upregulated, and 43 genes downregulated between these two time points (FDR ≤ 5%, Fig. 4-11A). We used the upregulated DEGs to establish a "response" signature for Tx + αCD4. We then asked if this gene signature was expressed in any other treatment conditions/time points. Indeed, this signature was highly expressed only in the Tx + αCD4 late time point, indicating this was a bona fide response signature unique to Tx + αCD4 treated mice (Fig. 4-11B). We then performed pathway enrichment analysis to determine what pathways these genes were associated with. Confirming our previous flow data, we saw effector and effector memory T cell signatures. Additionally, we saw genes associated with TCR signaling, interleukin-2 (IL-2) signaling and Stat5a activity (Fig. 4-11C). Recent literature has highlighted a role for IL-2, or more broadly Stat5a activity, in amplifying T cell populations that drive responses to checkpoint blockade (222–224). Taken together, the tumor transcriptional data support the notion that Tx + αCD4 drives a robust cytotoxic T cell program leading to tumor rejection.

Treg depletion results in equivalent efficacy as whole CD4 compartment depletion

We hypothesized that Treg depletion was the primary functional consequence of αCD4 therapy, and that Treg specific elimination would lead to similar efficacy in combination with Tx. To test this

hypothesis, we turned to Foxp3-DTR mice, which express the diphtheria toxin receptor (DTR) and GFP under control of the Foxp3 promoter. In these mice, all $Foxp3^+$ cells are also DTR^+, and thus susceptible to diphtheria toxin (DT) mediated cell death. Systemic administration of DT to these mice leads to rapid and complete depletion of nearly all $Foxp3^+$ Tregs. However, with repeat dosing these mice succumb to lethal autoimmunity within 10-20 days of DT administration (207). In order to facilitate long term depletion of Tregs in the tumor and TdLN without inducing lethal autoimmunity, we developed a low dose, intratumoral diphtheria regimen. Every other day intratumoral dosing of 75ng or 125ng of DT depleted tumor and TdLN to similar levels as 1μg of systemically administered DT, with reduced impacts on splenic Treg populations (Fig. 4-12A). Additionally, we did not observe signs of toxicity, as measured by weight loss, with intratumoral low dose DT, while mice receiving systemic DT showed trends of weight loss at time of euthanasia (Fig. 4-12B). Thus, we felt confident that low dose intratumoral DT was a safe and effective model system to achieve long term intratumoral and intranodal Treg depletion.

B16F10 tumor-bearing Foxp3-DTR mice were treated with Tx + αCD4, Tx + DT, or DT alone. To allow for lesions of sufficient size for intratumoral administration of DT, the absolute timing of therapy administration was delayed two days for all groups (such that DT and αCD4 were initiated on day 6). Mice receiving Tx + DT responded equally as well as mice receiving Tx + αCD4, with a trend (but not statistically significant) towards a higher complete response rate in the Tx + DT group (Fig. 4-12C). Interestingly, DT on its own also resulted in significant growth delay, but ultimately almost all mice succumbed to their tumor burden. To confirm that the effect of DT was purely a result of Treg depletion, we treated WT mice with DT, which resulted in no different growth kinetics over PBS treated mice. No signs of toxicity, as assessed by weight loss, were observed throughout the course of

treatment (Fig. 4-12D). A previously published study demonstrated that transient DT given with systemic α4-1BB agonist therapy led to severe immune related adverse events (irAEs) in MC38 tumor bearing mice, further highlighting the advantages of our collagen anchored α4-1BB agonists (225). Notably, when cured mice were rechallenged >100 days after their primary tumor inoculation, the majority of the Tx + αCD4 mice cured did not reject rechallenge, consistent with previous results, while 100% of mice cured with Tx + DT rejected this rechallenge, demonstrating that these mice had developed robust immunological memory against B16F10 tumor antigens (Fig. 4-12E). This result demonstrated that 1) elimination of Tregs is sufficient to boost the efficacy of Tx and 2) elimination of Tregs alone while maintaining the $CD4^+$ effector population allows for the proper formation of long-term immune memory.

Therapy induced *de novo* priming is necessary for therapeutic efficacy

Our data suggest that αCD4 mediates an increase in $CD8^+$ T cell priming in the TdLN, which then leads to accumulation of newly primed $CD8^+$ T cells in the tumor. However, an alternative explanation is that endogenous T cells already in the tumor locally proliferate and expand after αCD4 treatment. To test this hypothesis and assess if this intratumoral T cell expansion is critical to therapeutic efficacy, we treated tumor bearing mice with FTY720 concurrent with Tx + αCD4. FTY720 is a small molecule S1PR antagonist that prevents lymphocyte egress from lymphoid tissues, thus blocking any contributions from therapy-induced *de novo* priming to efficacy (226). FTY720 was initiated concurrently with the start of αCD4 treatment. To give sufficient time for the endogenous T cell response to develop before FTY720 initiation, treatment initiation was delayed two days (such that αCD4 and FTY720 were initiated on day 6 following tumor inoculation).

The addition of FTY720 to Tx + αCD4 abrogated therapeutic efficacy, with no complete responders and only minor tumor growth delay in this treatment cohort (Fig. 4-13A). Indeed, when we examined the tumor compartment via flow cytometry, addition of FTY720 to Tx + αCD4 dropped $CD8^+$ T cell counts back to baseline (PBS/DMSO) levels (Fig. 4-13B). This confirmed that increases in $CD8^+$ T cells in the tumor after Tx + αCD4 were due to *de novo* priming and trafficking from the TdLN and not local proliferation of T cells already in the tumor. The increased activation and proliferation in the TdLN (as measured by increased $Ki67^+$ $CD8^+$ T cells, increased $CD25^+$ $CD8^+$ T cells, and a shift to an effector/effector memory phenotype in the $CD8^+$ T cell population) was preserved with the addition of FTY720, confirming that FTY720 prevented trafficking of these newly primed T cells to the tumor (Fig. 4-13C-E). Indeed, beginning αCD4 therapy 8 days before tumor inoculation maintained some efficacy of the combination; but, delaying initiation of αCD4 therapy to day 10 abrogated efficacy, consistent with αCD4's role in priming (Fig. 4-13F).

Interestingly, if initiation of FTY720 therapy was delayed just two days (concurrent with α4-1BB-LAIR), therapeutic efficacy of this combination was restored and T cell counts in the tumor were restored to the same levels as Tx + αCD4 (Fig. 4-14A-C). For all FTY720 dosing schemes, blood T cell levels were significantly reduced compared to untreated mice, confirming that FTY720 was functioning as expected after treatment initiation (Fig. 4-14D). These data suggest that only a single priming wave is sufficient for efficacy of Tx + αCD4, and this priming wave occurs in a narrow time frame of two days following αCD4 initiation.

αCTLA-4 therapy also synergizes with TA99 + α4-1BB-LAIR

Based on the presented data, we concluded that αCD4 synergizes with Tx by initiating a wave of *de novo* priming, that these new tumor-infiltrating T cells are supported by the local α4-1BB-LAIR agonist and TA99, and that this two-step process ultimately drives therapeutic efficacy. We therefore hypothesized that other modalities capable of improving priming, such as αCTLA-4, would also synergize well with TA99 + α4-1BB-LAIR. Although the dominant mechanism of αCTLA-4 is contested, literature supports that treatment with αCTLA-4 improves T cell priming and infiltration into the tumor (227). We therefore treated B16F10-bearing mice with Tx + αCTLA-4, and found that this combination was also highly efficacious, with an ~80% complete response rate (Fig. 4-15A). We hypothesized that mice cured with Tx + αCTLA-4 would also generate robust immune memory and reject rechallenge as their $CD4^+$ effector T cell pool remained intact. In agreement with this hypothesis, 100% of survivors rechallenged >100 days after initial tumor inoculation rejected this secondary tumor rechallenge (Fig. 4-15B).

4.3: Discussion

α4-1BB agonist antibodies have demonstrated robust efficacy as both a monotherapy and in combination with other immunotherapy agents in preclinical mouse models but have so far failed in the clinic due to dose-limiting toxicities. In this work, we set out to develop α4-1BB antibodies with tumor-restricted activity via collagen anchoring. We have previously demonstrated that fusion of collagen binding proteins lumican or LAIR to extended half-life versions of IL-2 and IL-12 improves efficacy and limits toxicities when directly injected into tumors, even in relatively collagen-sparse B16F10 melanoma tumors, such as those used in this study (86, 92, 155).

To generate collagen anchored α4-1BB antibodies, we fused murine LAIR1 to the C-terminus of the heavy chain of an α4-1BB agonist antibody. We tested this agonist combination with a systemic antitumor antibody, TA99. We chose this combination because 1) α4-1BB agonist Urelumab is currently being tested in combination with antitumor antibodies Cetuximab, Rituximab, and Elotuzumab and 2) a wide range of other antitumor antibodies which recognize antigens expressed on tumor cells are currently in the clinic (228). Antitumor antibodies have been demonstrated to improve antitumor immune responses by both generating antigenic cell debris to enhance T cell priming and by reprogramming myeloid cells in the tumor through Fc:FcγR interactions (229). In agreement with preliminary phase 1 data, this combination did not result in robust efficacy in our hands, with only minor growth delay and complete responses in ~5% of treated mice (177). However, we unexpectedly discovered that depletion of the entire $CD4^+$ T cell compartment throughout the course of this combination therapy dramatically improved response rates, with >90% of mice achieving durable complete responses. A similarly efficacious combination (systemic α4-1BB + αCD4) has been reported in the literature, although durable responses were not seen, with all mice succumbing to their tumors between day 70-80 (214). To our knowledge, this is the highest complete response rate seen of any α4-1BB agonist antibody therapy in the poorly immunogenic B16F10 melanoma tumor model.

As Tregs comprise a sizable portion of the $CD4^+$ T cell compartment, we tested Treg depletion in lieu of whole $CD4^+$ T cell depletion using Foxp3-DTR mice in combination with TA99 + α4-1BB-LAIR and observed equivalent efficacy. While Tregs play a crucial role in preventing autoimmunity, they also constrain productive antitumor immune responses. Intratumoral Treg infiltration is correlated with poor prognosis across many different tumor types and there is evidence that intranodal Tregs

infiltration is a better predictor of survival than blood or intratumoral Tregs in certain contexts (230–233). Tregs exert their effects through multiple different pathways, including secretion of immunosuppressive cytokines such as IL-10, Transforming Growth Factor-beta (TGF-β), and IL-35, acting as a sink for IL-2 due to their high expression of the IL-2 high affinity receptor CD25, generation of immunosuppressive adenosine through expression of CD39, and expression of inhibitory receptors such as CTLA-4 and LAG-3 (211, 212).

Tregs are a major contributor to the immunosuppressive environment of the tumor, but they can also interfere with $CD8^+$ T cell priming in lymphoid tissues (234, 235). Even prior to the identification of the transcription factor Foxp3 as the canonical driver of Tregs, seminal work found that depletion of $CD25^+$ T cells (a subset of which are Tregs) before tumor implantation can lead to enhanced antitumor immune responses and eventual spontaneous tumor rejection (236). Although how Tregs constrain priming is multifaceted, it is well established that CTLA-4 expressed on Tregs can transendocytose CD80 and CD86 off the surface of dendritic cells, hampering their ability to provide proper co-stimulation and prime $CD8^+$ T cells (237–239). Blocking this transendocytosis is thought to at least partially explain the mechanism of how αCTLA-4 therapy functions to improve priming. Indeed, we show αCTLA-4 synergized as well as complete $CD4^+$ T cell or Treg specific depletion with TA99 + α4-1BB-LAIR. Our work supports the notion that intranodal Tregs dampen antitumor immune responses by constraining proper priming, and that relieving this constraint can bolster the magnitude of the antitumor T cell response and synergize robustly with T cell directed agonist immunotherapies, particularly in immunologically cold tumors such as the one used in this study.

Although long-term $CD4^+$ T cell compartment depletion leads to obvious defects in both T and B cell adaptive immune responses, transient $CD4^+$ T cell depletion has been clinically tested in cancer and other disease states using an αCD4 antibody. Transient αCD4 depletion resulted in similar increases in *de novo* priming and $CD8^+$ T cell infiltration in the tumor, consistent with our own data (217, 218). However, although no adverse events have been reported in these small phase 1 trials, these patients are still at risk of severe and possibly fatal infections if exposed to pathogens while devoid of their $CD4^+$ compartment. Additionally, although αCD4 depletion therapy synergized well with TA99 + α4-1BB-LAIR, mice failed to form immunological memory, which can be important for long term tumor control and control of distant metastases. In patients, the presence of memory T cells corresponds with breast cancer survival and memory T cells have been reported to persist in survivors of melanoma treated with immunotherapy for at least 9 years (240, 241). With this in mind, we set out to understand the mechanism of how $CD4^+$ T cell compartment depletion synergized with TA99 + α4-1BB-LAIR and develop new combination therapies with higher translational potential. Our data demonstrated that $CD4^+$ T cell depletion eliminated Tregs in the TdLN, removing immunosuppressive constraints on proper $CD8^+$ T cell priming, and induced a wave of freshly primed T cells to enter the TME. The combination of TA99 + α4-1BB-LAIR is able to reprogram the TME into a more supportive environment for these newly primed T cells, allowing them to maintain their cytotoxic phenotype, leading to tumor regression and clearance (Fig. 4-15C). Indeed, recent data has suggested a two-step model for $CD8^+$ T cell activation in cancer, with initial activation in the TdLN and effector differentiation occurring with co-stimulation in the tumor (242). The two components of our therapy mirror this paradigm, with αCD4 increasing activation in the TdLN and TA99 + α4-1BB-LAIR enhancing effector functions of these newly activated $CD8^+$ T cells directly in the tumor.

This localized therapy is reliant on intratumoral administration of the α4-1BB-LAIR component, which is clinically feasible with advances in interventional radiology (80, 84, 243). Indeed, the oncolytic virus therapy talimogene laherparepvec (T-vec) has been approved since 2015 and is routinely injected into cutaneous and subcutaneous unresectable melanoma lesions (78, 79). Preclinical and clinical development around intratumorally administered therapies have been steadily on the rise.

This study has the potential for immediate translational impact. Since both antitumor antibodies and αCTLA-4 antagonists are approved and routinely used in the clinic, they could easily be combined with clinical stage localized α4-1BB agonists. Indeed, our data demonstrated that even non-collagen anchored α4-1BB agonists synergize fairly well with antitumor antibodies in combination with αCTLA-4 therapy, identifying a potential triple combination therapy whose individual components are all already in clinical use.

In conclusion, we found that effective TA99 + α4-1BB-LAIR therapy requires a wave of *de novo* $CD8^+$ T cell priming to achieve maximum efficacy. In this study, we generated this enhanced priming wave through whole $CD4^+$ T cell compartment depletion with an αCD4 depleting antibody, Treg specific ablation using Foxp3-DTR mice, or treatment with αCTLA-4, a modality known to increase priming. These combinations resulted in high levels of primary tumor efficacy, with ~80-100% complete response rates. However, only in the latter two strategies, which preserved $CD4^+$ effector T cells, did mice also develop robust long-term immunological memory, with 100% of cured mice rejecting secondary tumor rechallenge. Our data demonstrate that at baseline, proper $CD8^+$ T cell priming is constrained by Tregs present in the TdLN. All three priming enhancing strategies are directed towards Tregs, either depleting them completely (αCD4 and DT), or blocking their immunosuppressive

pathways (αCTLA-4). This provides strong rationale for development of Treg-directed therapies that modulate Treg function in the TdLN which, in combination with proper immune agonists, can drive high levels of efficacy even in immunologically cold tumors.

4.4: Figures

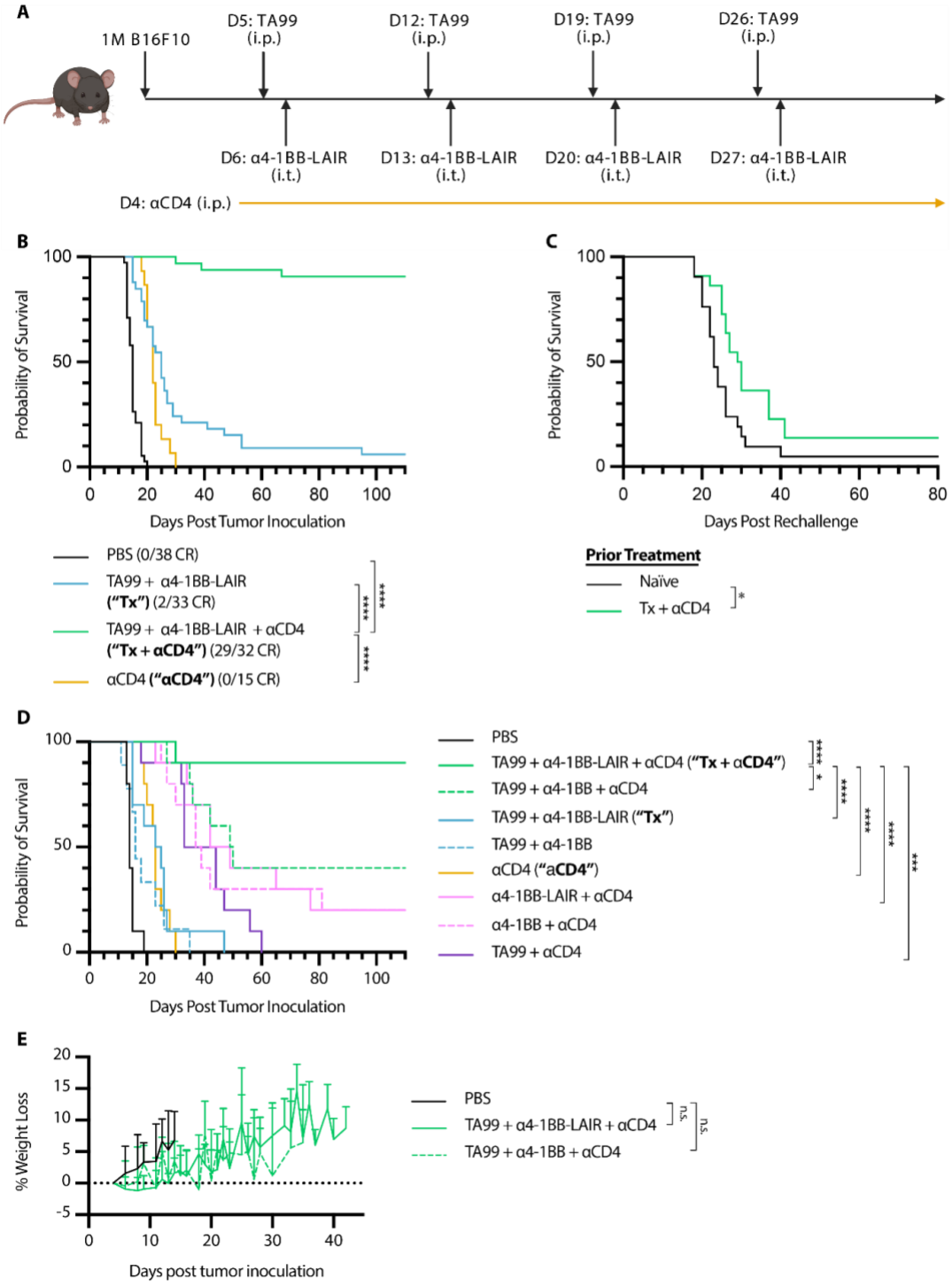
A
1M B16F10
D5: TA99 (i.p.)
D12: TA99 (i.p.)
D19: TA99 (i.p.)
D26: TA99 (i.p.)
D6: α4-1BB-LAIR (i.t.)
D13: α4-1BB-LAIR (i.t.)
D20: α4-1BB-LAIR (i.t.)
D27: α4-1BB-LAIR (i.t.)
D4: αCD4 (i.p.)
B
Probability of Survival
Days Post Tumor Inoculation
PBS (0/38 CR)
TA99 + α4-1BB-LAIR ("Tx") (2/33 CR)
TA99 + α4-1BB-LAIR + αCD4 ("Tx + αCD4") (29/32 CR)
αCD4 ("αCD4") (0/15 CR)
C
Probability of Survival
Days Post Rechallenge
Prior Treatment
Naïve
Tx + αCD4
D
Probability of Survival
Days Post Tumor Inoculation
PBS
TA99 + α4-1BB-LAIR + αCD4 ("Tx + αCD4")
TA99 + α4-1BB + αCD4
TA99 + α4-1BB-LAIR ("Tx")
TA99 + α4-1BB
αCD4 ("αCD4")
α4-1BB-LAIR + αCD4
α4-1BB + αCD4
TA99 + αCD4
E
% Weight Loss
Days post tumor inoculation
PBS
TA99 + α4-1BB-LAIR + αCD4
TA99 + α4-1BB + αCD4
n.s.

Figure 4-1: TA99 + α4-1BB-LAIR synergizes robustly with $CD4^+$ T cell depletion

Mice were inoculated with 1 x 10^6 B16F10 cells on day 0. **(A)** Treatment schedule of TA99 + α4-1BB-LAIR + αCD4. Mice were treated with 200 μg of TA99 (i.p.) on days 5, 12, 19, and 26, treated with 36.1 μg α4-1BB-LAIR (i.t.) on days 6, 13, 20, and 27 (molar equivalent to 30 μg α4-1BB), and treated with 400 μg αCD4 (i.p.) every 3 days starting 1 day before the first dose of TA99 and ending one week after the last dose of α4-1BB-LAIR (days 4 to 34). **(B)** Aggregate survival of mice treated with PBS (n = 38), TA99 + α4-1BB-LAIR ("**Tx**") (n = 33), TA99 + α4-1BB-LAIR + αCD4 ("**Tx + αCD4**") (n = 32), or αCD4 (n = 15) (eight independent studies). **(C)** Survival of complete responders to Tx + αCD4 re-challenged on the contralateral flank >100 days after primary tumor inoculation. **(D)** Overall survival of mice treated with indicated combination variants, demonstrating all components are necessary for maximum efficacy (n = 9-10, two independent experiments). **(E)** Weight loss of mice treated with PBS (n = 10), TA99 + α4-1BB-LAIR + αCD4 (n = 10), or TA99 + α4-1BB + αCD4 (n = 9) from survival study shown in Fig. 1D (two independent studies). Survival was compared using log-rank Mantel-Cox test and weight loss data were compared using two-way ANOVA with Tukey's multiple hypothesis testing correction. *$P < 0.05$, **$P < 0.01$, ***$P < 0.001$, ****$P < 0.0001$.

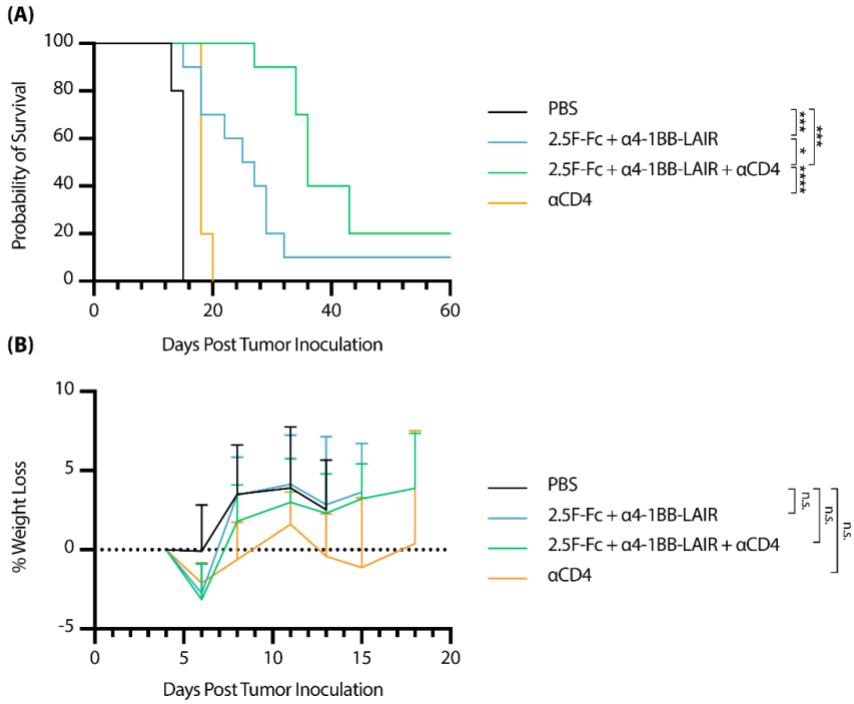

Figure 4-2: 2.5F-Fc + α4-1BB-LAIR also synergizes with $CD4^+$ T cell depletion in the MC38 tumor model

Mice were inoculated with 1 x 10^6 MC38 cells on day 0. Mice were treated with 400 μg of 2.5F-Fc (i.p.) on days 5, 12, 19, and 26, treated with 36.1 μg α4-1BB-LAIR (i.t.) on days 6, 13, 20, and 27 (molar equivalent to 30 μg α4-1BB), and treated with 400 μg αCD4 (i.p.) every 3 days starting 1 day before the first dose of TA99 and ending one week after the last dose of α4-1BB-LAIR (days 4 to 34). **(A)** Survival of mice treated with PBS (n = 5), 2.5F-F + α4-1BB-LAIR ("**Tx**") (n = 10), 2.5F-Fc + α4-1BB-LAIR + αCD4 ("**Tx + αCD4**") (n = 10), α4-1BB-LAIR (n = 10), α4-1BB-LAIR + αCD4 (n = 10), or αCD4 (n = 10). **(B)** Weight loss of mice treated in **(A)**. Survival was compared using log-rank Mantel-Cox test and weight loss data were compared using two-way ANOVA with Tukey's multiple hypothesis testing correction. *$P < 0.05$, **$P < 0.01$, ***$P < 0.001$, ****$P < 0.0001$.

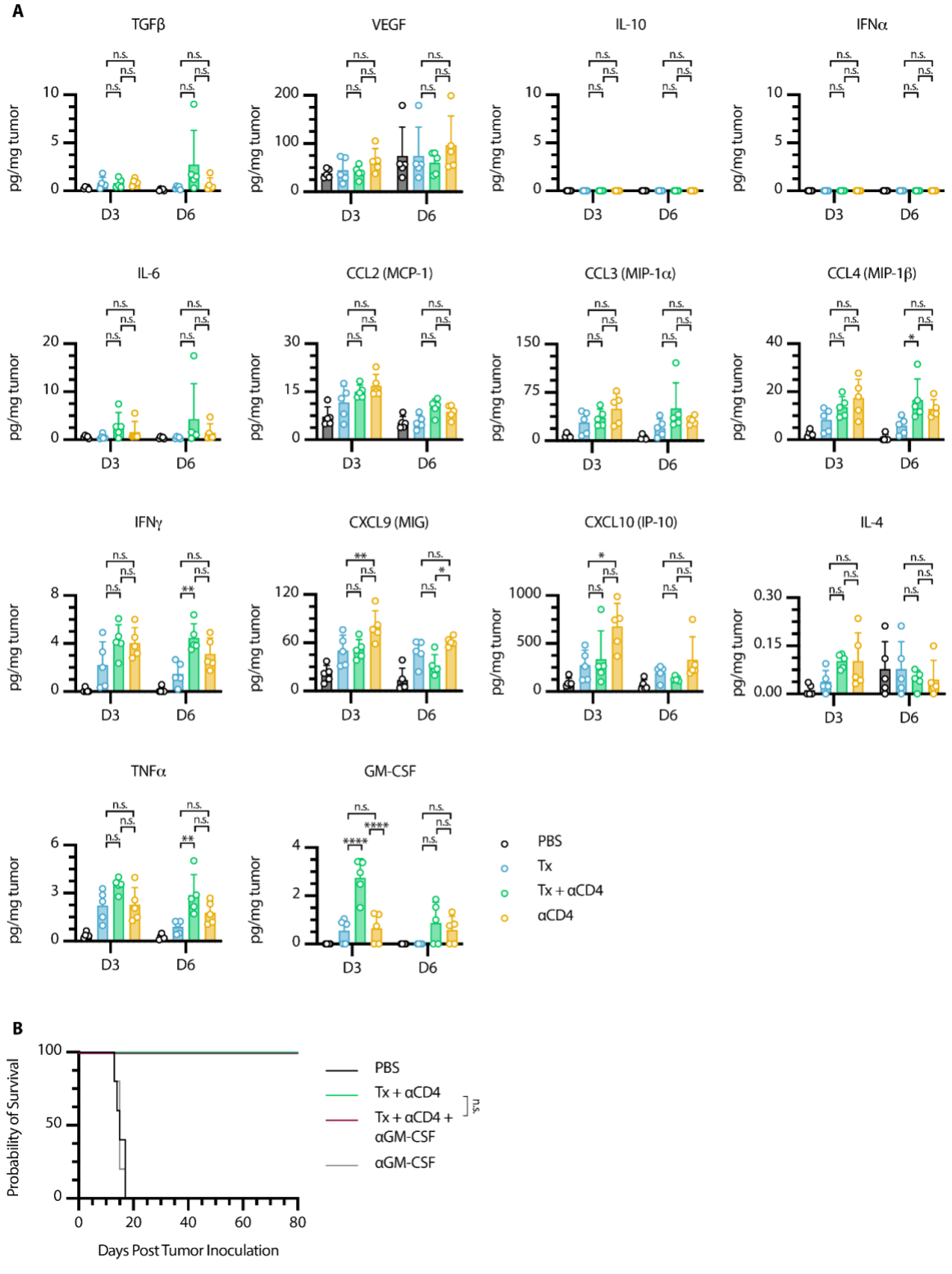
A
TGFβ
VEGF
IL-10
IFNα
IL-6
CCL2 (MCP-1)
CCL3 (MIP-1α)
CCL4 (MIP-1β)
IFNγ
CXCL9 (MIG)
CXCL10 (IP-10)
IL-4
TNFα
GM-CSF
pg/mg tumor
D3
D6
n.s.
PBS
Tx
Tx + αCD4
αCD4
B
Probability of Survival
Days Post Tumor Inoculation
PBS
Tx + αCD4
Tx + αCD4 + αGM-CSF
αGM-CSF

Figure 4-3: Tumor supernatant cytokine/chemokine analysis does not explain differences in efficacy

(A) Measured levels of indicated soluble cytokines/chemokines in tumor supernatant 3 and 6 days after first α4-1BB-LAIR treatment (n = 5). **(B)** Survival of mice treated with PBS (n = 5), Tx + αCD4 (n = 7), Tx + αCD4 + αGM-CSF (n = 7), or αGM-CSF (n = 5). Chemokine/cytokine measurements were compared using two-way ANOVA with Tukey's multiple hypothesis testing correction. Survival was compared using the log-rank Mantel-Cox test. $*P < 0.05$, $**P < 0.01$, $***P < 0.001$, $****P < 0.0001$.

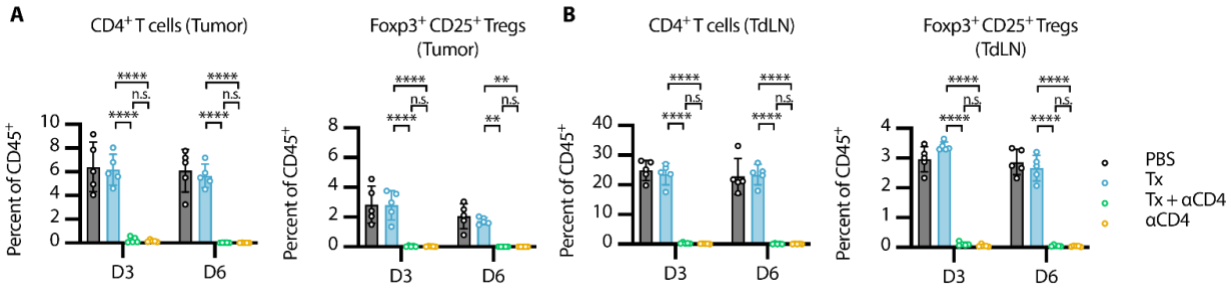

Figure 4-4: αCD4 leads to near complete depletion of $CD4^+$ T cells in the tumor and TdLN

(A-B) Flow cytometry quantification (mean±SD) of $CD4^+$ T cells (gated on single cell/live/$CD45^+$/$CD3^+NK1.1^-$/$CD4^+$) and Tregs (gated on single cell/live/$CD45^+$/$CD3^+NK1.1^-$/$CD4^+$/$Foxp3^+CD25^+$) in the **(A)** tumor and **(B)** TdLN 3 and 6 days after first α4-1BB-LAIR treatment (n = 5). Flow cytometry data was compared using two-way ANOVA with Tukey's multiple hypothesis testing correction. $*P < 0.05$, $**P < 0.01$, $***P < 0.001$, $****P < 0.0001$.

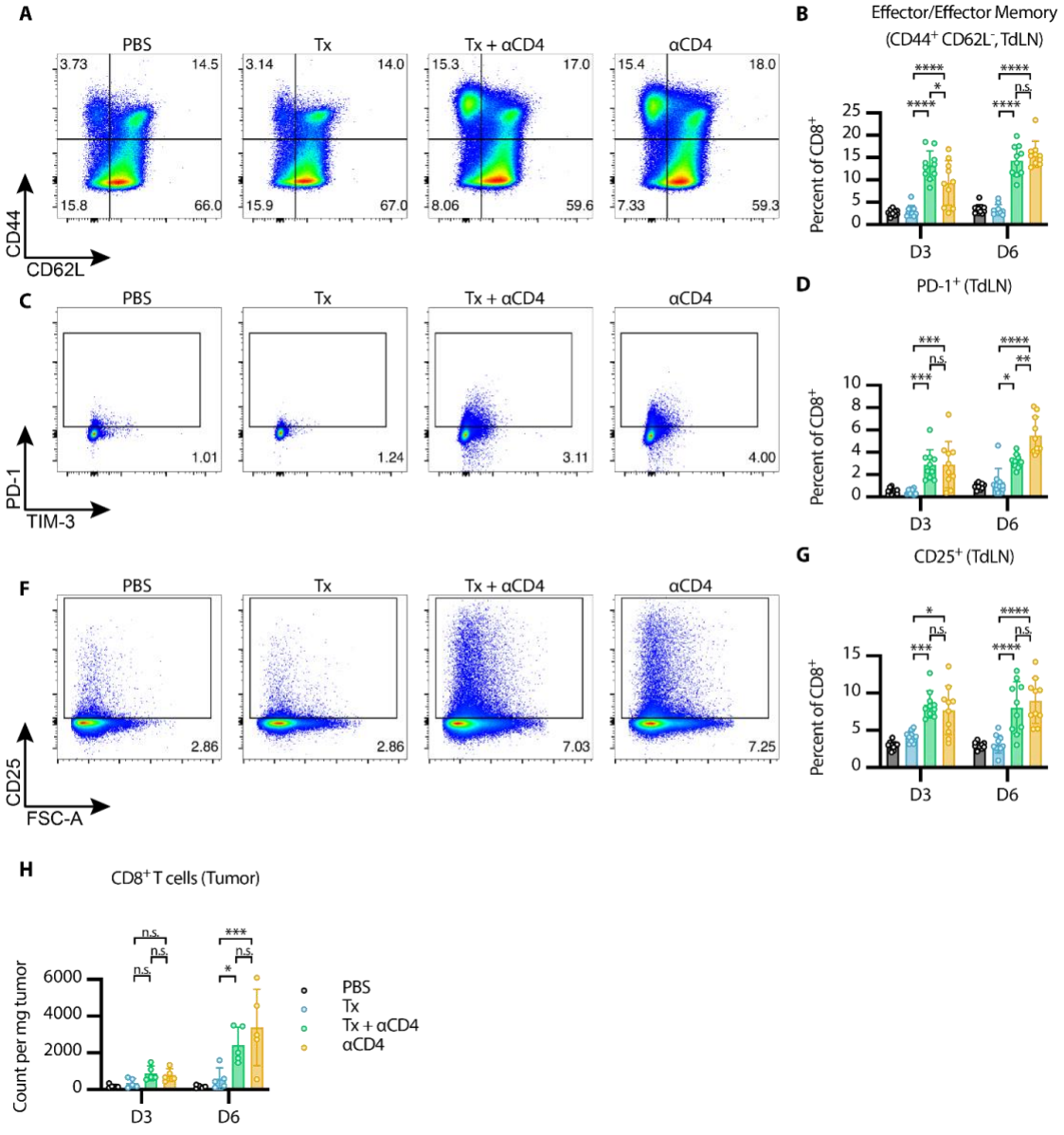

Figure 4-5: αCD4 leads to new wave of CD8$^+$ T cell priming

(A) Representative gating on CD44 and CD62L to define effector/effector memory CD8$^+$ T cells in TdLN 6 days after first α4-1BB-LAIR treatment and **(B)** quantification (mean±SD) of these cell populations 3 and 6 days after first α4-1BB-LAIR treatment (gated on single cell/live/CD45$^+$/CD3$^+$NK1.1$^-$/CD8$^+$/CD44$^+$CD62L$^-$, n = 10, two independent experiments). **(C)** Representative gating of PD-1$^+$ CD8$^+$ T cells 6 days after first α4-1BB-LAIR treatment and **(D)**

quantification (mean±SD) of these cell populations 3 and 6 days after first αα4-1BB-LAIR treatment (gated on single cell/live/$CD45^+$/$CD3^+NK1.1^-$/$CD8^+$/$PD\text{-}1^+$, n = 10, two independent experiments) **(E)** Representative gating of $CD25^+$ $CD8^+$ T cells 6 days after first αα4-1BB-LAIR treatment and **(F)** quantification (mean±SD) of these cell populations 3 and 6 days after first αα4-1BB-LAIR treatment (gated on single cell/live/$CD45^+$/$CD3^+NK1.1^-$/$CD8^+$/$CD25^+$, n = 10, two independent experiments). **(H)** Flow cytometry quantification (mean±SD) of $CD8^+$ T cells (gated on single cell/live/$CD45^+$/$CD3^+NK1.1^-$/$CD8^+$) in the tumor 3 and 6 days after first αα4-1BB-LAIR treatment (n = 5). Flow cytometry data was compared using two-way ANOVA with Tukey's multiple hypothesis testing correction. $*P < 0.05$, $**P < 0.01$, $***P < 0.001$, $****P < 0.0001$.

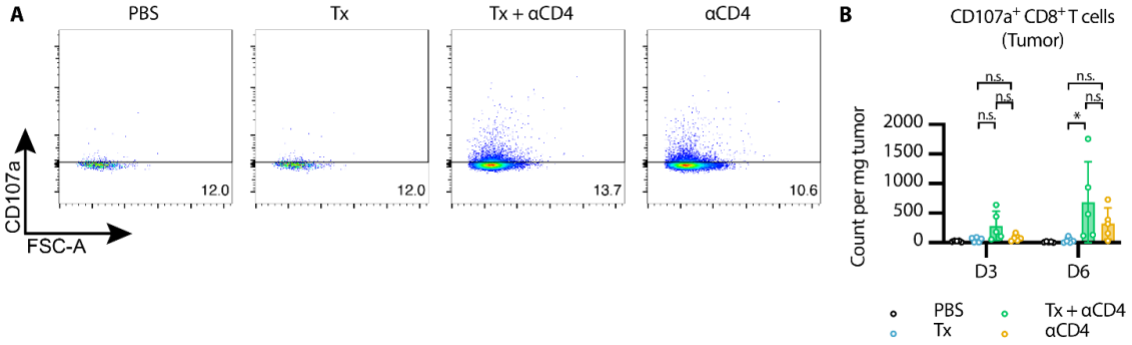

Figure 4-6: Tx supports cytotoxicity of newly primed $CD8^+$ T cells in the tumor

(A) Representative gating of $CD107a^+$ $CD8^+$ T cells 6 days after first α4-1BB-LAIR treatment and **(B)** quantification (mean±SD) of these cell populations in the tumor 3 and 6 days after first α4-1BB-LAIR treatment (gated on single cell/live/$CD45^+$/$CD3^+NK1.1^-$/$CD8^+$/$CD107a^+$, n = 5). Flow cytometry data was compared using two-way ANOVA with Tukey's multiple hypothesis testing correction. $^*P < 0.05$, $^{**}P < 0.01$, $^{***}P < 0.001$, $^{****}P < 0.0001$.

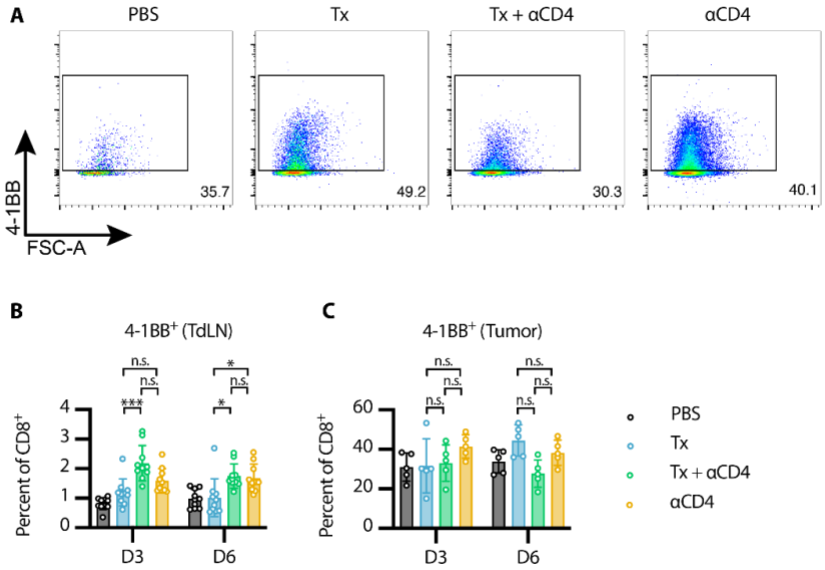

Figure 4-7: 4-1BB expression on $CD8^+$ TILs uniform across treatment groups

(A) Representative gating of 4-1BB$^+$ $CD8^+$ T cells in the tumor 6 days after first α4-1BB-LAIR treatment. Flow cytometry quantification (mean±SD) of 4-1BB$^+$ $CD8^+$ T cells in the **(B)** TdLN and **(C)** tumor 3 and 6 days after first α4-1BB-LAIR treatment (gated on single cell/live/$CD45^+$/$CD3^+$$NK1.1^-$/$CD8^+$, n = 5-10, two independent experiments). Flow data were compared using two-way ANOVA with Tukey's multiple hypothesis testing correction. $*P < 0.05$, $**P < 0.01$, $***P < 0.001$, $****P < 0.0001$.

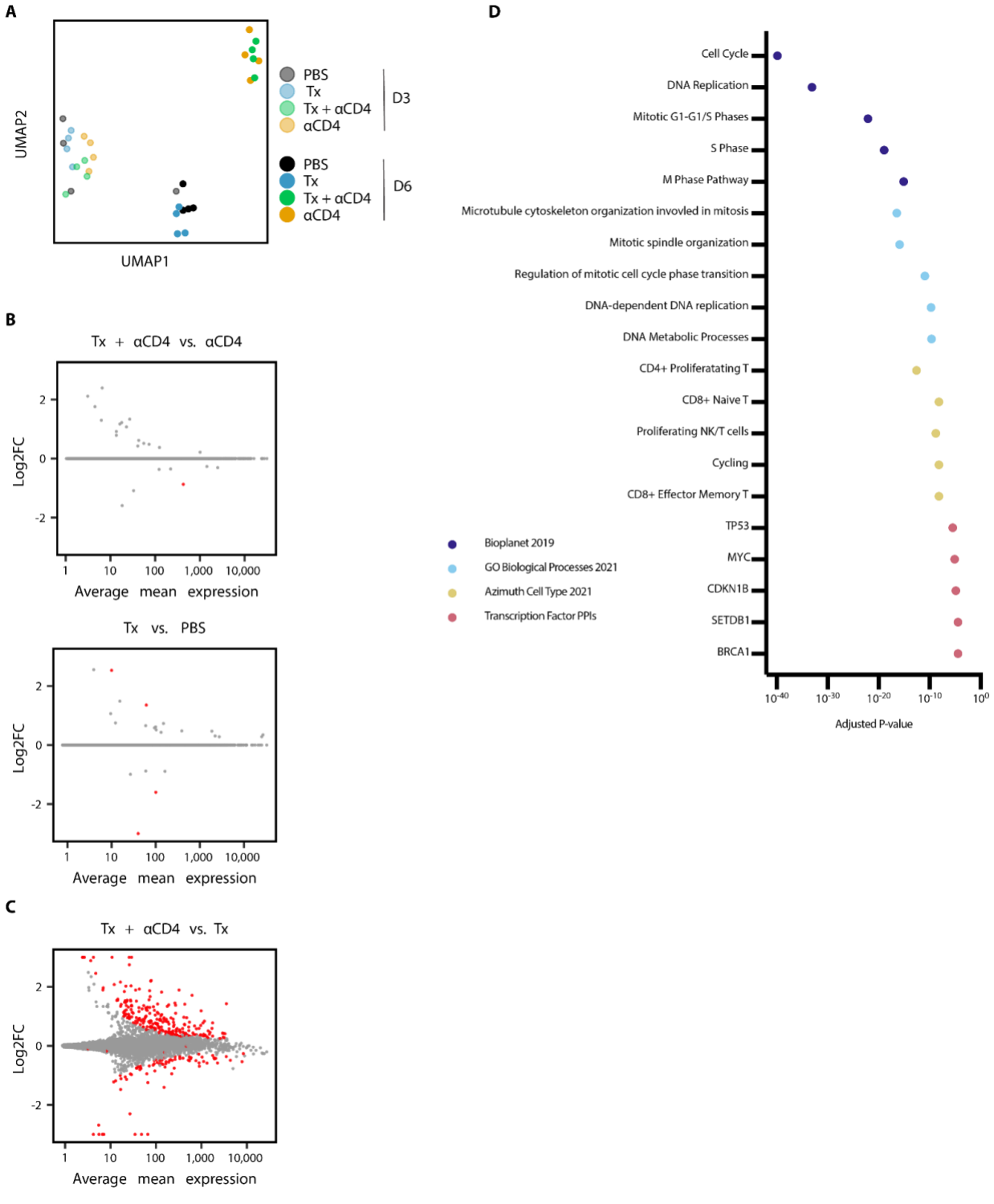
A
UMAP2
UMAP1
PBS
Tx
Tx + αCD4
αCD4
D3
PBS
Tx
Tx + αCD4
αCD4
D6
B
Tx + αCD4 vs. αCD4
Log2FC
Average mean expression
Tx vs. PBS
Log2FC
Average mean expression
C
Tx + αCD4 vs. Tx
Log2FC
Average mean expression
D
Cell Cycle
DNA Replication
Mitotic G1-G1/S Phases
S Phase
M Phase Pathway
Microtubule cytoskeleton organization involved in mitosis
Mitotic spindle organization
Regulation of mitotic cell cycle phase transition
DNA-dependent DNA replication
DNA Metabolic Processes
CD4+ Proliferatating T
CD8+ Naive T
Proliferating NK/T cells
Cycling
CD8+ Effector Memory T
TP53
MYC
CDKN1B
SETDB1
BRCA1
Bioplanet 2019
GO Biological Processes 2021
Azimuth Cell Type 2021
Transcription Factor PPIs
Adjusted P-value

Figure 4-8: αCD4 drives proliferation in the TdLN

(A) UMAP plot of TdLN transcriptomes (n = 4 per group) **(B)** Differential expression testing of Tx + αCD4 vs. αCD4 and Tx vs. PBS TdLN samples 6 days after first α4-1BB-LAIR treatment, with statistically significant hits highlighted in red (FDR ≤ 5%). **(C)** Differential expression testing of Tx + αCD4 vs. Tx TdLN samples 6 days after to first α4-1BB-LAIR treatment, with statistically significant hits highlighted in red (FDR ≤ 5%). **(D)** Pathway enrichment analysis of upregulated DEGs identified in **(C)**.

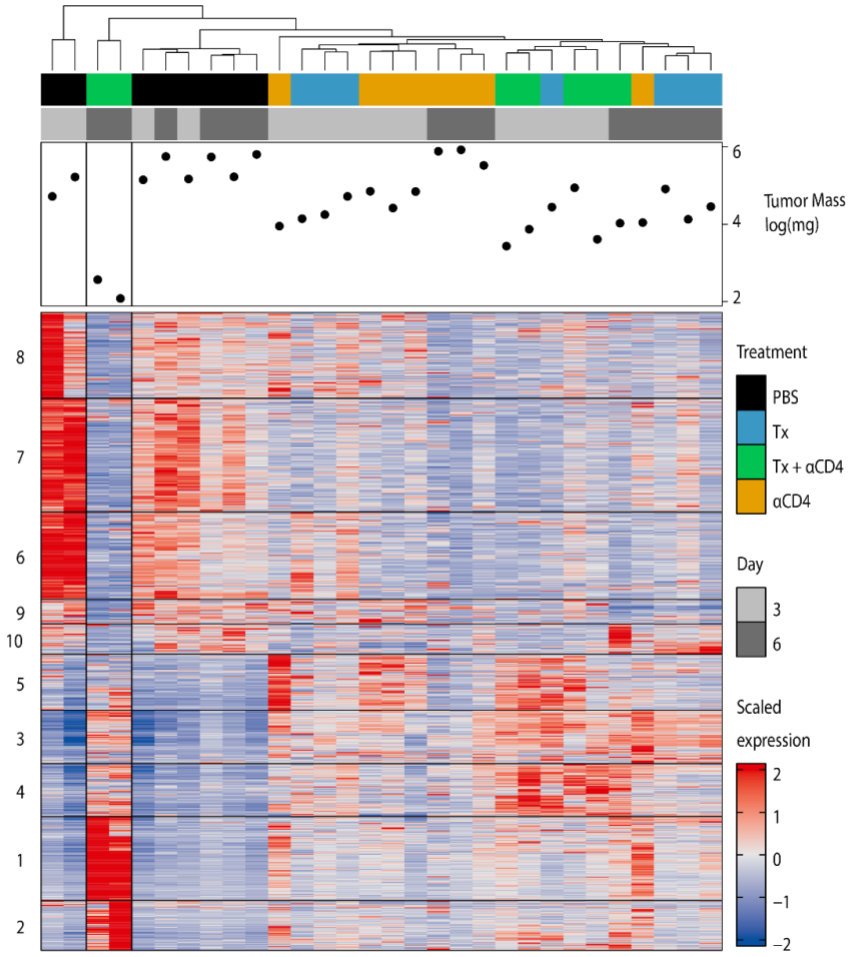

Figure 4-9: Day 6 Tx + αCD4 samples have unique gene signature

Heatmap of *k*-means clustered DEGs (absolute value lfc ≥ 2, FDR ≤ 10%) and tumor samples hierarchically clustered (n = 3-4)

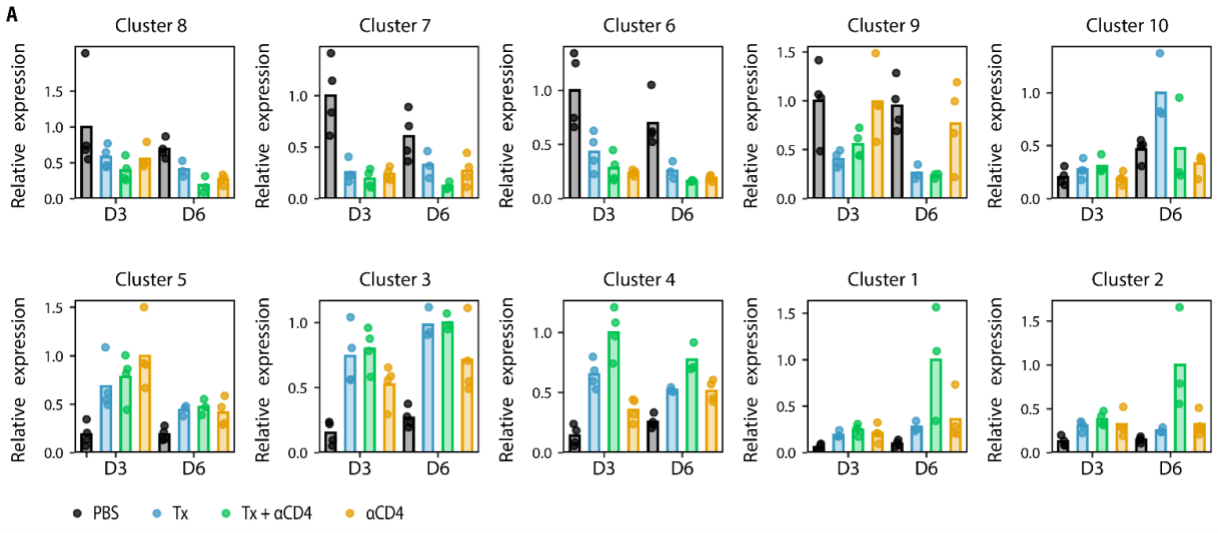
A
Cluster 8
Cluster 7
Cluster 6
Cluster 9
Cluster 10
Cluster 5
Cluster 3
Cluster 4
Cluster 1
Cluster 2
Relative expression
D3
D6
PBS
Tx
Tx + αCD4
αCD4

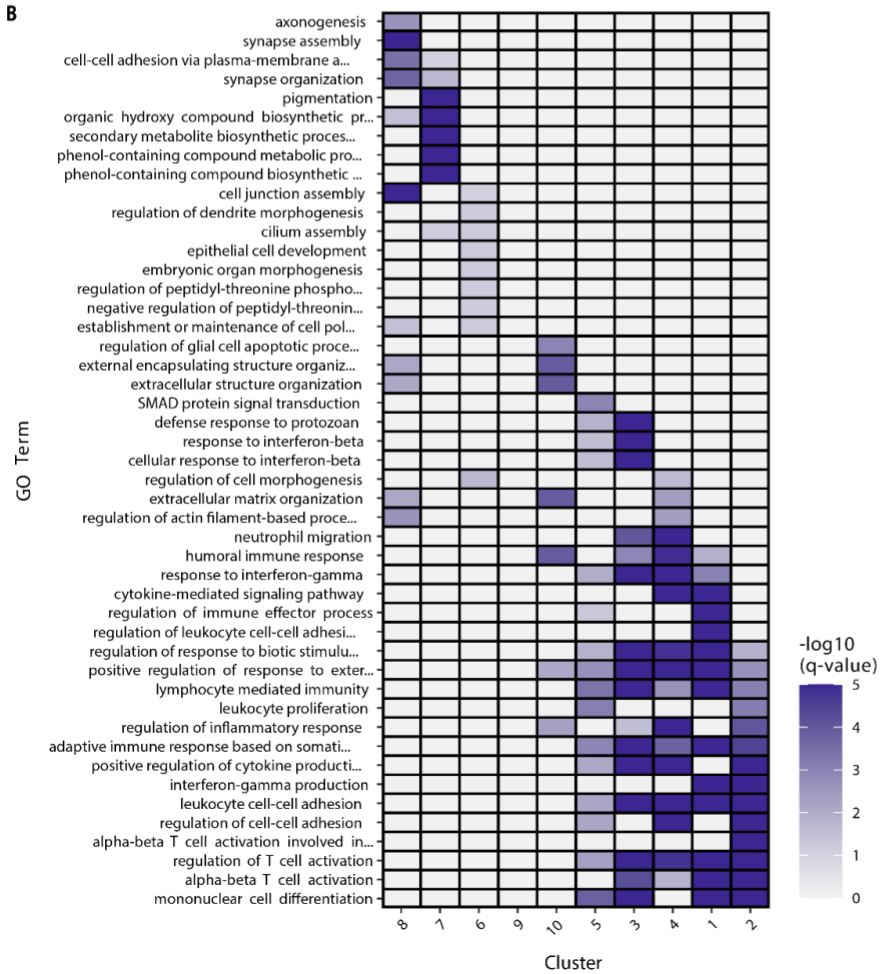
B
axonogenesis
synapse assembly
cell-cell adhesion via plasma-membrane a...
synapse organization
pigmentation
organic hydroxy compound biosynthetic pr...
secondary metabolite biosynthetic proces...
phenol-containing compound metabolic pro...
phenol-containing compound biosynthetic ...
cell junction assembly
regulation of dendrite morphogenesis
cilium assembly
epithelial cell development
embryonic organ morphogenesis
regulation of peptidyl-threonine phospho...
negative regulation of peptidyl-threonin...
establishment or maintenance of cell pol...
regulation of glial cell apoptotic proce...
external encapsulating structure organiz...
extracellular structure organization
SMAD protein signal transduction
defense response to protozoan
response to interferon-beta
cellular response to interferon-beta
regulation of cell morphogenesis
extracellular matrix organization
regulation of actin filament-based proce...
neutrophil migration
humoral immune response
response to interferon-gamma
cytokine-mediated signaling pathway
regulation of immune effector process
regulation of leukocyte cell-cell adhesi...
regulation of response to biotic stimulu...
positive regulation of response to exter...
lymphocyte mediated immunity
leukocyte proliferation
regulation of inflammatory response
adaptive immune response based on somati...
positive regulation of cytokine producti...
interferon-gamma production
leukocyte cell-cell adhesion
regulation of cell-cell adhesion
alpha-beta T cell activation involved in...
regulation of T cell activation
alpha-beta T cell activation
mononuclear cell differentiation
GO Term
8
7
6
9
10
5
3
4
1
2
Cluster
-log10
(q-value)
5
4
3
2
1
0

Figure 4-10: Tx + αCD4 upregulated gene clusters enriched for $CD8^+$ effector programs and IFNγ signature

(A) Normalized expression of individual gene clusters identified in Fig. 4-7 for each experimental condition. **(C)** Pathway enrichment analysis for each gene cluster identified in Fig. 4-7**.**

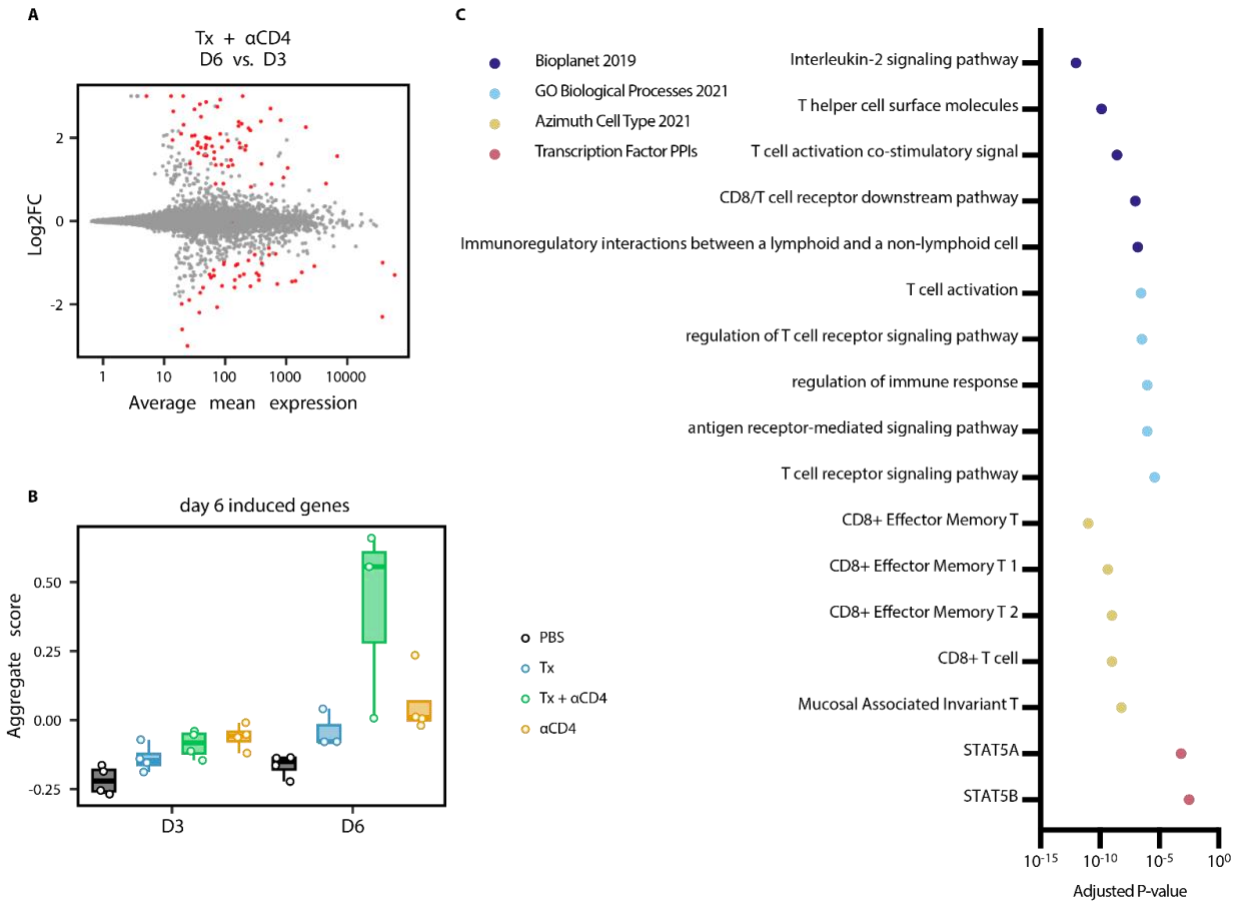

Figure 4-11: Tx + αCD4 associated with cytotoxic T cell signature in the tumor

(A) Differential expression testing of Tx + αCD4 on day 3 vs. day 6 tumor samples relative to first α4-1BB-LAIR treatment, with statistically significant hits highlighted in red (FDR ≤ 5%). **(B)** Average expression level of significantly upregulated DEGs identified in **(A)** across all treatment groups. **(C)** Pathway enrichment analysis of upregulated DEGs identified in **(A)**.

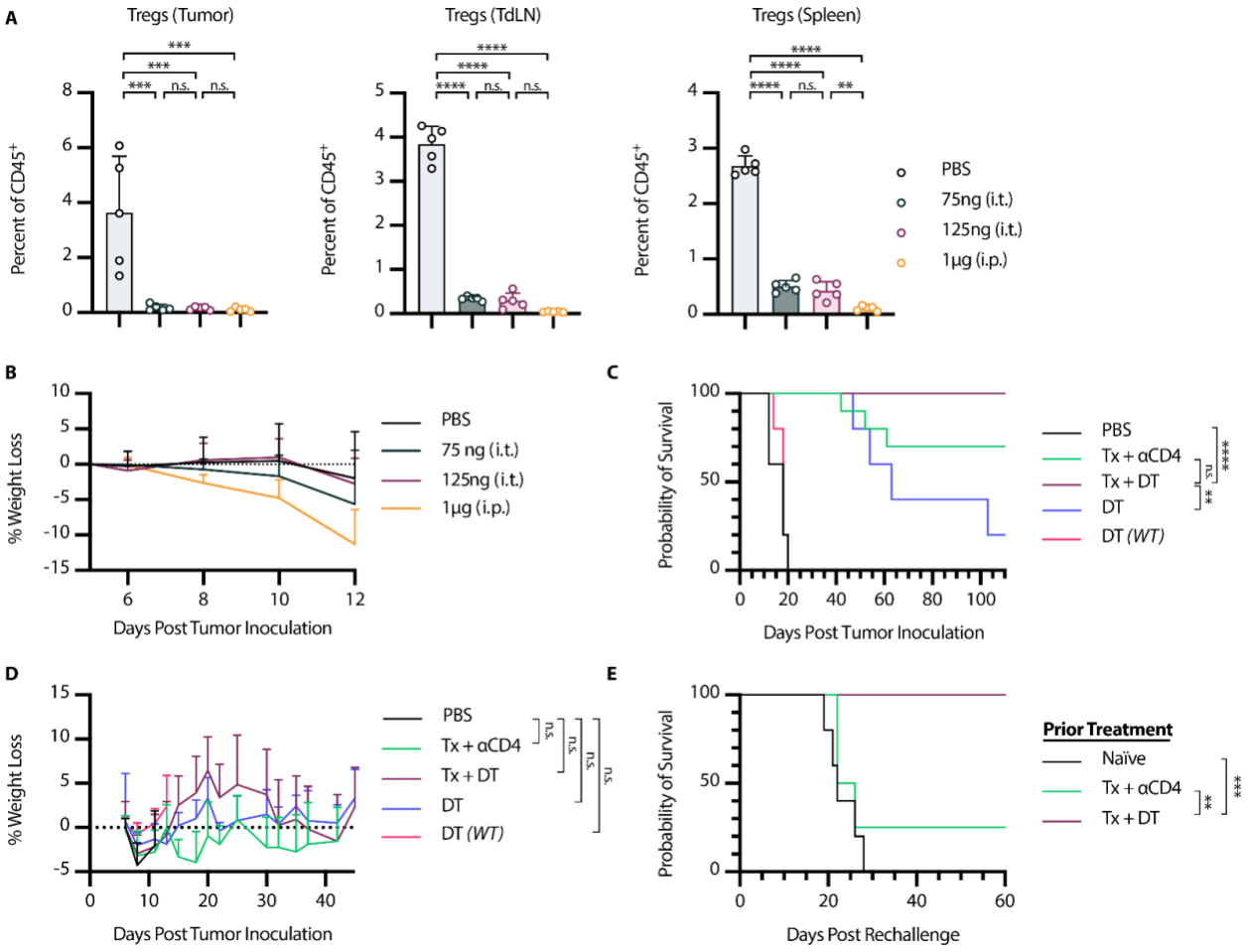

Figure 4-12: Tx + αCD4 efficacy is Treg dependent

Foxp3-DTR Mice were inoculated with 1 x 10^6 B16F10 cells on day 0. **(A)** Mice were treated on days 6, 8, and 10 with either 125 ng DT (i.t.), 75 ng DT (i.t.), or 1 μg DT (i.p.). Flow cytometry quantification (mean±SD) of Tregs in tumor, TdLN, or spleen on day 12 (gated on single cell/live/$CD45^+$/$CD3^+NK1.1^-$/$CD4^+$/GFP(*Foxp3*)$^+$, n = 5). **(B)** Weight loss (mean±SD) of mice from **(A)**. **(C)** Survival of Foxp3-DTR mice treated with PBS (n = 5), Tx + αCD4 (n = 10), Tx + DT (n = 10), DT (n = 5), WT mice treated with DT (n = 5). Mice were treated with the same relative dose/dose schedule as in Fig 1A, but treatment initiation was delayed two days. DT treated mice received 125 ng DT (i.t.) every other day from day 6 to day 36. **(D)** Survival of complete responders

to Tx + αCD4 or Tx + DT re-challenged on the contralateral flank >100 days after primary tumor inoculation. Flow cytometry data were compared using one-way ANOVA with Tukey's multiple hypothesis testing correction. Weight loss data were compared using two-way ANOVA with Tukey's multiple hypothesis testing correction. Survival was compared using log-rank Mantel Cox test. *P < 0.05, **P < 0.01, ***P < 0.001, ****P < 0.0001.

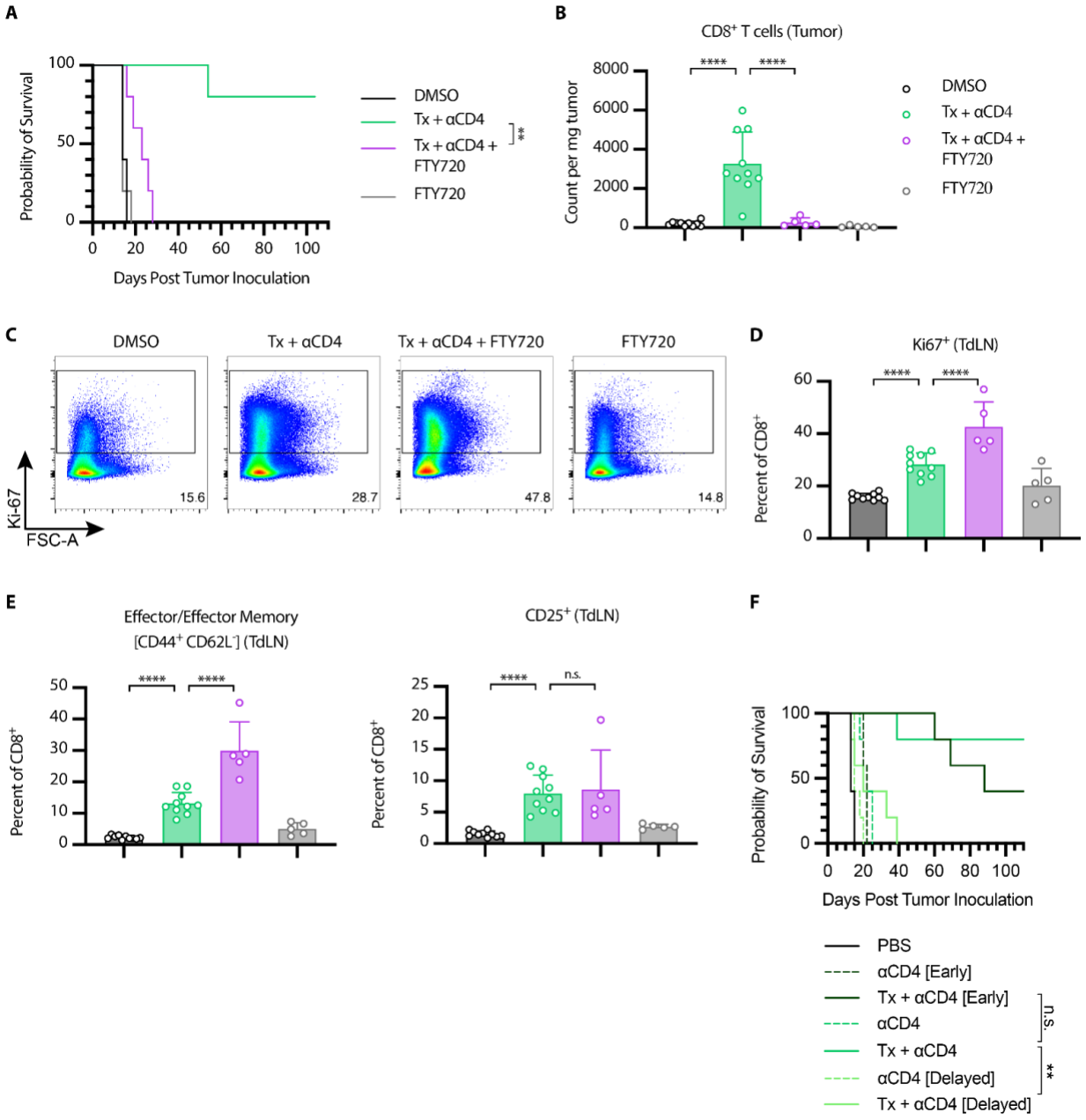

Figure 4-13: Tx + αCD4 requires de novo priming for efficacy

WT mice were inoculated with 1 x 10^6 B16F10 cells on day 0. **(A)** Overall survival of mice treated with PBS/DMSO (n = 5), Tx + αCD4 (n = 5), Tx + αCD4 + FTY720 (n = 5), or FTY720 (n = 5). Mice were treated with the same relative dose/dose schedule as in Fig 1A, but treatment initiation was delayed two days. Mice were treated with 30 μg of FTY720 (i.p.) every other day from days 6 to 36.

(B) Representative gating of Ki67$^+$ CD8$^+$ T cells 6 days after first αα4-1BB-LAIR treatment and (**C)** Flow cytometry quantification (mean±SD) of CD8$^+$ T cell counts in tumor 6 days after first αα4-1BB-LAIR treatment. (gated on single cell/Live/CD45$^+$/CD3$^+$NK1.1$^-$/CD8$^+$, n = 5-10, two independent experiments). **(D)** Flow cytometry quantification (mean±SD) of effector/effector memory (CD44$^+$ CD62L$^-$), and CD25$^+$ CD8$^+$ T cells in the TdLN 6 days after αα4-1BB-LAIR treatment (gated on single cell/live/CD45$^+$/CD3$^+$NK1.1$^-$/CD8$^+$, n = 5-10, two independent experiments). **(E)** Overall Survival of mice treated with PBS, Tx + ααCD4, or ααCD4 with ααCD4 initiated on day 4 as outlined in Fig. 4-1A, day 10 ("delayed"), or day -8 ("early") (n = 5). Flow cytometry data was compared using one-way ANOVA with Tukey's multiple hypothesis testing correction. Survival was compared using log-rank Mantel Cox test. *$P < 0.05$, **$P < 0.01$, ***$P < 0.001$, ****$P < 0.0001$.

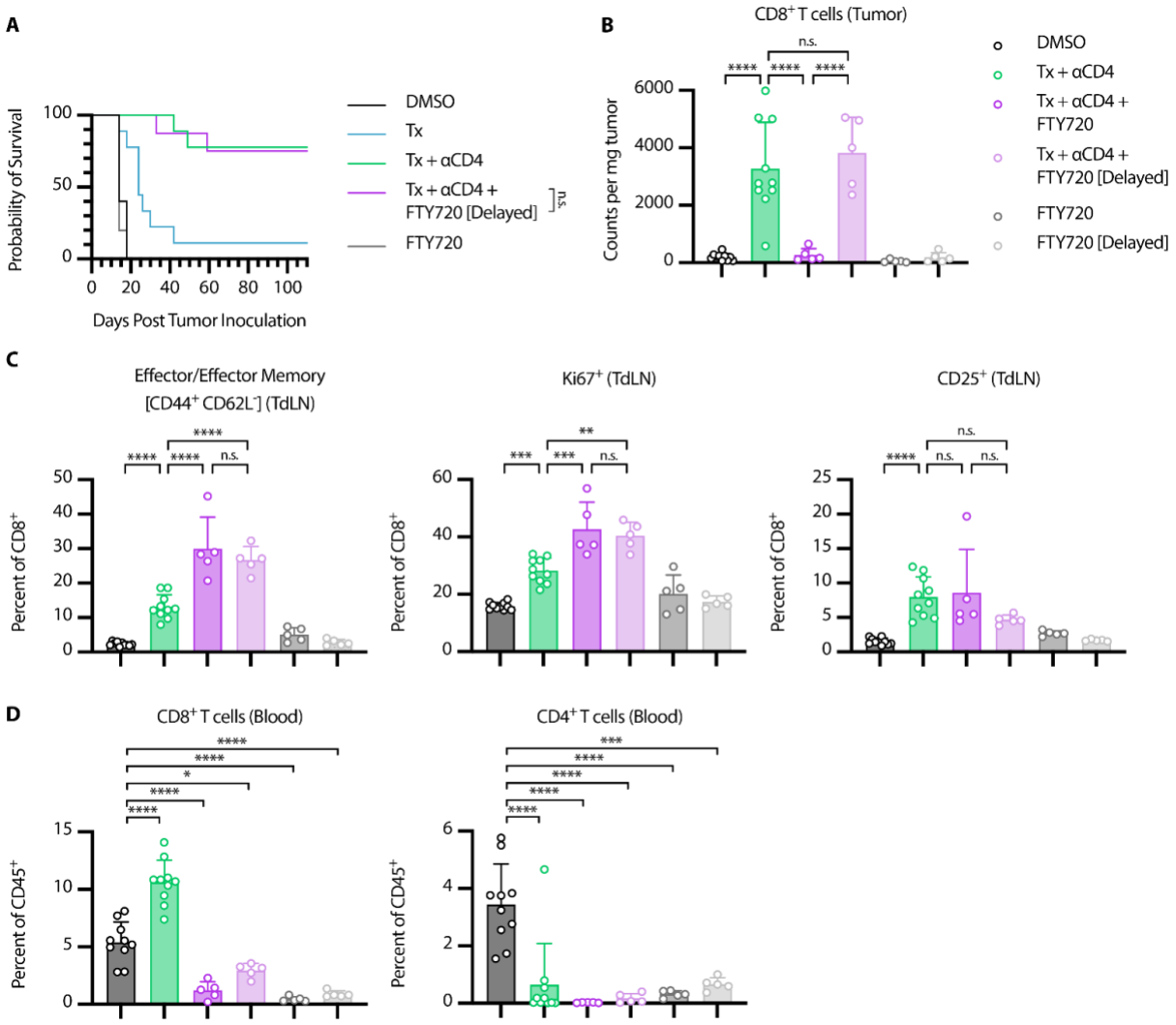

Figure 4-14: Delayed FTY720 initiation does not affect therapeutic efficacy of Tx + αCD4

Delayed FTY720 refers to FTY720 initiation concurrent with α4-1BB-LAIR treatment, while FTY720 refers to FTY720 initiation concurrent with αCD4. **(A)** Overall survival of mice treated with PBS/DMSO (n = 5), Tx (n = 9), Tx + αCD4 (n = 9), Tx + αCD4 + delayed FTY720 (n = 8), or delayed FTY720 (n = 5). Mice were treated with the same dose/dose schedule as in Fig 1A, with delayed FTY720 treatment initiated on day 6 and continued every other day until day 34. **(B)** Flow cytometry quantification (mean±SD) of $CD8^+$ T cells in the tumor 6 days after first α4-1BB-LAIR

treatment (gated on single cell/live/$CD45^+$/$CD3^+NK1.1^-$/$CD8^+$, n = 5-10, two independent experiments). **(C)** Flow cytometry quantification (mean±SD) of effector/effector memory ($CD44^+$ $CD62L^-$), $CD25^+$, and $Ki67^+$ $CD8^+$ T cells in the TdLN 6 days after first α4-1BB-LAIR treatment (gated on single cell/live/$CD45^+$/$CD3^+NK1.1^-$/$CD8^+$, n = 5-10, two independent experiments). **(D)** Flow cytometry quantification (mean±SD) of $CD8^+$ T cells and $CD4^+$ T cells in the blood 6 days after first α4-1BB-LAIR treatment (gated on single cell/live/$CD45^+$/$CD3^+NK1.1^-$/$CD8^+$, n = 5-10, two independent experiments).

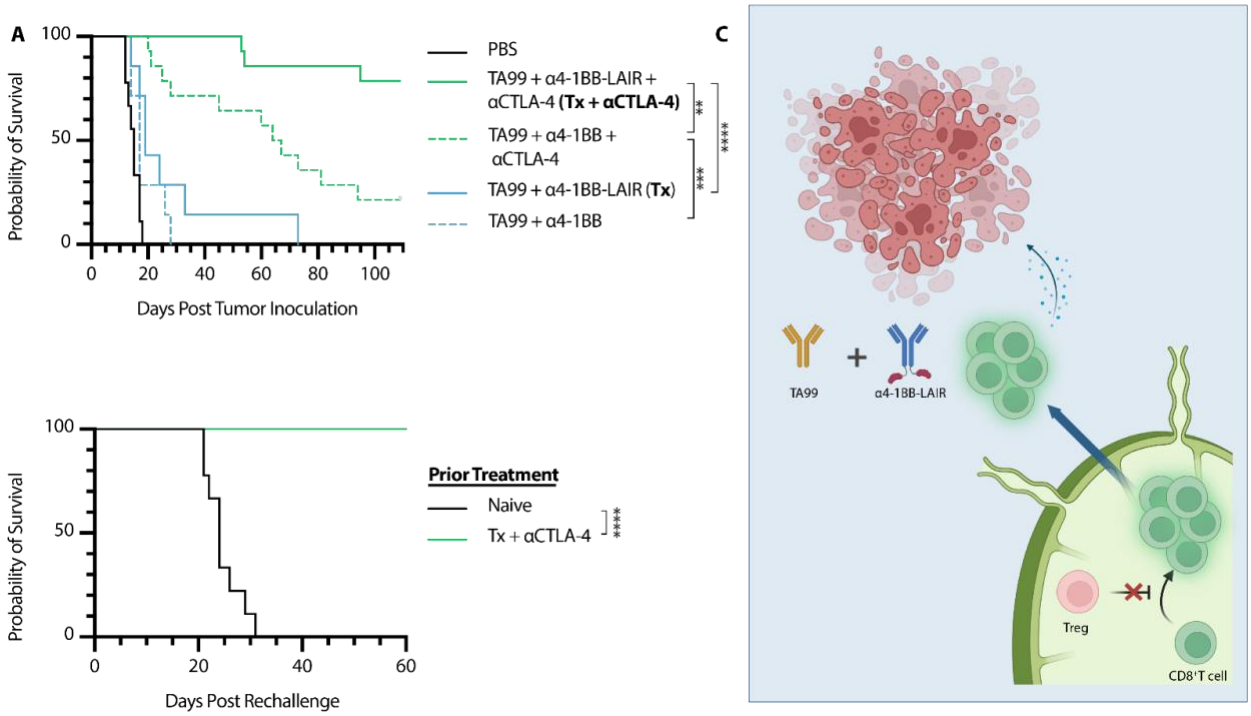

Figure 4-15: αCTLA-4 can replace αCD4 while maintaining efficacy and rescuing memory formation

Mice were inoculated with 1 x 10^6 B16F10 cells on day 0. **(A)** Overall survival of mice treated either with PBS (n = 9, two independent studies), TA99 + α4-1BB-LAIR + αCTLA-4 ("Tx +αCTLA-4", n = 14, two independent studies), TA99 + α4-1BB + αCTLA-4 (n = 14, two independent studies), TA99 + α4-1BB-LAIR (n = 7), or TA99 + α4-1BB (n = 7). Mice were treated with the same dose/dose schedule as in Fig. 4-1A with 200 μg αCTLA-4 (i.p.) given on days 6, 9, 13, 16, 20, 23, and 27. **(B)** Survival of complete responders to Tx + αCTLA-4 re-challenged on the contralateral flank >100 days after primary tumor inoculation. **(C)** Graphical Abstract of proposed mechanism of action. Tregs in the TdLN constrain proper priming of tumor reactive $CD8^+$ T cells, and inhibition or depletion of these cells results in a wave of newly primed $CD8^+$ T cells entering the tumor, where their cytotoxic program is supported by TA99 and collagen anchored α4-1BB-LAIR. Survival was compared using log-rank Mantel-Cox test. *$P < 0.05$, **$P < 0.01$, ***$P < 0.001$, ****$P < 0.0001$.

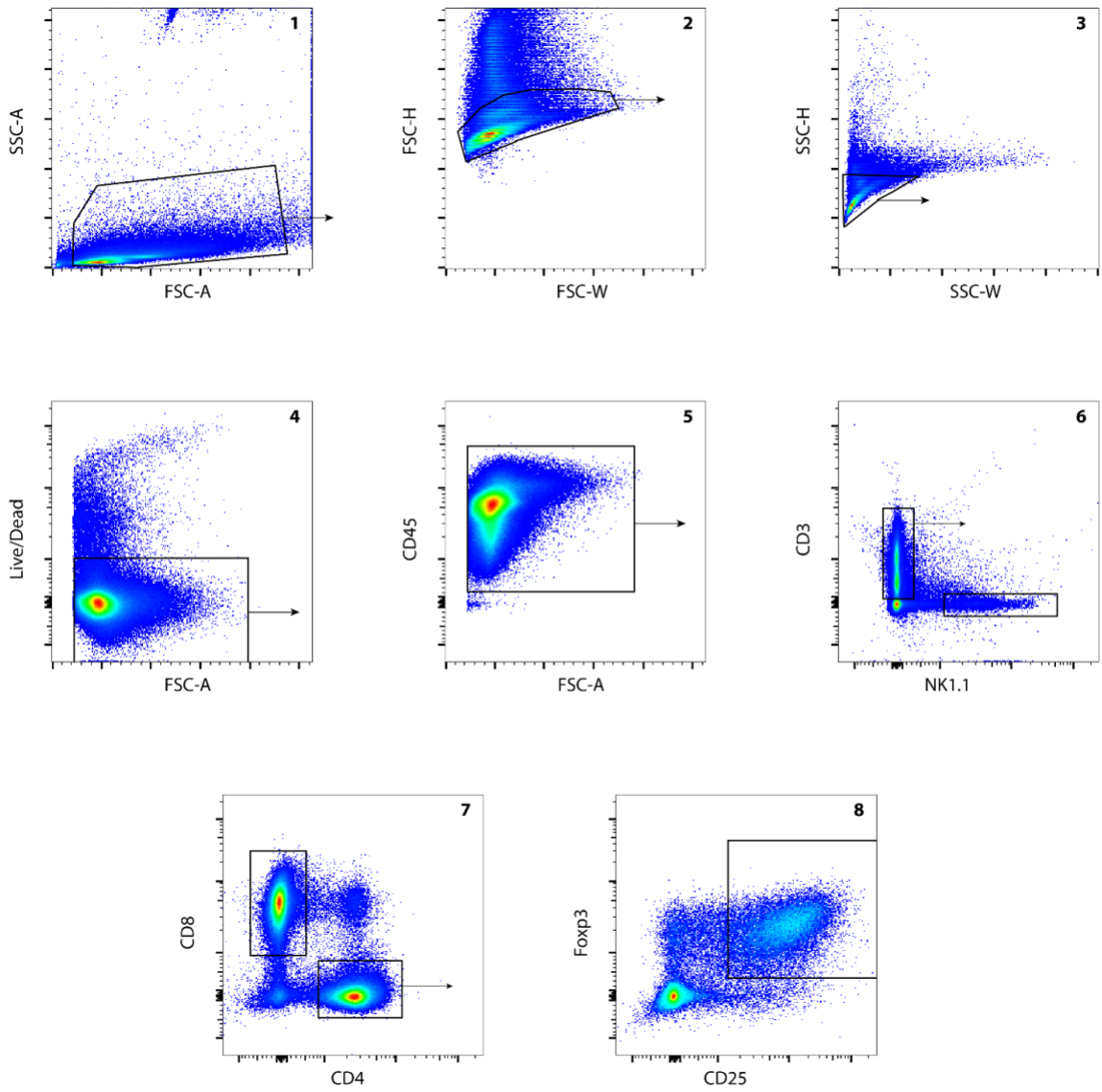

Figure 4-16: Example gating

Gating strategy for $CD8^+$ T cells, $CD4^+$ T cells, and $Foxp3^+$ $CD25^+$ Tregs, shown on a TdLN sample.

Identical gating strategies were used for tumor, spleen, and blood samples.

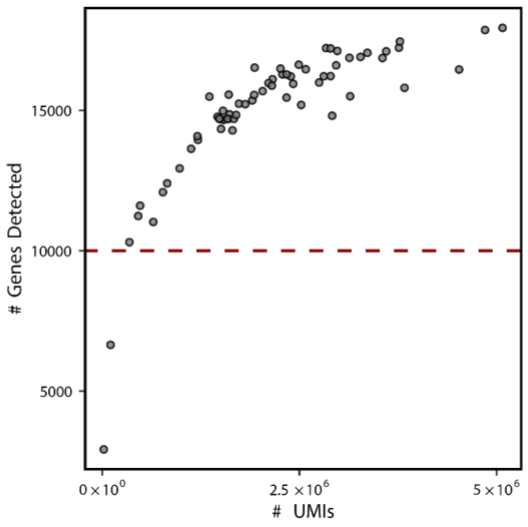

Figure 4-17: Low read samples removed from RNA-sequencing analysis

Plot of number of genes detected versus number of unique reads per sample for all tumor and TdLN bulk-RNA seq samples. Samples with less than 10,000 unique genes detected were excluded from analysis. Two samples (one Tx D6 and one Tx + αCD4 D6) met this exclusion criteria.

4.5: Tables

Table 4-1: Amino acid sequence table

Note that these sequences for α4-1BB and α4-1BB-LAIR are identical to the sequences in table 3-1 but are repeated here for posterity.

Key: signal peptide, variable region, constant region, linker, LAIR

α4-1BB Light Chain (Murine kappa constant region)	MSVLTQVLALLLLWLTGARCADIQMTQSPASLSASLEEIVT ITCQASQDIGNWLAWYHQKPGKSPQLLIYGSTSLADGVP SRFSGSSSGSQYSLKISRLQVEDIGIYYCLQAYGAPWTFGG GTKLELKRADAAPTVSIFPPSSEQLTSGGASVVCFLNNFYP KDINVKWKIDGSERQNGVLNSWTDQDSKDSTYSMSSTL TLTKDEYERHNSYTCEATHKTSTSPIVKSFNRNEC
α4-1BB Heavy Chain (Murine IgG1 constant region)	MKWSWVFLFLMAMVTGVNSDVQLVESGGGLVQPGRSL KLSCAASGFIFSYFDMAWVRQAPTKGLEWVASISPDGSIP YYRDSVKGRFTVSRENAKSSLYLQMDSLRSEDTATYYCAR RSYGGYSEIDYWGQGVMVTVSSATTKGPSVYPLAPGSAA QTNSMVTLGCLVKGYFPEPVTVTWNSGSLSSGVHTFPAV LQSDLYTLSSSVTVPSSTWPSQTVTCNVAHPASSTKVDKKI VPRDCGCKPCICTVPEVSSVFIFPPKPKDVLTITLTPKVTC VVVDISKDDPEVQFSWFVDDVEVHTAQTKPREEQINSTF RSVSELPIMHQDWLNGKEFKCRVNSAAFPAPIEKTISKTK GRPKAPQVYTIPPPKEQMAKDKVSLTCMITNFFPEDITVE WQWNGQPAENYKNTQPIMDTDGSYFVYSKLNVQKSNW EAGNTFTCSVLHEGLHNHHTEKSLSHSPGK
α4-1BB-LAIR Heavy Chain (Murine IgG1 constant region)	MKWSWVFLFLMAMVTGVNSDVQLVESGGGLVQPGRSL KLSCAASGFIFSYFDMAWVRQAPTKGLEWVASISPDGSIP YYRDSVKGRFTVSRENAKSSLYLQMDSLRSEDTATYYCAR RSYGGYSEIDYWGQGVMVTVSSATTKGPSVYPLAPGSAA QTNSMVTLGCLVKGYFPEPVTVTWNSGSLSSGVHTFPAV LQSDLYTLSSSVTVPSSTWPSQTVTCNVAHPASSTKVDKKI VPRDCGCKPCICTVPEVSSVFIFPPKPKDVLTITLTPKVTC VVVDISKDDPEVQFSWFVDDVEVHTAQTKPREEQINSTF RSVSELPIMHQDWLNGKEFKCRVNSAAFPAPIEKTISKTK GRPKAPQVYTIPPPKEQMAKDKVSLTCMITNFFPEDITVE WQWNGQPAENYKNTQPIMDTDGSYFVYSKLNVQKSNW EAGNTFTCSVLHEGLHNHHTEKSLSHSPGKGGGGSGGG

	GSGGGGSQEGSLPDITIFPNSSLMISQGTFVTVVCSYSDKH DLYNMVRLEKDGSTFMEKSTEPYKTEDEFEIGPVNETIT GHYSCIYSKGITWSERSKTLELKVIKENVIQTPAPGPTSDT SWLKTYSIY
TA99 Light Chain (Murine kappa constant region)	MSVLTQVLALLLLWLTGARCAIQMSQSPASLSASVGETVTI TCRASGNIYNYLAWYQQKQGKSPHLLVYDAKTLADGVP SRFSGSGSGTQYSLKISSLQTEDSGNYYCQHFWSLPFTFGS GTKLEIKRADAAPTVSIFPPSSEQLTSGGASVVCFLNNFYP KDINVKWKIDGSERQNGVLNSWTDQDSKDSTYSMSSTL TLTKDEYERHNSYTCEATHKTSTSPIVKSFNRNEC
TA99 Heavy Chain (Murine IgG2c constant region)	MKWSWVFLFLMAMVTGVNSEVQLQQSGAELVRPGALV KLSCKTSGFNIKDYFLHWVRQRPDQGLEWIGWINPDNG NTVYDPKFQGTASLTADTSSNTVYLQLSGLTSEDTAVYFC TRRDYTYEKAALDYWGQGASVIVSSAKTTAPSVYPLAPVC GGTTGSSVTLGCLVKGYFPEPVTLTWNSGSLSSGVHTFPA LLQSGLYTLSSSVTVTSNTWPSQTITCNVAHPASSTKVDK KIEPRVPITQNPCPPLKECPPCAAPDLLGGPSVFIFPPKIKD VLMISLSPMVTCVVVDVSEDDPDVQISWFVNNVEVHTAQ TQTHREDYNSTLRVVSALPIQHQDWMSGKEFKCKVNNR ALPSPIEKTISKPRGPVRAPQVYVLPPPAEEMTKKEFSLTC MITGFLPAEIAVDWTSNGRTEQNYKNTATVLDSDGSYFM YSKLRVQKSTWERGSLFACSVVHEGLHNHLTTKTISRSLG K
2.5F-Fc (Murine IgG2c constant region)	MRVPAQLLGLLLLWLPGARCGCPRPRGDNPPLTCSQDSD CLAGCVCGPNGFCGGRLEPRVPITQNPCPPLKECPPCAAP DLLGGPSVFIFPPKIKDVLMISLSPMVTCVVVDVSEDDPD VQISWFVNNVEVHTAQTQTHREDYNSTLRVVSALPIQHQ DWMSGKEFKCKVNNRALPSPIEKTISKPRGPVRAPQVYV LPPPAEEMTKKEFSLTCMITGFLPAEIAVDWTSNGRTEQ NYKNTATVLDSDGSYFMYSKLRVQKSTWERGSLFACSVV HEGLHNHLTTKTISRSLGK

4.6: Materials and Methods

Study Design

The purpose of this study was to (i) evaluate the efficacy and safety of collagen anchoring α4-1BB-LAIR and subsequently to (ii) understand the mechanism driving synergy between TA99 + α4-1BB-LAIR and αCD4 and finally to (iii) identity more clinically relevant therapies that synergize with TA99 + α4-1BB-LAIR. We used the syngeneic murine melanoma line B16F10 for all studies. Mice were randomized before beginning treatment to ensure equal tumor size in all groups and were monitored for tumor size and weight loss until euthanasia or until complete tumor regression. Investigators were not blinded during the studies. In all studies there were at least 5 mice per experimental group, except for the bulk RNA-sequencing experiment which had 3-4 mice per group. No data/experiments were excluded unless there were technical issues with the experiment, and outliers were not excluded. Many experiments were repeated twice, and number of mice per group, number of experimental repeats, and statistical methods are noted in figure legends.

Mice

C57Bl/6 (C57Bl/6NTac) mice were purchased from Taconic. C57Bl/6 albino (B6(Cg)-Tyr^{c-2J}/J) mice were purchased from The Jackson Laboratory. C67Bl/6 Foxp3-DTR (B6.129(Cg)-$Foxp3^{tm3(DTR/GFP)Ayr}$/J) mice were a gift from the Spranger lab (MIT). B6 Foxp3-DTR mice were bred in house and genotyped using Transnetyx. All animal work was conducted under the approval of the Massachusetts Institute of Technology Committee on Animal Care in accordance with federal, state, and local guidelines.

Cells

B16F10 cells were purchased from ATCC. Apigmented B16F10 cells used for imaging were generated by genetic deletion of Tyrosinase-related-protein-2 (TRP2), referred to as B16F10-Trp2 KO cells (194). Tumor cells were cultured in Dulbecco's Modified Eagle Medium (DMEM, ATCC) supplemented with 10% Fetal Bovine Serum (FBS, Gibco). FreeStyle 293-F cells and Expi293 cells were purchased from Invitrogen and cultured in FreeStyle expression medium (Gibco) and Expi293 expression medium (Gibco), respectively. CHO DG44 cells were cultured in ProCHO5 (Lonza) supplemented with 4 mM L-glutamine, 0.1 mM hypoxanthine, and 16 μM thymidine. Tumor cells were maintained at 37°C and 5% CO_2 and FreeStyle 293-F cells, Expi293 cells, and CHO DG44 cells were maintained at 37°C and 8% CO_2. All cells tested negative for mycoplasma contamination.

Cloning and Protein Production

The heavy chain and light chain variable regions of α4-1BB antibody (clone LOB12.3) were synthesized as gBlock gene fragments (Integrated DNA technologies) and cloned into the gWiz expression vector (Genlantis) using In-fusion cloning (Takara Bio). Antibodies were expressed as chimeras with a murine kappa light chain constant region and a murine IgG1 heavy chain constant region. Antibodies were encoded in a single expression cassette with a T2A peptide inserted between the light chain and heavy chain. αFITC (clone 4420) were constructed in the same fashion, but a murine IgG2c isotype with LALA-PG silencing mutations was used for the heavy chain constant region (173). For LAIR fusions, the murine LAIR1 gene was synthesized as a gBlock gene fragment (Integrated DNA technologies) and cloned as a fusion to the C-terminus of the heavy chain constant region separated by a flexible $(G_4S)_3$ linker. Plasmids were transformed into Stellar competent cells for amplification and isolated with Nucleobond Xtra endotoxin-free kits (Macherey-Nagel).

a4-1BB, a4-1BB-LAIR, αFITC, and αFITC-LAIR were produced using the Expi293 expression system (Gibco) following manufacturer's instructions. Briefly, 1 mg/L of DNA and 3.2 mg/L of ExpiFectamine 293 were individually diluted into OptiMEM media (Gibco) and then combined dropwise. This mixture was then added dropwise to Expi293F suspension cells and 18-24 hours later ExpiFectamine 293 Transfection enhancers 1 and 2 (Gibco) were added to the culture. 7 days after transfection, supernatants were harvested and antibodies were purified using Protein G Sepharose 4 Fast Flow resin (Cytiva).

TA99 was produced using a FreeStyle 293-F stable production line generated in-house. Cells were expanded and then seeded at a density of 1 M/mL and supernatant was harvested 7 days later. 9D9 was produced using a CHO DG44 stable production line gifted to us by David Hacker. Cells were expanded and then seeded at a density of 0.5M/mL and supernatant was harvested 7 days later. Both TA99 and 9D9 were purified using rProtein A Sepharose Fast Flow resin (Cytiva).

Following purification, proteins were buffer exchanged into PBS (Corning) using Amicon Spin Filters (Sigma Aldrich), 0.22 μm sterile filtered (Pall), and confirmed for minimal endotoxin (<0.1 EU/dose) using the Endosafe LAL Cartridge Technology (Charles River). Molecular weight was confirmed with SDS-PAGE. Proteins run alongside a Novex Sharp Pre-Stained Protein Standard (Invitrogen) on a NuPAGE 4 to 12% Bis-Tris gel (Invitrogen) with 2-(*N*-morpholino) ethanesulfonic acid (MES) running buffer (VWR) and stained for visualization with SimplyBlue Safe Stain (Life Technologies). Proteins were confirmed to be free of aggregates by size exclusion chromatography using a Superdex 200 Increase 10/300 GL column on an Äkta Explorer FPLC system (Cytiva). All proteins were flash frozen in liquid nitrogen and stored at -80°C.

Collagen I ELISA

96 well plates precoated with rat collagen I (Gibco) were blocked overnight with PBSTA (PBS (Corning) + 2% w/v BSA (Sigma Aldrich) + 0.05% v/v Tween-20 (Millipore Sigma)) at 4°C. After washing with 3 times PBST (PBS (Corning) + 0.05% v/v Tween-20 (Millipore Sigma)) and 3 times with PBS (Corning), a4-1BB and a4-1BB-LAIR were incubated in PBSTA overnight at 4°C while shaking. Wells were washed 3 times with PBST and 3 times with PBS and then incubated with goat αmIgG1-Horseradish peroxidase (HRP) (1:2000, Abcam) in PBSTA for 1 hour at RT while shaking. Wells were again washed 3 times with PBST and 3 times with PBS and then 1-Step Ultra TMB-ELISA Substrate Solution (Thermo Fisher) was added for 5-15 min, followed by 1 M sulfuric acid to quench the reaction. Absorbance at 450 nm (using absorbance at 570 nm as a reference) was measured on an Infinite M200 microplate reader (Tecan). Binding curves were generated with GraphPad Prism software V9. K_D values were calculated using a nonlinear regression fit for one site total binding with no non-specificity and curves were normalized to the B_{max} values.

Surface 4-1BB Binding Assay

The gene for murine 4-1BB (OriGene) was cloned into the pIRES2 expression vector, which encodes for GFP downstream of the inserted 4-1BB gene using an IRES site, using In-Fusion cloning (Takara Bio). Freestyle 293-F cells were transiently transfected by mixing 1 mg/mL of plasmid DNA and 2 mg/mL of polyethylenimine (Polysciences) in OptiPRO Serum Free Medium (Gibco) and, after incubating, adding dropwise to the cells. 3-5 days after transfection, cells were harvested and pelleted in V-bottom 96 well plates. Cells were titrated with a4-1BB or a4-1BB-LAIR and incubated for 3 hours shaking at 4°C. Cells were washed with PBSA (PBS (Corning) + 0.1% BSA (Sigma Aldrich)) and incubated with αmIgG1-APC (diluted 1:250, clone M1-14D12, Biolegend) for 30 minutes shaking at 4°C. Data was collected on a BD LSR II cytometer (BD Biosciences). Binding curves were generated

with GraphPad Prism software V9. K_D values were calculated using a nonlinear regression fit for one site total binding with no non-specificity and curves were normalized to the B_{max} values.

Tumor Inoculation and Treatment

Mice were aged six to twelve weeks before tumor inoculations. 1 x 10^6 B16F10 or B16F10-Trp2KO cells were suspended in 50uL sterile PBS (Corning) and injected subcutaneously on the right flank.

Mice were randomized before beginning treatment to ensure equal tumor size in all groups. TA99 was administered intraperitoneally (i.p) at a dose of 200 μg in 200 μL sterile PBS (Corning). α4-1BB or α4-1BB-LAIR was administered intratumorally (i.t.) in 20 μL of sterile PBS (Corning) at a dose of 30 μg or 36.1 μg (molar equivalents), respectively. αCD4 (Clone GK1.5, BioXcell) was administered i.p. at a dose of 400 μg in 100 μL sterile PBS (Corning). αCTLA-4 (Clone 9D9, mIgG2c isotype) was administered i.p. at a dose of 200 μg in 100 μL of sterile PBS (Corning). Diphtheria Toxin (DT, Sigma Aldrich) was administered i.p. at a dose of 1 μg in 100 μL sterile PBS (Corning) or i.t. at a dose of 75 ng or 125 ng in 20 μL sterile PBS (Corning). Stock solutions of FTY720 (Sigma Aldrich) were resuspended at 10 mg/mL in DMSO and diluted to a dose of 30 μg in sterile PBS (Corning) to a final volume of 150 μL and administered i.p.

TA99 was dosed on days 5, 12, 19, and 26 and α4-1BB and α4-1BB-LAIR were administered on days 6, 13, 20, and 27. αCD4 was administered starting on day 4 and continued every three days until day 37 (Fig. 4-1A). For some studies, therapy initiation was delayed by 2 days to allow for larger tumors at time of analysis (flow cytometry, chemokine/cytokine analysis, and bulk-RNA-sequencing; Fig. 4-3 through Fig. 4-11), sufficiently sized tumors for intratumoral DT administration (DT survival

studies; Fig. 4-12), or to avoid interfering with the endogenous T cell response (FTY720 studies; Fig. 4-13 and Fig. 4-14, except Fig. 4-13F and Fig. 4-14A which followed Fig. 4-1A dosing scheme). DT was administered every other day starting on day 6 and continued until day 36. FTY720 was administered starting concurrently with αCD4 and continued every other day until one week after final α4-1BB-LAIR dose. "Delayed" FTY720 was administered starting concurrently with α4-1BB-LAIR and continued every other day until one week after final α4-1BB-LAIR dose. αCTLA-4 was given on days 6, 9, 13, 16, 20, 23, and 27.

During all tumor studies, mice were monitored continuously for tumor growth and weight change. Tumor growth was assessed by direct measurement with calipers and mice were euthanized when their tumor area (length × width) reached 100 mm^2 or mice lost more than 20% of their body weight. Mice that were cured of their primary tumor but later euthanized due to overgrooming related dermatitis were still classified as complete responders and included in analysis.

For rechallenge studies, mice that rejected their primary tumors were inoculated with 1 x 10^5 B16F10 tumor cells on the left, or contralateral, flank 100-110 days after primary tumor inoculation and monitored for tumor outgrowth. Age matched naïve mice were used as controls in these studies.

IVIS

Proteins were labeled with Alexa Fluor 647 NHS Ester (Life Technologies) and a Zeba desalting column (Thermo Scientific) was used to remove excess dye. Total molar amount of dye injected per sample was normalized between groups before injection. 20 μg of αFITC mIgG2c LALA-PG and a molar equivalent of αFITC-LAIR mIgG2c LALA-PG were used for *in vivo* retention studies. B6 albino

mice were inoculated with 10^6 B16F10-Trp2 KO cells and labeled proteins were injected i.t. on day 7. Fluorescence at the site of the tumor was measured longitudinally using the IVIS Spectrum Imaging System (Perkin Elmer). One week prior to study initiation, mice were switched to an alfalfa-free casein chow (Test Diet) to reduce background fluorescence. Total radiant efficiency was calculated after subtracting background fluorescence and normalizing to the maximum value for each protein using Living Image software (Caliper Life Sciences).

Tumor Cytokine/Chemokine Analysis

Tumors were excised, weighed, mechanically dissociated, and incubated in tissue protein extraction reagent (T-PER, Thermo Fisher Scientific) with 1% Halt protease and phosphatase inhibitors (Thermo Fisher Scientific) for 30 minutes at 4°C while rotating. The lysates were then centrifuged and supernatants filtered through a Costar 0.22 μm SpinX filter (Corning) to remove any remaining debris. Lysates were flash frozen and stored at -20°C until time of analysis. Lysates were analyzed with the 13-plex mouse cytokine release syndrome LEGENDplex panel and the Mouse/Rat Total/Active TGF-β1 LEGENDplex kit (Biolegend). Data was collected on a BD LSR II cytometer (BD Biosciences).

Flow Cytometry

Tumors were excised, weighed, and mechanically dissociated before being enzymatically digested using a gentleMACS Octo Dissociator with Heaters (Miltenyi Biotec) in gentleMACS C tubes (Miltenyi Biotec) and enzymes from the Mouse Tumor Dissociation Kit (Miltenyi Biotec). Tumors were digested using the 37C_m_TDK_1 program for soft tumors. Following digestion, tumors were filtered through a 40 μm filter and transferred to a V-bottom 96 well plate for staining. TdLN and

spleens were excised, weighed, and mechanically dissociated through a 70 μm filter. Spleen samples were resuspended with 5 mL of ACK Lysis buffer (Gibco) to lyse red blood cells before being re-filtered through a 70 μm filter. TdLN and spleen samples were then transferred to a V-bottom 96 well plate for staining. Blood samples were collected via cardiac puncture into K3 EDTA coated tubes (MiniCollect). 200 μL of blood was mixed with 1 mL of ACK lysis buffer (Gibco) to lyse red blood cells before being transferred to a V-bottom 96 well plate for staining. Precision Counting Beads (Biolegend) were added to each well to account for sample loss during processing and obtain accurate counts. Cells were washed once with PBS and then resuspended in Zombie UV Fixable Viability Dye (Biolegend) to stain dead cells for 30 minutes at RT in the dark. Cells were then washed with FACS buffer (PBS (Corning) + 0.1% BSA (Sigma Aldrich) + 2mM EDTA (Gibco)) and blocked with αCD16/CD32 antibody (Clone 93, eBioscience) for 20 minutes on ice in the dark and then stained for extracellular markers for 30 minutes on ice in the dark. Samples not requiring intracellular staining were washed with FACS buffer and fixed with BD Cytofix (BD Biosciences) for 30 minutes at RT in the dark. Cells were then washed and resuspended in FACS buffer. For samples requiring intracellular staining, cells were washed after extracellular staining, fixed and permeabilized with the Foxp3/Transcription Factor Staining Buffer Set (eBiosciences), and stained for 30 minutes at RT in the dark, before being washed and resuspended in FACS buffer. Samples were analyzed with a BD FACS Symphony A3 (BD Biosciences), and data was processed and analyzed with FlowJo V10. See Fig. 4-16 for example gates.

Tumor and TdLN samples in Fig. 4-3, 4-4, 4-5, 4-6, and 4-7 were stained with αCD45-BUV395 (30-F11, BD Biosciences), αCD4-BUV563 (RM4-4, BD Biosciences), αCD8α-BUV737 (53-6.7 BD Biosciences), αCD62L-BUV805 (MEL-14, BD Biosciences), αCD44-BV421 (1M7, Biolegend),

αKi67-BV605 (16A8, Biolegend), αCD3-BV711 (17A2, Biolegend), αTIM-3-BV785 (RMT3-23, Biolegend), αTCF1/TCF7-AF488 (C63D9, Cell Signaling Technology), αPD-1-PerCp/Cy5.5 (29F.1A12, Biolegend), αFoxp3-PE (FJK-16s, Invitrogen), αCD25-PE-Cy5 (PC61, Biolegend), αNK1.1-PE-Cy7 (PK126, Biolegend), α4-1BB-APC (17B5, Biolegend), αCD107a-APC-Cy7 (1D4B, Biolegend).

Tumor, TdLN, and spleen samples in Fig. 4-12 were stained with αCD45-BUV395 (30F-11, BD Bioscience), αCD8a-BUV737 (53-6.7, BD Biosciences), αCD3-BV785 (17A2, Biolegend), αNK1.1-PE-Cy7 (PK-136, Biolegend), αCD4-APC-Cy7 (GK1.5, Biolegend), and Foxp3$^+$ cells were identified using the GFP reporter expressed under the *Foxp3* locus in Foxp3-DTR mice.

Tumor, TdLN and blood samples in Fig. 4-13 and 4-14 were stained with αCD45-BUV395 (30-F11, BD Biosciences), αCD4-BUV563 (RM4-4, BD Biosciences), αCD44-BUV737 (1M7 BD Biosciences), αKi67-BV421 (16A8, Biolegend), αCD3-BV711 (17A2, Biolegend), αCD8a-FITC (53-6.7, Biolegend) αFoxp3-PE (FJK-16s, Invitrogen), αCD25-PE-Cy5 (PC61, Biolegend), αNK1.1-PE-Cy7 (PK126, Biolegend), αCD62L-APC (MEL-14, Biolegend), αCD107a-APC-Cy7 (1D4B, Biolegend).

RNA extraction for Sequencing

Tumor samples were processed as previously described. Samples were enriched for CD45$^+$ cells using an EasySep Mouse TIL (CD45) Positive Selection kit (STEMCELL) and RNA was extracted with an RNeasy Plus Mini Kit (Qiagen). TdLN samples were processed as previously described. Samples were again enriched for CD45$^+$ cells using an EasySep Mouse CD45 Positive Selection kit (STEMCELL)

and RNA was extracted with an RNeasy Plus Mini Kit (Qiagen). RNA was stored at -80°C until further processing.

RNA-seq Library Preparation and Sequencing

RNA-sequencing was performed by the BioMicro Center at MIT using a modified version of the SCRB-seq protocol (244). Libraries were sequenced on a NextSeq 500 using a 75-cycle kit.

RNA-seq Alignment, Quantification, and Quality Control

Data preprocessing and count matrix construction were performed using the Smart-seq2 Multi-Sample v2.2.0 Pipeline (RRID:SCR_018920) on Terra. For each cell in the batch, single-end FASTQ files were first processed with the Smart-seq2 Single Sample v5.1.1 Pipeline (RRID:SCR_021228). Reads were aligned to the GENCODE mouse (M21) reference genome using HISAT2 v2.1.0 with default parameters in addition to --k 10 options. Metrics were collected and duplicate reads marked using the Picard v.2.10.10 CollectMultipleMetrics and CollectRnaSeqMetrics, and MarkDuplicates functions with validation_stringency=silent. For transcriptome quantification, reads were aligned to the GENCODE transcriptome using HISAT2 v2.1.0 with --k 10 --no-mixed --no-softclip --no-discordant --rdg 99999999,99999999 --rfg 99999999,99999999 --no-spliced-alignment options. Gene expression was calculated using RSEM v1.3.0's rsem-calculate-expression --calc-pme --single-cell-prior. QC metrics, RSEM TPMs and RSEM estimated counts were exported to a single Loom file for each sample. All individual Loom files for the entire batch were aggregated into a single Loom file for downstream processing. The final output included the unfiltered Loom and the tagged, unfiltered individual BAM files. Sequencing data can be found in the GEO database under accession GSE223087.

RNA-Seq Analysis

Samples with less than 10,000 genes detected were excluded from analysis. This led to exclusion of two tumor samples, one from the Tx + αCD4 group and one from the αCD4 group at the day 6 time point (Fig. 4-17). UMAP embedding of TdLN samples was generated from the top 5 principal components and top 3000 variable features. *DEseq2* was used to conduct differential expression testing and *apeglm* was used for effect size estimation (245, 246). Pathways enrichment analysis for statistically significant upregulated genes was performed using *enrichR* to query the databases indicated in the text (219–221). A score for the derived response gene signature was calculated for each experimental cohort using Seurat (*AddModuleScore*) (247). Differential expression testing was performed as described above comparing all tumor sample cohorts to the D3 PBS, D6 PBS, D3 Tx + aCD4, and D6 Tx + aCD4 cohorts. All statistically significant hits (*p*-adj ≦5 with absolute value log2 fold-change ≥ 2 were included for further analysis. Gene clusters were defined using k-means clustering and the *complexHeatmap* package was used to generate expression heatmaps for these genes (248). Relative expression profiles of these gene clusters were generated by summarizing the percent expression using Seurat (*PercentageFeatureSet*) per sample and dividing by the highest average percent per condition (247). Gene sets were obtained from MSigDB and enrichment of genes from each cluster in these gene sets was calculated using the *enrichGO* package (249).

Statistical Methods

Statistics were computed in GraphPad Prism v9 as indicated in figure captions. Survival studies were compared using the log-rank (Mantel-Cox) test. Flow data and tumor supernatant cytokine/chemokine data were compared using one- or two-way ANOVA with Tukey's multiple comparison correction. Differential expression analysis using DESeq2 models counts for each gene using a negative binomial model and tests for significance using Wald tests (246). Gene set enrichment

is calculated by the Fisher's exact test. *P* values are corrected for multiple hypothesis testing using the Benjamini-Hochberg procedure for all RNA-sequencing analysis. Sample size and *P*-value cutoffs are indicated in figure captions.

Acknowledgements

We thank the Koch Institute's Robert A. Swanson (1969) Biotechnology Center (National Cancer Institute Grant P30-CA14051) for technical support, specifically the Flow Cytometry Core Facility and the BioMicro Center. We thank the Spranger lab for the gift of the Foxp3-DTR breeding pair. We thank the Protein Production and Structure Core Facility at the École polytechnique fédérale de Lausanne for the development of the 9D9 stable line. Figures partially created with biorender.com.

Chapter 5: Conclusions and Future Outlooks

This thesis details our effort to develop collagen anchored agonist antibodies for cancer immunotherapy applications. Although agonist antibodies are highly effective antitumor therapeutics in preclinical mouse models, their translation into humans has been hampered by on-target, off-tumor toxicities. In this thesis, we leveraged a collagen anchoring strategy to restrict the activity of agonist antibodies to the tumor microenvironment (TME). In chapter two, we attempted to develop a generalizable platform for collagen anchoring of agonist antibodies by fusing several IgG binding domains (IgGBs) to lumican, a collagen binding protein. Although we saw indirect evidence that these IgGB-lumican fusions were retained in the TME, they did a poor job of retaining pre-loaded IgG, presumably due to rapid exchange *in vivo* with endogenous IgG. Without extensive protein engineering efforts to improve the affinity of our IgGBs, this strategy did not appear to be a viable route for tumor localization of agonist antibodies. Despite the potential utility of a generalizable platform for retention of any agonist antibody off-the-shelf allowing rapid screening of a wide array of antibodies, we instead chose to focus our efforts on engineering direct fusions of agonist antibodies to collagen binding domains.

Chapter three contains our studies developing and testing direct agonist antibody fusions to collagen binding domains. We saw that this was a widely applicable strategy to several different antibodies and collagen binding domains but focused our *in vivo* efficacy studies on αCD137-LAIR and αCD28-LAIR. We demonstrated via longitudinal fluorescence imaging that control (αFITC) IgG-LAIR fusions were retained in the TME over free IgG. Unfortunately, we did not see uniform increases in efficacy or decreases in toxicity with our collagen anchored agonists (In fact, in the context of collagen anchored

αCD28-LAIR we consistently saw preclinically activity *only* in the non-collagen anchored format, suggesting that perhaps collagen localization spatially separates αCD28-LAIR from cells poised to respond to CD28 signaling). The lack of toxicity improvement stems from a lack of toxicity seen even with our non-collagen anchored agonists. However, because we know that toxicities are driven by on-target, off-tumor activity and we have demonstrated enhanced tumor retention (and thus decreased systemic dissemination) of our agonists, we are confident that this strategy would result in an improved safety profile. In this chapter, we identified one combination where we found a modest but consistent improvement in efficacy driven by collagen anchoring. Specifically, we found that in B16F10 melanoma bearing mice treatment with antitumor antibody TA99 + α4-1BB-LAIR resulted in improved survival over TA99 + α4-1BB treatment.

In chapter four, we further explored this combination therapy. We observed that when we depleted the entire $CD4^+$ compartment using an αCD4 antibody, we were able to cure over 90% of mice of their primary tumor. However, these mice failed to form immunological memory, with nearly all of the survivors succumbing to tumor rechallenge. We then set out to understand: 1) what was the immunological mechanism driving this synergy? and 2) could we identify more clinically relevant agents to replace αCD4 to achieve the same primary tumor efficacy while also rescuing the memory defect? We determined that the primary effect of αCD4 treatment is depletion of Tregs, and importantly TdLN Tregs, which allows for *de novo* priming of $CD8^+$ T cells. This new wave of primed T cells then enters the tumor where TA99 + local α4-1BB-LAIR supports these T cells and maintains their cytotoxic program, eventually leading to tumor regression. As the primary effect of αCD4 was to drive enhanced $CD8^+$ T cell priming, we instead treated mice with TA99 + α4-1BB-LAIR + αCTLA-4, as αCTLA-4 is known to improve $CD8^+$ T cell priming (227). Indeed, we observed that

this combination is also highly efficacious and, likely because $CD4^+$ T cells were spared in this combination, all of these mice formed robust immunological memory and rejected tumor rechallenge. This result is particularly encouraging, as antitumor antibodies and αCTLA-4 therapy are both clinically approved and many localized α4-1BB agonists are undergoing clinical testing, meaning this triple combination could feasibly be explored in the clinic with existing agents. Overall, we think this work identifies a generalizable two-step approach to designing combination immunotherapies. Specifically, efficacious therapies should seek to: 1) Increase $CD8^+$ T cell priming through nodal Treg depletion/inhibition and 2) support newly primed $CD8^+$ T cells through local, tumor restricted agonism (ex. α4-1BB-LAIR, in our work).

In addition to the work presented in this thesis we also used yeast surface display in an effort to engineer both higher and lower affinity LAIR binders to study the relationship between affinity and retention/efficacy (in collaboration with Dr. Noor Momin). Previous publications contain specifics of this project (92, 103). To summarize here, we displayed murine LAIR on the surface of yeast using standard yeast display methods developed in our lab (250). Using error prone PCR, we developed libraries of mutant LAIR and isolated weakened affinity and "dead" no binding mutants using an equilibrium sort strategy and isolated higher affinity mutants using a kinetic sort strategy. Although we were eventually able to successfully engineer weakened affinity and dead LAIR mutants, we were unable to isolate high affinity binders. This was largely due to poor antigen quality. Collagen is not soluble, and thus for biochemical and structural studies many different soluble collagen related peptides (CRPs), or collagen mimics, have been developed (90). For our studies, we utilized peptide consisting of 10 glycine-proline-hydroxyproline repeats, which represents the most frequent triplet repeat of collagen (251). However, we found that binding characteristics to this "stripped down"

collagen mimic did not always match binding of our recombinantly expressed LAIR mutants to collagen coated plates. Indeed, our initial "dead" mutants had no binding to our CRP antigen but still displayed residual binding to collagen I coated plates, and our higher affinity mutants displayed tighter binding to CRP but in fact displayed *weaker* binding to collagen I coated plates. Thus, this protein engineering campaign highlighted the importance of having a high-quality antigen.

Future work

As with all good scientific endeavors, we are often left with more questions than answers. In this section, we try to summarize major outstanding questions with our work and unexplored areas. Although we propose that chapter 4 represents a generalizable framework for designing combination immunotherapies, this hypothesis could use additional pressure testing. We explored three different ways to improve $CD8^+$ T cell priming (whole $CD4^+$ T cell depletion, Treg specific depletion, and treatment with αCTLA-4 therapy). Certainly, there are other clinically relevant agents we could have explored to improve priming including radiation, certain immunogenic chemotherapies, cancer vaccines, adoptive cell therapy, and a host of myeloid directed therapies. Perhaps more importantly, our story was exclusively focused on combinations with α4-1BB, and in future work it would be interesting to see if other costimulatory pathways, such as CD28, OX40, GITR, ICOS, CD27, or even cytokine therapies such as IL-12 also synergize robustly with priming enhancing therapies (such as αCD4 used in our study). Mechanistically, perhaps the largest open question is whether the αCD4 therapy employed in our study solely enhanced the number of $CD8^+$ T cells entering the tumor or if it also induced meaningful phenotypic changes. Put differently, will any strategy to boost $CD8^+$ T cell counts synergize with local agonism (again in our specific example local agonism being TA99 + α4-1BB-LAIR), or were the newly primed T cells phenotypically better poised to respond to this local

agonism? Bulk RNA-sequencing of isolated $CD8^+$ T cells (comparing TILs that enter after αCD4 therapy vs. those there at baseline) or single cell sequencing of $CD45^+$ tumor cells would be a logical next step to get at this question.

As mentioned in the introduction, different ECM proteins and collagen isoforms can have vastly different expression levels and spatial distributions within a given tumor (and these can also vary from tumor to tumor). In our work here (and previous work led by Dr. Noor Momin), we did not explore these more granular differences. However, the existence of these differing spatial distributions opens up the possibility of targeting specific payloads to different parts of the tumor (and thus different immunological niches, as immune cell infiltrates are also not spatially uniform within a tumor). This is an active area of research in our group and preliminary data suggests that even targeting different isoforms of collagen in the case of collagen anchored cytokines can result in a meaningfully different toxicity profile, albeit efficacy is unchanged (unpublished ongoing studies lead by A. Sheen and L. Fink).

As discussed in the introduction, agonist antibodies often rely on FcγR mediated cross-linking to achieve sufficient targeting receptor clustering to drive signaling. One intriguing feature of our approach is the possibility for collagen-mediated crosslinking. If the collagen anchored agonists can pack to a sufficient density on collagen fibrils, then this may be sufficient to drive receptor clustering and signaling (the alternative hypothesis is that collagen anchoring purely provides increased residence time and FcγR mediated cross-linking is still necessary for proper agonism and therapeutic outcomes). Although we did not explore this, testing collagen anchored agonists with "silent" Fc regions that are unable to interact with FcγRs would allow us to probe this question. If collagen-mediated clustering

(without any FcγR mediated contributions) is possible, this could vastly improve the safety profile of these agonist antibodies. By using a silent Fc, any drug that is not bound to collagen (such as any quantity that leaks out over time into systemic circulation) would be functionally inert. Indeed, our pilot αCD3-LAIR/αCD28-LAIR *in vitro* T cell stimulation assays performed on collagen plates suggest that this may be possible (Fig. 3-14). Many bispecific antibodies targeting co-stimulatory receptors and tumor specific antigens in clinical development also contain silent Fc regions, suggesting that in this context FcγR independent signaling is possible. Thus, although we did not explore the contributions of FcγR mediated clustering for the efficacy of our therapies, from a translational perspective this would be an important and interesting line of questioning to pursue to further improve the safety of these therapeutics.

Overall, this thesis contributes to the growing body of literature on tumor localized agonist antibodies for cancer immunotherapy as well as additionally providing immunological guidelines for successful design of agonist antibody containing combination immunotherapies.

References

1. M. Roser, H. Ritchie, Cancer (2015), (available at https://ourworldindata.org/cancer).

2. S. A. H. Cann, J. P. van Netten, C. van Netten, D. W. Glover, Spontaneous regression: a hidden treasure buried in time. *Med Hypotheses.* **58**, 115–119 (2002).

3. P. Dobosz, T. Dzieciątkowski, The Intriguing History of Cancer Immunotherapy. *Front Immunol.* **10**, 2965 (2019).

4. W. B. Coley, Contribution to the Knowledge of Sarcoma. *Ann Surg.* **14**, 199–220 (1891).

5. E. F. McCarthy, The toxins of William B. Coley and the treatment of bone and soft-tissue sarcomas. *Iowa Orthop J*. **26**, 154–8 (2006).

6. R. L. Steinberg, L. J. Thomas, M. A. O'Donnell, Bacillus Calmette-Guérin (BCG) Treatment Failures in Non-Muscle Invasive *Bladder Cancer*: What Truly Constitutes Unresponsive Disease. *Bladder Cancer*. **1**, 105–116 (2015).

7. S. A. Rosenberg, IL-2: The First Effective Immunotherapy for Human Cancer. *J Immunol*. **192**, 5451–5458 (2014).

8. L. M. Pfeffer, C. A. Dinarello, R. B. Herberman, B. R. Williams, E. C. Borden, R. Bordens, M. R. Walter, T. L. Nagabhushan, P. P. Trotta, S. Pestka, Biological properties of recombinant alpha-interferons: 40th anniversary of the discovery of interferons. *Cancer Res*. **58**, 2489–99 (1998).

9. H. F. Stephen, O. S. J., M. D. F., W. R. W., S. J. A., H. J. B., G. Rene, R. Caroline, S. Dirk, H. J. C., A. Wallace, van den E. A. J.M., L. Jose, L. Paul, V. J. M., L. G. P., H. David, O. C. H., L. Celeste, P. Christian, Q. Ian, C. J. I., W. J. D., W. J. S., T. Jason, Y. M. J., N. G. M., H. Axel, U. W. J., Improved Survival with Ipilimumab in Patients with Metastatic Melanoma. *New Engl J Med*. **363**, 711–723 (2010).

10. J. Couzin-Frankel, Cancer Immunotherapy. *Science*. **342**, 1432–1433 (2013).

11. C. J. Bashor, I. B. Hilton, H. Bandukwala, D. M. Smith, O. Veiseh, Engineering the next generation of cell-based therapeutics. *Nat Rev Drug Discov*. **21**, 655–675 (2022).

12. A. J. Korman, S. C. Garrett-Thomson, N. Lonberg, The foundations of immune checkpoint blockade and the ipilimumab approval decennial. *Nat Rev Drug Discov*. 21, 509–528 (2022).

13. J. X. Yu, V. M. Hubbard-Lucey, J. Tang, Immuno-oncology drug development goes global. *Nat Rev Drug Discov*. **18**, 899–900 (2019).

14. I. Mellman, G. Coukos, G. Dranoff, Cancer immunotherapy comes of age. *Nature*. **480**, 480–489 (2011).

15. I. Melero, S. Hervas-Stubbs, M. Glennie, D. M. Pardoll, L. Chen, Immunostimulatory monoclonal antibodies for cancer therapy. *Nat Rev Cancer*. **7**, 95–106 (2007).

16. P. A. Mayes, K. W. Hance, A. Hoos, The promise and challenges of immune agonist antibody development in cancer. *Nat Rev Drug Discov*. **17**, 509–527 (2018).

17. F. Nimmerjahn, S. Gordan, A. Lux, FcγR dependent mechanisms of cytotoxic, agonistic, and neutralizing antibody activities. *Trends Immunol*. **36**, 325–336 (2015).

18. F. Nimmerjahn, J. V. Ravetch, Antibodies, Fc receptors and cancer. *Curr Opin Immunol*. **19**, 239–245 (2007).

19. F. Nimmerjahn, J. V. Ravetch, Fcγ Receptors: Old Friends and New Family Members. *Immunity*. **24**, 19–28 (2006).

20. J. M. M. Caaveiro, M. Kiyoshi, K. Tsumoto, Structural analysis of Fc/FcγR complexes: a blueprint for antibody design. *Immunol Rev*. **268**, 201–221 (2015).

21. S. L. Buchan, L. Dou, M. Remer, S. G. Booth, S. N. Dunn, C. Lai, M. Semmrich, I. Teige, L. Mårtensson, C. A. Penfold, H. T. C. Chan, J. E. Willoughby, C. I. Mockridge, L. N. Dahal, K. L. S. Cleary, S. James, A. Rogel, P. Kannisto, M. Jernetz, E. L. Williams, E. Healy, J. S. Verbeek, P. W. M. Johnson, B. Frendéus, M. S. Cragg, M. J. Glennie, J. C. Gray, A. Al-Shamkhani, S. A. Beers, Antibodies to Costimulatory Receptor 4-1BB Enhance Anti-tumor Immunity via T Regulatory Cell Depletion and Promotion of CD8 T Cell Effector Function. *Immunity*. **49**, 958-970.e7 (2018).

22. A. L. White, H. T. C. Chan, A. Roghanian, R. R. French, C. I. Mockridge, A. L. Tutt, S. V. Dixon, D. Ajona, J. S. Verbeek, A. Al-Shamkhani, M. S. Cragg, S. A. Beers, M. J. Glennie, Interaction with FcγRIIB Is Critical for the Agonistic Activity of Anti-CD40 Monoclonal Antibody. *J Immunol*. **187**, 1754–1763 (2011).

23. F. Li, J. V. Ravetch, Inhibitory Fcγ Receptor Engagement Drives Adjuvant and Anti-Tumor Activities of Agonistic CD40 Antibodies. Science. **333**, 1030–1034 (2011).

24. R. Dahan, B. C. Barnhart, F. Li, A. P. Yamniuk, A. J. Korman, J. V. Ravetch, Therapeutic Activity of Agonistic, Human Anti-CD40 Monoclonal Antibodies Requires Selective FcγR Engagement. *Cancer Cell*. **29**, 820–831 (2016).

25. D. A. Knorr, R. Dahan, J. V. Ravetch, Toxicity of an Fc-engineered anti-CD40 antibody is abrogated by intratumoral injection and results in durable antitumor immunity. *Proc National Acad Sci*. **115**, 11048-11053 (2018).

26. T. Bartkowiak, A. R. Jaiswal, C. R. Ager, R. Chin, C.-H. Chen, P. Budhani, M. Ai, M. J. Reilley, M. M. Sebastian, D. S. Hong, M. A. Curran, Activation of 4-1BB on Liver Myeloid Cells Triggers Hepatitis via an Interleukin-27 dependent Pathway. *Clin Cancer Res*. **24**, 1138-1151 (2018)

27. J. H. Esensten, Y. A. Helou, G. Chopra, A. Weiss, J. A. Bluestone, CD28 Costimulation: From Mechanism to Therapy. *Immunity*. **44**, 973–988 (2016).

28. J. A. Gross, E. Callas, J. P. Allison, Identification and distribution of the costimulatory receptor CD28 in the mouse. *J Immunol.* **149**, 380–388 (1992).

29. A. V. Collins, D. W. Brodie, R. J. C. Gilbert, A. Iaboni, R. Manso-Sancho, B. Walse, D. I. Stuart, P. A. van der Merwe, S. J. Davis, The Interaction Properties of Costimulatory Molecules Revisited. *Immunity*. **17**, 201–210 (2002).

30. T. Pentcheva-Hoang, J. G. Egen, K. Wojnoonski, J. P. Allison, B7-1 and B7-2 Selectively Recruit CTLA-4 and CD28 to the Immunological Synapse. *Immunity*. **21**, 401–413 (2004).

31. P. A. Bretscher, A two-step, two-signal model for the primary activation of precursor helper T cells. *Proc National Acad Sci.* **96**, 185–190 (1999).

32. Y. Xing, K. A. Hogquist, T-Cell Tolerance: Central and Peripheral. *Csh Perspect Biol.* **4**, a006957 (2012).

33. P. Riha, C. E. Rudd, CD28 co-signaling in the adaptive immune response. *Self Nonself.* **1**, 231–240 (2010).

34. S. Townsend, J. Allison, Tumor rejection after direct costimulation of CD8+ T cells by B7-transfected melanoma cells. *Science*. **259**, 368–370 (1993).

35. X.-F. Bai, J. Bender, J. Liu, H. Zhang, Y. Wang, O. Li, P. Du, P. Zheng, Y. Liu, Local Costimulation Reinvigorates Tumor-Specific Cytolytic T Lymphocytes for Experimental Therapy in Mice with Large Tumor Burdens. *J Immunol.* **167**, 3936–3943 (2001).

36. S. Ganesh, P. M. R., W. Stephen, B. S. J., C.-C. Andrew, B. M. D., P. Nicki, Cytokine Storm in a Phase 1 Trial of the Anti-CD28 Monoclonal Antibody TGN1412. *New Engl J Med.* **355**, 1018–1028 (2006).

37. T. Hünig, The storm has cleared: lessons from the CD28 superagonist TGN1412 trial. *Nat Rev Immunol.* **12**, 317–318 (2012).

38. D. Skokos, J. C. Waite, L. Haber, A. Crawford, A. Hermann, E. Ullman, R. Slim, S. Godin, D. Ajithdoss, X. Ye, B. Wang, Q. Wu, I. Ramos, A. Pawashe, L. Canova, K. Vazzana, P. Ram, E. Herlihy, H. Ahmed, E. Oswald, J. Golubov, P. Poon, L. Havel, D. Chiu, M. Lazo, K. Provoncha, K. Yu, J. Kim, J. J. Warsaw, N. S. Oristian, C.-J. Siao, D. Dudgeon, T. Huang, T. Potocky, J. Martin, D. MacDonald, A. Oyejide, A. Rafique, W. Poueymirou, J. R. Kirshner, E. Smith, W. Olson, J. Lin, G. Thurston, M. A. Sleeman, A. J. Murphy, G. D. Yancopoulos, A class of costimulatory CD28-bispecific antibodies that enhance the antitumor activity of CD3-bispecific antibodies. *Sci Transl Med.* **12**, eaaw7888 (2020).

39. J. C. Waite, B. Wang, L. Haber, A. Hermann, E. Ullman, X. Ye, D. Dudgeon, R. Slim, D. K. Ajithdoss, S. J. Godin, I. Ramos, Q. Wu, E. Oswald, P. Poon, J. Golubov, D. Grote, J. Stella, A. Pawashe, J. Finney, E. Herlihy, H. Ahmed, V. Kamat, A. Dorvilliers, E. Navarro, J. Xiao, J. Kim, S. N. Yang, J. Warsaw, C. Lett, L. Canova, T. Schulenburg, R. Foster, P. Krueger, E. Garnova, A. Rafique, R. Babb, G. Chen, N. S. Oristian, C.-J. Siao, C. Daly, C. Gurer, J. Martin, L. Macdonald, D. MacDonald, W. Poueymirou, E. Smith, I. Lowy, G. Thurston, W. Olson, J. C. Lin, M. A. Sleeman, G. D. Yancopoulos, A. J. Murphy, D. Skokos, Tumor-targeted CD28 bispecific antibodies enhance the antitumor efficacy of PD-1 immunotherapy. *Sci Transl Med.* **12** (2020), doi:10.**11**26/scitranslmed.aba2325.

40. E. Seung, Z. Xing, L. Wu, E. Rao, V. Cortez-Retamozo, B. Ospina, L. Chen, C. Beil, Z. Song, B. Zhang, M. Levit, G. Deng, A. Hebert, P. Kirby, A. Li, E.-J. Poulton, R. Vicente, A. Garrigou, P. Piepenhagen, G. Ulinski, M. Sanicola-Nadel, D. S. Bangari, H. Qiu, L. Pao, D. Wiederschain, R. Wei, Z. Yang, G. J. Nabel, A trispecific antibody targeting HER2 and T cells inhibits breast cancer growth via CD4 cells. *Nature.* **603**, 328–334 (2022).

41. J. Wei, W. Montalvo-Ortiz, L. Yu, A. Krasco, K. Olson, S. Rizvi, N. Fiaschi, S. Coetzee, F. Wang, E. Ullman, H. S. Ahmed, E. Herlihy, K. Lee, L. Havel, T. Potocky, S. Ebstein, D. Frleta, A. Khatri, S. Godin, S. Hamon, J. Brouwer-Visser, T. Gorenc, D. MacDonald, A. Hermann, A. Chaudhry, A. Sirulnik, W. Olson, J. Lin, G. Thurston, I. Lowy, A. J. Murphy, E. Smith, V. Jankovic, M. A. Sleeman, D. Skokos, CD22-targeted CD28 bispecific antibody enhances antitumor efficacy of odronextamab in refractory diffuse large B cell lymphoma models. *Sci Transl Med.* **14**, eabn1082 (2022).

42. V. Zeng, G. Moore, J. Diaz, C. Bonzon, K. Avery, R. Love, M. Dragovich, R. Rashid, I. Leung, M. Hackett, J. Qi, C. Bakhit, U. Muchhal, N. Barlow, J. Desjarlais, M. Hedvat, PD-L1 targeted CD28 costimulatory bispecific antibodies enhance T cell activation in solid tumors. *J Immunother Cancer.* **9**, A726–A726 (2021).

43. M. Johnson, N. Lakhani, E. Girda, A. Olszanski, L. Fong, H. Han, K. Casey, S. Li, J. Visich, D. Skokos, F. Seebach, I. Lowy, M. Fury, M. Mathias, N. Segal, A phase 1/2 study of REGN7075 (EGFRxCD28 costimulatory bispecific antibody) in combination with cemiplimab (anti–PD-1) in patients with advanced solid tumors: initial dose-escalation results. *J Immunother Cancer.* **10**, A767–A768 (2022).

44. I. S. Winer, A. F. Shields, O. O. Yeku, J. F. Liu, M. J. Peterman, S. Y. Yoo, I. Lowy, N. A. Yama-Dang, P. H. Goncalves, G. Kroog, A phase I/II, multicenter, open-label study of REGN5668 (mucin [MUC]16 x CD28 bispecific antibody [bsAb]) with cemiplimab (programmed death [PD]-1 Ab) or REGN4018 (MUC16 x CD3 bsAb) in recurrent ovarian cancer (rOVCA). *Journal of Clinical Oncology.* **39**, TPS5602 (2021).

45. J. Zhang, M. N. Stein, W. K. Kelly, C.-K. Tsao, G. S. Falchook, Y. Xu, F. A. Seebach, I. Lowy, K. K. Mohan, G. Kroog, E. Miller, A phase I/II study of REGN5678 (Anti-PSMAxCD28, a costimulatory bispecific antibody) with cemiplimab (anti–PD-1) in patients with metastatic castration-resistant prostate cancer. *Journal of Clinical Oncology.* **39**, TPS174 (2021).

46. J. C. Moser, M. Voskoboynik, N. J. Lakhani, M. Millward, D. Davar, W. A. Harb, J. Yang, G. Means, K. Manjarrez, A. Tercero, H. Zayed, J. Hillson, C. D. Cruz, G. N. Perez, S. L. Peng, First-in-human dose escalation of ALPN-202, a conditional CD28 costimulator and dual checkpoint inhibitor, in advanced malignancies. *Journal of Clinical Oncology*. **39**, 2547 (2021).

47. M. F. Maurer, K. E. Lewis, J. L. Kuijper, D. Ardourel, C. J. Gudgeon, S. Chandrasekaran, S. L. Mudri, K. N. Kleist, C. Navas, M. F. Wolfson, M. W. Rixon, R. Swanson, S. R. Dillon, S. D. Levin, Y. R. Kimbung, M. Akutsu, D. T. Logan, B. Walse, K. M. Swiderek, S. L. Peng, The engineered CD80 variant fusion therapeutic davoceticept combines checkpoint antagonism with conditional CD28 costimulation for anti-tumor immunity. *Nat Commun*. **13**, 1790 (2022).

48. D. S. Vinay, B. S. Kwon, Role of 4-1BB in immune responses. *Semin Immunol*. **10**, 481–489 (1998).

49. D. S. Vinay, B. S. Kwon, 4-1BB signaling beyond T cells. *Cell Mol Immunol*. **8**, 281–284 (2011).

50. D. Drenkard, F. M. Becke, J. Langstein, T. Spruss, L. A. Kunz-Schughart, T. E. Tan, Y. C. Lim, H. Schwarz, CD137 is expressed on blood vessel walls at sites of inflammation and enhances monocyte migratory activity. *Faseb J*. **21**, 456–463 (2007).

51. Á. Teijeira, A. Palazón, S. Garasa, D. Marré, C. Aubá, A. Rogel, O. Murillo, I. Martínez-Forero, F. Lang, I. Melero, A. Rouzaut, CD137 on inflamed lymphatic endothelial cells enhances CCL21-guided migration of dendritic cells. *Faseb J*. **26**, 3380–3392 (2012).

52. K. E. Pollok, Y. J. Kim, Z. Zhou, J. Hurtado, K. K. Kim, R. T. Pickard, B. S. Kwon, Inducible T cell antigen 4-1BB. Analysis of expression and function. *J Immunol*. **150**, 771–781 (1993).

53. R. N. Gilbreth, V. Y. Oganesyan, H. Amdouni, S. Novarra, L. Grinberg, A. Barnes, M. Baca, Crystal structure of the human 4-1BB/4-1BBL complex. *J Biol Chem*. **293**, 9880–9891 (2018).

54. E.-Y. Won, K. Cha, J.-S. Byun, D.-U. Kim, S. Shin, B. Ahn, Y. H. Kim, A. J. Rice, T. Walz, B. S. Kwon, H.-S. Cho, The *Structure* of the Trimer of Human 4-1BB Ligand Is Unique among Members of the Tumor Necrosis Factor Superfamily. *J Biol Chem*. **285**, 9202–9210 (2010).

55. J. M. Zapata, G. Perez-Chacon, P. Carr-Baena, I. Martinez-Forero, A. Azpilikueta, I. Otano, I. Melero, CD1**3**7 (4-1BB) Signalosome: Complexity Is a Matter of TRAFs. *Front Immunol*. **9**, 2618 (2018).

56. A. R. Sanchez-Paulete, S. Labiano, M. E. Rodriguez-Ruiz, A. Azpilikueta, I. Etxeberria, E. Bolaños, V. Lang, M. Rodriguez, M. A. Aznar, M. Jure-Kunkel, I. Melero, Deciphering CD137 (4-1BB) signaling in T-cell costimulation for translation into successful cancer immunotherapy. *Eur J Immunol*. **46**, 513–522 (2016).

57. Y. Kim, S. H. Kim, P. Mantel, B. S. Kwon, Human 4-1BB regulates CD28 co-stimulation to promote Th1 cell responses. *Eur J Immunol*. **28**, 881–890 (1998).

58. H.-W. Lee, S.-J. Park, B. K. Choi, H. H. Kim, K.-O. Nam, B. S. Kwon, 4-1BB Promotes the Survival of CD8+ T Lymphocytes by Increasing Expression of Bcl-xL and Bfl-1. *J Immunol.* **169**, 4882–4888 (2002).

59. B. K. Choi, D. Y. Lee, D. G. Lee, Y. H. Kim, S.-H. Kim, H. S. Oh, C. Han, B. S. Kwon, 4-1BB signaling activates glucose and fatty acid metabolism to enhance CD8+ T cell proliferation. *Cell Mol Immunol.* **14**, 748–757 (2017).

60. H. S. Oh, B. K. Choi, Y. H. Kim, D. G. Lee, S. Hwang, M. J. Lee, S. H. Park, Y.-S. Bae, B. S. Kwon, 4-1BB Signaling Enhances Primary and Secondary Population Expansion of CD8+ T Cells by Maximizing Autocrine IL-2/IL-2 Receptor Signaling. *Plos One.* **10**, e0126765 (2015).

61. I. Melero, J. V. Johnston, W. W. Shufford, R. S. Mittler, L. Chen, NK1.1 Cells Express 4-1BB (CDw137) Costimulatory Molecule and Are Required for Tumor Immunity Elicited by Anti-4-1BB Monoclonal Antibodies. *Cell Immunol.* **190**, 167–172 (1998).

62. C. Chester, S. Ambulkar, H. E. Kohrt, 4-1BB agonism: adding the accelerator to cancer immunotherapy. *Cancer Immunol Immunother.* **65**, 1243–1248 (2016).

63. C. Chester, M. F. Sanmamed, J. Wang, I. Melero, Immunotherapy targeting 4-1BB: mechanistic rationale, clinical results, and future strategies. *Blood.* **131**, 49–57 (2018).

64. R. A. Wilcox, K. Tamada, S. E. Strome, L. Chen, Signaling Through NK Cell-Associated CD137 Promotes Both Helper Function for CD8+ Cytolytic T Cells and Responsiveness to IL-2 But Not Cytolytic Activity. *J Immunol.* **169**, 4230–4236 (2002).

65. I. Melero, W. W. Shuford, S. A. Newby, A. Aruffo, J. A. Ledbetter, K. E. Hellström, R. S. Mittler, L. Chen, Monoclonal antibodies against the 4-1BB T-cell activation molecule eradicate established tumors. *Nat Med.* **3**, 682–685 (1997).

66. I. Melero, M. F. Sanmamed, J. Glez-Vaz, C. Luri-Rey, J. Wang, L. Chen, CD137 (4-1BB)-Based Cancer Immunotherapy on Its 25th Anniversary. *Cancer Discov*, **13**, 552-569 (2022).

67. N. H. Segal, T. F. Logan, F. S. Hodi, D. McDermott, I. Melero, O. Hamid, H. Schmidt, C. Robert, V. Chiarion-Sileni, P. A. Ascierto, M. Maio, W. J. Urba, T. C. Gangadhar, S. Suryawanshi, J. Neely, M. Jure-Kunkel, S. Krishnan, H. Kohrt, M. Sznol, R. Levy, Results from an Integrated Safety Analysis of Urelumab, an Agonist Anti-CD137 Monoclonal Antibody. *Clin Cancer Res.* **23**, 1929–1936 (2017).

68. S. M. Chin, C. R. Kimberlin, Z. Roe-Zurz, P. Zhang, A. Xu, S. Liao-Chan, D. Sen, A. R. Nager, N. S. Oakdale, C. Brown, F. Wang, Y. Yang, K. Lindquist, Y. A. Yeung, S. Salek-Ardakani, J. Chaparro-Riggers, Structure of the 4-1BB/4-1BBL complex and distinct binding and functional properties of utomilumab and urelumab. *Nat Commun.* **9**, 4679 (2018).

69. N. H. Segal, A. R. He, T. Doi, R. Levy, S. Bhatia, M. J. Pishvaian, R. Cesari, Y. Chen, C. B. Davis, B. Huang, A. D. Thall, A. K. Gopal, Phase I Study of Single-Agent Utomilumab (PF-05082566), a 4-1BB/CD137 Agonist, in Patients with Advanced Cancer. *Clin Cancer Res.* **24**, 1816–1823 (2018).

70. C. Claus, C. Ferrara-Koller, C. Klein, The emerging landscape of novel 4-1BB (CD137) agonistic drugs for cancer immunotherapy. *Mabs.* **15**, 2167189 (2023).

71. I. Etxeberria, E. Bolaños, A. Teijeira, S. Garasa, A. Yanguas, A. Azpilikueta, W. M. Kavanaugh, O. Vasiljeva, M. Belvin, B. Howng, B. Irving, K. Tipton, J. West, L. Mei, A. J. Korman, E. Sega, I. Olivera, A. Cirella, M. C. Ochoa, M. E. Rodriguez, A. Melero, M. F. Sanmamed, J. J. Engelhardt, I. Melero, Antitumor efficacy and reduced toxicity using an anti-CD137 Probody therapeutic. *Proc National Acad Sci.* **118**, e2025930118 (2021).

72. M. J. Hinner, R. S. B. Aiba, T. J. Jaquin, S. Berger, M. C. Dürr, C. Schlosser, A. Allersdorfer, A. Wiedenmann, G. Matschiner, J. Schüler, U. Moebius, C. Rothe, L. Matis, S. A. Olwill, Tumor-Localized Costimulatory T-Cell Engagement by the 4-1BB/HER2 Bispecific Antibody-Anticalin Fusion PRS-343. *Clin Cancer Res.* **25**, 5878–5889 (2019).

73. C. Claus, C. Ferrara, W. Xu, J. Sam, S. Lang, F. Uhlenbrock, R. Albrecht, S. Herter, R. Schlenker, T. Hüsser, S. Diggelmann, J. Challier, E. Mössner, R. J. Hosse, T. Hofer, P. Brünker, C. Joseph, J. Benz, P. Ringler, H. Stahlberg, M. Lauer, M. Perro, S. Chen, C. Küttel, P. L. B. Mohan, V. Nicolini, M. C. Birk, A. Ongaro, C. Prince, R. Gianotti, G. Dugan, C. T. Whitlow, K. K. S. Sai, D. L. Caudell, A. G. Burgos-Rodriguez, J. M. Cline, M. Hettich, M. Ceppi, A. M. Giusti, F. Crameri, W. Driessen, P. N. Morcos, A. Freimoser-Grundschober, V. Levitsky, M. Amann, S. Grau-Richards, T. von Hirschheydt, S. Tournaviti, M. Mølhøj, T. Fauti, V. Heinzelmann-Schwarz, V. Teichgräber, S. Colombetti, M. Bacac, A. Zippelius, C. Klein, P. Umaña, Tumor-targeted 4-1BB agonists for combination with T cell bispecific antibodies as off-the-shelf therapy. *Sci Transl Med.* **11**, eaav5989 (2019).

74. M. Kamata-Sakurai, Y. Narita, Y. Hori, T. Nemoto, R. Uchikawa, M. Honda, N. Hironiwa, K. Taniguchi, M. Shida-Kawazoe, S. Metsugi, T. Miyazaki, N. A. Wada, Y. Ohte, S. Shimizu, H. Mikami, T. Tachibana, N. Ono, K. Adachi, T. Sakiyama, T. Matsushita, S. Kadono, S. Komatsu, A. Sakamoto, S. Horikawa, A. Hirako, K. Hamada, S. Naoi, N. Savory, Y. Satoh, M. Sato, Y. Noguchi, J. Shinozuka, H. Kuroi, A. Ito, T. Wakabayashi, M. Kamimura, F. Isomura, Y. Tomii, N. Sawada, A. Kato, O. Ueda, Y. Nakanishi, M. Endo, K. Jishage, Y. Kawabe, T. Kitazawa, T. Igawa, Antibody to CD137 Activated by Extracellular Adenosine Triphosphate Is Tumor Selective and Broadly Effective In Vivo without Systemic Immune Activation. *Cancer Discov.* **11**, 158–175 (2020).

75. A. Muik, E. Garralda, I. Altintas, F. Gieseke, R. Geva, E. Ben-Ami, C. Maurice-Dror, E. Calvo, P. M. LoRusso, G. Alonso, M. E. Rodriguez-Ruiz, K. B. Schoedel, J. M. Blum, B. Sänger, T. W. Salcedo, S. M. Burm, E. Stanganello, D. Verzijl, F. Vascotto, A. Sette, J. Quinkhardt, T. S. Plantinga, A. Toker, E. N. van den Brink, M. Fereshteh, M. Diken, D. Satijn, S. Kreiter, E. C. W. Breij, G. Bajaj, E. Lagkadinou, K. Sasser, Ö. Türeci, U. Forssmann, T. Ahmadi, U. Şahin, M. Jure-Kunkel, I. Melero, Preclinical Characterization and Phase I Trial Results of a Bispecific Antibody Targeting PD-L1 and 4-1BB (GEN1046) in Patients with Advanced Refractory Solid TumorsGEN1046, a Bispecific Antibody Targeting PD-L1 and 4-1BB. *Cancer Discov.* **12**, 1248–1265 (2022).

76. D. L. Morton, F. R. Eilber, E. C. Holmes, J. S. Hunt, A. S. Ketcham, M. J. Silverstein, F. C. SPARKS, BCG lmmunotherapy of Malignant Melanoma. *Ann Surg.* **180**, 635–643 (1974).

77. J. Bier, H. J. Rapp, T. Borsos, B. Zbar, S. Kleinschuster, H. Wagner, M. Röllinghoff, Randomized clinical study on intratumoral BCG-cell wall preparation (CWP) therapy in patients with squamous cell carcinoma in the head and neck region. *Cancer Immunol Immunother.* **12**, 71–79 (1981).

78. R. H. I. Andtbacka, H. L. Kaufman, F. Collichio, T. Amatruda, N. Senzer, J. Chesney, K. A. Delman, L. E. Spitler, I. Puzanov, S. S. Agarwala, M. Milhem, L. Cranmer, B. Curti, K. Lewis, M. Ross, T. Guthrie, G. P. Linette, G. A. Daniels, K. Harrington, M. R. Middleton, W. H. M. Jr, J. S. Zager, Y. Ye, B. Yao, A. Li, S. Doleman, A. VanderWalde, J. Gansert, R. S. Coffin, Talimogene Laherparepvec Improves Durable Response Rate in Patients With Advanced Melanoma. *J Clin Oncol.* **33**, 2780–2788 (2015).

79. H. Rehman, A. W. Silk, M. P. Kane, H. L. Kaufman, Into the clinic: Talimogene laherparepvec (T-VEC), a first-in-class intratumoral oncolytic viral therapy. *J Immunother Cancer.* **4**, 53 (2016).

80. I. Melero, E. Castanon, M. Alvarez, S. Champiat, A. Marabelle, Intratumoural administration and tumour tissue targeting of cancer immunotherapies. *Nat Rev Clin Oncol*, **18**, 558-576 (2021).

81. A. Marabelle, R. Andtbacka, K. Harrington, I. Melero, R. Leidner, T. de Baere, C. Robert, P. A. Ascierto, J.-F. Baurain, M. Imperiale, S. Rahimian, D. Tersago, E. Klumper, M. Hendriks, R. Kumar, M. Stern, K. Öhrling, C. Massacesi, I. Tchakov, A. Tse, J.-Y. Douillard, J. Tabernero, J. Haanen, J. Brody, Starting the fight in the tumor: expert recommendations for the development of human intratumoral immunotherapy (HIT-IT). *Ann Oncol.* **29**, 2163–2174 (2018).

82. M. A. Aznar, N. Tinari, A. J. Rullán, A. R. Sánchez-Paulete, M. E. Rodriguez-Ruiz, I. Melero, Intratumoral Delivery of Immunotherapy—Act Locally, Think Globally. *J Immunol.* **198**, 31–39 (2017).

83. S. Champiat, L. Tselikas, S. Farhane, T. Raoult, M. Texier, E. Lanoy, C. Massard, C. Robert, S. Ammari, T. D. Baère, A. Marabelle, Intratumoral Immunotherapy: From Trial Design to Clinical Practice. *Clin Cancer Res.* **27**, 665–679 (2021).

84. A. Marabelle, L. Tselikas, T. de Baere, R. Houot, Intratumoral immunotherapy: using the tumor as the remedy. *Ann Oncol.* **28**, xii33–xii43 (2017).

85. H. L. Kaufman, T. Amatruda, T. Reid, R. Gonzalez, J. Glaspy, E. Whitman, K. Harrington, J. Nemunaitis, A. Zloza, M. Wolf, N. N. Senzer, Systemic versus local responses in melanoma patients treated with talimogene laherparepvec from a multi-institutional phase II study. *J Immunother Cancer.* **4**, 12 (2016).

86. N. Momin, N. K. Mehta, N. R. Bennett, L. Ma, J. R. Palmeri, M. M. Chinn, E. A. Lutz, B. Kang, D. J. Irvine, S. Spranger, K. D. Wittrup, Anchoring of intratumorally administered cytokines to collagen safely potentiates systemic cancer immunotherapy. *Sci Transl Med.* **11**, eaaw2614 (2019).

87. B. Kwong, H. Liu, D. J. Irvine, Induction of potent anti-tumor responses while eliminating systemic side effects via liposome-anchored combinatorial immunotherapy. *Biomaterials.* **32**, 5134–5147 (2011).

88. C. M. V. Herpen, R. Huijbens, M. Looman, J. D. Vries, H. Marres, J. V. D. Ven, R. Hermsen, G. J. Adema, P. H. D. Mulder, Pharmacokinetics and immunological aspects of a phase Ib study with intratumoral administration of recombinant human interleukin-12 in patients with head and neck squamous cell carcinoma: a decrease of T-bet in peripheral blood mononuclear cells. *Clin Cancer Res.* **9**, 2950–6 (2003).

89. H. H. Bartsch, K. Pfizenmaier, M. Schroeder, G. A. Nagel, Intralesional application of recombinant human tumor necrosis factor alpha induces local tumor regression in patients with advanced malignancies. *European J Cancer Clin Oncol.* **25**, 287–291 (1989).

90. M. D. Shoulders, R. T. Raines, Collagen Structure and Stability. *Annu Rev Biochem.* **78**, 929–958 (2009).

91. N. I. Nissen, M. Karsdal, N. Willumsen, Collagens and Cancer associated fibroblasts in the reactive stroma and its relation to Cancer biology. *J Exp Clin Canc Res.* **38**, 115 (2019).

92. N. Momin, J. R. Palmeri, E. A. Lutz, N. Jailkhani, H. Mak, A. Tabet, M. M. Chinn, B. H. Kang, V. Spanoudaki, R. O. Hynes, K. D. Wittrup, Maximizing response to intratumoral immunotherapy in mice by tuning local retention. *Nat Commun.* **13**, 109 (2022).

93. V. P. Sharma, B. T. Beaty, A. Patsialou, H. Liu, M. Clarke, D. Cox, J. S. Condeelis, R. J. Eddy, Reconstitution of in vivo macrophage-tumor cell pairing and streaming motility on one-dimensional micro-patterned substrates. *Intravital.* **1**, 77–85 (2012).

94. T. E. Sutherland, D. P. Dyer, J. E. Allen, The extracellular matrix and the immune system: A mutually dependent relationship. *Science.* **379**, eabp8964 (2023).

95. G. Alexandrakis, E. B. Brown, R. T. Tong, T. D. McKee, R. B. Campbell, Y. Boucher, R. K. Jain, Two-photon fluorescence correlation microscopy reveals the two-phase nature of transport in tumors. *Nat Med.* **10**, 203–207 (2004).

96. A. Mansurov, J. Ishihara, P. Hosseinchi, L. Potin, T. M. Marchell, A. Ishihara, J.-M. Williford, A. T. Alpar, M. M. Raczy, L. T. Gray, M. A. Swartz, J. A. Hubbell, Collagen-binding IL-12 enhances tumour inflammation and drives the complete remission of established immunologically cold mouse tumours. *Nat Biomed Eng.* **4**, 531–543 (2020).

97. J. Ishihara, A. Ishihara, L. Potin, P. Hosseinchi, K. Fukunaga, M. Damo, T. F. Gajewski, M. A. Swartz, J. A. Hubbell, Improving Efficacy and Safety of Agonistic Anti-CD40 Antibody Through Extraceullular Matrix Affinity. *Mol Cancer Ther.* **17**, 2399-2411 (2018).

98. J. Ishihara, K. Fukunaga, A. Ishihara, H. M. Larsson, L. Potin, P. Hosseinchi, G. Galliverti, M. A. Swartz, J. A. Hubbell, Matrix-binding checkpoint immunotherapies enhance antitumor efficacy and reduce adverse events. *Sci Transl Med.* **9**, eaan0401 (2017).

99. A. Mansurov, P. Hosseinchi, K. Chang, A. L. Lauterbach, L. T. Gray, A. T. Alpar, E. Budina, A. J. Slezak, S. Kang, S. Cao, A. Solanki, S. Gomes, J.-M. Williford, M. A. Swartz, J. L. Mendoza, J. Ishihara, J. A. Hubbell, Masking the immunotoxicity of interleukin-12 by fusing it with a domain of its receptor via a tumour-protease-cleavable linker. *Nat Biomed Eng.* 6, 819-829 (2022).

100. J.-M. Williford, J. Ishihara, A. Ishihara, A. Mansurov, P. Hosseinchi, T. M. Marchell, L. Potin, M. A. Swartz, J. A. Hubbell, Recruitment of CD103+ dendritic cells via tumor-targeted chemokine delivery enhances efficacy of checkpoint inhibitor immunotherapy. *Sci Adv.* **5**, eaay1357 (2019).

101. J. Ishihara, A. Ishihara, K. Sasaki, S. S.-Y. Lee, J.-M. Williford, M. Yasui, H. Abe, L. Potin, P. Hosseinchi, K. Fukunaga, M. M. Raczy, L. T. Gray, A. Mansurov, K. Katsumata, M. Fukayama, S. J. Kron, M. A. Swartz, J. A. Hubbell, Targeted antibody and cytokine cancer immunotherapies through collagen affinity. *Sci Transl Med.* **11,** eeau3259 (2019)

102. Y. Li, Z. Su, W. Zhao, X. Zhang, N. Momin, C. Zhang, K. D. Wittrup, Y. Dong, D. J. Irvine, R. Weiss, Multifunctional oncolytic nanoparticles deliver self-replicating IL-12 RNA to eliminate established tumors and prime systemic immunity. *Nat Cancer.* **1**, 882–893 (2020).

103. N. Momin, thesis (2021).

104. M. Sifaki, M. Assouti, D. Nikitovic, K. Krasagakis, N. K. Karamanos, G. N. Tzanakakis, Lumican, a small leucine-rich proteoglycan substituted with keratan sulfate chains is expressed and secreted by human melanoma cells and not normal melanocytes. *Iubmb Life.* **58**, 606–610 (2006).

105. D. Nikitovic, P. Katonis, A. Tsatsakis, N. K. Karamanos, G. N. Tzanakakis, Lumican, a small leucine-rich proteoglycan. *Iubmb Life.* **60**, 818–823 (2008).

106. A. V. Kajava, Structural diversity of leucine-rich repeat proteins11Edited by F. Cohen. *J Mol Biol.* **277**, 519–527 (1998).

107. F. Wu, N. Vij, L. Roberts, S. Lopez-Briones, S. Joyce, S. Chakravarti, A Novel Role of the Lumican Core Protein in Bacterial Lipopolysaccharide-induced Innate Immune Response. *J Biol Chem.* **282**, 26409–26417 (2007).

108. X. Tang, L. Tian, G. Esteso, S.-C. Choi, A. D. Barrow, M. Colonna, F. Borrego, J. E. Coligan, Leukocyte-Associated Ig-like Receptor-1–Deficient Mice Have an Altered Immune Cell Phenotype. *J Immunol.* **188**, 548–558 (2012).

109. T. Okazaki, T. Honjo, The PD-1–PD-L pathway in immunological tolerance. *Trends Immunol.* **27**, 195–201 (2006).

110. P. Waterhouse, J. M. Penninger, E. Timms, A. Wakeham, A. Shahinian, K. P. Lee, C. B. Thompson, H. Griesser, T. W. Mak, Lymphoproliferative Disorders with Early Lethality in Mice Deficient in Ctla-4. *Science.* **270**, 985–988 (1995).

111. E. A. Tivol, F. Borriello, A. N. Schweitzer, W. P. Lynch, J. A. Bluestone, A. H. Sharpe, Loss of CTLA-4 leads to massive lymphoproliferation and fatal multiorgan tissue destruction, revealing a critical negative regulatory role of CTLA-4. *Immunity*. **3**, 541–547 (1995).

112. D. H. Peng, B. L. Rodriguez, L. Diao, L. Chen, J. Wang, L. A. Byers, Y. Wei, H. A. Chapman, M. Yamauchi, C. Behrens, G. Raso, L. M. S. Soto, E. R. P. Cuentes, I. I. Wistuba, J. M. Kurie, D. L. Gibbons, Collagen promotes anti-PD-1/PD-L1 resistance in cancer through LAIR1-dependent CD8+ T cell exhaustion. *Nat Commun*. **11**, 4520 (2020).

113. L. A. Horn, P. L. Chariou, S. R. Gameiro, H. Qin, M. Iida, K. Fousek, T. J. Meyer, M. Cam, D. Flies, S. Langermann, J. Schlom, C. Palena, Remodeling the tumor microenvironment via blockade of LAIR-1 and TGF-β signaling enables PD-L1-mediated tumor eradication. *J Clin Invest*. **132**, e155148 (2022).

114. N. Kruljec, T. Bratkovič, Alternative Affinity Ligands for Immunoglobulins. *Bioconjugate Chem.* **28**, 2009–2030 (2017).

115. P. K. Peterson, J. Verhoef, L. D. Sabath, P. G. Quie, Effect of protein A on staphylococcal opsonization. *Infect Immun*. **15**, 760–764 (1977).

116. D. P. Nitsche-Schmitz, H. M. Johansson, I. Sastalla, S. Reissmann, I.-M. Frick, G. S. Chhatwal, Group G Streptococcal IgG Binding Molecules FOG and Protein G Have Different Impacts on Opsonization by C1q*. *J Biol Chem*. **282**, 17530–17536 (2007).

117. A. Cassedy, R. O'Kennedy, Affinity Chromatography, Methods and Protocols. *Methods Mol Biology*. **2466**, 3–22 (2022).

118. L. Jendeberg, B. Persson, R. Andersson, R. Karlsson, M. Uhlén, B. Nilsson, Kinetic analysis of the interaction between protein a domain variants and human Fc using plasmon resonance detection. *J Mol Recognit*. **8**, 270–278 (1995).

119. L. Cedergren, R. Andersson, B. Jansson, M. Uhlén, B. Nilsson, Mutational analysis of the interaction between staphylococcal protein A and human IgG 1. *Protein Eng Des Sel*. **6**, 441–448 (1993).

120. B. Nilsson, T. Moks, B. Jansson, L. Abrahmsén, A. Elmblad, E. Holmgren, C. Henrichson, T. A. Jones, M. Uhlén, A synthetic IgG-binding domain based on staphylococcal protein A. *Protein Eng Des Sel*. **1**, 107–113 (1987).

121. M. Tashiro, R. Tejero, D. E. Zimmerman, B. Celda, B. Nilsson, G. T. Montelione, High-resolution solution NMR structure of the Z domain of staphylococcal protein A11Edited by P. E. Wright. *J Mol Biol*. **272**, 573–590 (1997).

122. A. Konrad, A. E. Karlström, S. Hober, Covalent Immunoglobulin Labeling through a Photoactivable Synthetic Z Domain. *Bioconjugate Chem*. **22**, 2395–2403 (2011).

123. Y. Gong, L. Zhang, J. Li, S. Feng, H. Deng, Development of the Double Cyclic Peptide Ligand for Antibody Purification and Protein Detection. *Bioconjugate Chem.* **27**, 1569–1573 (2016).

124. T. Sagawa, M. Oda, H. Morii, H. Takizawa, H. Kozono, T. Azuma, Conformational changes in the antibody constant domains upon hapten-binding. *Mol Immunol.* **42**, 9–18 (2005).

125. B. Akerström, E. Nielsen, L. Björck, Definition of IgG- and albumin-binding regions of streptococcal protein G. *J Biol Chem.* **262**, 13388–13391 (1987).

126. A. E. Sauer-Eriksson, G. J. Kleywegt, M. Uhlén, T. A. Jones, Crystal structure of the C2 fragment of streptococcal protein G in complex with the Fc domain of human IgG. *Structure.* **3**, 265–278 (1995).

127. A. M. Gronenborn, G. M. Clore, Identification of the Contact Surface of a Streptococcal Protein G Domain Complexed with a Human Fc Fragment. *J Mol Biol.* **233**, 331–335 (1993).

128. B. Guss, M. Eliasson, A. Olsson, M. Uhlén, A. K. Frej, H. Jörnvall, J. I. Flock, M. Lindberg, Structure of the IgG-binding regions of streptococcal protein G. *Embo J.* **5**, 1567–1575 (1986).

129. S. R. Fahnestock, P. Alexander, J. Nagle, D. Filpula, Gene for an immunoglobulin-binding protein from a group G streptococcus. *J Bacteriol.* **167**, 870–880 (1986).

130. M. Acchione, H. Kwon, C. M. Jochheim, W. M. Atkins, Impact of linker and conjugation chemistry on antigen binding, Fc receptor binding and thermal stability of model antibody-drug conjugates. *Mabs.* **4**, 362–372 (2012).

131. M. Oda, H. Kozono, H. Morii, T. Azuma, Evidence of allosteric conformational changes in the antibody constant region upon antigen binding. *Int Immunol.* **15**, 417–426 (2003).

132. Y. Jung, J. M. Lee, J. Kim, J. Yoon, H. Cho, B. H. Chung, Photoactivable Antibody Binding Protein: Site-Selective and Covalent Coupling of Antibody. *Anal Chem.* **81**, 936–942 (2009).

133. A. Koide, C. W. Bailey, X. Huang, S. Koide, The fibronectin type III domain as a scaffold for novel binding proteins11Edited by J. Wells. *J Mol Biol.* **284**, 1141–1151 (1998).

134. I. D. Campbell, C. Spitzfaden, Building proteins with fibronectin type III modules. *Structure.* **2**, 333–337 (1994).

135. A. Koide, S. Koide, Monobodies: Antibody Mimics Based on the Scaffold of the Fibronectin Type III Domain. *Methods Mol Biology Clifton N J.* **352**, 95–109 (2006).

136. C. D. Dickinson, B. Veerapandian, X.-P. Dai, R. C. Hamlin, N. Xuong, E. Ruoslahti, K. R. Ely, Crystal structure of the tenth type III cell adhesion module of human fibronectin. *J Mol Biol.* **236**, 1079–1092 (1994).

137. B. J. Hackel, thesis (2009).

138. L. Xu, P. Aha, K. Gu, R. G. Kuimelis, M. Kurz, T. Lam, A. C. Lim, H. Liu, P. A. Lohse, L. Sun, S. Weng, R. W. Wagner, D. Lipovsek, Directed Evolution of High-Affinity Antibody Mimics Using mRNA Display. *Chem Biol.* **9**, 933–942 (2002).

139. E. Karatan, M. Merguerian, Z. Han, M. D. Scholle, S. Koide, B. K. Kay, Molecular Recognition Properties of FN3 Monobodies that Bind the Src SH3 Domain. *Chem Biol.* **11**, 835–844 (2004).

140. A. W. Tolcher, C. J. Sweeney, K. Papadopoulos, A. Patnaik, E. G. Chiorean, A. C. Mita, K. Sankhala, E. Furfine, J. Gokemeijer, L. Iacono, C. Eaton, B. A. Silver, M. Mita, Phase I and Pharmacokinetic Study of CT-322 (BMS-844203), a Targeted Adnectin Inhibitor of VEGFR-2 Based on a Domain of Human Fibronectin. *Clin Cancer Res.* **17**, 363–371 (2011).

141. R. Mamluk, I. M. Carvajal, B. A. Morse, H. K. Wong, J. Abramowitz, S. Aslanian, A.-C. Lim, J. Gokemeijer, M. J. Storek, J. Lee, M. Gosselin, M. C. Wright, R. T. Camphausen, J. Wang, Y. Chen, K. Miller, K. Sanders, S. Short, J. Sperinde, G. Prasad, S. Williams, R. S. Kerbel, J. Ebos, A. Mutsaers, J. D. Mendlein, A. S. Harris, E. S. Furfine, Anti-tumor effect of CT-322 as an Adnectin inhibitor of vascular endothelial growth factor receptor-2. *Mabs.* **2**, 199–208 (2010).

142. D. Schiff, S. Kesari, J. de Groot, T. Mikkelsen, J. Drappatz, T. Coyle, L. Fichtel, B. Silver, I. Walters, D. Reardon, Phase 2 study of CT-322, a targeted biologic inhibitor of VEGFR-2 based on a domain of human fibronectin, in recurrent glioblastoma. *Invest New Drug.* **33**, 247–253 (2015).

143. D. Lipovšek, S. M. Lippow, B. J. Hackel, M. W. Gregson, P. Cheng, A. Kapila, K. D. Wittrup, Evolution of an Interloop Disulfide Bond in High-Affinity Antibody Mimics Based on Fibronectin Type III Domain and Selected by Yeast Surface Display: Molecular Convergence with Single-Domain Camelid and Shark Antibodies. *J Mol Biol.* **368**, 1024–1041 (2007).

144. K. H. Roux, A. S. Greenberg, L. Greene, L. Strelets, D. Avila, E. C. McKinney, M. F. Flajnik, Structural analysis of the nurse shark (new) antigen receptor (NAR): Molecular convergence of NAR and unusual mammalian immunoglobulins. *Proc National Acad Sci.* **95**, 11804–11809 (1998).

145. S. Muyldermans, T. Atarhouch, J. Saldanha, J. A. R. G. Barbosa, R. Hamers, Sequence and structure of V H domain from naturally occurring camel heavy chain immunoglobulins lacking light chains. *Protein Eng Des Sel.* **7**, 1129–1135 (1994).

146. B. J. Hackel, A. Kapila, K. D. Wittrup, Picomolar Affinity Fibronectin Domains Engineered Utilizing Loop Length Diversity, Recursive Mutagenesis, and Loop Shuffling. *J Mol Biol.* **381**, 1238–1252 (2008).

147. B. J. Hackel, M. E. Ackerman, S. W. Howland, K. D. Wittrup, Stability and CDR Composition Biases Enrich Binder Functionality Landscapes. *J Mol Biol.* **401**, 84–96 (2010).

148. N. Gera, A. B. Hill, D. P. White, R. G. Carbonell, B. M. Rao, Design of pH Sensitive Binding Proteins from the Hyperthermophilic Sso7d Scaffold. *Plos One.* **7**, e48928 (2012).

149. N. Gera, M. Hussain, R. C. Wright, B. M. Rao, Highly Stable Binding Proteins Derived from the Hyperthermophilic Sso7d Scaffold. *J Mol Biol.* **409**, 601–616 (2011).

150. M. W. Traxlmayr, J. D. Kiefer, R. R. Srinivas, E. Lobner, A. W. Tisdale, N. K. Mehta, N. J. Yang, B. Tidor, K. D. Wittrup, Strong Enrichment of Aromatic Residues in Binding Sites from a Charge-neutralized Hyperthermostable Sso7d Scaffold Library*. *J Biol Chem.* **291**, 22496–22508 (2016).

151. J. D. Bloom, S. T. Labthavikul, C. R. Otey, F. H. Arnold, Protein stability promotes evolvability. *Proc National Acad Sci.* **103**, 5869–5874 (2006).

152. C.-W. Tsai, S.-L. Jheng, W.-Y. Chen, R.-C. Ruaan, Strategy of Fc-Recognizable Peptide Ligand Design for Oriented Immobilization of Antibody. *Anal Chem.* **86**, 2931–2938 (2014).

153. W. L. DeLano, M. H. Ultsch, A. M. de, Vos, J. A. Wells, Convergent Solutions to Binding at a Protein-Protein Interface. *Science.* **287**, 1279–1283 (2000).

154. K. S. Midelfort, H. H. Hernandez, S. M. Lippow, B. Tidor, C. L. Drennan, K. D. Wittrup, Substantial Energetic Improvement with Minimal Structural Perturbation in a High Affinity Mutant Antibody. *J Mol Biol.* **343**, 685–701 (2004).

155. J. Riegler, Y. Labyed, S. Rosenzweig, V. Javinal, A. Castiglioni, C. X. Dominguez, J. E. Long, Q. Li, W. Sandoval, M. R. Junttila, S. J. Turley, J. M. Schartner, R. Carano, Tumor Elastography and Its Association with Collagen and the Tumor Microenvironment. *Clin Cancer Res.* **24**, 4455-4467 (2018).

156. M. T. Kim, Y. Chen, J. Marhoul, F. Jacobson, Statistical Modeling of the Drug Load Distribution on Trastuzumab Emtansine (Kadcyla), a Lysine-Linked Antibody Drug Conjugate. *Bioconjugate Chem.* **25**, 1223–1232 (2014).

157. A. Beck, L. Goetsch, C. Dumontet, N. Corvaïa, Strategies and challenges for the next generation of antibody–drug conjugates. *Nat Rev Drug Discov.* **16**, 315–337 (2017).

158. L. Meyaard, G. J. Adema, C. Chang, E. Woollatt, G. R. Sutherland, L. L. Lanier, J. H. Phillips, LAIR-1, a Novel Inhibitory Receptor Expressed on Human Mononuclear Leukocytes. *Immunity.* **7**, 283–290 (1997).

159. R. J. Lebbink, T. de Ruiter, G. J. A. Kaptijn, D. G. Bihan, C. A. Jansen, P. J. Lenting, L. Meyaard, Mouse leukocyte-associated Ig-like receptor-1 (mLAIR-1) functions as an inhibitory collagen-binding receptor on immune cells. *Int Immunol.* **19**, 1011–1019 (2007).

160. E. Hui, J. Cheung, J. Zhu, X. Su, M. J. Taylor, H. A. Wallweber, D. K. Sasmal, J. Huang, J. M. Kim, I. Mellman, R. D. Vale, T cell costimulatory receptor CD28 is a primary target for PD-1–mediated inhibition. *Science.* **355**, 1428–1433 (2017).

161. A. O. Kamphorst, A. Wieland, T. Nasti, S. Yang, R. Zhang, D. L. Barber, B. T. Konieczny, C. Z. Daugherty, L. Koenig, K. Yu, G. L. Sica, A. H. Sharpe, G. J. Freeman, B. R. Blazar, L. A. Turka, T. K. Owonikoko, R. N. Pillai, S. S. Ramalingam, K. Araki, R. Ahmed, Rescue of exhausted CD8 T cells by PD-1–targeted therapies is CD28-dependent. *Science*. **355**, 1423–1427 (2017).

162. J. Duraiswamy, R. Turrini, A. Minasyan, D. Barras, I. Crespo, A. J. Grimm, J. Casado, R. Genolet, F. Benedetti, A. Wicky, K. Ioannidou, W. Castro, C. Neal, A. Moriot, S. Renaud-Tissot, V. Anstett, N. Fahr, J. L. Tanyi, M. A. Eiva, C. A. Jacobson, K. T. Montone, M. C. W. Westergaard, I. M. Svane, L. E. Kandalaft, M. Delorenzi, P. K. Sorger, A. Färkkilä, O. Michielin, V. Zoete, S. J. Carmona, P. G. Foukas, D. J. Powell, S. Rusakiewicz, M.-A. Doucey, D. D. Laniti, G. Coukos, Myeloid antigen-presenting cell niches sustain antitumor T cells and license PD-1 blockade via CD28 costimulation. *Cancer Cell*. **39**, 1623-1642.e20 (2021).

163. S. L. Meier, A. T. Satpathy, D. K. Wells, Bystander T cells in cancer immunology and therapy. *Nat Cancer*. **3**, 143–155 (2022).

164. Y. Simoni, E. Becht, M. Fehlings, C. Y. Loh, S.-L. Koo, K. W. W. Teng, J. P. S. Yeong, R. Nahar, T. Zhang, H. Kared, K. Duan, N. Ang, M. Poidinger, Y. Y. Lee, A. Larbi, A. J. Khng, E. Tan, C. Fu, R. Mathew, M. Teo, W. T. Lim, C. K. Toh, B.-H. Ong, T. Koh, A. M. Hillmer, A. Takano, T. K. H. Lim, E. H. Tan, W. Zhai, D. S. W. Tan, I. B. Tan, E. W. Newell, Bystander CD8+ T cells are abundant and phenotypically distinct in human tumour infiltrates. *Nature*. **557**, 575–579 (2018).

165. M. Shakiba, P. Zumbo, G. Espinosa-Carrasco, L. Menocal, F. Dündar, S. E. Carson, E. M. Bruno, F. J. Sanchez-Rivera, S. W. Lowe, S. Camara, R. P. Koche, V. P. Reuter, N. D. Socci, B. Whitlock, F. Tamzalit, M. Huse, M. D. Hellmann, D. K. Wells, N. A. Defranoux, D. Betel, M. Philip, A. Schietinger, TCR signal strength defines distinct mechanisms of T cell dysfunction and cancer evasion. *J Exp Med*. **219**, e20201966 (2021).

166. R. Upadhyay, J. A. Boiarsky, G. Pantsulaia, J. Svensson-Arvelund, M. J. Lin, A. Wroblewska, S. Bhalla, N. Scholler, A. Bot, J. M. Rossi, N. Sadek, S. Parekh, A. Lagana, A. Baccarini, M. Merad, B. D. Brown, J. D. Brody, A Critical Role for Fas-Mediated Off-Target Tumor Killing in T-cell Immunotherapy. *Cancer Discov*. **11**, 599–613 (2021).

167. E. A. Lutz, Y. Agarwal, N. Momin, S. C. Cowles, J. R. Palmeri, E. Duong, V. Hornet, A. Sheen, B. M. Lax, A. M. Rothschilds, D. J. Irvine, S. Spranger, K. D. Wittrup, Alum-anchored intratumoral retention improves the tolerability and antitumor efficacy of type I interferon therapies. *Proc National Acad Sci*. 119, e2205983119 (2022).

168. Y. Agarwal, L. E. Milling, J. Y. H. Chang, L. Santollani, A. Sheen, E. A. Lutz, A. Tabet, J. Stinson, K. Ni, K. A. Rodrigues, T. J. Moyer, M. B. Melo, D. J. Irvine, K. D. Wittrup, Intratumourally injected alum-tethered cytokines elicit potent and safer local and systemic anticancer immunity. *Nat Biomed Eng*. **6**, 129–143 (2022).

169. E. A. Lutz, thesis (2022).

170. Y. Agarwal, thesis (2022).

171. R. E. Flarend, S. L. Hem, J. L. White, D. Elmore, M. A. Suckow, A. C. Rudy, E. A. Dandashli, In vivo absorption of aluminium-containing vaccine adjuvants using 26Al. *Vaccine.* **15**, 1314–1318 (1997).

172. T. J. Moyer, Y. Kato, W. Abraham, J. Y. H. Chang, D. W. Kulp, N. Watson, H. L. Turner, S. Menis, R. K. Abbott, J. N. Bhiman, M. B. Melo, H. A. Simon, S. H.-D. la Mata, S. Liang, G. Seumois, Y. Agarwal, N. Li, D. R. Burton, A. B. Ward, W. R. Schief, S. Crotty, D. J. Irvine, Engineered immunogen binding to alum adjuvant enhances humoral immunity. *Nat Med.* **26**, 430–440 (2020).

173. M. Lo, H. S. Kim, R. K. Tong, T. W. Bainbridge, J.-M. Vernes, Y. Zhang, Y. L. Lin, S. Chung, M. S. Dennis, Y. J. Y. Zuchero, R. J. Watts, J. A. Couch, Y. G. Meng, J. K. Atwal, R. J. Brezski, C. Spiess, J. A. Ernst, Effector-attenuating Substitutions That Maintain Antibody Stability and Reduce Toxicity in Mice. *J Biol Chem.* **292**, 3900–3908 (2017).

174. B. Kwong, S. A. Gai, J. Elkhader, K. D. Wittrup, D. J. Irvine, Localized Immunotherapy via Liposome-Anchored Anti-CD137 + IL-2 Prevents Lethal Toxicity and Elicits Local and Systemic Antitumor Immunity. *Cancer Res.* **73**, 1547–1558 (2013).

175. S. I. S. Mosely, J. E. Prime, R. C. A. Sainson, J.-O. Koopmann, D. Y. Q. Wang, D. M. Greenawalt, M. J. Ahdesmaki, R. Leyland, S. Mullins, L. Pacelli, D. Marcus, J. Anderton, A. Watkins, J. C. Ulrichsen, P. Brohawn, B. W. Higgs, M. McCourt, H. Jones, J. A. Harper, M. Morrow, V. Valge-Archer, R. Stewart, S. J. Dovedi, R. W. Wilkinson, Rational Selection of Syngeneic Preclinical Tumor Models for Immunotherapeutic Drug Discovery. *Cancer Immunol Res.* **5**, 29–41 (2017).

176. H. Escuin-Ordinas, M. W. Elliott, M. Atefi, M. Lee, C. Ng, L. Wei, B. Comin-Anduix, E. Montecino-Rodriguez, E. Avramis, C. Radu, L. L. Sharp, A. Ribas, PET imaging to non-invasively study immune activation leading to antitumor responses with a 4-1BB agonistic antibody. *J Immunother Cancer.* **1**, 14 (2013).

177. J. Timmerman, C. Herbaux, V. Ribrag, A. D. Zelenetz, R. Houot, S. S. Neelapu, T. Logan, I. S. Lossos, W. Urba, G. Salles, R. Ramchandren, C. Jacobson, J. Godwin, C. Carpio, D. Lathers, Y. Liu, J. Neely, S. Suryawanshi, Y. Koguchi, R. Levy, Urelumab alone or in combination with rituximab in patients with relapsed or refractory B-cell lymphoma. *Am. J. Hematol.* **95**, 510–520 (2020).

178. R. M. Zemek, E. D. Jong, W. L. Chin, I. S. Schuster, V. S. Fear, T. H. Casey, C. Forbes, S. J. Dart, C. Leslie, A. Zaitouny, M. Small, L. Boon, A. R. R. Forrest, D. O. Muiri, M. A. Degli-Esposti, M. J. Millward, A. K. Nowak, T. Lassmann, A. Bosco, R. A. Lake, W. J. Lesterhuis, Sensitization to immune checkpoint blockade through activation of a STAT1/NK axis in the tumor microenvironment. *Sci Transl Med.* **11**, eaav7816 (2019).

179. A. Makkouk, V. Sundaram, C. Chester, S. Chang, A. D. Colevas, J. B. Sunwoo, H. Maecker, M.

Desai, H. E. Kohrt, Characterizing CD137 upregulation on NK cells in patients receiving monoclonal antibody therapy. *Ann Oncol.* **28**, 415–420 (2017).

180. R. M. Srivastava, S. Trivedi, F. Concha-Benavente, S. P. Gibson, C. Reeder, S. Ferrone, R. L. Ferris, CD137 Stimulation Enhances Cetuximab-Induced Natural Killer: Dendritic Cell Priming of Antitumor T-Cell Immunity in Patients with Head and Neck Cancer. *Clin Cancer Res.* **23**, 707–716 (2017).

181. L. Niu, S. Strahotin, B. Hewes, B. Zhang, Y. Zhang, D. Archer, T. Spencer, D. Dillehay, B. Kwon, L. Chen, A. T. Vella, R. S. Mittler, Cytokine-Mediated Disruption of Lymphocyte Trafficking, Hemopoiesis, and Induction of Lymphopenia, Anemia, and Thrombocytopenia in Anti-CD137-Treated Mice. *J Immunol.* **178**, 4194–4213 (2007).

182. X. Qi, F. Li, Y. Wu, C. Cheng, P. Han, J. Wang, X. Yang, Optimization of 4-1BB antibody for cancer immunotherapy by balancing agonistic strength with FcγR affinity. *Nat Commun.* **10**, 2141 (2019).

183. A. Mirsoian, M. N. Bouchlaka, G. D. Sckisel, M. Chen, C.-C. S. Pai, E. Maverakis, R. G. Spencer, K. W. Fishbein, S. Siddiqui, A. M. Monjazeb, B. Martin, S. Maudsley, C. Hesdorffer, L. Ferrucci, D. L. Longo, B. R. Blazar, R. H. Wiltrout, D. D. Taub, W. J. Murphy, Adiposity induces lethal cytokine storm after systemic administration of stimulatory immunotherapy regimens in aged mice. *J Exp Medicine.* **211**, 2373–2383 (2014).

184. M. N. Bouchlaka, G. D. Sckisel, M. Chen, A. Mirsoian, A. E. Zamora, E. Maverakis, D. E. C. Wilkins, K. L. Alderson, H.-H. Hsiao, J. M. Weiss, A. M. Monjazeb, C. Hesdorffer, L. Ferrucci, D. L. Longo, B. R. Blazar, R. H. Wiltrout, D. Redelman, D. D. Taub, W. J. Murphy, Aging predisposes to acute inflammatory induced pathology after tumor immunotherapyCytokine-mediated toxicity with aging. *J Exp Medicine.* **210**, 2223–2237 (2013).

185. L. J. Appleman, A. Berezovskaya, I. Grass, V. A. Boussiotis, CD28 Costimulation Mediates T Cell Expansion Via IL-2-Independent and IL-2-Dependent Regulation of Cell Cycle Progression. *J Immunol.* **164**, 144–151 (2000).

186. N. M. Edner, G. Carlesso, J. S. Rush, L. S. K. Walker, Targeting co-stimulatory molecules in autoimmune disease. *Nat Rev Drug Discov.* **19**, 860–883 (2020).

187. S. P. Rer, G. Carlesso,z, B. G. Vassallo, A. Hunter, M. K. Wall, J. H. Badger, J. A. McCulloch, D. G. Anastasakis, A. A. Sarshad, I. Leonardi, N. Collins, J. A. Blatter, S.-J. Han, S. Tamoutounour, S. Potapova, M. B. F. St. Claire, W. Yuan, S. K. Sen, M. S. Dreier, B. Hild, M. Hafner, D. Wang, I. D. Iliev, Y. Belkaid, G. Trinchieri, B. Rehermann, Laboratory mice born to wild mice have natural microbiota and model human immune responses. *Science.* **365**, eaaw4361 (2019).

188. K. A. Connolly, M. Kuchroo, A. Venkat, A. Khatun, J. Wang, I. William, N. Hornick, B. Fitzgerald, M. Damo, M. Y. Kasmani, C. Cui, E. Fagerberg, I. Monroy, A. Hutchins, J. F. Cheung, G. G. Foster, D. L. Mariuzza, M. Nader, H. Zhao, W. Cui, S. Krishnaswamy, N. S. Joshi, A reservoir of

stem-like CD8+ T cells in the tumor-draining lymph node preserves the ongoing anti-tumor immune response. *Sci Immunol.* **6**, eabg7836 (2021).

189. J. Textor, J. N. Mandl, R. J. de Boer, The Reticular Cell Network: A Robust Backbone for Immune Responses. *Plos Biol.* **14**, e2000827 (2016).

190. N. Poirier, G. Blancho, B. Vanhove, CD28-Specific Immunomodulating Antibodies: What Can Be Learned From Experimental Models? *Am J Transplant.* **12**, 1682–1690 (2012).

191. N. Beyersdorf, T. Hanke, T. Kerkau, T. Hünig, Superagonistic anti-CD28 antibodies: potent activators of regulatory T cells for the therapy of autoimmune diseases. *Ann Rheum Dis.* **64**, iv91 (2005).

192. H. J. Park, K. W. Kim, J. Pyo, C. H. Suh, S. Yoon, H. Hatabu, M. Nishino, Incidence of Pseudoprogression during Immune Checkpoint Inhibitor Therapy for Solid Tumors: A Systematic Review and Meta-Analysis. *Radiology.* **297**, 87–96 (2020).

193. J. R. Palmeri, B. M. Lax, J. M. Peters, L. R. Duhamel, J. A. Stinson, L. Santollani, E. A. Lutz, W. Pinney, B. D. Bryson, K. D. Wittrup, Tregs constrain CD8+ T cell priming required for curative intratumorally anchored anti-4-1BB immunotherapy. *BioRxiv* (2023), doi:10.1101/2023.01.30.526116.

194. K. D. Moynihan, C. F. Opel, G. L. Szeto, A. Tzeng, E. F. Zhu, J. M. Engreitz, R. T. Williams, K. Rakhra, M. H. Zhang, A. M. Rothschilds, S. Kumari, R. L. Kelly, B. H. Kwan, W. Abraham, K. Hu, N. K. Mehta, M. J. Kauke, H. Suh, J. R. Cochran, D. A. Lauffenburger, K. D. Wittrup, D. J. Irvine, Eradication of large established tumors in mice by combination immunotherapy that engages innate and adaptive immune responses. *Nat Med.* **22**, 1402–1410 (2016).

195. A. M. Scott, J. D. Wolchok, L. J. Old, Antibody therapy of cancer. *Nat Rev Cancer.* **12**, 278–287 (2012).

196. H. S. Jhajj, T. S. Lwo, E. L. Yao, P. M. Tessier, Unlocking the potential of agonist antibodies for treating cancer using antibody engineering. *Trends Mol Med.* **29**, 48-60 (2022).

197. H. Borghaei, S. Gettinger, E. E. Vokes, L. Q. M. Chow, M. A. Burgio, J. de C. Carpeno, A. Pluzanski, O. Arrieta, O. A. Frontera, R. Chiari, C. Butts, J. Wójcik-Tomaszewska, B. Coudert, M. C. Garassino, N. Ready, E. Felip, M. A. García, D. Waterhouse, M. Domine, F. Barlesi, S. Antonia, M. Wohlleber, D. E. Gerber, G. Czyzewicz, D. R. Spigel, L. Crino, W. E. E. Eberhardt, A. Li, S. Marimuthu, J. Brahmer, Five-Year Outcomes From the Randomized, Phase III Trials CheckMate 017 and 057: Nivolumab Versus Docetaxel in Previously Treated Non–Small-Cell Lung Cancer. *J Clin Oncol.* **39**, 723–733 (2021).

198. J. D. Wolchok, V. Chiarion-Sileni, R. Gonzalez, J.-J. Grob, P. Rutkowski, C. D. Lao, C. L. Cowey, D. Schadendorf, J. Wagstaff, R. Dummer, P. F. Ferrucci, M. Smylie, M. O. Butler, A. Hill, I. Márquez-Rodas, J. B. A. G. Haanen, M. Guidoboni, M. Maio, P. Schöffski, M. S. Carlino, C. Lebbé, G. McArthur, P. A. Ascierto, G. A. Daniels, G. V. Long, T. Bas, C. Ritchings, J. Larkin, F. S. Hodi, Long-

Term Outcomes With Nivolumab Plus Ipilimumab or Nivolumab Alone Versus Ipilimumab in Patients With Advanced Melanoma. *J Clin Oncol.* **40**, 127–137 (2022).

199. T. H. Watts, TNF/TNFR family members in costimulation of T cell responses. *Annu Rev Immunol.* **23**, 23–68 (2005).

200. B. S. Kwon, S. M. Weissman, cDNA sequences of two inducible T-cell genes. *Proc National Acad Sci.* 86, 1963–1967 (1989).

201. H. Lee, K. Nam, S. Park, B. S. Kwon, 4-1BB enhances CD8+ T cell expansion by regulating cell cycle progression through changes in expression of cyclins D and E and cyclin-dependent kinase inhibitor p27kip1. *Eur J Immunol.* **33**, 2133–2141 (2003).

202. J. E. Willoughby, J. P. Kerr, A. Rogel, V. Y. Taraban, S. L. Buchan, P. W. M. Johnson, A. Al-Shamkhani, Differential Impact of CD27 and 4-1BB Costimulation on Effector and Memory CD8 T Cell Generation following Peptide Immunization. *J Immunol.* **193**, 244–251 (2014).

203. W. W. Shuford, K. Klussman, D. D. Tritchler, D. T. Loo, J. Chalupny, A. W. Siadak, T. J. Brown, J. Emswiler, H. Raecho, C. P. Larsen, T. C. Pearson, J. A. Ledbetter, A. Aruffo, R. S. Mittler, 4-1BB Costimulatory Signals Preferentially Induce CD8+ T Cell Proliferation and Lead to the Amplification In Vivo of Cytotoxic T Cell Responses. *J Exp Medicine*. **186**, 47–55 (1997).

204. I. Etxeberria, J. Glez-Vaz, Á. Teijeira, I. Melero, New emerging targets in cancer immunotherapy: CD137/4-1BB costimulatory axis. *Esmo Open*. **4**, e000733 (2019).

205. S. Hori, T. Nomura, S. Sakaguchi, Control of Regulatory T Cell Development by the Transcription Factor Foxp3. *Science.* **299**, 1057–1061 (2003).

206. J. D. Fontenot, M. A. Gavin, A. Y. Rudensky, Foxp3 programs the development and function of CD4+CD25+ regulatory T cells. *Nat Immunol.* **4**, 330–336 (2003).

207. J. M. Kim, J. P. Rasmussen, A. Y. Rudensky, Regulatory T cells prevent catastrophic autoimmunity throughout the lifespan of mice. *Nat Immunol.* **8**, 191–197 (2007).

208. K. Lahl, C. Loddenkemper, C. Drouin, J. Freyer, J. Arnason, G. Eberl, A. Hamann, H. Wagner, J. Huehn, T. Sparwasser, Selective depletion of Foxp3+ regulatory T cells induces a scurfy-like disease. *J Exp Medicine*. **204**, 57–63 (2007).

209. M. E. Brunkow, E. W. Jeffery, K. A. Hjerrild, B. Paeper, L. B. Clark, S.-A. Yasayko, J. E. Wilkinson, D. Galas, S. F. Ziegler, F. Ramsdell, Disruption of a new forkhead/winged-helix protein, scurfin, results in the fatal lymphoproliferative disorder of the scurfy mouse. *Nat Genet.* **27**, 68–73 (2001).

210. C. L. Bennett, J. Christie, F. Ramsdell, M. E. Brunkow, P. J. Ferguson, L. Whitesell, T. E. Kelly, F. T. Saulsbury, P. F. Chance, H. D. Ochs, The immune dysregulation, polyendocrinopathy,

enteropathy, X-linked syndrome (IPEX) is caused by mutations of FOXP3. *Nat Genet.* **27**, 20–21 (2001).

211. L. E. Lucca, M. Dominguez-Villar, Modulation of regulatory T cell function and stability by co-inhibitory receptors. *Nat Rev Immunol.* **20**, 680–693 (2020).

212. E. N. Scott, A. M. Gocher, C. J. Workman, D. A. A. Vignali, Regulatory T Cells: Barriers of Immune Infiltration Into the Tumor Microenvironment. *Front Immunol.* **12**, 702726 (2021).

213. V. Y. Taraban, T. F. Rowley, L. O'Brien, H. T. C. Chan, L. E. Haswell, M. H. A. Green, A. L. Tutt, M. J. Glennie, A. Al-Shamkhani, Expression and costimulatory effects of the TNF receptor superfamily members CD134 (OX40) and CD137 (4-1BB), and their role in the generation of anti-tumor immune responses. *Eur. J. Immunol.* **32**, 3617–3627 (2002).

214. B. K. Choi, Y. H. Kim, W. J. Kang, S. K. Lee, K. H. Kim, S. M. Shin, W. M. Yokoyama, T. Y. Kim, B. S. Kwon, Mechanisms Involved in Synergistic Anticancer Immunity of Anti-4-1BB and Anti-CD4 Therapy. *Cancer Res.* **67**, 8891–8899 (2007).

215. B. H. Kwan, E. F. Zhu, A. Tzeng, H. R. Sugito, A. A. Eltahir, B. Ma, M. K. Delaney, P. A. Murphy, M. J. Kauke, A. Angelini, N. Momin, N. K. Mehta, A. M. Maragh, R. O. Hynes, G. Dranoff, J. R. Cochran, K. D. Wittrup, Integrin-targeted cancer immunotherapy elicits protective adaptive immune responsesIntegrin-targeted cancer immunotherapy. *J Exp Medicine.* **214**, 1679–1690 (2017).

216. H. Aoki, S. Ueha, S. Shichino, H. Ogiwara, S. Hashimoto, K. Kakimi, S. Ito, K. Matsushima, TCR Repertoire Analysis Reveals Mobilization of Novel CD8+ T Cell Clones Into the Cancer-Immunity Cycle Following Anti-CD4 Antibody Administration. *Front Immunol.* **9**, 3185 (2019).

217. K. Shitara, S. Ueha, S. Shichino, H. Aoki, H. Ogiwara, T. Nakatsura, T. Suzuki, M. Shimomura, T. Yoshikawa, K. Shoda, S. Kitano, M. Yamashita, T. Nakayama, A. Sato, S. Kuroda, M. Wakabayashi, S. Nomura, S. Yokochi, S. Ito, K. Matsushima, T. Doi, First-in-human phase 1 study of IT1208, a defucosylated humanized anti-CD4 depleting antibody, in patients with advanced solid tumors. *J Immunother Cancer.* **7**, 195 (2019).

218. H. Aoki, S. Ueha, S. Shichino, H. Ogiwara, K. Shitara, M. Shimomura, T. Suzuki, T. Nakatsura, M. Yamashita, S. Kitano, S. Kuroda, M. Wakabayashi, M. Kurachi, S. Ito, T. Doi, K. Matsushima, Transient Depletion of CD4+ Cells Induces Remodeling of the TCR Repertoire in Gastrointestinal Cancer. *Cancer Immunol Res.* **9**, 624–636 (2021).

219. E. Y. Chen, C. M. Tan, Y. Kou, Q. Duan, Z. Wang, G. V. Meirelles, N. R. Clark, A. Ma'ayan, Enrichr: interactive and collaborative HTML5 gene list enrichment analysis tool. *Bmc Bioinformatics.* **14**, 128 (2013).

220. M. V. Kuleshov, M. R. Jones, A. D. Rouillard, N. F. Fernandez, Q. Duan, Z. Wang, S. Koplev, S. L. Jenkins, K. M. Jagodnik, A. Lachmann, M. G. McDermott, C. D. Monteiro, G. W. Gundersen,

A. Ma'ayan, Enrichr: a comprehensive gene set enrichment analysis web server 2016 update. *Nucleic Acids Res.* **44**, W90–W97 (2016).

221. Z. Xie, A. Bailey, M. V. Kuleshov, D. J. B. Clarke, J. E. Evangelista, S. L. Jenkins, A. Lachmann, M. L. Wojciechowicz, E. Kropiwnicki, K. M. Jagodnik, M. Jeon, A. Ma'ayan, Gene Set Knowledge Discovery with Enrichr. *Curr Protoc.* **1**, e90 (2021).

222. J. C. Beltra, M. S. Abdel-Hakeem, S. Manne, Z. Zhang, H. Huang, M. Kurachi, L. Su, L. Picton, Y. Muroyama, V. Casella, Y. J. Huang, J. R. Giles, D. Mathew, J. Belman, M. Klapholz, H. Decaluwe, A. C. Huang, S. L. Berger, C. K. Garcia, J. E. Wherry, Enhanced STAT5a activation rewires exhausted CD8 T cells during chronic stimulation to acquire a hybrid durable effector like state. *BioRxiv* (2022), doi:10.1101/2022.10.03.509766.

223. M. Hashimoto, K. Araki, M. A. Cardenas, P. Li, R. R. Jadhav, H. T. Kissick, W. H. Hudson, D. J. McGuire, R. C. Obeng, A. Wieland, J. Lee, D. T. McManus, J. L. Ross, S. J. Im, J. Lee, J.-X. Lin, B. Hu, E. E. West, C. D. Scharer, G. J. Freeman, A. H. Sharpe, S. S. Ramalingam, A. Pellerin, V. Teichgräber, W. J. Greenleaf, C. Klein, J. J. Goronzy, P. Umaña, W. J. Leonard, K. A. Smith, R. Ahmed, PD-1 combination therapy with IL-2 modifies CD8+ T cell exhaustion program. *Nature*, **610**, 173-181 (2022).

224. L. C. Deak, V. Nicolini, M. Hashimoto, M. Karagianni, P. C. Schwalie, L. Lauener, E. M. Varypataki, M. Richard, E. Bommer, J. Sam, S. Joller, M. Perro, F. Cremasco, L. Kunz, E. Yanguez, T. Hüsser, R. Schlenker, M. Mariani, V. Tosevski, S. Herter, M. Bacac, I. Waldhauer, S. Colombetti, X. Gueripel, S. Wullschleger, M. Tichet, D. Hanahan, H. T. Kissick, S. Leclair, A. Freimoser-Grundschober, S. Seeber, V. Teichgräber, R. Ahmed, C. Klein, P. Umaña, PD-1-cis IL-2R agonism yields better effectors from stem-like CD8+ T cells. *Nature*, **610,** 161-172 (2022).

225. J. Liu, S. J. Blake, H. Harjunpää, K. A. Fairfax, M. C. R. Yong, S. Allen, H. E. Kohrt, K. Takeda, M. J. Smyth, M. W. L. Teng, Assessing Immune-Related Adverse Events of Efficacious Combination Immunotherapies in Preclinical Models of Cancer. *Cancer Res.* **76**, 5288–5301 (2016).

226. V. Brinkmann, A. Billich, T. Baumruker, P. Heining, R. Schmouder, G. Francis, S. Aradhye, P. Burtin, Fingolimod (FTY720): discovery and development of an oral drug to treat multiple sclerosis. *Nat Rev Drug Discov.* **9**, 883–897 (2010).

227. E. M. Sotomayor, I. Borrello, E. Tubb, J. P. Allison, H. I. Levitsky, In vivo blockade of CTLA-4 enhances the priming of responsive T cells but fails to prevent the induction of tumor antigen-specific tolerance. *Proc National Acad Sci.* **96**, 11476–11481 (1999).

228. L.-C. Tsao, J. Force, Z. C. Hartman, Mechanisms of Therapeutic Antitumor Monoclonal Antibodies. *Cancer Res.* **81**, 4641-4651 (2021).

229. K. D. Wittrup, Antitumor Antibodies Can Drive Therapeutic T Cell Responses. *Trends Cancer.* **3**, 615–620 (2017).

230. L. Deng, H. Zhang, Y. Luan, J. Zhang, Q. Xing, S. Dong, X. Wu, M. Liu, S. Wang, Accumulation

of Foxp3+ T Regulatory Cells in Draining Lymph Nodes Correlates with Disease Progression and Immune Suppression in Colorectal Cancer Patients. *Clin Cancer Res.* **16**, 4105–4112 (2010).

231. P. Devi-Marulkar, S. Fastenackels, P. Karapentiantz, J. Goc, C. Germain, H. Kaplon, S. Knockaert, D. Olive, M. Panouillot, P. Validire, D. Damotte, M. Alifano, J. Murris, S. Katsahian, M. Lawand, M.-C. Dieu-Nosjean, Regulatory T cells infiltrate the tumor-induced tertiary lymphoïd structures and are associated with poor clinical outcome in NSCLC. *Commun Biology.* **5**, 1416 (2022).

232. T. J. Curiel, G. Coukos, L. Zou, X. Alvarez, P. Cheng, P. Mottram, M. Evdemon-Hogan, J. R. Conejo-Garcia, L. Zhang, M. Burow, Y. Zhu, S. Wei, I. Kryczek, B. Daniel, A. Gordon, L. Myers, A. Lackner, M. L. Disis, K. L. Knutson, L. Chen, W. Zou, Specific recruitment of regulatory T cells in ovarian carcinoma fosters immune privilege and predicts reduced survival. *Nat Med.* **10**, 942–949 (2004).

233. J. Shou, Z. Zhang, Y. Lai, Z. Chen, J. Huang, Worse outcome in breast cancer with higher tumor-infiltrating FOXP3+ Tregs: a systematic review and meta-analysis. *Bmc Cancer.* **16**, 687 (2016).

234. N. S. Joshi, E. H. Akama-Garren, Y. Lu, D.-Y. Lee, G. P. Chang, A. Li, M. DuPage, T. Tammela, N. R. Kerper, A. F. Farago, R. Robbins, D. M. Crowley, R. T. Bronson, T. Jacks, Regulatory T Cells in Tumor-Associated Tertiary Lymphoid Structures Suppress Anti-tumor T Cell Responses. *Immunity.* **43**, 579–590 (2015).

235. A. Boissonnas, A. Scholer-Dahirel, V. Simon-Blancal, L. Pace, F. Valet, A. Kissenpfennig, T. Sparwasser, B. Malissen, L. Fetler, S. Amigorena, Foxp3+ T Cells Induce Perforin-Dependent Dendritic Cell Death in Tumor-Draining Lymph Nodes. *Immunity.* **32,** 266–278 (2010).

236. J. Shimizu, S. Yamazaki, S. Sakaguchi, Induction of tumor immunity by removing CD25+CD4+ T cells: a common basis between tumor immunity and autoimmunity. *J Immunol.* **163**, 5211–8 (1999).

237. O. S. Qureshi, Y. Zheng, K. Nakamura, K. Attridge, C. Manzotti, E. M. Schmidt, J. Baker, L. E. Jeffery, S. Kaur, Z. Briggs, T. Z. Hou, C. E. Futter, G. Anderson, L. S. K. Walker, D. M. Sansom, Trans-Endocytosis of CD80 and CD86: A Molecular Basis for the Cell-Extrinsic Function of CTLA-4. *Science.* **332**, 600–603 (2011).

238. K. Wing, Y. Onishi, P. Prieto-Martin, T. Yamaguchi, M. Miyara, Z. Fehervari, T. Nomura, S. Sakaguchi, CTLA-4 Control over Foxp3+ Regulatory T Cell Function. *Science.* **322**, 271–275 (2008).

239. V. Ovcinnikovs, E. M. Ross, L. Petersone, N. M. Edner, F. Heuts, E. Ntavli, A. Kogimtzis, A. Kennedy, C. J. Wang, C. L. Bennett, D. M. Sansom, L. S. K. Walker, CTLA-4–mediated transendocytosis of costimulatory molecules primarily targets migratory dendritic cells. *Sci Immunol.* **4**, eaaw0902 (2019).

240. J. Han, Y. Zhao, K. Shirai, A. Molodtsov, F. W. Kolling, J. L. Fisher, P. Zhang, S. Yan, T. G. Searles, J. M. Bader, J. Gui, C. Cheng, M. S. Ernstoff, M. J. Turk, C. V. Angeles, Resident and circulating memory T cells persist for years in melanoma patients with durable responses to immunotherapy. *Nat Cancer.* **2**, 300–311 (2021).

241. P. Savas, B. Virassamy, C. Ye, A. Salim, C. P. Mintoff, F. Caramia, R. Salgado, D. J. Byrne, Z. L. Teo, S. Dushyanthen, A. Byrne, L. Wein, S. J. Luen, C. Poliness, S. S. Nightingale, A. S. Skandarajah, D. E. Gyorki, C. M. Thornton, P. A. Beavis, S. B. Fox, K. C. F. C. for R. into F. B. C. (kConFab), P. K. Darcy, T. P. Speed, L. K. Mackay, P. J. Neeson, S. Loi, Single-cell profiling of breast cancer T cells reveals a tissue-resident memory subset associated with improved prognosis. *Nat Med.* **24**, 986–993 (2018).

242. N. Prokhnevska, M. A. Cardenas, R. M. Valanparambil, E. Sobierajska, B. G. Barwick, C. Jansen, A. R. Moon, P. Gregorova, L. delBalzo, R. Greenwald, M. A. Bilen, M. Alemozaffar, S. Joshi, C. Cimmino, C. Larsen, V. Master, M. Sanda, H. Kissick, CD8+ T cell activation in cancer comprises an initial activation phase in lymph nodes followed by effector differentiation within the tumor. *Immunity,* **56**, 107-124.e5 (2022).

243. J. Humeau, J. L. Naour, L. Galluzzi, G. Kroemer, J. G. Pol, Trial watch: intratumoral immunotherapy. *Oncoimmunology*. **10**, 1984677 (2021).

244. M. Soumillon, D. Cacchiarelli, S. Semrau, A. van Oudenaarden, T. S. Mikkelsen, Characterization of directed differentiation by high-throughput single-cell RNA-Seq. *BioRxiv*, (2014). doi: 10.1101/003236

245. A. Zhu, J. G. Ibrahim, M. I. Love, Heavy-tailed prior distributions for sequence count data: removing the noise and preserving large differences. *Bioinformatics*. **35**, 2084–2092 (2018).

246. M. I. Love, W. Huber, S. Anders, Moderated estimation of fold change and dispersion for RNA-seq data with DESeq2. *Genome Biol.* **15**, 550 (2014).

247. A. Butler, P. Hoffman, P. Smibert, E. Papalexi, R. Satija, Integrating single-cell transcriptomic data across different conditions, technologies, and species. *Nat Biotechnol.* **36**, 411–420 (2018).

248. Z. Gu, R. Eils, M. Schlesner, Complex heatmaps reveal patterns and correlations in multidimensional genomic data. *Bioinformatics*. **32**, 2847–2849 (2016).

249. T. Wu, E. Hu, S. Xu, M. Chen, P. Guo, Z. Dai, T. Feng, L. Zhou, W. Tang, L. Zhan, X. Fu, S. Liu, X. Bo, G. Yu, clusterProfiler 4.0: A universal enrichment tool for interpreting omics data. *Innovation*. **2**, 100141 (2021).

250. B. H. Kang, B. M. Lax, K. D. Wittrup, Yeast Surface Display. *Methods Mol Biology*. **2491**, 29–62 (2022).

251. J. A. M. Ramshaw, N. K. Shah, B. Brodsky, Gly-X-Y Tripeptide Frequencies in Collagen: A Context for Host–Guest Triple-Helical Peptides. *J Struct Biol.* **122**, 86–91 (1998).